FINAL REPORT

Project Title: Reduction of Annealing Times for Energy Conservation in Aluminum Processing

Covering Period: August 1, 2001 through August 30, 2005

Date of Report: August 31st, 2005

Recipient: Carnegie Mellon University, 5000 Forbes Av., Pittsburgh, PA 15213

Award Number: DE-FC07-01ID14194

Subcontractors: N/A

Other Partners: Alcoa Technical Center

Contact(s): Prof. Anthony D. Rollett, 412 268 3177, rollett@andrew.cmu.edu
Dr. Hasso Weiland, 724 337 3133, Hasso.Weiland@alcoa.com
Mohammed Alvi, malvi@andrew.cmu.edu (Ph.D. Student)
Abhijit Brahme, abrahme@andrew.cmu.edu (Ph.D. Student)

Project Team: DOE-OIT Manager: Thomas Robinson; Field Office Program Manager: Bradley Ring, DOE/Golden

Project Objective: Carnegie Mellon University was teamed with the Alcoa Technical Center with support from the US Dept. of Energy (Office of Industrial Technology) and the Pennsylvania Technology Investment Authority (PTIA) to make processing of aluminum less costly and more energy efficient. Researchers in the Department of Materials Science and Engineering have investigated how annealing processes in the early stages of aluminum processing affect the structure and properties of the material. Annealing at high temperatures consumes significant amounts of time and energy. By making detailed measurements of the crystallography and morphology of internal structural changes they have generated new information that will provide a scientific basis for shortening processing times and consuming less energy during annealing.

Background: The status of the Domestic Technology for the thermomechanical processing of aluminum alloy intended for sheet and plate product is as follows. Hot rolling processes are aimed at breaking down as-cast structures in Direct-Chill (DC) ingots. Critical to the success of this stage of the processing is the refinement of the as-cast microstructure in terms of both grain morphology and the crystallographic orientations present; we will refer to the latter as *texture*. Achieving correct texture is

particularly important to the application of such materials as 5xxx for can closures and 3xxx for beverage can stock. In particular, it is standard practice to anneal partially broken-down slabs for long times in order to ensure that recrystallization is completed before continuing the hot rolling process. Simple models exist that describe the rate at which the recrystallization process takes place but no information is available on the texture development. This proposal project will remedy that lack by measuring texture-dependent recrystallization rates (kinetics).

Status: The project is complete. Three different commercial purity aluminum alloys (AA1050, AA5005 and AA3003) were studied. The main applications of these (non-heat treatable) alloys are beverage cans, automotive products etc. Recrystallization and texture evolution are two very important transformations in the thermo-mechanical processing of these alloys. These transformations are of critical importance for aluminum industry as they are directly related to energy consumption and properties of the finished products. The main aim of this project is to further increase our current understanding of recrystallization and texture evolution using advanced analytical tools like Electron Backscatter Diffraction (EBSD).
The project was divided into two main parts - experimental data collection and extraction of critical parameters from experimental data forming one part and simulation of recrystallization from the experimental data and comparison of experimental results with simulation being the other part. The experimental data collection and analysis involved annealing of as-received samples and scanning them in an EBSD system. The main approach followed in the experimental analysis was that of identification of the most important parameters required for quantification of recrystallization and texture evolution. This analysis required development of algorithms for extraction of the parameters from the experimental data. All experimental data collection and analysis was completed for the three alloys. Similar procedures were applied to the three alloys; therefore the differences in their behavior delineated the effect of variation of different alloying elements on recrystallization and texture evolution in aluminum alloys. To aid in understanding the effect of processing conditions (temperature and strain), the as-received hot rolled samples were also deformed in a specially designed deformation simulator capable of controlling deformation parameters.

Accomplishments: Recrystallization and texture evolution in three commercial purity aluminum alloys were studied to understand the effect of composition and processing conditions. All the as-received metals were hot rolled to high strains. Annealing treatments were carried out on these as received hot rolled samples followed by scanning in a Scanning Electron Microscope

(SEM) with an EBSD system attached. Some of the main experimental accomplishments of the project are summarized as follows:-

1. New procedures and parameters were established for quantifying the extent of recrystallization from electron back scatter diffraction (EBSD) scans based on orientation spread within grains: high orientation spread was found to be a reliable indicator of deformed grains versus low orientation spread for recrystallized grains.
2. The software for performing computer simulation of recrystallization has been transferred to the industrial partner (Alcoa) and is being used to study in-house thermomechanical processing.
3. Controlling mechanisms were determined for recrystallization in hot rolled aluminum alloys (migration of high angle grain boundaries).
4. The differences between deformed, recovered and recrystallized grains were demonstrated based on easily identifiable parameters (GAM and GOS).
5. The activation enthalpy associated with recrystallization in commercial purity Al (AL-1050) was similar to that of diffusion of iron in aluminum. This result is in agreement with previous work and suggests that the kinetics of recrystallization are dominated by solute drag of the grain boundaries by impurities such as iron.
6. The results of performing tests in Alcoa's Deformation Simulator showed that low deformation temperatures (200°C) result in deformed microstructures similar to those in the material supplied by Alcoa. High temperatures around 400°C, however, resulted in nearly recrystallized microstructures.
7. By observing the nucleation and growth of recrystallized cube-oriented grains, we were able to quantify the preference for their growth in different deformation orientations.
8. Similar observations on the variations in volume fractions of deformation texture components during annealing showed that the S component is consumed more rapidly when compared to the Brass and Copper components.
9. Variations in composition affected the recrystallization process. Addition of Mg accelerated recrystallization kinetics (most likely because solid solution hardening giving rise to larger driving forces); addition of Mn leads to precipitation of second phase particles.
10. A set of tools called "Microstructure Builder" (MS Builder) were assembled that permit generate 3 dimensional microstructures which statistically similar to the experimental input microstructures (2 dimensional).
11. The effectiveness of MS Builder was demonstrated by generating 3-D microstructure to simulate hot rolled Al1050 samples. The

generated microstructures showed reasonable agreement with the size distribution in the experimental observations. The crystallographic orientations distributions were a good match to those observed in the Al1050 samples.

12. A method for calculating the stored energy using electron backscatter data was developed. With this method, we calculated the variation in stored energy as a function of crystallographic orientation and inserted the values into the simulations of recrystallization thereby improving the accuracy of texture development.
13. A method was devised for adding nuclei to the generated 3-D microstructure to reflect the experimental observations. The analysis of the data provided the following information:
    a. Most nuclei have similar texture to the parent grains. This conforms to the subgrain coarsening theory for generation of nuclei (from the deformed structure).
    b. Most of the nuclei occurred on, or close to grain boundaries in the deformed microstructure.
    c. Grain boundaries adjacent to the S oriented grains had the highest probability of nuclei formation.
14. The recrystallization kinetics were most sensitive to grain geometry and nuclei placement.
15. A method was developed to predict texture evolution during the process of recrystallization.
16. A basic sensitivity analysis on the factors that control or influence the process of recrystallization revealed the following ranking of the factors in order of decreasing importance:
    a. Oriented nucleation.
    b. Oriented growth.
    c. Stored energy.

This summarizes the main findings of the study. More detailed information about the actual experimental details can be found in the attached theses by Mohammed Alvi (experimental) and Abhijit Brahme (simulation) and the separate report on AA3003.

Abstract from thesis submitted by Mohammed Alvi for his PhD.

The kinetics of recrystallization and texture evolution in hot rolled aluminum alloys 1050 and 5005 have been analyzed. The as-received samples were given isothermal annealing treatments at different temperatures and their recrystallization kinetics and texture evolution were obtained as a function of annealing temperatures and times. Two different methods were used to measure recrystallization kinetics - microhardness

variations and mapping with Electron BackScattered Diffraction (EBSD) also known as Orientation Imaging Microscopy (OIM). Microhardness variations represent an average behavior against which the methods based on EBSD were compared. Intragranular orientation variation (short-range and long-range) was found to be an important parameter for partitioning EBSD maps into deformed and recrystallized regions. Comparable recrystallization kinetics were obtained from microhardness variations and EBSD. Microstructural Path Modeling (MPM) was used for analyzing recrystallization kinetics. Recrystallization in hot rolled aluminum alloys 1050 and 5005 was determined to be site-saturated and controlled by migration of high-angle boundaries.

The ability to partition deformed and recrystallized regions based on intragranular orientation variations provided an important tool for analyzing and understanding the texture evolution in deformed and recrystallized grains independently of each other. Rolling orientation components S and Brass exhibited very different effects on annealing. While the deformed S orientation was observed to decay very fast, Brass deformed grains remained stable to annealing. Recrystallized grains had Cube as the main texture component, which nucleated from the deformed Cube bands. The recrystallized Cube grains exhibited both a nucleation and growth advantage when compared to the other recrystallized orientations. Although the nucleation advantage of Cube recrystallized grains was observed to be present at all annealing temperatures, the growth advantage for these grains were present only at low annealing temperatures.

Abstract from PhD thesis submitted by Abhijit Brahme for his PhD:

The main aim of this work was to model microstructural evolution during recrystallization. This was achieved by characterizing it in terms of recrystallization kinetics and texture development and by identifying factors that exert the greatest effect on the recrystallization process. To achieve the above, geometric and crystallographic observations from two orthogonal sections through a polycrystal were used. Using these as input to the computer simulations, a statistically representative three-dimensional model was created. Assignment of orientations to the grains was done such that nearest neighbor relationships match the observed distributions. The microstructures thus obtained were allowed to evolve using a Monte-Carlo simulation. A parametric study was done to study the effects of various factors on recrystallization kinetics and texture development during microstructural evolution.

A set of software tools (*Microstructure builder*) were developed to generate the microstructures. The process involved the use of a ellipsoidal packing method combined with a voxel-based tessellation technique to create a 3 dimensional digital microstructure having the desired set of grain aspect ratios. Orientation assignment to the grains in the microstructure was done using a simulated annealing method that minimized the error between the orientation distribution function (ODF) and misorientation distribution function (MDF) of the measured and simulated materials.

The effect of grain geometry and placement of nuclei on recrystallization kinetics was studied. A close match in the recrystallization kinetics as measured in the experiments and the simulations was found to be most sensitive to the accuracy with which the geometry of the simulated microstructure matched that observed in experiments.

Also the effects of anisotropy, both in energy and in mobility, stored energy and oriented nucleation on overall texture development were studied in the light of various established competing theories of oriented nucleation (**ON**), oriented growth (**OG**) and orientation pinning (**OP**). The results from the simulations suggested that all of oriented nucleation, mobility anisotropy, stored energy and energy anisotropy (listed in order of their relative importance) influence texture development.

Patents: No patents were generated under this project.

Publications/Presentations: (Cumulative List)

Publications

A. Brahme, D. M. Saylor, J. Fridy, A. D. Rollett, "Statistically Representative Three-Dimensional Microstructures for Modeling Microstructural Evolution in Aluminum," in 1st International Symposium on Metallurgical Modeling for Aluminum Alloys, *in press*, ed. Tiryakioglu, M. Lalli, L.A. (2003)

Alvi, M.H., El-Dasher, B.S., Rollett, A.D. "Analysis of recrystallization kinetics from microstructural evolution and micro-hardness determination," in Hot Deformation of Aluminum Alloys III, p.3-12, ed. Jin, Z., Beaudoin, A., Bieler, T., and Radhakrishnan, B. (2003).

Alvi, M.H., Cheong, S., Weiland, H., Rollett, A.D. "Microstructural evolution during recrystallization in hot rolled Aluminum Alloy 1050," in 1st International Symposium on Metallurgical Modeling for Aluminum Alloys, *in press*, ed. Tiryakioglu, M. Lalli, L.A. (2003)

Alvi, M.H., Cheong, S., Weiland, H., Rollett, A.D. "Recrystallization and Texture Development in Hot Rolled 1050 Aluminum", in 2nd International Conference on Recrystallization and Grain Growth, *Materials Science Forum*, **467-470**, pp. 357-362 (2004).

Rollett, A.D., Alvi, M.H., Brahme, A.P., Fridy, J., Weiland, H., Suni, J., and Cheong, S. "Texture dependent recrystallization in Aluminum 5005", in 9th International Conference of Aluminum Alloys (ICAA-9), *Materials Forum*, **28**, pp. 1173-1178 (2004).

"Statistically Representative Three-Dimensional Microstructures Based on Orthogonal Observation Sections," D.M. Saylor, J. Fridy, B.S. El-Dasher, K.-Y. Jung, and A.D. Rollett, *Metallurgical & Materials Transactions*, **35A**, 1969-1979 (2004).

Presentations

A. D. Rollett, M. H. Alvi, A. Brahme, S. Cheong, H. Weiland, E. A. Holm, M. Miodownik, "Recrystallization in Hot Rolled Al 1050; Abnormal Grain Growth in Subgrain Structures," invited seminar at the Materials Department of the Risø National Laboratory, Roskilde, Denmark, 5th December, 2003.

A.D. Rollett, M. Miodownik, E.A. Holm, D. Saylor, and J. Fridy, "3D Simulation of Grain Growth & Recrystallization," invited presentation at a workshop organized by the Air Force Office of Scientific Research (AFOSR) entitled "*Quantification of Microstructure and the Linkage to Property Modeling,"* Hinterzarten, Germany, 27 – 30 July 2003.

A. D. Rollett, "Some Aspects of Recrystallization," invited seminar at the Department of Materials Physics and Technology, Technical University of Hamburg-Harburg, Germany, 3rd December, 2003.

A.D. Rollett, A. Brahme, M. Alvi, C.-C. Yang, M. Demirel, A. Kuprat, D. George, "Realistic 3D Microstructures for Computer Simulation of Microstructural Evolution," invited lecture at the Annual Meeting of the American Ceramics Society, Nashville, TN, 28-30th April, 2003.

Mohammed Haroon Alvi, "Recrystallization kinetics in Aluminum Alloy 1050", General Abstract, TMS Fall Conference, October 2002.

Mohammed Haroon Alvi, "Analysis of recrystallization kinetics from microstructural evolution and micro-hardness determination," Hot Deformation of Aluminum Alloys III, TMS Annual Conference, March 2003.

Mohammed Haroon Alvi, "Microstructural evolution during recrystallization in hot rolled Aluminum Alloy 1050", 1st International Symposium on Metallurgical Modeling for Aluminum Alloys, ASM Materials Solutions Conference, October 2003.

Abhijit Brahme "Statistical Representative Three Dimensional Microstructures for Modeling Microstructural evolution in Aluminum" Material Solutions Conference 2003, October 13-15, 2003, Pittsburgh, PA.

Abhijit Brahme "The 3-D Microstructure Builder" MS&T '04, September 26-29, 2004, New Orleans, Louisiana

Abhijit Brahme "Simulation of Texture-Dependent Recrystallization in 1050 Aluminum" 2005 TMS Annual Meeting & Exhibition, February 13-17, 2005, San Francisco, CA

A.D. Rollett, B.S. El-Dasher and B.L. Adams, “Why should one study grain boundaries? Electrical Steels, Electro-ceramics and more,” invited Seminar at the Physics Department, University of Saarland, Saarbrücken, Germany, 9th December, 2003.

A. D. Rollett, B. S. El-Dasher, B. L. Adams, “Grain boundaries as a barrier to slip”, Workshop on Multiscale Modeling Methods, Berkeley, January 2004.

A.D. Rollett, D. Saylor, J. Fridy, A. Brahme, C. Cornwell, R. Noack, “3D Polycrystal Microstructures for Simulation based on Measurements”, seminar at CISD/ARL, 10 February, 2004.

A.D. Rollett, “Edge Matching at Grain Boundaries and the Five Macroscopic Degrees of Freedom”, for the Hume-Rothery Symposium: Structure and Diffusional Growth Mechanisms of Irrational Interphase Boundaries, TMS Annual Meeting, March 2004, Charlotte, NC.

P. A. Manohar, A. D. Rollett and J. R. Morris: "Development of an Efficient, Parallel Potts Model for Computer Simulation of Grain Growth in 2D", invited presentation for the Symposium on Computational Thermodynamics and Phase Transformations at the TMS Annual Meeting, March 2004, Charlotte, NC.

A.D. Rollett, S. Kalidindi, J. Houskamp, B.L. Adams, “Texture Optimization via Grain Growth and Recrystallization”, invited presentation at the Symposium on Microstructural Design, TMS Annual Meeting, March 2004, Charlotte, NC.

A.D. Rollett, “Growth of the Cube Component in FCC Deformation Textures: Simulation & Theory,” for the Roger Doherty Symposium, TMS Annual Meeting, March 2004, Charlotte, NC.

A.D. Rollett, D. Saylor, J. Fridy, A. Brahme, C. Cornwell, R. Noack, “3D Polycrystal Microstructures for Simulation based on Measurements”, seminar at NRL, 6 May 2004.

A.D. Rollett, “Abnormal Grain Growth and the Potts Model”, invited lecture at the Society for Industrial and Applied Mathematics (SIAM) Meeting, Los Angeles, May 2004.

A.D. Rollett, G.S. Rohrer, D.J. Srolovitz, M. Taheri, P. Manohar, M. Alvi, A. Brahme, “Grain Boundary Properties and Their Impact on Texture Development,” invited lecture at ITAP-2 (2nd Intl. Conf. on Textures and Properties), University of Metz, July 4th, 2004.

A.D. Rollett, D. Saylor, J. Fridy, A. Brahme, S.-B. Lee, R. Campman, C. Cornwell, R. Noack, “3D Polycrystal Microstructures for Simulation Based on Measurements,” seminar (invited) at the Materials Laboratory, Air Force Research Laboratory, Wright-Patterson Air Force Base, Dayton, OH, 9th August 2004.

"In-Situ Quantification of Solute Effects on Grain Boundary Mobility and Character in Aluminum Alloys During Recrystallization," Mitra L. Taheri, Anthony D. Rollett, and Hasso Weiland,. 2nd Intl. Conf. on Recrystallization and Grain Growth, Annécy, France, August 2004 (poster).

"Recrystallization and Texture Development in Hot Rolled 1050 Aluminum," M.H. Alvi, S. Cheong, H. Weiland, A.D. Rollett, 2nd Intl. Conf. on Recrystallization and Grain Growth, Annécy, France, August 2004 (poster).

"3D Microstructure Builder", A.D. Rollett, D. Saylor, A. Brahme, J. Fridy, S.-B. Lee, Invited Lecture in the Symposium on 3-Dimensional Materials Science, Materials Science & Technology 2004, New Orleans, Sept. 2004.

"3D Microstructure Generation with Grain Shape & Crystallographic Orientation", A.D. Rollett, D. Saylor, J. Fridy, A. Brahme, S.-B. Lee, C. Cornwell, R. Noack, Plasticity-05, Kauai, January 2005.

"Simulation of Texture-Dependent Recrystallization in 1050 Aluminum", Abhijit Brahme, Joseph Fridy, Anthony D. Rollett, Hasso Weiland, Jaakko Suni, TMS Annual Mtg., San Francisco, Feb. 14th -17th 2005.

"Growth of Special Texture Components during Grain Growth: Simulation (& Theory)", A.D. Rollett, A. Brahme, J. Gruber, TMS Annual Mtg., San Francisco, Feb. 14th -17th 2005.

"Recrystallization and Texture Evolution in Aluminum Alloy 1050", M.H. Alvi, A.D. Rollett, TMS Annual Mtg., San Francisco, Feb. 14th -17th 2005.

"3D Digital Microstructures and Microstructural Evolution", A.D. Rollett, D. Saylor, J. Fridy, A. Brahme, S.-B. Lee, R. Campman, S. Sintay, 3rd Conference on Microstructology, Birmingham, AL, May, 2005.

"3D Digital Microstructures and Microstructural Evolution", D. Saylor, J. Fridy, A. Brahme, S.-B. Lee, R. Campman, S. Sintay, Seminar at the Texture Laboratory (LETAM), University of Metz, June 20th 2005.

"Grain Boundaries: Populations, Energy, Mobility, Application", G.S. Rohrer, D.M. Saylor, A.D. Rollett, T. Bennett, H. Miller, B. El Dasher (LLNL), Y. Pang, M. Taheri, P. Wynblatt, Seminar at the Texture Laboratory (LETAM), University of Metz, July 5th 2005.

"3D Digital Microstructures and Microstructure Evolution", A.D. Rollett, D. Saylor, J. Fridy, A. Brahme, S.-B. Lee, R. Campman, S. Sintay, R. Lebensohn, Keynote Lecture at the International Conference on Micromechanics & Microstructure Evolution, Madrid, Spain, Sept. 14th, 2005.

"Bridging Simulations and Experiments in Microstructural Evolution: Example of Recrystallization in Aluminum", A.D. Rollett, J. Gruber, M. Alvi, A. Brahme, D. Saylor, J. Fridy, S.-B. Lee, invited seminar at the National Institute of Standards and Technology (NIST), 5th October, 2005.

"Bridging Simulations and Experiments in Microstructural Evolution: Example of Recrystallization in Aluminum", A.D. Rollett, J. Gruber, M. Alvi, A. Brahme, D. Saylor, J. Fridy, S.-B. Lee, invited seminar at Drexel University, Dept. of Materials Engineering, 11th November, 2005.

Milestone Status Table:

Identification Number	Description	Planned Completion Date	Actual Completion Date	Comments
1/ Month 3	Preliminary optical and scanning electron microscopy on 1050, 5005.	Start+3	15 Jan 02	Completed
2/ Month 6	Complete preliminary hot deformation experiments on 1050.	Start+6	30 Sept. 02	Completed
3/ Month 9	Construct preliminary model of recrystallization kinetics.	Start+9	15 Apr 02	Completed. A series of isothermal annealing experiments were analyzed in terms of the JMAK theory to obtain an activation energy and growth exponent for 1050.
4/ Month 12	Complete recrystallization experiments on 1050.	Start+12	May 04	Completed
5/ Month 15	Characterization of recrystallization kinetics on 1050.	Start+15	May-05	Completed
6/ Month 18	Complete hot deformation experiments on 5005.	Start+18	30 June 02	Completed.
7/ Month 24	Development of analysis of recrystallization kinetics with model and OIM.	Start+24	June 04	Completed
8/ Month 27	Complete modeling of 1050.	Start+27	August 05	Completed. Results showed that all the factors considered in the literature play a role in the development of microstructure and texture during recrystallization in this material.

9/ Month 30	Complete recrystallization experiments on 5005.	Start+30	March 04	Completed
10/ Month 36	Analysis of texture, recrystallization kinetics data: transfer to modeling group at commercial partner.	Start+36	September 05	Recrystallization kinetics for the as-received 1050 transmitted to industrial partner (Dr. S. Cheong).
11/ Month 39	Design of experiment, with emphasis on contrasting current, conventional process with a single new, proposed process. New process will be designed so as to provide full recovery of the materials (i.e. complete recrystallization).	Start+39	Feb-05	Completed
12/ Month 42	Conventional material obtained. Annealed material from the new trial process obtained.	Start+42	Jan-05	Alcoa supplied samples of 3003 from 3 different processing histories
13/ Month 45	Conventional and New Process materials analyzed. Analysis will include, at a minimum, grain size and shape, texture (orientation distribution), fraction recrystallized.	Start+45	September-05	Completed
14/ Month 48	Delivery of final report including evaluation of the degree to which the program has succeeded in reducing annealing times, in addition to more basic information on quantification of recrystallization behavior and simulation techniques.	Start+48	December-05	

Budget Data (as of Dec. '05):

			Approved Spending Plan			Actual Spent (Dec. '05)		
Phase / Budget Period			DOE Amount	Cost Share	Total	DOE Amount	Cost Share	Total
	From	To						
Year 1	8/01	7/02	80,000	70,000*	150,000			
Year 2	8/02	7/03	80,000	70,000*	150,000			
Year 3	8/03	7/04	80,000	70,000*	150,000			
Year 4	8/04	7/05	80,000	70,000*	150,000			
		Totals	320,000	280,000*	600,000	331,120	*284,683	616,966

No Spending Plan is included because the project is complete.

* The cost sharing includes $66,076 of in-kind cost-share by the industrial partner, Alcoa, which was expended in the form of materials supplied, and research services provided to the project at the Alcoa Technical Center. Services included assistance with development of characterization

and performing tests in the Deformation Simulator (a specialized mechanical testing system that emulates real life processing in rolling mills).

Hot rolling of Aluminum Alloy 3003

M.H. Alvi, September 2005

1. Introduction

Hot rolled samples of Aluminum Alloy 3003 (AA3003) were analyzed for microstructural and textural evolution, by using the GOS-GAM approach developed for Aluminum Alloys 1050 and 5005. This report presents the analysis of as received samples of AA3003 at two different deformation conditions. Delayed delivery of the material to Carnegie Mellon University meant that only the deformed condition could be analyzed and no annealing was attempted.

2. Chemical Composition

Aluminum Alloy 3003 is a commercial purity alloy used typically for beverage cans and other light weight applications. One of the main components for AA3003 is Manganese (Mn), which has low solubility in Al and forms large second phase particles in the alloy. These particles not only have a strong influence on the mechanical properties of the material, but also influence microstructural and textural evolution of the alloy upon deformation and annealing of deformed samples. Chemical composition of hot rolled AA3003 used in present analysis is given in Table 1.

Table 1 Chemical composition of AA3003 (wt %)

Element	**Al**	**Si**	**Fe**	**Cu**	**Mn**	**Mg**	**Cr**	**Ni**	**Zn**	**Ti**
Wt %	98.103	0.200	0.500	0.100	1.070	0.001	0.002	0.007	0.010	0.007

Compared to AA1050 and AA5005, the concentration of Al in AA3003 is between the two alloys, whereas the concentration of Fe and Si is similar in all three alloys.

3. Processing history and experimentation

The deformation history of hot rolled AA3003 used in present study is given in Table 2.

Table 2 Deformation history of AA3003

Pass No.	Slab Temperature (°F)	Gauge (in.)	% Reduction
0	926	21.4	0
1	926	20.5	4.2
2	926	19.3	5.9
3	926	18.1	6.2
4	926	16.8	7.2
5	926	15.4	8.3
6	926	14	9.1
7	926	12.6	10.0
8	926	11.1	11.9
9	926	9.6	13.5
10	926	8.1	15.6
11	926	6.7	17.3
12	926	5.3	20.9
13	823	3.9	26.4
14	823	2.6	33.3
15	**796**	**1.3**	**50**
16	734	0.66	49.2
17	687	0.4	39.4
18	658	0.25	37.5
19	**527**	**0.125**	**50**

The samples for present analysis were obtained from the two 50% reduction passes (pass 15 and 19), shown in bold in Table 2. Microstructure and texture of these samples were analyzed by using EBSD scans (see PhD thesis by M.H. Alvi and other standard references for a description of this method). Small samples for EBSD analysis were obtained from the as-received slab. These samples were polished with 1μm alumina powder followed by electropolishing with a perchloric acid solution. Due to the presence of elongated grains in plan view (RD-TD sections), samples were taken on longitudinal cross-section (RD-ND section) in order to maximize the number of grains included in each scan. As it has been pointed out earlier for the case of AA1050 and AA5005, the elongated grains observed in the conventional RD-TD cross-section cannot be scanned completely, even with scan dimension of 1mm×1mm. Thus a scan on plan view captures only partial grains and therefore provides incomplete texture information. This problem was solved by changing the scan section to one with smaller grain dimensions. The texture of samples scanned on longitudinal cross section in EBSD compares well with that obtained from X-ray diffraction. A step size between 1μm and 2μm was used for EBSD scans.

4. Microstructural Evolution

The EBSD scans for deformed samples were analyzed for microstructural evolution. Microstructural features like fraction recrystallized, grain size, Grain Orientation Spread (GOS) and Grain Average Misorientation (GAM) were estimated for each grain within the scan. On average, three scans were obtained on each sample surface. Microstructures of samples deformed at the two temperatures are shown in Figure 1 and 2. These

microstructures are Inverse Pole Figure (IPF) representations where the color of each grain represents a given orientation. The orientation information is given in the standard triangle shown in Figure 3.

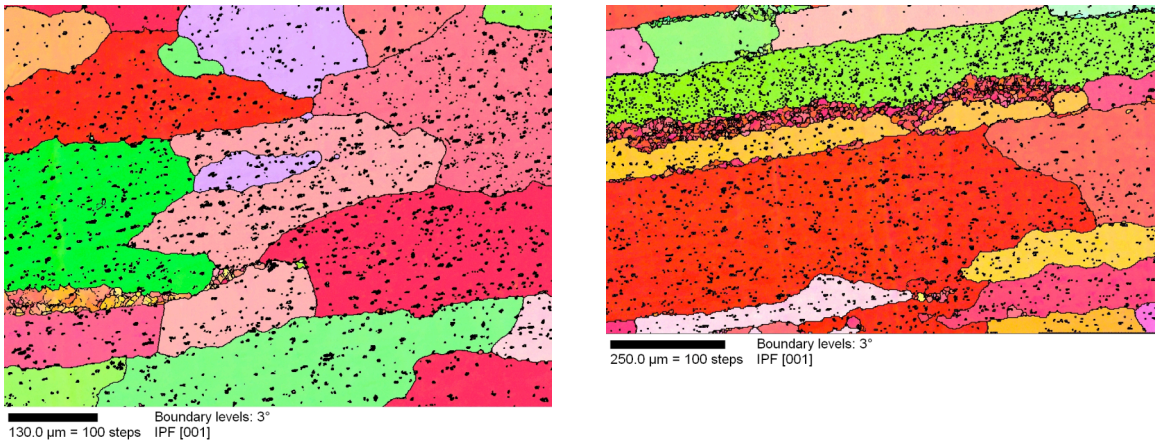

(a) (b)

Figure 1. Microstructures of samples hot deformed at 796°F. The samples were scanned in longitudinal cross section (RD-ND section), rolling direction being left to right for each microstructure. Second phase particles are clearly visible in these scans. Only a small fraction of grains have undergone large-scale deformation. (a) and (b) show different regions of the same sample surface.

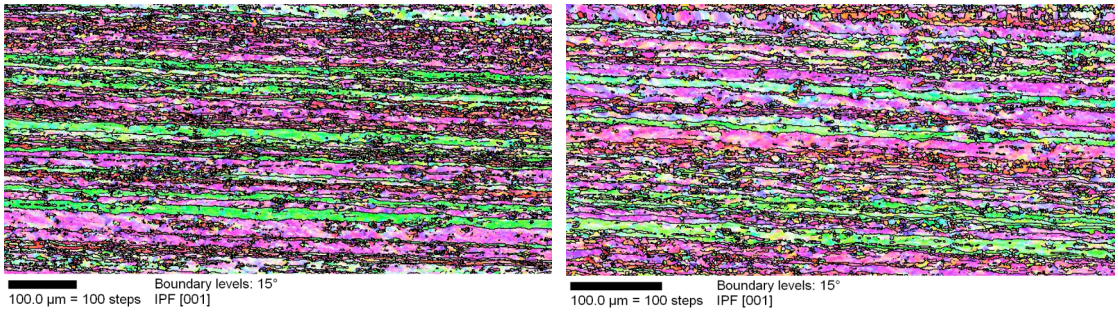

(a) (b)

Figure 2. Microstructures of samples hot deformed at 527°F. Two different regions of the sample surface were scanned as shown in (a) and (b). The samples were scanned in

longitudinal cross section (RD-ND section), rolling direction being left to right for each microstructure. Long bands of deformed grains can be observed in this section.

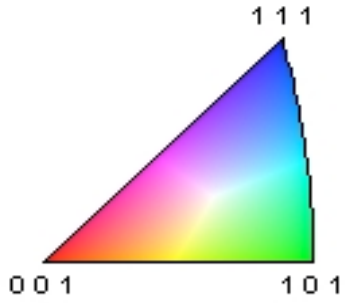

Figure 3. Standard stereographic triangle showing the relationship between surface orientation of a point and color.

The as-received hot deformed samples were also analyzed for fraction recrystallized. Samples deformed at 796°F were 90±2% recrystallized, while the samples deformed at 527°F were 10±3% recrystallized. The microstructures shown in Figure 1 clearly indicate the extent of deformation for the two treatments. The samples obtained from pass 15 have large undeformed grains and only selected regions have undergone some deformation. Although second phase particles are present in these grains, no low angle boundaries can be observed even at 3^{o} boundary misorientation (uniform solid color). For the samples deformed at 527°F (pass 19), the extent of deformation is large. Almost all grains have some orientation variations within them, indicated by the changes in color within each grain.

An important parameter to estimate the extent of deformation in a grain is the spread in orientation. This spread in orientation within a grain can be described by two alternative methods of Grain Orientation Spread (GOS) and Grain Average

Misorientation (GAM). GOS represents long range orientation variations within a grain and is obtained as the average misorientation between all the pixel pairs in a grain. GAM on the other hand represent short range orientation variations within a grain and is obtained as the average misorientation between neighboring pixel pairs only. GOS and GAM values of a grain can be used to describe its state as deformed, recovered and recrystallized. Deformed grains have large GOS (long range orientation variations) and GAM values (short range orientation variations). Recrystallized grains have low GOS and GAM values. Recovered grains on the other hand have and intermediate state of local rearrangement by subgrain formation and growth, given by low GAM and high GOS values. Thus a grain by grain comparison of GAM and GOS values can be used to completely describe the state of sample as deformed, recovered or recrystallized. Figure 4 (a) and (b) shows a comparison of GAM and GOS values for microstructures shown in Figure 1 (a) and (b) respectively, for samples deformed at high temperature (Pass # 15).

As seen in Figure 1(a), all the grains are still in recrystallized state (undeformed, no internal boundaries), therefore, have GOS and GAM nearly equal to each other. All the points in Figure 4 (a) have GOS and GAM values less than 3° and lie near to the 1:1 line, indicating that all grains are still recrystallized. The grains in Figure 1 (b) show some deformation in the center of microstructure, seen as a long thin band of red grains with many boundaries. This result is also evident in Figure 4 (b), where few points have high GOS and GAM values (GOS greater than 3°). Another important feature observed in Figure 4 (b) is that the GOS is greater than GAM for these high GOS grains. As pointed out earlier, this microstructural feature of high GOS and low GAM indicates

recovery of deformed samples. Since the deformation temperature is high (796F), extensive recovery of deformed grains is expected.

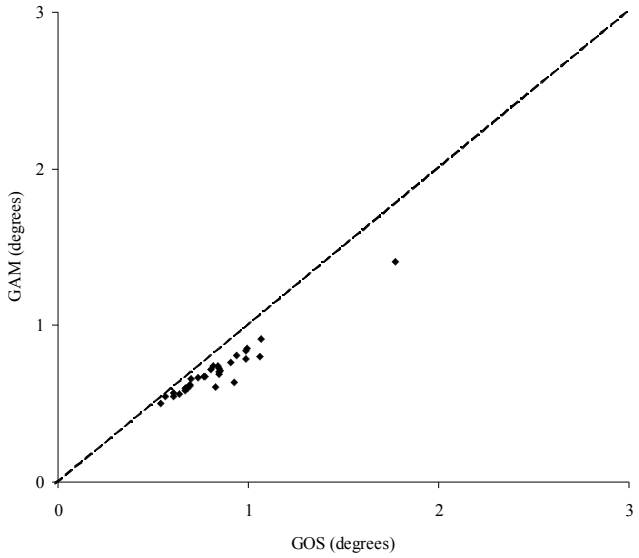

Figure 4 (a) Comparison of GAM and GOS values of microstructure in Figure 1 (a). All the points lie near the 1:1 line, indicating recrystallized grains.

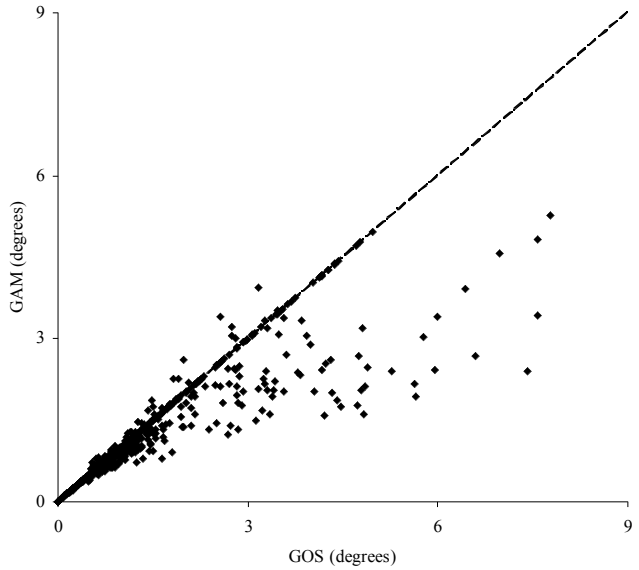

Figure 4 (b) Comparison of GAM and GOS values of microstructure in Figure 1 (b). Points lying below 1:1 line and have GOS greater than 3° represent deformed grains.

For the microstructures shown in Figure 2 (a) and (b), the GAM and GOS values are shown in Figure 5 (a) and (b), respectively. The elongated deformed grains are shown here by points having GOS greater than 3° and GAM greater than 1°. Since the two microstructures are similar, the plots in Figure 5 (a) and (b) also show similar variations. Since the deformation is high, some concurrent recovery of deformed samples also takes place, indicated here by grains having GOS values greater than the corresponding GAM values. The points lying below 1:1 line in Figures 5 (a) and (b) represent the grains with GOS greater than GAM.

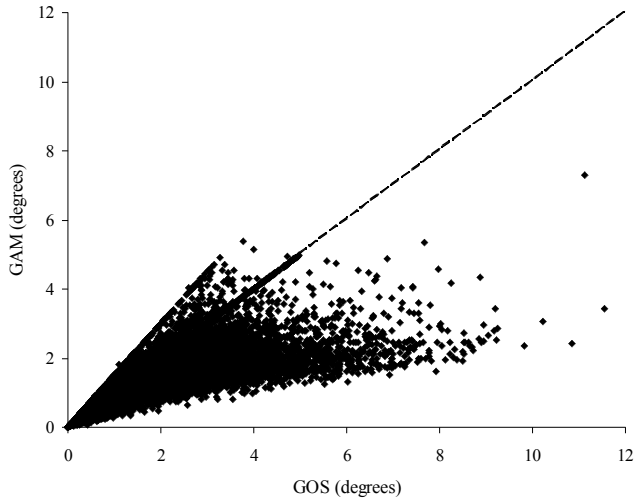

Figure 5 (a) GOS and GAM values for microstructure shown Figure 2 (a). Elongated deformed grains are shown hereby high GOS values.

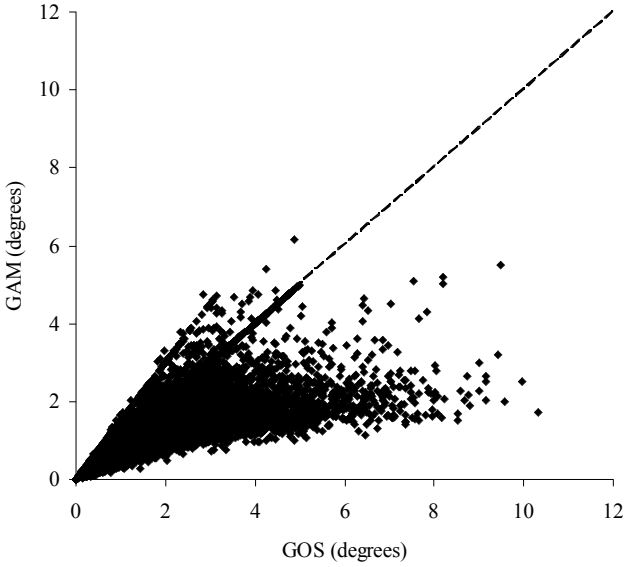

Figure 5 (b) GOS and GAM values for the microstructure shown Figure 2 (b). High GOS and GAM values were observed, indicating deformed microstructure, and GOS values higher than the corresponding GAM values were observed for grains, suggesting recovery of deformed grains.

5. Texture of hot rolled samples

Texture analysis of hot rolled samples was performed from EBSD scans for samples deformed at the two temperatures. The present study provides an important opportunity to analyze the effect of deformation conditions on evolution rolling texture in aluminum alloys. The differences in rolling temperatures and total strain in the samples can be used to understand the effect of deformation parameters on the volume fraction of different texture components. Orientation Distribution Functions (ODF's) corresponding to the microstructures shown in Fig 1 and 2 are shown in Figure 6 and 7.

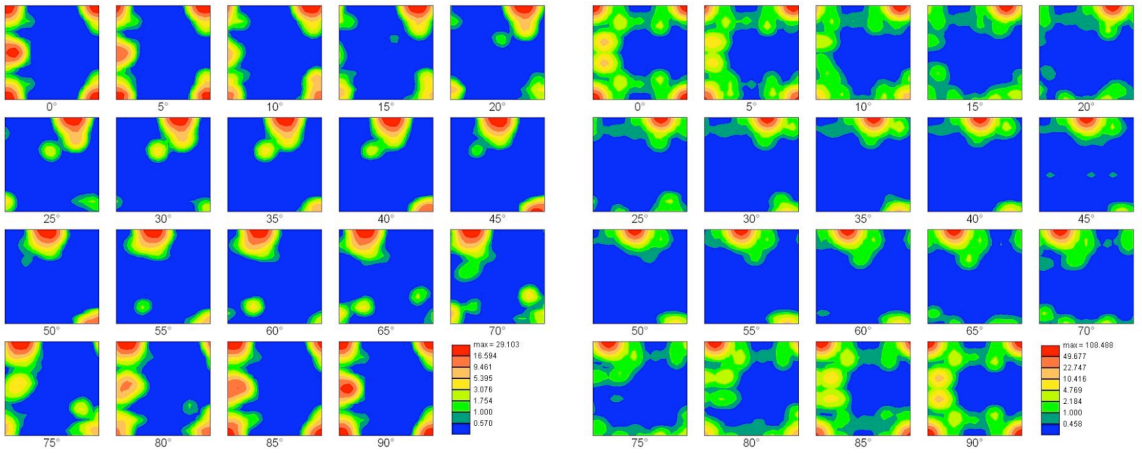

(a) (b)

Figure 6 ODF's corresponding to the microstructures shown in Figure 1 (a) and (b) respectively, for samples deformed at 796F. Cube texture is the dominant texture component. However, due to the large grain size, not much can be said about the average texture of the deformed samples. Significant differences were also observed for the two scans due to the heterogeneity of samples and large grain sizes.

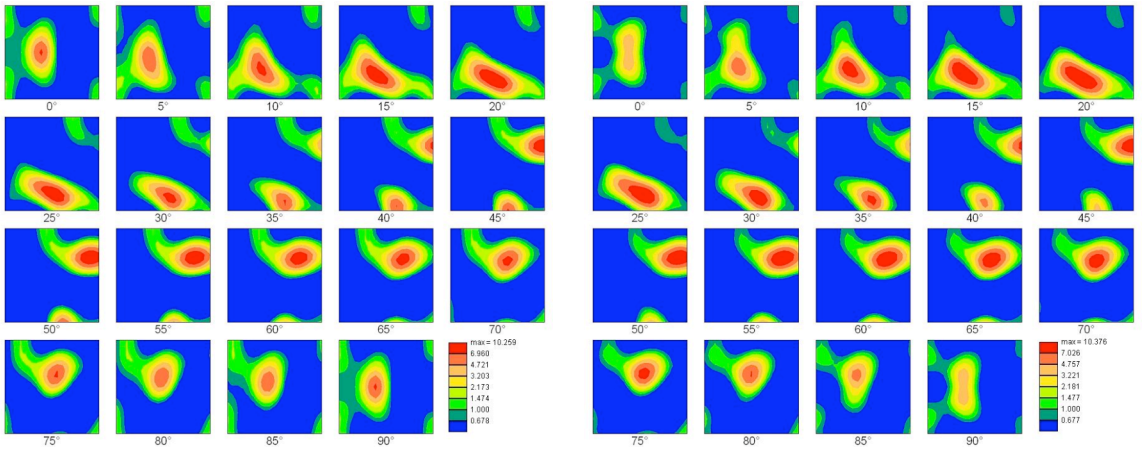

Figure 7 ODF's corresponding to the microstructures shown in Figure 2 (a) and (b) respectively, for samples deformed at 527 F. Strong rolling texture was observed for these samples. Almost similar textures were obtained from the two scans, indicating uniformity of microstructures for samples rolled at 527F.

The deformation textures at the two rolling temperatures clearly indicate the differences due to the deformation parameters. The main parameter affecting the overall texture of deformed samples is the total strain in the sample. For the samples deformed at 527F (Pass # 15), the overall strain was higher as compared to the samples deformed at 796F (Pass # 19). Elongated grains were formed at the higher strains, leading to rolling texture (Brass, Copper and S components). Another important feature observed in these scans is the small amount of cube texture. These cube grains might have been formed due the second phase particles. When the overall strain was low, no significant deformation was observed in the grains and the grains remain essentially dislocation free. Some Cube texture was observed for these grains, but this is not representative of the overall texture of the sample as the grain size was quite large and only free grains were captured in the EBSD scans. Thus an important point is observed about the effect of rolling conditions on the texture evolution. The evolution of rolling texture depends upon the overall strain in the material.

6. Conclusions.

Hot rolled samples of AA3003 were analyzed at two different deformation temperatures. Although strain in the pass was same for the two temperatures, the overall strain was different. Microstructures for the samples deformed at higher temperature show dislocation free grains (low GOS and GAM) and no changes in the texture. Elongated deformation bands were observed for the samples deformed at 527F. Grains had high GOS and GAM values indicating extensive dislocation accumulation in these grains.

Strong rolling textures were observed in these samples. Significant contribution from recovery is also observed for these samples.

RECRYSTALLIZATION KINETICS AND MICROSTRUCTURAL EVOLUTION IN HOT ROLLED ALUMINUM ALLOYS

BY

MOHAMMED HAROON ALVI

A DISSERTATION SUBMITTED IN PARTIAL FULFILLMENT OF THE REQUIREMENTS FOR THE DEGREE OF

DOCTOR OF PHILOSOPHY

IN

MATERIALS SCIENCE AND ENGINEERING

CARNEGIE MELLON UNIVERSITY

2005

Abstract

The kinetics of recrystallization and texture evolution in hot rolled aluminum alloys 1050 and 5005 have been analyzed. The as-received samples were given isothermal annealing treatments at different temperatures and their recrystallization kinetics and texture evolution were obtained as a function of annealing temperatures and times. Two different methods were used to measure recrystallization kinetics - microhardness variations and mapping with Electron BackScattered Diffraction (EBSD) also known as Orientation Imaging Microscopy (OIM). Microhardness variations represent an average behavior against which the methods based on EBSD were compared. Intragranular orientation variation (short-range and long-range) was found to be an important parameter for partitioning EBSD maps into deformed and recrystallized regions. Comparable recrystallization kinetics were obtained from microhardness variations and EBSD. Microstructural Path Modeling (MPM) was used for analyzing recrystallization kinetics. Recrystallization in hot rolled aluminum alloys 1050 and 5005 was determined to be site-saturated and controlled by migration of high-angle boundaries.

The ability to partition deformed and recrystallized regions based on intragranular orientation variations provided an important tool for analyzing and understanding the texture evolution in deformed and recrystallized grains independently of each other. Rolling orientation components S and Brass exhibited very different effects on annealing. While the deformed S orientation was observed to decay very fast, Brass deformed grains remained stable to annealing. Recrystallized grains had Cube as the main texture component, which nucleated from the deformed Cube bands. The recrystallized Cube grains exhibited both a nucleation and growth advantage when compared to the other recrystallized orientations. Although the nucleation advantage of Cube recrystallized grains was observed to be present at all annealing temperatures, the growth advantage for these grains were present only at low annealing temperatures.

Acknowledgments

This thesis is a part of a Department Of Energy (DOE) project to reduce annealing times during processing of aluminum alloys. This thesis presents not only my efforts but a significant contribution from a number of people, whose direct and indirect help made the goals achievable. Foremost among the people I would like to acknowledge are my advisors Prof. Anthony D. Rollett and Dr. Hasso Weiland. Prof. Rollett's directions along with his patience and persistence at every stage of this project were instrumental in achieving the final results. Dr. Weiland's critical suggestions provided the much needed understanding about the materials and the significance of the results for industrial applications.

I would also like to thank my committee members Prof. Gregory Rohrer, Prof. Katayun Barmak and Dr. Jaakko Suni for their very important suggestions that helped me in completing the work and filling the gaps. I also appreciate the suggestions provided by members of Dr. Weiland's research group at ALCOA Center, Pittsburgh. I would also like to thank Soonwuk Cheong and Bassem Samy El-Dasher, who helped me in the analysis of results and all the experimental problems that I faced. I would also like to thank all my group members, especially Abhijit Brahme, who always helped me through their suggestions and remarks at the group meetings. I also appreciate help from Heiskell Rogan, Jason Wolf and Tom Nuhfer in the experimental work. I would like to thank the MRSEC and the DOE for providing the necessary funds and facilities which made this project possible. I would also like to thank the Materials Science and Engineering Department for ensuring that my stay here was as smooth as possible.

This work is dedicated to my parents Mohammad Rafi Ahmad and R. Asmat, whose persistence and efforts all these years made possible for me to reach this place. Lastly, I would like to thank a very close friend whose help I cannot overstate. Despite the long distance, the continuous love and support that I received always motivated me to finish this project to the best of my abilities.

Table of Contents

List of Tables

List of Figures

List of Symbols

X_V	Volume fraction recrystallized in real space
X_{Vex}	Volume fraction recrystallized in extended space
S_V	Interfacial area per unit volume in real space
S_{Vex}	Interfacial area per unit volume in extended space
C_r	Contiguity ratio between recrystallized grains
N_V	Number of nuclei per unit volume
$\dot{N}$	Nucleation rate per unit volume
$< V >_{CH}$	Average Cahn-Hagel interface migration rate
t	Annealing Time
G	Interface migration rate; also shear modulus
T	Annealing Temperature
R	Universal Gas Constant
Q	Activation energy
H	Microhardness
θ	Misorientation angle
δ	Subgrain diameter
V_d	Volume fraction of a deformation texture component
V_r	Volume fraction of a recrystallization texture component
M	Mobility of a grain boundary

Δf	Driving force for boundary migration
n	JMAK exponent
k	Temperature dependent JMAK parameter
a	Area of contact; also grain diameter
b	Burgers vector
ν	Poisson's ratio
ρ	Dislocation density
γ	Specific energy of (low) angle grain boundaries

1 Introduction

Hot rolling processes form an integral part of processing of wrought aluminum alloys. The hot rolling processes are aimed at breaking down the cast structures in direct chill ingots and at refinement of the as-cast microstructure in terms of grain morphology and the crystallographic orientation (texture). The mechanical properties after subsequent cold rolling and other forming operations are determined primarily by the texture present after the hot rolling stages. For example, a balanced texture is essential for reducing the earing tendency during the beverage can forming operation. The annealing treatments during the hot rolling processes are therefore aimed at forming a strain-free microstructure in the metal which can be deformed further with less stress on the metal, thus avoiding crack formation during subsequent deformation. It is a standard industrial practice to anneal the partially broken down hot rolled slabs and plates for time periods long enough to recrystallize the metal completely before continuing with further hot rolling processes. The aim of the present study is to reduce the annealing times in hot deformation while improving the control of texture in production of plates and sheets. Two obvious benefits of reductions in annealing times are increased process and energy efficiency. Given the high volume of flat rolled aluminum products produced every year, shorter annealing times mean faster turnaround and less energy used to maintain furnace temperature.

The main aim of the annealing treatment is to obtain a recrystallized microstructure. Recrystallization can be defined as the formation of strain-free grains in a previously deformed matrix. It requires long range motion of grain boundaries to restore the mechanical state of an undeformed condition. Although recrystallization is well understood as a process, very little is known quantitatively about the influences of impurities and crystallography on the evolution of recrystallized grains. The goal of the current study is to measure the kinetics of recrystallization as a function of the crystallographic orientations of the grains. In a number of studies on recrystallization kinetics and texture evolution in different aluminum alloys, the kinetics of formation of recrystallized grains is found to be strongly dependent on processing conditions (strain, strain rate and temperature) as well as the microstructure and texture of the deformed

metal. The deformed grains of certain orientations, e.g. Brass, have been observed to be relatively stable to annealing treatments, have large subgrain sizes and low stored energies and therefore recrystallize at the final stages of annealing. Similarly deformed grains of other orientations, e.g. S and Copper, are observed to have smaller subgrain sizes and larger stored energies therefore resulting in more rapid recrystallization of these components. The nucleation and growth of a recrystallized grain is strongly dependent on its spatial location in the deformed microstructure. The ability to control the deformation texture evolution from the processing parameters will help to determine the conditions for faster recrystallization of the hot rolled metal.

An important aspect of the current study is to provide new information on data that can be used in engineering models for process control. Data on texture evolution, nucleation of recrystallized grains and variation in stored energies in deformed grains of different orientations will help significantly in improving the current models of recrystallization.

The aluminum alloys used in the present study are commercial purity non-heat treatable alloys 1050 and 5005. These alloys are used primarily for can closures and beverage can stock. The kinetics of recrystallization after hot rolling were determined as a function of orientation. The use of Electron Backscattered Diffraction (EBSD) in a Scanning Electron Microscope (SEM) has lead to the emergence of Orientation Imaging Microscopy (OIM) which is an important tool for analyzing microstructural and textural evolution at relatively rapid rates without tedious sample preparation. OIM was used extensively in this project. A technique for determining the fraction recrystallized in deformed and annealed samples was developed by using the concept of Grain Orientation Spread (GOS). GOS represents an average orientation spread within a grain. A comparison of recrystallization kinetics obtained from the GOS approach and the microhardness variations revealed good agreement between the two methods. The GOS approach has also provided the ability to partition OIM maps into deformed and recrystallized grains and to analyze them independently for texture evolution and their growth and decay kinetics. The recrystallized grains were also analyzed for their deformed neighbors of different

orientations. Variations in the neighborhood of recrystallized grains revealed the relative stability of deformed grains. Samples were also deformed in a specially designed machine at the Alcoa Technical Center, known as a deformation simulator, to simulate the industrial rolling process and also allow the control of process parameters (temperature, strain and strain rate). An analysis of these samples will help to determine the stability of different orientations relative to various processing conditions.

The results obtained from this study will help to improve our current understanding of the process of recrystallization. Data from the experiments are expected to help in improving the current mathematical models and provide an accurate prediction of microstructure and texture variations as a function of processing conditions, leading to improvements in process control and optimization.

2 Literature Review

Deformation and recrystallization processes form an integral part of thermomechanical processing during the mechanical forming of aluminum alloys. The two processes are closely related as the microstructural and textural evolution during recrystallization is strongly dependent on the deformation parameters and processing conditions. The heterogeneities formed during the deformation of metals act as nucleation sites for recrystallized grains. Dislocation generation and rearrangement during deformation processes form the most important microstructural features of the deformation microstructure. Annealing of deformed metals generally results in growth of recrystallized grains, driven by the stored energy of deformation. Since deformation takes place by slip on selected planes along specific directions, preferred orientations are developed in the grains during deformation. The stored energy of these grains is dependent primarily on the magnitude of slip and therefore indirectly on the orientation developed during deformation. The stored energy provides the driving force for recrystallization and formation of new grains with low stored energies and, often, different texture from the deformation texture.

This chapter reviews the current literature on deformation and recrystallization. The effect of dislocation slip in polycrystalline metals on the storage of dislocations is examined first, followed by the formation of dislocation structures in deformed metals. Deformation microstructures from cold and hot rolling processes are also compared. The kinetics of recrystallization are reviewed along with microstructural and textural evolution during recrystallization. The theories of recrystallization texture evolution are also reviewed briefly.

2.1 Deformed State

The industrial rolling of aluminum alloys is generally conducted in multistage schedules of 10-15 passes, partly on reversing mills and partly on continuous mills with temperature declining from 500^oC to between 300^oC and 250^oC [13]. Microstructural evolution during deformation is determined by the deformation parameters which includes strain, strain rate and temperature of deformation. An important parameter along with the shape and size of deformed

grains is their orientation. The orientations of deformed grains play an important role in the nucleation and growth of recrystallized grains. The energy stored during deformation is also determined by the orientation of grains to some extent. The basic mechanisms and structures formed during deformation are discussed in this next section.

2.1.1 Microstructural evolution during deformation

Deformation of a metal changes its microstructure in several ways. The grains change their shape from nearly equiaxed to an elongated shape and there is a significant increase in total grain boundary area. New grain boundary area is created by incorporation of dislocations, which are created continuously during deformation process. At the microscopic level, a substructure appears within a grain. This substructure is also created by the dislocations generated during the deformation process [6].

The main mechanisms of deformation in cubic metals are slip and twinning. The parameter for deciding the actual choice of deformation mechanism is the value of the stacking fault energy, γ_{SFE}. The stacking fault energy of aluminum is 166 mJm^{-2} [6]. This value is relatively high therefore the main mechanism of deformation for aluminum alloys is dislocation slip. Slip usually takes place on close packed planes and along closed packed directions. The combination of close packed planes and directions form a slip system and the most common observed slip system for fcc metals is $\{111\}\ \langle 110\rangle$. As in a single crystal, the slip systems that are activated in a grain depends on which planes experience the greatest resolved shear stress and these planes are oriented differently in different grains in a polycrystalline aggregate. The individual grains in an aggregate are however, not free to change their shape arbitrarily and are subjected to constraints imposed by all of their neighbors, each of which deforms in a unique manner. To first order, however, each grain deforms as the aggregate does. The contiguity of the material must be maintained for the deformation to continue and thus different parts of a particular grain may have different deformation processes. A deformation band can be defined as a volume of constant orientation that is significantly different from the orientations present elsewhere in a grain. A transition band is defined as the region of orientation change between

various parts of a grain and it can have a finite width. A deformation band with parallel sides and involving equal and opposite orientation change across the two boundaries is defined as a kink band [6].

Dislocation structures and arrangements

The microstructure of metals deforming by slip typically comprises a three-dimensional structure of regions of low dislocation density, bounded by walls of high dislocation density. If the boundary is diffuse, consisting of a tangled array of dislocations, it is a cell structure. If the boundary is sharp and consists of a well ordered dislocation array then it is more properly described as a subgrain structure. The earliest microstructures evolve with strain from tangled dislocations, to structures consisting of cells and then subgrains [6]. In high-SFE polycrystalline metals, individual grains subdivide into volume elements (Cell Blocks) which can deform by fewer slip systems than the five specified by the Taylor criterion for strain accommodation. The cell blocks in turn are divided into ordinary dislocation cells. The observed behavior can be understood in terms of general theoretical principles applied to individual dislocations and their group behavior, which influences the selection and interaction of locally different glide system combinations and the reduction of free dislocation energy, via the formation of low-energy dislocation structures (LEDS). “The increase in dislocation density during straining is due to the mutual trapping of dislocations. The dislocation trapping implies mutual stress-screening of the resolved shear stress components to the level of the frictional stress among near-neighbor dislocations. Among the configurations accessible to the dislocations, that particular dislocation microstructure forms which minimizes the energy per unit length of dislocation line at least on a local basis. The relative level of stress screening of the other stress components besides the resolved shear stress causes some LEDS to form in preference to others. It is a general principle that in all dislocations structures the energy decreases with increasing number of participating Burgers vectors since it permits effective stress screening” [14].

The trapping of dislocations into LEDS often leads to the formation of two-dimensional

dislocations arrays (i.e. walls). These dislocation arrays are generally favored over a quasi-uniform three-dimensional distribution since for a given total dislocation density, the dislocation spacing (and thereby the energy per unit length of dislocation line) is smaller in the arrays. The dislocations cells are thus the very type of structure theoretically expected. Many planar arrays are geometrically possible but only a small fraction are free of long range stress as required to be LEDS as indicated below:-

- Dipolar or multipolar walls in which parallel dislocation segments of the same type, but with Burgers vectors of opposite sign, are equally frequent on a small scale.
- Dislocation rotation boundaries, across which the lattice rotation changes abruptly.

Deformation structures have been observed to shrink in scale as the applied stress is increased. The refinement of a cell structure requires dissociation of dislocation walls or generation of new dislocation walls within preexisting cells. The latter can occur via the formation and subsequent splitting of dipolar and multipolar walls into two similar walls but with opposite angle of rotations [14].

Effect of polycrystalline slip on Dislocation structures

Polycrystalline slip has been modeled by various researchers involving different constraints on strain. According to the Taylor model, slip is uniform within each grain of a polycrystal and strain compatibility is achieved by simultaneous operation of at least five slip systems. Equivalently, five independent glide systems can accommodate any arbitrary strain. The Taylor model accounts for texture development in a reasonably successful fashion in polycrystals.

At a microscopic level, however, the number of simultaneously acting glide systems is presumably the result of two competing effects. The flow stress is lower with fewer glide systems because the number of intersecting dislocation jogs decreases. Alternatively, stress screening becomes more effective as the number of different Burgers vectors increases. The number of Burgers vectors increases with increasing glide systems. However, the individual contribution to stress screening from an additional Burgers vector diminishes significantly when the total

number of Burgers vectors increases beyond three or four. Consequently, the number of glide systems may fall short of the five systems expected on the basis of the Taylor model. The number of active glide systems may be realistically estimated at three to four, even when the imposed stress is entirely uniform. Independent of number of slip systems operating, strain accommodation is required. Thus deformation of polycrystals with a reduced number of slip systems can take place by volume elements of individual grains each characterized by a specific selection of glide system. While each cell block will conform as well as possible to the Taylor criterion, but because less than five systems cannot fulfill it, neighboring cell blocks must fulfill it collectively [14].

According to Hughes *et al.* [14, 15] at the start of deformation, different slip system combinations are activated in different parts of any one grain through interaction among grains. Heterogeneity of slip activity is apparent in the variations in slip line patterns. This break-up of grains into differently oriented regions means that any individual location does not exactly satisfy the Taylor condition. For grain sizes above a few microns, the regions that deform with a particular selection of slip systems are initially much larger than the cell size, implying that each cell block contains several dislocation cells. Since the deformation within a cell block does not fully conform to Taylor's criterion, the average orientations of neighboring cell blocks diverge. As a result, the boundaries between cell blocks are both longer and associated with larger average rotation angles than ordinary cell walls. These boundaries are termed "dense dislocation walls" (DDW). The gradual lattice reorientation will differ among neighboring cell blocks, and so the cell blocks will begin to interact in the same manner as did the initial grains. As a result, new cell blocks will be required to accommodate strains that are formed by the subdivision of initial cell blocks.

The new cell blocks are nucleated by splitting of existing DDW's into two or more roughly parallel walls. The result of this splitting is approximately parallel double or multiple DDW's, which appear as bands of morphologically distinct dislocation cells in TEM and are called micro-bands (MB1's). In the volume opened up between the edges of a split DDW, a different selection of glide systems operates than on either side. The zone between the split parts is

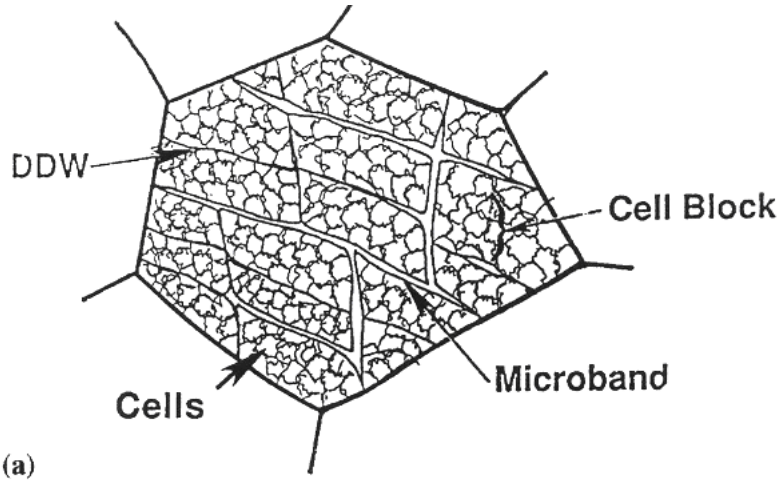

Figure 2.1: Schematic view of various microstructural features observed during deformation of metals.[2]

therefore a new cell block that is bounded by new DDW's that arise from the pre-existing DDW. Another way of nucleating cell blocks is through the intersection of the cell structure by glide on a previously dormant glide plane. The initiation of glide on an intersecting plane requires jogging of a large fraction of dislocations threading the planes. The glide initiation on this intersecting plane requires a slightly higher stress than further glide on a prior plane. These also appear as bands and are called second generation micro-bands (MB2's) owing to the fact that they are formed at a latter stage than the previously formed micro-bands which are also known as first generation micro-bands.

At large strains, the structure consists of individual subgrains that are formed as the rotation angles across cell walls increase and cells become subgrains. The increase in strain leads to an increase in dislocation density and since the rate of rotation increase across a DDW is slower at large strains, this will cause the rotation across the ordinary dislocation walls to increase. Ultimately cells within each cell block can no longer operate with the same glide system combination which leads to the formation of high average misorientation across the wall, thus forming subgrains from the cells. The cell blocks become very flat and sandwiched by lamellar dislocation boundaries that have replaced the small strain DDW and MB structures. In contrast to the small strain blocks, the cell blocks at large strains are usually one to two cells deep and several

along their length. The average misorientation between cells and subgrains is generally found to increase with strain. An important feature, along with the mean subgrain misorientation, is the presence of long range orientation gradients in deformed metals. Although the nearest neighbor misorientations are generally low, there are often significant orientation gradients in each grain which are different in the rolling and normal directions [16].

Formation of high angle boundaries during deformation

Cell boundaries that have low misorientation angles on average are classified as incidental dislocation boundaries (IDB). DDWs, MBs, LBs and subgrain boundaries are classified as geometrically necessary boundaries (GNBs) that separate differently deforming regions. Both GNBs and IDBs increase their average misorientation angle and decrease their spacing with increasing strain and stress. However, GNBs increase their misorientation angle and decrease their spacing at a much higher rate than IDBs do. At medium to large strains, some part of the population of the GNBs have increased their misorientation angle to the extent that they are classified as high angle boundaries. Another important source of high angle boundaries is texture evolution during the deformation process. Large crystal rotations occur as a part of preferred crystallographic texture evolution, leading to rotation of different parts of a grain to different end positions due to the grain subdivision by dislocation boundaries that start at the beginning of deformation. The high angle boundary thus generated serves as an important site for nucleation during recrystallization as it is able to migrate through deformed microstructure causing the nucleus to grow. The driving force for the boundary migration is provided by the stored energy of deformation. The driving force depends on various material parameters including deformation and annealing parameters and also on the crystallographic orientation of the deformed matrix [12].

Microstructural evolution during hot rolling in aluminum alloys

The plastic flow of crystalline metals requires the same motion of dislocations regardless of temperature, although at high temperature, sliding and diffusion flow at grain boundaries become significant as strain rate and grain size are reduced. The rolling temperature at different

stages of processing affects the overall microstructural and textural evolution. Based on the actual temperature being used during the rolling process, it can be divided into hot (above 0.6 of the melting temperature), warm (between 0.3 and 0.6 of the melting temperature) and cold (below 0.3 of the melting temperature) rolled regimes [15]. A comparison between the hot and cold worked states is given in Table 1 [13].

Hot Working ($T > 0.6Tm, Al > 300^oC$)	Cold Working ($T < 0.3Tm, Al < 100^oC$)
Dislocation climb, cross slip, glides on additional slip systems.	Dislocation glide, limited cross slip, forms microbands. Polygonized subgrains Elongated cells
Substructure regenerated continuously	Cell divided into blocks by microbands
Misorientation angle between subgrains remains low	Misorientation angle between cell blocks becomes high
Static recovery and recrystallization between stages	Static recovery and recrystallization in annealing
Disorientation boundaries permanent, rather narrow walls forming grain boundaries	Disorientation bands of many cellular layers ultimately becomes grain boundary

Table 2.1: Comparison of hot worked and cold worked states

Dynamic recovery is found to be a dominant softening mechanism in hot rolled aluminum alloys. The formation of deformation bands and development of disorientation walls between different oriented regions are temperature independent. The degree of break-up is less at higher temperature however, because additional straining mechanisms relax the Taylor constraints. The constraints are reduced due to grain boundary sliding, migrations and vacancy flows. Consequently, there are only two or three bands per grain per $100\mu m$, much less than in cold work. Dense dislocation walls, microbands, lamellar boundaries, equiaxed subgrains and cells are also observed during hot deformation. The relative proportions of these different structures depend on the temperature, strain rate, stacking fault energy and friction stress. Microstructural evolution during hot rolling of commercial purity aluminum (1050) also produces features observed for cold rolled microstructures with DDW's and MB's outlining cell blocks as shown

in Fig. 2.2. However, regions containing primarily equiaxed cells and subgrains are more frequently observed at high temperature than following room temperature deformation. An increase in temperature further increases the proportion of equiaxed cells and subgrains [14]. The temperature of deformation has a significant effect on the microstructural evolution during hot deformation. In a series of hot deformation experiments conducted on AA1050, the microstructures obtained had very different characteristics. A high temperature deformation (500^oC) leads to formation of Grain Boundary Serrations (GBS), whereas for deformation at lower temperature (350^oC) in-grain inclined lines (IIL) were observed. The inclined lines were oriented 35^o to the RD. The formation of GBS and IIL is shown in Fig. 2.3 [3].

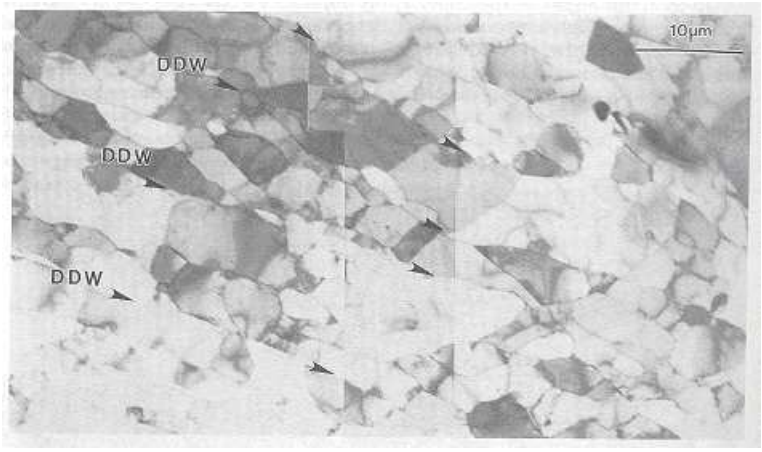

Figure 2.2: DDWs and cell block walls observed in commercial purity aluminum alloy (AA1050) hot rolled to 50% reduction at 573K [3].

2.1.2 Stored Energy

The work expended in deforming a metal is released mainly as heat and only a very small amount (1%) remains as stored energy [6]. This stored energy provides the source of all the property changes that are typical of deformed metals and is mainly derived from dislocations generated during deformation with only a small contribution from point defects. The mobility of interstitials and vacancies is very high and except for the special cases of deformation at very low temperatures, the contribution of point defects to the stored energy is not significant. Deformation at ambient temperatures usually involves energy stored due to accumulation

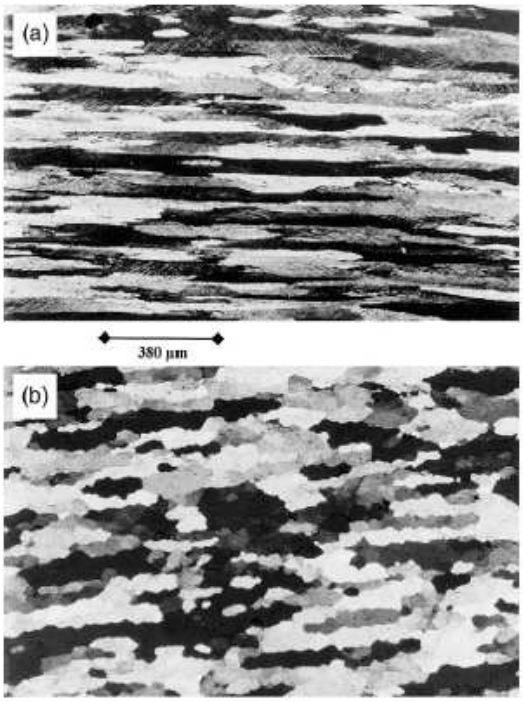

Figure 2.3: Microstructural evolution during hot working (a) Low temperature deformation (350^oC) causes IIL formation (b) High temperature deformation (500^oC) leads to GBS formation [3].

of dislocations. The increase in dislocation density is due to the continued trapping of newly created mobile dislocations by existing dislocations and their incorporation into the existing dislocation structure. The new grain boundary area created due the shape change of grains undergoing deformation also involves incorporation of dislocations generated during deformation. The energy associated with increase in area represents a significant part of stored energy and is greater for small grain sizes and large strains. The appearance of internal structure within grains involves creation of boundaries which are also generated from the newly created dislocations.

The stored energy of deformation is the main driving force for the restoration mechanisms (recovery and recrystallization) occurring during the annealing of deformed metals. A typical lightly deformed metal has a stored energy of about $10^5 Jm^{-3}$ which is small compared to other transformation energies such as the heat of fusion and phase transformations. This small amount of stored energy is the source of all the strengthening that occurs during deformation.

The stored energy of deformation is usually measured directly by calorimetry or indirectly

from the change in some physical or mechanical property of materials such as X-ray line broadening. The calorimetric observations involve measurement of heat flux emitted by a specimen during heating with reference to a standard whereas the X-ray line broadening technique involves the measurement of inhomogeneous lattice strain energy.

The stored energy of deformation due to the dislocations can be obtained from the energy per unit length of a dislocation multiplied by the density. The energy per unit length of a dislocation line is approximately given by

$$E_{dis} = \frac{Gb^2 f(v)}{4\pi} \ln \frac{R}{R_o} \tag{2.1}$$

Here, R is the upper cut-off radius (usually taken to be the separation of dislocations ($\rho^{-1/2}$), R_o is the inner cut-off radius (usually taken as between b and 5b),
f(v) is a function of Poisson's ratio (v), which, for an average population of edge and screw dislocations is $\frac{1-v/2}{1-v}$.

The stored energy for a dislocation density is thus

$$E_D = \rho E_{Dis} \tag{2.2}$$

The energies of the dislocations present in real materials are not wholly represented by such simple considerations as the above expression is appropriate only if the dislocations are arranged in such ways that stress fields of other dislocations are screened. In most cases it is appropriate to say that the approximate dislocation energy can be represented as

$$E_{Dis} = cGb^2 \tag{2.3}$$

where $c \approx 0.5$, and the stored energy can be represented as

$$E_D = c\rho Gb^2 \tag{2.4}$$

The energy stored in the substructure can be estimated from the subgrain diameter (δ) and specific energy (γ) of the low angle grain boundaries which comprise the subgrain walls. The area of low angle boundary per unit volume is $3/\delta$ and hence the energy per unit volume (E_S) is given by

$$E_S \approx \frac{3\gamma}{\delta} \tag{2.5}$$

The above expression can also be expressed in form of the boundary misorientation angle (θ), which can be measured experimentally. The stored energy is therefore

$$E_S = \frac{3\gamma_o\theta(A - \ln\theta)}{\delta} = \frac{K\theta}{\delta} \tag{2.6}$$

Here, $\gamma_o = \frac{Gb}{4\pi(1-\nu)}$, $A = 1 + \ln\frac{b}{2\pi r_o}$, r_o is radius of the dislocation core usually taken as being between b and 5b.

The total stored energy can be computed from the individual contributions from dislocation energy and substructure energy as

$$E_T = E_D + E_S \tag{2.7}$$

It has been found experimentally that both cell/subgrain size and the misorientation are dependent on the grain orientation and therefore the stored energy can be expected to vary in different texture components of the material [6]. The differences in stored energy of deformation have important effects on the nucleation and growth of recrystallized grains. The rate of nucleation and growth of recrystallization nuclei will be enhanced in components with the highest stored energy. Similarly a component with lower energy that is situated adjacent to a component with higher energy will be likely to create a recrystallization nucleus. The nucleation of cube recrystallized grains occurs from deformed cube bands that have a large subgrain size and a correspondingly lower energy. The nucleation from cube bands has further been found to be promoted when the bands have an S component as a neighbor, which could be ascribed to

higher stored energy of S deformed grains [8, 17].

Stored energy analysis of different aluminum alloys has shown higher stored energy for S deformed grains by an amount of 10-30% relative to the average stored energy and lower stored energy for Brass grains by up to an amount of 25% relative to the average stored energy. The subgrain sizes and sub-boundary misorientations were obtained using TEM and SEM analysis. The internal dislocation content was however, obtained from TEM only and the contribution of the internal dislocations to the total stored energy can be neglected for the hot deformed samples [8, 18, 19].

2.1.3 Texture evolution during deformation

The orientation changes that take place during deformation are not random. They are a consequence of the fact the deformation occurs on the most favorably oriented slip systems and deformed metal therefore acquires a preferred orientation (texture). The texture evolution during deformation affects the nucleation behavior of recrystallizing metal as nucleation occurs preferentially in association with specific regions of particular orientation. Texture is usually characterized by the Orientation Distribution Function (ODF) which describes the orientations in the aggregate. The orientations in an ODF are typically parameterized in terms of three Euler angles (ϕ_1, Φ, ϕ_2). Several different notations have been used to define these angles, but that of Bunge is most common and will be used here. For rolled fcc materials the data are normally shown as a series of slices taken through the three dimensional ODF space at $\phi_2 = 0, 5, 10 \ldots 90^o$ as indicated in the figure below. Texture evolution during deformation and recrystallization is dramatic in the sense that a strong deformation texture is replaced by an entirely different recrystallization texture. Recrystallization textures are insensitive to annealing conditions but have a very strong sensitivity to the prior plastic deformation. This indicates that the entire recrystallization process is latent in the deformed state. An increase in deformation temperature results in greater homogeneity in microstructure therefore leading to strengthening and sharpening of texture after hot deformation as compared to cold deformation. The textures of rolled fcc metals can be represented by a continuous tube of orientations that runs from {110}

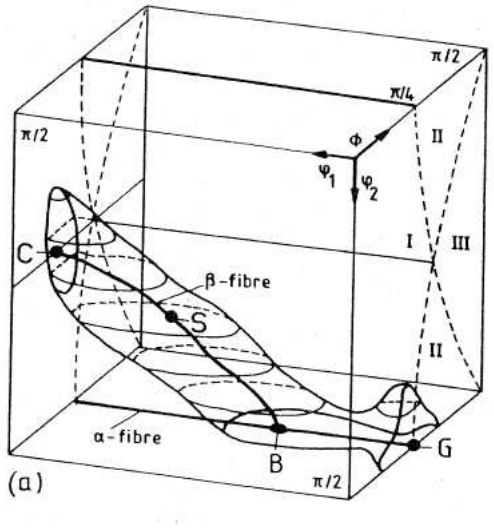

Figure 2.4: Important fibers found in fcc rolling textures [4]

$\langle 112 \rangle$ (Brass) at $\phi_1 = 35^o$, $\Phi = 45^o$ and $\phi_2 = 90^o$ through $\{123\}\ \langle 634 \rangle$ (S) at $\phi_1 = 59^o$, $\Phi = 37^o$ and $\phi_2 = 63^o$ to $\{112\}\ \langle 111 \rangle$ (Copper) at $\phi_1 = 90^o$, $\Phi = 35^o$ and $\phi_2 = 45^o$. The axis of the tube is called the β fiber and texture data is often reported only in the form of orientation density along this fiber. While the β-fiber represents the characteristic features of the textures at medium and high degrees, low degrees of rolling are associated with the presence of the α-fiber which runs from the Goss orientation $\{011\}\langle 100 \rangle$ to the Brass orientation $\{011\}\langle 112 \rangle$ [4]. Fig. 2.4 shows the location of different fibers observed for fcc rolling. The relative intensities of different texture components along the beta fiber are strongly influenced by deformation conditions as well as the initial texture of the undeformed polycrystalline aggregate.

The textures obtained after rolling also depend strongly on the starting texture as shown in Fig. 2.5. Although the same texture components are obtained, their intensities vary considerably with the starting texture. A Plane Strain Compression (PSC) test carried out for commercial purity aluminum alloy revealed that, while deformation of a randomly textured sample results in a copper texture, the cube texture material evolved into a strong near-Brass texture [20]. Alloys with solid solution forming elements deform like pure metals and develop similar textures at low reductions. An increase in deformation causes the Brass and Goss components to increase. The presence of shearable particles causes an increase in the formation of shear

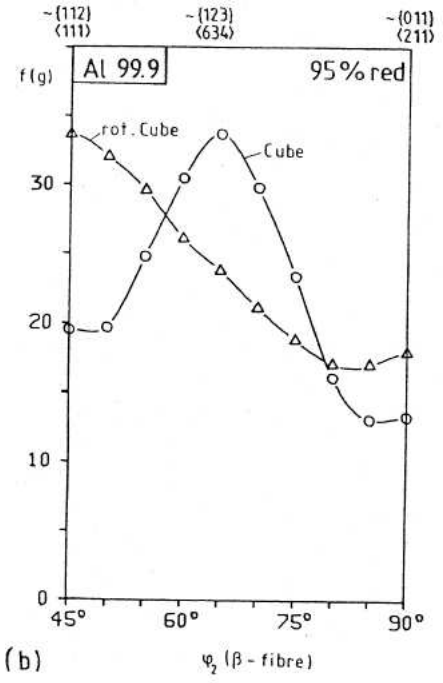

Figure 2.5: Effect of different starting textures on deformation texture evolution [4]

bands and leads to a pronounced reduction in the texture sharpness [4]. Non-shearable particles cause extensive pile-ups of dislocations, leading to the formation of deformation zones around the particles. A large number of the deformation zones give rise to a general weakening of the rolling texture. An interesting variation is obtained at intermediate size particles, where a strong rolling texture similar to a pure metal, is obtained. This is caused by a reduction in the mean free path of the dislocations leading to homogenization of deformation and enhancement of texture formation [4].

Adding Mg to Al-alloys is known to affect the development of rolling texture. It strongly suppresses the development of β-fiber texture components. The {111} pole figures shown in Fig. 2.6 illustrate this effect of Mg addition on rolling texture evolution. A detailed texture analysis has revealed the following variations. For low Mg content (⟨3%),the S component decreases much more rapidly than other main components of rolling texture with increasing Mg content. With increasing Mg content (between 3-5%), the Brass component increases at the expense of the Copper component. High Mg content (⟩5%) suppresses the development of all the main components equally and a weaker rolling texture is obtained [5, 21, 22, 23].

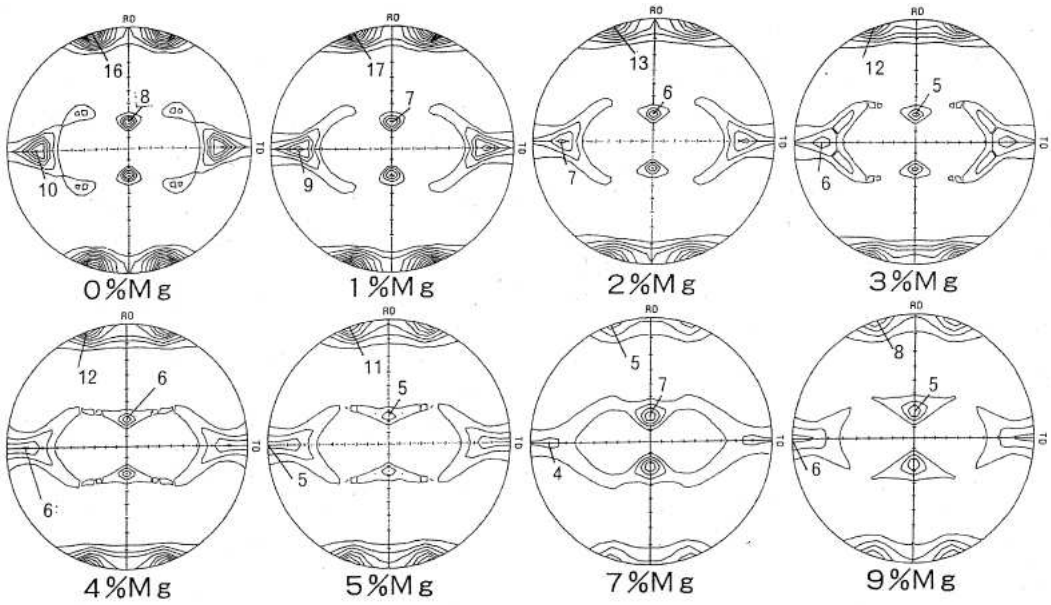

Figure 2.6: {111} pole figures for different Al-Mg alloys. An increase in Mg-content leads to reduction in the deformation texture strength [5].

The cube grains that are present in the microstructure prior to deformation play an important role in the texture evolution of recrystallized metal. They remain metastable during hot deformation. During deformation the old cube grains are flattened into bands. The bands are typically $2\mu m$ wide and extend for several microns along the rolling direction [24]. The subgrains within the cube bands have a size advantage compared with the subgrains of other orientations. This makes cube bands very potent nucleation sites. The strength of cube texture upon recrystallization is found to be enhanced by a high initial cube fraction (large amount of cube bands), a low Zener-Hollomon parameter (higher stability of the cube grains during deformation) and a high strain (large surface area of cube bands) [25].

Microtexture measurements on hot plane strain compressed aluminum crystals clearly indicated that subgrain sizes vary in the various deformation components in the order $Brass > Copper > S$ [8]. The cube subgrains are found to have a large size advantage in hot worked polycrystals. The earlier papers on rolled copper have shown that the first S oriented grains to disappear are those adjacent to cube bands. Calculations of stored energies from the subgrain sizes and misorientation angles indicate that the stored energy in deformed cube grains is nearly

half of that of S grains so that there is significant driving force for cube to grow into S [8].

2.2 Annealing of deformed metals

The mechanical properties and behavior of a metal depend, to a large extent, on the dislocation content and their arrangements. The typical dislocation content in the annealed state is ($10^{11}m^{-2}$) which increases significantly during deformation ($10^{16}m^{-2}$). The increase in dislocation content is the main reason for the high yield strength and lower ductility of a deformed metal. However, annealing of a deformed metal at a temperature above about $T_m/3$ leads to a significant dislocation loss and rearrangement, as manifested by a decrease in strength and increase in ductility. The deformation energy stored in the material in the form of dislocations is released in three main processes of recovery, recrystallization and grain growth. For metallic alloys based on copper, nickel and aluminum, which do not undergo a phase change on cooling, recrystallization after deformation is the only method for producing a completely new grain structure with modified grain size, shape and texture. Recrystallization can be defined as the formation of a new grain structure in a deformed material by the formation and migration of high angle boundaries driven by the stored energy of deformation. Recovery usually refers to all annealing processes occurring in deformed materials that occur without the long range migration of high angle boundaries. Recovery typically involves rearrangement of dislocations to lower their energy. Grain growth is defined as processes involving the migration of grain boundaries when the driving force for migration is solely the reduction of the grain boundary area itself [6].

The structural transformations such as recovery, recrystallization and grain growth can be classified into two different types, as originally recognized by Gibbs, in a manner similar to phase transformation. “In first of these, Gibbs I, typically called ’nucleation and growth’, the transformation is extensive in the magnitude of the structural change but is initially spatially localized with a sharp interface between the old and new structures. The second type of transformation, Gibbs II, often described as ’continuous’ or ’homogeneous’, the transformation is

initially small in magnitude of the structural change, but it occurs throughout the parent structure" [2]. In the range of processes seen on annealing plastically deformed materials, both dislocation recovery, that takes place before and during recrystallization and also normal grain growth are clearly Gibbs II transformations which occur uniformly throughout the sample while recrystallization and abnormal grain growth are Gibbs I transformations. The newly recrystallized grain or the abnormally large grains are seen to be growing into a prior structure with a sharp interface between transformed and untransformed regions. The usual name of 'nucleation and growth' for Gibbs I transformation is based on the two apparently distinct steps of the initial formation of new grains and their growth, as applied to recrystallization [2].

2.2.1 Recovery

The term recovery refers to changes in the properties of a deformed material which occur prior to recrystallization. These changes are such as to partially restore the properties to their values before deformation. Recovery is primarily due to changes in the dislocation structure of the material. The dislocation recovery process involves a series of micromechanisms whose rate depend on a number of parameters, including the material, purity, strain, deformation temperature and annealing temperature. When the recovery of dislocations occurs during the deformation, it is termed dynamic recovery. The typical changes associated with dislocation rearrangement and structures that can be attributed to the recovery process are shown in Fig. 2.7. The driving force for recovery as well as recrystallization is the dislocation energy stored during deformation and the two processes often compete during the thermomechanical processing of material. The extent of recovery depends on the ease with which recrystallization can occur, as after the onset of recrystallization when the deformation microstructure is consumed no further recovery will occur. Conversely if a significant amount of recovery has occurred, the driving force for recrystallization is reduced and the nature and kinetics of recrystallization are influenced. In this work, however, we present some evidence that recovery can infact occur concurrently with recrystallization.

The measurement of the extent of recovery in deformed metals is usually directly observed

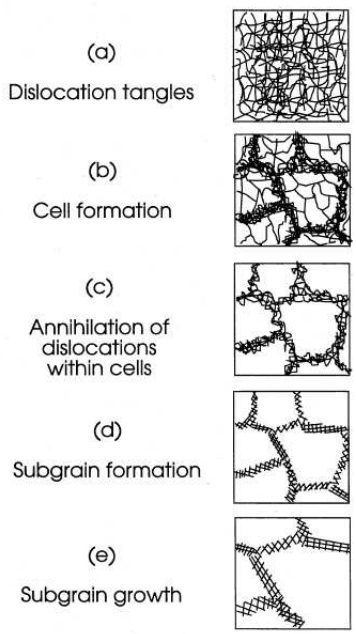

Figure 2.7: Various stages of recovery of plastically deformed material [6]

by calorimetry. The indirect measurement of recovery involves measurements of properties such as electrical resistivity and hardness. Since the microstructural changes associated with recovery are small, the direct as well as indirect measurements of recovery will lead to significantly lower values of stored energy as compared to recrystallization. A logarithmic decay in mechanical properties is usually observed for dislocation recovery. An increase in the strain of a material is found to increase the fraction of the property change associated with recovery during annealing at a constant temperature. A similar trend is also obtained with an increase in deformation temperature, where more recovery is found for high temperature deformation because of the increased mobility of dislocations. The material's stacking fault energy is another important parameter determining the extent of recovery in deformed microstructure. Metals with low stacking fault energy like copper, α-brass and austenitic stainless steel show little recovery of dislocation structures due to reduced climb and cross slip. Metals such as aluminum and α-iron, which have high γ_{SFE}, show a significant amount of recovery. The amount of solute content in an alloy also determines the extent of dislocation recovery by affecting the stacking fault energy values or by pinning of dislocations. Addition of magnesium to aluminum for

example is known to pin dislocations and therefore retard dynamic recovery. This will lead to an increase in stored energy and rapid recovery occurs during annealing of deformed samples.

The two primary processes of reducing the stored energy during recovery are annihilation of dislocations and the rearrangement of dislocations into low energy configurations. These processes are achieved by glide, climb and cross-slip of dislocations. The annihilation of dislocations takes place by movement of dislocations of opposite Burgers vectors and canceling each other. The rearrangement of dislocations can take place via subgrain formation. The formation of low angle tilt boundaries from alignment of dislocations of similar Burgers vectors is an example of a polygonization mechanism. The energy per dislocation decreases with increasing the misorientation across a tilt boundary. Therefore there is a driving force to form highly misoriented boundaries as recovery proceeds. Subgrain formation from tangles of dislocations in the cell structure during annealing involves annihilation of redundant dislocations and rearrangement of others into low angle grain boundaries. Dynamic recovery during hot deformation has been observed to occur to such an extent that the dislocations are already in the form of a well developed subgrain structure after deformation and post-deformation recovery involves mainly a coarsening of the subgrains. The main factors that tend to promote the formation of a subgrain structure during deformation are high stacking fault energy, low solute content, large strain and high temperature of deformation. A further reduction in stored energy can be obtained by subgrain coarsening. The driving force for subgrain coarsening arises from the boundary energy and any reduction in subgrain boundary area will lead to a reduction in stored energy [6].

2.2.2 Recrystallization

Recrystallization involves the formation of strain-free grains in certain parts of the specimen, and the subsequent growth of these to consume the deformed and recovered microstructure. The microstructure at any stage can be partitioned into deformed and recrystallized regions which can be quantified by the fraction recrystallized. Recrystallization of deformed

microstructures is often called primary recrystallization to distinguish it from processes of exaggerated grain growth which may occur in fully recrystallized materials and which are sometimes called secondary recrystallization or abnormal grain growth. As stated previously, recrystallization usually involves nucleation of new grains and their subsequent growth. A recrystallized grain is usually distinguished from a deformed grain by the low internal energy indicated by the absence of any internal dislocation substructure and is surrounded by a high angle boundary [2].

Recrystallized grains grow by migration of high angle boundaries. The driving force for migration is the stored energy of deformation, which can be expressed in terms of the dislocation density, ρ, as

$$E_D = \alpha \rho G b^2 \tag{2.8}$$

where α is a constant of order 0.5. The driving force for primary recrystallization of a typical metal is of the order of 1MPa. An opposing force also exists on the boundary at small sizes, due to boundary specific energy γ_b, which will reduce the boundary area and thereby lowering the energy of a grain. The retarding pressure on the boundary is given by the Gibbs-Thomson relationship:

$$E_G = \frac{2\gamma_b}{R} \tag{2.9}$$

where R is the radius of growing spherical nucleus. For the driving force discussed above, the curvature driven retarding force is significant for nuclei of size less than $1\mu m$. Below this grain size there would be a negative net driving force for recrystallization [2].

Factors affecting the rate of recrystallization

Recrystallization of a deformed metal is affected by a number of parameters including the nature of the deformed structure, grain orientation, concentration of solutes, temperature and strain rate of deformation and annealing conditions.

The stored energy of deformation and microstructural heterogeneities are increased by the amount of strain in a material. Also recrystallization does not occur until a minimum amount of strain has accumulated, indicating that a minimum stored energy is required. Thus the deformation mode and strain path have a significant effect on recrystallization behavior of the material. Texture evolution of a grain during deformation is determined by the active slip systems and the initial orientation of the grain. Therefore the stored energy of a deformed grain is strongly dependent on its orientation. This directly affects the driving force for both nucleation and growth in recrystallization. Variation in texture obtained after hot rolling and annealing of aluminum alloys lead to different recrystallization kinetics when the material is subsequently cold rolled and annealed [6]. The same variability and underlying causes apply to all materials

Fine grained materials are found to recrystallize more rapidly than the coarse grained materials. Stored energy increases with reduction in grain size. Also, the number (density) of nucleation sites available at grain boundaries increases as the grain size decreases because grain boundary nucleation is important in the nucleation of recrystallized grains.

Solute atoms are found to have a significant effect on the recrystallization behavior of metals by varying the stored energy via dislocation interaction. The mobility of high angle grain boundaries is also reduced by solute drag thus decreasing the growth rates of recrystallizing grains. The stored energy of deformation varies with temperature and strain rate. As the temperature is increased, microstructural heterogeneity decreases therefore reducing the stored energy. Similarly, increasing strain rate also increases stored energy thereby reducing the recrystallization temperature [6].

Kinetics of Recrystallization

The kinetic aspects of the nucleation and growth phenomena during recrystallization are similar to those observed in typical Gibbs I phase transformations. Although the similarities are confined to the microstructural level, a similar transformation kinetics treatment can be applied for recrystallization as for phase transformations. The fraction recrystallized can be measured

directly from microstructural observations or indirectly by means of different physical properties of deformed and recrystallized regions e.g. microhardness and electrical resistivity. The main models typically used for analysis of recrystallization kinetics are:-

1. Johnson Mehl Avrami Kolmogorov (JMAK) model

   According to this model, the fraction of recrystallized material appearing after a given annealing time is related to annealing time as

$$X_V = 1 - \exp[-(kt)^n] \tag{2.10}$$

   The above expression can be derived by considering the nucleation rate ($\dot{N}$), the growth rate of a recrystallized grain growing into the deformed matrix ($\dot{G}$) and the volume fraction recrystallized (X_v). The total number of nuclei appearing in time interval is given by

$$d\dot{N} = \dot{N}dt = dN + \dot{N}X_V dt \tag{2.11}$$

   The above expression includes the contribution from newly emerging nuclei dN as well as nuclei assumed to form in the regions already recrystallized . The fraction of material recrystallized at time t can be obtained from the volume of recrystallized grains V as

$$X_{VEX} = \int V d\dot{N} \tag{2.12}$$

   The volume of each growing grain (assuming spherical shape) is given by

$$V = \frac{4\pi(\dot{G}t)^3}{3} \tag{2.13}$$

   Therefore

$$X_{VEX} = \frac{4\pi}{3}\dot{G}^3 \int \dot{N}t^3 dt \tag{2.14}$$

Assuming constant nucleation rate ($\dot{N}$):

$$X_{VEX} = \frac{\pi}{3}\dot{N}\dot{G}^3 t^4 \tag{2.15}$$

In a time interval *dt* the extended volume is increased by dX_{VEX} and is related to the actual incremental fraction recrystallized dX_V as

$$dX_V = (1 - X_V)dX_{Vex} \tag{2.16}$$

This on integration leads to

$$X_V = 1 - \exp(-X_{VEX}) \tag{2.17}$$

$$X_V = 1 - \exp(-\frac{\pi}{3}\dot{N}\dot{G}^3 t^4) \tag{2.18}$$

$$X_V = 1 - \exp(-kt^4) \tag{2.19}$$

The exponent *n* in above equation is referred as the Avrami or JMAK exponent and is closely related to the growth morphology of the recrystallized grains. In the ideal case of three-dimensional growth and constant nucleation rate the exponent value is 4. However, in case of site saturation, when all the nuclei are formed at time t = 0, the extended volume is given by $X_{VEX} = \frac{4\pi}{3}N(\dot{G}t)^3$, where N is total number of nuclei, and the exponent value is found to be 3 [6].

The important assumptions for the JMAK model include random distribution of nucleation sites and uniform growth of recrystallizing grains in three dimensions. However, if the grains are constrained by sample geometry or some internal constraints to grow only in one or two dimensions, then the JMAK exponent is lower than 3. An important insight is obtained from recent results obtained from recrystallization simulations. The variation in JMAK exponents with annealing temperature is found to be strongly affected by the distribution of stored energy. A low value of the JMAK exponent can be the result of

an inhomogeneous distribution of stored energy at low annealing temperatures. JMAK exponents are found to approach ideal values at high annealing temperatures when the inhomogeneous distribution in stored energy is minimal [25]. The effect of different nucleation and growth conditions on different n values is given in Table 2.2.

Conditions	N
Increasing nucleation rate	> 4
Constant nucleation rate	4
Decreasing nucleation rate	3-4
Site saturation (Zero nucleation rate)	3
Grain edge nucleation after saturation	2
Grain boundary nucleation after saturation	1

Table 2.2: Values of n in kinetics law $X_V = 1 - \exp[-(kt)^n]$. [1]

The analysis of recrystallization kinetics by the JMAK method is usually carried out by plotting $\ln(\ln(\frac{1}{1-X_V}))$ against $\ln(t)$. This plot is known as a JMAK plot. The slope of a linear regression fit of the data points yields the JMAK exponent n, whereas the intercept can be used to determine the temperature dependent coefficient k. An important conclusion obtained from recrystallization kinetics analysis of different materials using the JMAK method is that either the JMAK plot is not linear or the exponent is much less than 3, or both. It is therefore concluded that JMAK analysis is often too simple to quantitatively model a complex process like recrystallization. More parameters are needed to describe the changes in microstructure to derive quantities like nucleation and growth rates and the behavior of nucleation and growth processes [6]. The activation energy for recrystallization can be obtained by analyzing the temperature dependency of the parameter k. Typical values obtained for activation energy of recrystallization in aluminun are in the range 200-240 kJ/mol [26, 27].

2. Microstructural path methodology

The main difference between this approach and the JMAK model is that a more realistic

and more powerful model is obtained by using additional microstructural parameters in the analysis. In addition to volume fraction recrystallized (X_V), the other important quantities used in microstructural path modeling are the interfacial area density separating the new recrystallized grains from the as-yet deformed matrix (S_V) and the mean recrystallized grain chord length $\langle\lambda\rangle$. A quantity similar to extended volume fraction (X_{VEX}) can be defined for interfacial area (S_{VEX}) as

$$S_{VEX} = \frac{S_V}{1 - X_V} \tag{2.20}$$

The assumptions of random spatial distribution of nuclei and growth rates being global rather than local are common to the two approaches and equivalent to an assumption of homogeneous behavior in the material [6]. The kinetics of recrystallization for commercial purity aluminum alloys 1050 as modeled by microstructural path modeling has indicated recrystallization to be growth controlled for hot as well as cold deformed microstructures. Recrystallization is found to be site-saturated and the recrystallized grains sizes are 3-4 time large after hot deformation than after cold deformation to a similar strain [28, 29].

Nucleation of recrystallization

The nucleation and growth aspects of the recrystallization process are similar to those observed during phase transformations. However, the level of similarity is restricted to the microstructural level only. The thermal fluctuation model has been used for a long time for kinetic studies of solidification and solid state phase transformations. A critical sized nucleus in this model is usually obtained from random thermal fluctuations. The size of this nucleus is obtained from an energy balance between the reduction in energy due to formation of a stable phase and the amount of energy needed to form the surface of a critical sized nucleus. The major problem for the study of recrystallization with the thermal fluctuation model is that, given the typical low values of stored energy of deformation and high energy for a high angle grain boundary, the energy barrier for recrystallization is so large that new grains cannot form by this

mechanism even at high enough temperatures $T > 0.5T_m$ where grains do indeed nucleate and grow.

An alternative mechanism of nucleation of recrystallized grains during annealing of deformed metals was proposed by Cahn. According to this model, new recrystallized grains are formed from recovered subgrains and cells that are already present in the deformed microstructure. An important consequence of this idea is that the orientation of each new grain arises from the orientations present in the deformed state. In the deformed state, even though there is a very high defect density, the equilibrium crystal structure is still present everywhere. A typical subgrain size in deformed polycrystalline aluminum is $1\mu m$ however; the recrystallized grain size after primary recrystallization can evolve to a grain size as large as $100\mu m$. An increase in diameter of 100 indicates a volume increase from subgrain embryo to the final recrystallized grain of about 10^6. This estimate indicates that only one subgrain in a million becomes a successful recrystallized nucleus. The main reason for this low probability is the low mobility that most subgrain boundaries have because of their small misorientation. Only subgrains with a high misorientation angle to the adjacent deformed material have the necessary mobility to evolve into new recrystallized grains.

Typical nucleation sites, all of which have high local misorientation, include:-

1. Pre-existing high angle grain boundaries - Grain boundaries give rise to inhomogeneity of slip such that different combinations of slip systems will operate near a grain boundary, thereby giving rise to high local misorientations.

2. Transition bands - Transition bands represent regions of large orientation gradients, separating regions of different orientations within a grain. These are therefore an ideal site for recrystallization. The crystallographic orientations developed in transition bands are a direct consequence of the slip processes and local strain heterogeneities.

3. Shear bands - Shear bands are thin regions of highly strained material typically oriented at about 35^o to the rolling plane. They are formed due to strain heterogeneity and instability during rolling. High local misorientations between adjacent regions provide adequate

boundary mobility for subgrains to grow.

4. In the highly misoriented regions around large particles.

The existence of a high angle boundary is observed to be a necessary but not sufficient criterion for a subgrain to become a successful nucleus. The subgrain must usually have a larger size than the average to be able to grow in order and form a successful nucleus. Thus the combination of high local misorientation requirement and a size advantage makes the nucleation process rare [2]. A size advantage for a subgrain present in the deformed matrix can occur by the mechanisms of Strain Induced Boundary Migration (SIBM) and subgrain coalescence. SIBM involves bulging of part of a pre-existing grain boundary, leaving a dislocation free region behind the migrating boundary. The characteristic features are that the new grains have a similar orientation to the old grains from which they have grown. The mechanism is found to be dominant only at low strains in aluminum.

The coalescence of several subgrains on one side of a grain boundary has been observed to yield a subgrain large enough to grow rapidly into an adjacent grain. The formation of a single subgrain takes place through rotation by diffusional boundary processes until adjacent subgrains are of similar orientation. The driving force for coalescence is provided by reduction in total boundary energy [6].

Migration of high angle boundaries

Grain boundaries play a key role in the recrystallization process both in nucleation where prior grain boundaries and deformation induced boundaries can provide nucleation sites, and also during growth where grain boundary migration is the essential feature. A viable nucleus is surrounded, at least partly, by a high angle boundary which is able to migrate through the deformed microstructure causing the nucleus to grow. The driving force for migration of high angle grain boundaries is provided by the stored energy of deformation. The velocity of migration is the product of mobility M and driving force Δf :

$$v = M\Delta f \tag{2.21}$$

The mobility, the driving force and, therefore the velocity of migration depend on deformation as well as annealing parameters [2]. During the growth of a nucleus in a subdivided deformed matrix, the boundary will constantly meet new types of deformation microstructures and new crystallographic orientations. Its growth rate will therefore change continuously. Even nearby segments of a boundary may experience quite different growth conditions because of small scale variations in the deformed matrix. The recrystallizing grain will therefore not have a constant driving force along its perimeter. The mobility of a grain boundary also depends on the misorientation between the neighboring regions. Low angle grain boundaries are found to be much less mobile than high angle grain boundaries as low angle grain boundary motion involves a coordinated climb of the dislocation arrays. A grain growing into deformed matrix during recrystallization encounters regions with varying misorientation with respect to its own orientation. A phenomenon known as orientation pinning is observed when a migrating segment of a growing recrystallized grain impinges on a deformed volume element of the same or nearly same orientation and forms a low angle boundary [12].

The analysis of boundary migration rates has been carried out for different texture components. The cube component in deformed aluminum has been observed to have a slight growth advantage compared to other orientations. This growth advantage allows the cube component to persist throughout recrystallization, starting from a relatively weak initial texture. In a deformed material there are a number of different texture components that can be prevalent. An emerging nucleus of a weak texture component will encounter less orientation pinning than those emerging from the stronger components. This provides a growth advantage for the cube recrystallized grains [30]. The solute atoms present in a material have a significant effect on boundary mobility. The mobility of grain boundaries decreases with increasing solute concentration. The boundary mobility is then controlled by the rate of diffusion of the impurity atoms. At very low solute concentrations, the boundary mobility is little affected by solute atoms and the boundary can break away from the solute atmosphere if the driving force is high enough [6].

Texture evolution during recrystallization

Texture evolution during recrystallization of deformed metals is an important phenomenon. The texture of the (recrystallized) grains is largely responsible for the directionality of properties observed in many finished products. The development of recrystallization texture is dependent on a large number of parameters including the dependence of nucleation rate on inhomogeneities and orientation environment, and on the nature, energy and mobility of the boundaries between grains of various orientations. The evolution of a strong recrystallization texture from a deformation texture, which is often unlike the deformation texture, points to the fact that recrystallization can be considered to be a nucleation and growth process; new grains with new orientations grow into the deformed matrix, thereby eliminating the stored work of plastic deformation. An important observation from the vast experimental data on recrystallization texture evolution is the absence of sensitivity of texture evolution to annealing conditions and a strong dependence on prior deformation texture [2]. Texture evolution during recrystallization in fcc metals often involves a substantial increase in the cube component $\{001\}\langle 100\rangle$. The evolution of the cube component during recrystallization is significant for changes in anisotropic behavior during forming operations. The presence of a cube texture can balance the deformation texture in cold rolled sheet, thereby decreasing the anisotropy in forming [31].

The main theories of texture evolution during recrystallization are those of oriented nucleation (ON) and oriented growth (OG) [2]. The underlying principles of these theories are that the strength of the recrystallization texture is determined primarily by either the preferential nucleation of some selectively oriented grains or by preferential growth of these grains [32]. The ON mechanism of texture evolution has been found for a large number of examples for bcc and fcc metals. The formation of a deformation band with a particular orientation leads to evolution of nuclei of nearly the same orientation. The OG mechanism is based on the rapid migration rates of certain specific high angle boundaries during the growth of recrystallized grains e.g. the $40^o\langle 111\rangle$ boundary between the cube component in recrystallized regions and the S component in deformed regions. The high mobility of these boundaries allows cube recrystallized grains to grow rapidly compared to all other grains and to promote a dominant cube texture. The overall

recrystallization texture evolution however, is found to have significant contributions from the range of orientations available and the subsequent growth advantage enjoyed by any grain. It is now recognized that any recrystallization nucleus in a heavily deformed polycrystal is surrounded by a wide spread of orientations and these surroundings will change during growth [6].

Texture evolution during annealing of hot deformed samples is strongly influenced by the starting texture of the material. Of particular significance is the volume fraction of the cube component in the prior microstructure. The cube component is metastable during deformation and the strength of all its variants (e.g. RD and TD rotated cube) decreases with increases in the level of strain [33, 34]. Analysis of samples deformed in plane strain compression with different starting cube textures, indicate its importance in the texture evolution after recrystallization. The presence of cube oriented matrix after deformation is highly correlated with high cube fractions after annealing. The stability of cube grains is found to increase with rotations away from the exact orientation. The rate of decline is highest for the non-rotated samples as compared to the rotated ones. The effect of temperature and strain rate on the evolution of deformed cube grains can be correlated with the variation with Zener-Hollomon (Z) parameter. A lower volume fraction of deformed cube grains is obtained for the high Z values (low temperature-high strain rate) as compared to low Z values (high temperature-low strain rate). The sample orientation makes little contribution to the volume fraction of deformed cube grains [34].

The evolution of the cube component is strengthened by high rolling reductions and high annealing temperatures. The presence of magnesium in aluminum alloys is found to have a detrimental effect on cube texture evolution. Addition of magnesium, in the form of solid solutions is found to increase the strength of the alloy and promotes the formation of shear bands. Recrystallization at shear bands is known to reduce the strength of the cube component due to nucleation of components other than cube at the shear bands.

The presence of small amounts of iron and silicon in commercial purity aluminum alloys results in the formation of second phase particles, called constituent particles. Recrystallization

texture evolution involves a significant contribution from these particles to particle stimulated nucleation (PSN) [6] especially in cold rolling. The presence of second phase particles is known to affect recrystallization by the formation of highly misoriented zones near the particles during deformation especially during cold rolling. These particles act as preferred nucleation sites for recrystallization and lead to the formation of nuclei of various orientations. The texture strength due to PSN is inversely related to amount of strain in deformation. Small strains will result in formation of a fewer orientations during deformation. Since the recrystallized grain orientation is a direct consequence of the deformation orientation, the recrystallization texture in this case is quite sharp. In case of medium to large strain deformations, highly misoriented regions form and the deformation zones have a large number of orientations present. This weakens the recrystallization texture.

Small second phase particles in a fine dispersion are also known to reduce the mobility of high angle grain boundaries, thereby affecting recrystallization kinetics, and grain size and texture evolution. Small particles pin grain boundaries and a recrystallization texture similar to deformed texture is observed in bcc and fcc metals [6]. The commercial purity aluminum alloys (AA 1XXX series) contain iron and silicon among other elements, which are know to have an effect on recrystallization kinetics and texture evolution. Small amounts of iron may change the annealing texture from almost pure cube to a strong retained rolling texture. In aluminum alloys with low iron concentrations, the cube component dominates, however, an increase in iron content can lead to precipitation on the recrystallization front. The consequent solute drag and precipitation leads to slower growth of the dominant cube grains and allow the rolling components to develop, thereby reducing the strength of cube texture. An example of the effect of iron content on the cube recrystallization texture component is shown in Fig. 2.8 for Al-0.007%Fe. As indicated by the ODFs, while a high fraction of cube grains is obtained at low and high annealing temperatures, the texture of recrystallized samples annealed at intermediate temperatures such as 360^oC results in a mostly retained rolling texture. The above observations are explained from the fact that precipitation of an iron rich phase at intermediate annealing temperatures hindered the boundary migration. At the lower and high temperatures, however,

the effect on boundary migration is less drastic and a strong cube texture develops. The presence of silicon in aluminum alloys leads to formation of a stable Al-Fe-Si phase. This will reduce the Fe content in solid solution. The texture evolution in this case is found to be more random due to the PSN effect of coarse constituent particles and reduction in rolling component [6]. PSN is also found to be a dominant mechanism in the presence of large ($> 1\mu m$) Al_3Fe precipitates and leads to a large fraction of randomly oriented grains which therefore reduced the strength of the recrystallization texture components [31].

The recrystallization textures evolved during annealing of deformed samples also contain some orientations similar to rolling texture, apart from the cube orientation. The main mechanism for the formation of recrystallized grains with rolling orientations is Strain Induced Boundary Migration (SIBM). A difference in dislocation densities on either side of an existing grain boundary can lead to migration of the boundary into the grain with higher stored energy. In an Al-3%Mn alloy, SIBM is observed to nucleate Brass oriented recrystallized grains by migration of a high angle boundary into S oriented deformed grain. Texture analysis of consumed and recrystallized grains revealed formation of recrystallized grains with all rolling orientations with significant preference to Brass oriented grains as shown in Fig. 2.9 . The Brass oriented grains are found to have small intra-granular misorientations leading to small stored energies and high stability [7].

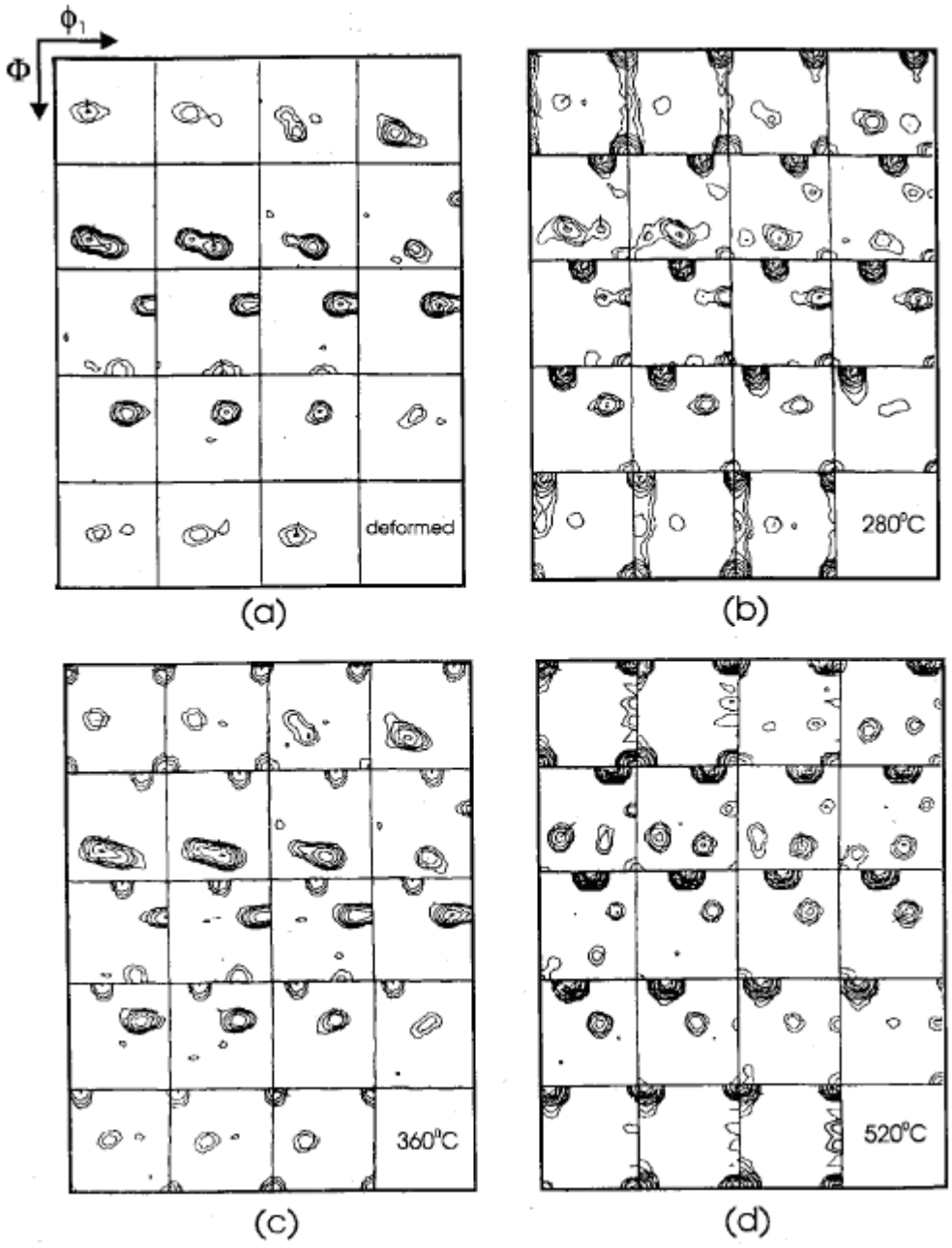

Figure 2.8: Recrystallization annealing of Al-0.007%Fe at different annealing temperatures revealing the effect of precipitation of iron particles. (a) Deformed sample (b) annealed at 280^oC, (c) 360^oC, (d) 520^oC [6].

The main source of cube grains during recrystallization is the metastable cube band which forms as a result of deformation on prior cube grains [35, 36, 37, 38]. The deformed cube bands act as the nucleation sites for cube recrystallization texture. Subgrains formed in these cube

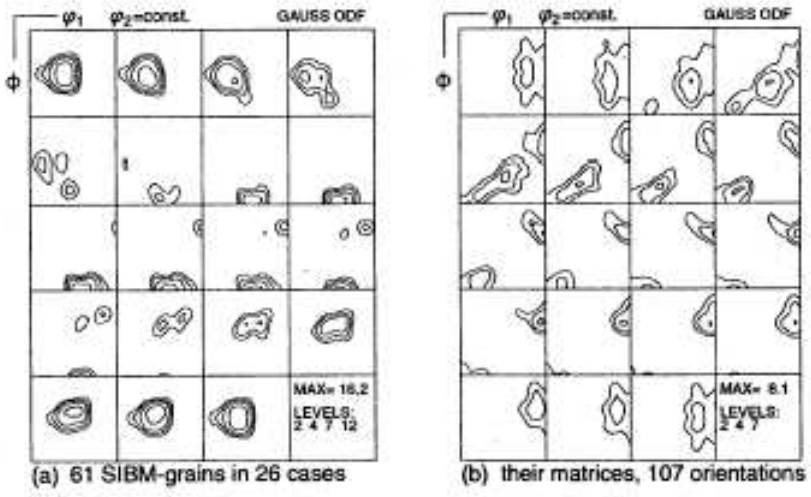

Figure 2.9: (a) Texture of recrystallized grains with rolling orientations (b) Texture of the adjacent matrix [7].

bands are found to have a significant size advantage compared to subgrains of other orientations as shown in Fig. 2.10, which may be a direct consequence of high recovery rates in these grains. The fraction of this retained cube decreases with strain, and the rate of decrease increases with the value of the Zener-Holloman parameter [39]. A recent study of formation of cube recrystallized grain during cold and warm rolling of aluminum alloys by Samajdar *et al.* shows large effects of orientation pinning on warm rolled materials which leads to an absence of rolling texture in warm rolled materials [40]. Orientation pinning is found to be absent in cold rolled materials and significant amounts of deformation components were observed in overall recrystallization textures [15]. Growth rate analysis of cube recrystallized grains in aluminum and copper alloys has revealed the presence of a lower fraction of low angle grain boundaries compared to the grains of other texture components, thereby providing the required growth advantage for cube grains leading to a dominant cube texture [3].

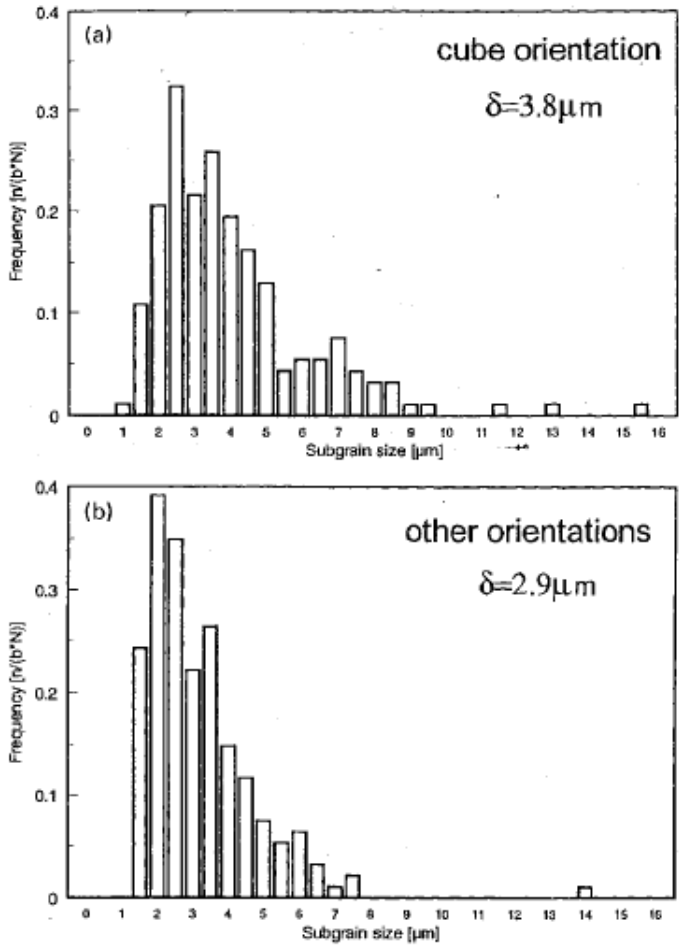

Figure 2.10: Variation in subgrain size for (a) Cube and (b) other orientations showing larger average subgrain size in cube regions [8].

3 Experimental Methods

The aluminum alloys used in the present study are hot rolled alloys 1050 and 5005 and were supplied by the Alcoa Technical Center, Pittsburgh. The chemical compositions of the two alloys are given in Table 3.1. The main compositional difference between the two alloys is the concentration of Mg. The present study therefore also reflects the effect of Mg concentration on recrystallization kinetics and texture evolution in hot rolled aluminum alloys. The thicknesses of the as-received sheets are about 6mm for AA1050 and about 3.5mm for AA5005. The AA1050 sheet was given a prior deformation treatment of hot rolling at 325^oC and allowed to cool in air. As a result of slow cooling to room temperature, the AA1050 and AA5005 samples showed a significant amount of recovery in the as-received state.

Element	Si	Fe	Cu	Mn	Mg	Zn	Ti	Al
AA1050	0.08	0.31	0.003	0.036	0.004	0.009	0.008	99.54
AA5005	0.30	0.70	0.20	0.20	1.10	0.25	0	97.00

Table 3.1: Chemical composition of AA1050 and AA5005 in wt%.

The as-received hot rolled sheet of AA1050 was machined to obtain small samples with dimensions $20mm \times 10mm \times 6mm$ for annealing treatments at different temperatures for varying lengths of time. The annealing treatments were carried out in molten salt pots to provide uniform heating of samples. The annealing temperatures were varied from 200^oC to 450^oC for AA1050 and 200^oC to 500^oC for AA5005, to determine the temperatures suitable for carrying out isothermal annealing treatments. Isothermal annealing was carried out at $325^oC, 350^oC, 375^oC$ and 400^oC for time periods ranging from 30s to 7200s for complete recrystallization of hot rolled AA1050 samples. AA5005 samples were isothermally annealed at $350^oC, 375^oC$ and 400^oC for times ranging from 30s to 3600s for complete recrystallization. The annealing treatment for each time and temperature was performed on two samples, to obtain an average value from the samples and minimize any variation due to local microstructural inhomogeneity. The experimental analysis of the two alloys involved obtaining microhardness values for indirect recrystallization kinetics evaluation and scanning the polished samples in

a Scanning Electron Microscope (SEM) for orientation measurement using an Electron Back Scatter Diffraction (EBSD) system. The EBSD analysis was carried out to evaluate recrystallization kinetics and observe texture evolution directly from microstructural and orientation information. The as-received and annealed samples were also analyzed by measuring X-ray diffraction pole figures with different sample orientations (RD-TD section and ND-TD section). The X-ray diffraction experiments were carried out for a comparison of texture evolution obtained from local EBSD scans and large X-ray diffraction scans, since the latter provides an average texture from a relatively large area.

3.1 Microhardness Analysis

The annealed samples were polished with various grade polishing papers followed by $1\mu m$ alumina powder for microhardness tests. Microhardness indentations were obtained at different locations on the samples. On average, 8 to 10 microhardness indentations were obtained on each sample. A schematic view of a microhardness indentation obtained from the diamond shaped indenter is shown in Fig. 3.1. The microhardness indentations were obtained on the plan (RD-TD) surface of the sample. The size of the indentation is measured from the diagonals d_1 and d_2. A 500gm load was used for indentations. Microhardness values were obtained from the size of the indentation as

$$H = \frac{2l\sin(\frac{\theta}{2})}{d^2} \tag{3.1}$$

Here, H is the microhardness of the sample (MPa),

l is the applied load (= 500gm),

θ is the angle at the tip of indenter ($\theta = 130^o$),

d is the average size of indenter ($d = \frac{d_1+d_2}{2}$).

The final microhardness value represents an average value obtained from two samples annealed at the particular time and temperature. An average hardness of 380MPa was obtained for the as-received (deformed) samples and 200MPa for completely recrystallized samples for AA1050. The corresponding values for AA5005 were 475MPa and 325MPa for deformed and recrystallized samples, respectively. An average microhardness indentation size of $150\mu m$ was

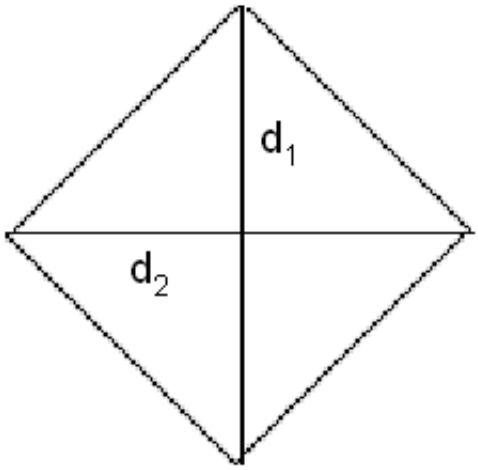

Figure 3.1: Schematic view of indent obtained from a Vickers microhardness machine.

obtained for deformed grains, whereas an average indentation size of 200μm was obtained for recrystallized grains for AA1050 samples. The average sizes for AA5005 samples were 130μm and 165μm for deformed and recrystallized grains, respectively. The microhardness values of partially recrystallized samples lie between the above extreme values of deformed and completely recrystallized samples.

3.2 EBSD Analysis

The annealed samples were ground and electropolished with a perchloric acid solution for characterization in a Philips FEI XL40 Field Emission Gun scanning electron microscope using TSL^{TM} EBSD software. Three scans, typically 600$\mu m \times 600\mu m$ in size, were obtained on each sample. Step sizes of 0.5μm and 0.75μm were used for as-received samples, which had a deformed microstructure consisting of cells and subgrains, while larger step sizes between 1μm and 2μm were used for partially and completely recrystallized samples where large recrystallized grains were present. The varying step sizes were used to optimize the data collection from OIM. Small step sizes provide better accuracy for cells and subgrains present in deformed grains but take much longer times. Large step size on the other hand is faster but the maps are

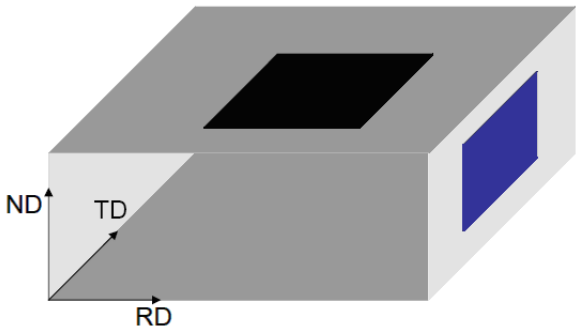

Figure 3.2: Schematic representation of the different scanned sections of a sample.

less accurate. A schematic of the different sample surfaces scanned is given in Fig. 3.2.

The as-received samples have large grain sizes of the order of a few millimeters along the rolling direction. Therefore a representative microstructure for the as-received sample containing deformed grains of different orientations could not be obtained in a plan view scan (TD-RD section) even with a scan size of $1000\mu m \times 1000\mu m$. A scan in this section yielded only a few partial grains as shown in Fig. 3.3(a). The texture from this scan was compared with that obtained from X-ray diffraction sample orientated in a similar manner (TD-RD section). An obvious difference was observed in the texture between the two methods of analysis, as indicated in Fig. 3.3 (b), (c). The pole figures obtained from X-ray diffraction measured an average texture over a larger number of grains scan and are typical of rolled fcc metals. The pole figures obtained from OIM analysis are indicative of a localized scan having only a few components of the overall texture. The texture obtained from the EBSD scan in Fig. 3.3(b) showed a large fraction of Brass oriented $\{110\}\langle 112\rangle$ deformed grains, indicated by a maximum at the center in (101) pole figure. Because of the large grain sizes in hot rolled samples and the inability to scan very large areas in OIM, the scans obtained on plan section were found to be inadequate to study textural evolution during annealing of as-received hot rolled samples.

This problem was solved by scanning the samples in a different sample orientation. A comparison of scans obtained from a deformed sample on a transverse cross section (ND-TD section) from OIM and X-ray diffraction revealed similar textures from the two methods, shown in Fig 3.4 (b), (c). Scanning the deformed samples along one of the short directions gave a

better representation of deformed microstructure and texture due to compression of the original grains. An accurate representation of deformation texture was therefore obtained from OIM in reasonable area scans. The texture of a deformed sample in terms of typical deformation texture components, based on the conventional frame of reference, was obtained by rotating the data points about transverse direction (TD) by 90^o. A rotated view of deformed sample in Fig. 3.3(a) is shown in Fig. 3.5(a). As indicated in Fig. 3.5(b), the texture of the rotated sample compares well with the texture obtained for the plan view (TD-RD section) in X-ray diffraction, Fig. 3.3(c). All the samples for microstructural and textural characterization from OIM are therefore scanned along the transverse cross section and rotated about the TD axis by 90^o to obtain the texture in the standard configuration.

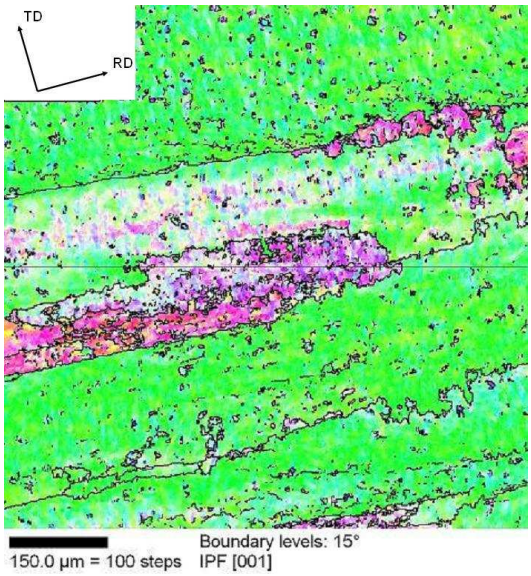

(a) Microstructure of a deformed sample scanned along TD-RD section obtained from OIM showing only a few of grains.

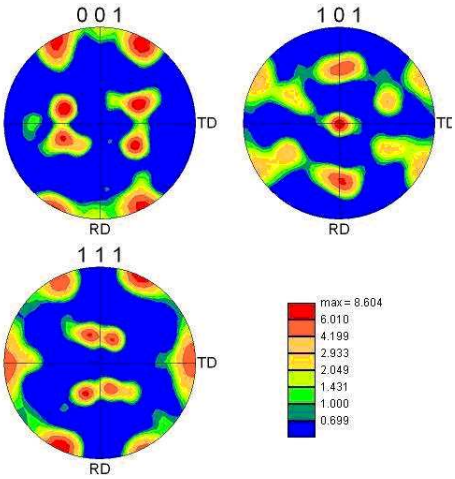

(b) Pole figure of sample scanned in (a), indicating corresponding peaks.

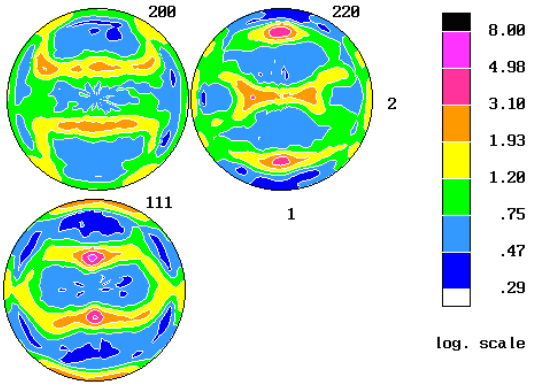

(c) Pole figures obtained from X-ray diffraction along the TD-RD section

Figure 3.3: Deformation microstructure and texture from a plan view OIM scan.

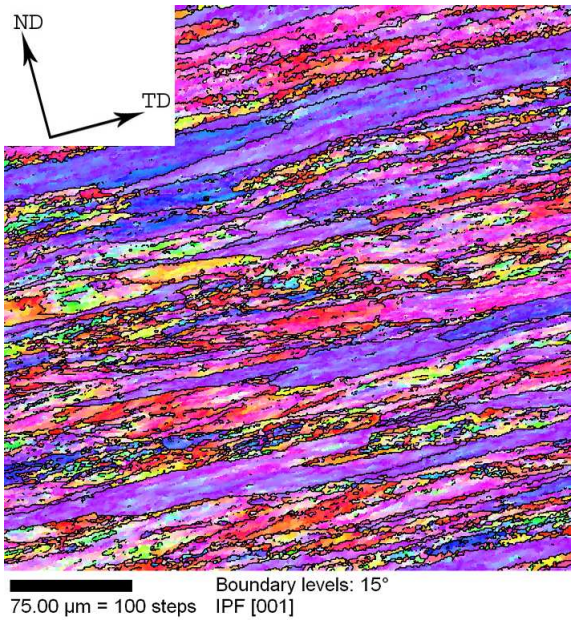

(a) Microstructure of a deformed sample scanned along ND-TD section obtained from OIM showing a large number of compressed grains.

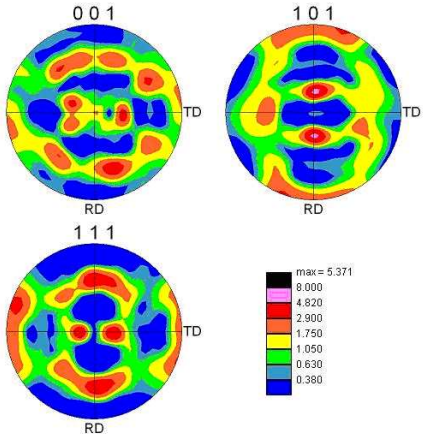

(b) Pole figure of sample scanned in (a), indicating corresponding peaks.

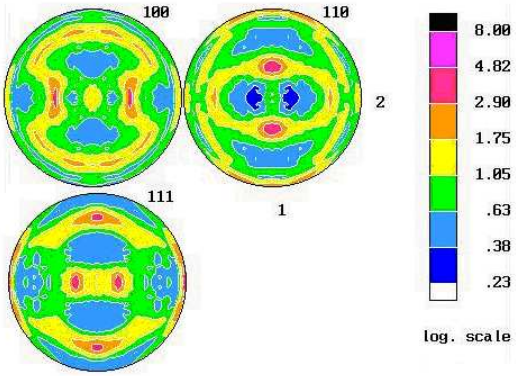

(c) Pole figures obtained from X-ray diffraction along the ND-TD section

Figure 3.4: Deformation microstructure and texture along the transverse cross section.

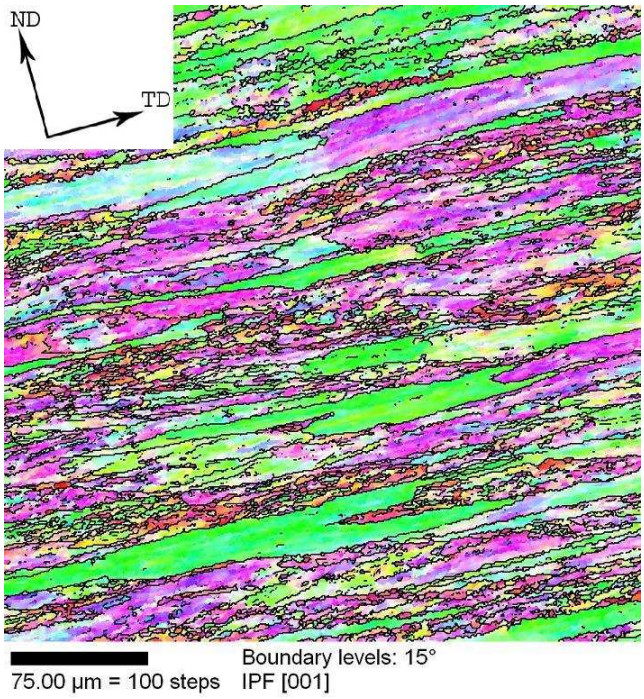

(a) Microstructure of a deformed sample scanned along ND-TD section after 90^o rotation about TD.

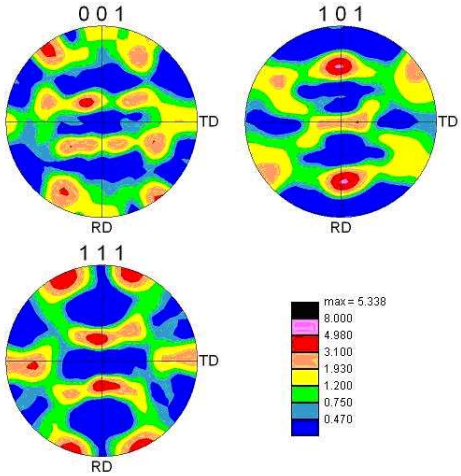

(b) Pole figure of sample scanned in (a), show a typical fcc rolling texture.

Figure 3.5: Deformation microstructure and texture along the transverse cross section after rotating about TD by 90^o.

3.3 Deformation Simulator

Hot deformation experiments simulating rolling experiments were also carried out on AA1050 and AA5005 samples. The hot deformation experiments were carried out at the Alcoa Center in a specially designed machine with attached furnaces which allowed precise control of deformation conditions (temperature, strain and strain-rate). The samples were deformed in plane strain compression at 200^oC and 400^oC. A thermocouple attached to the sample gave accurate measurement of the deformation temperature. The deformed samples were quenched in water within 5 seconds after completion of deformation. Table 3.2 gives the details of hot deformation conditions for two alloys. All the samples were deformed to a total strain of 50%, which was the maximum practicable strain.

The hot deformation experiments were carried out to determine the effect of deformation parameters on the microstructural and textural evolution in the two aluminum alloys. These deformation experiments were aimed at determining a window of operating conditions suitable for carrying out further hot deformation experiments. A schematic of the deformation simulator is given in Fig. 3.6. As it turned out, however, the experiments on the as-received material, allied with these deformation simulator experiments provided ample data for analysis.

Alloy	Temperature(^oC)	Strain rate (s^{-1})
AA1050	200	0.01
AA1050	200	1.00
AA1050	400	0.01
AA1050	400	1.00

Table 3.2: Hot deformation conditions for the deformation simulator experiments.

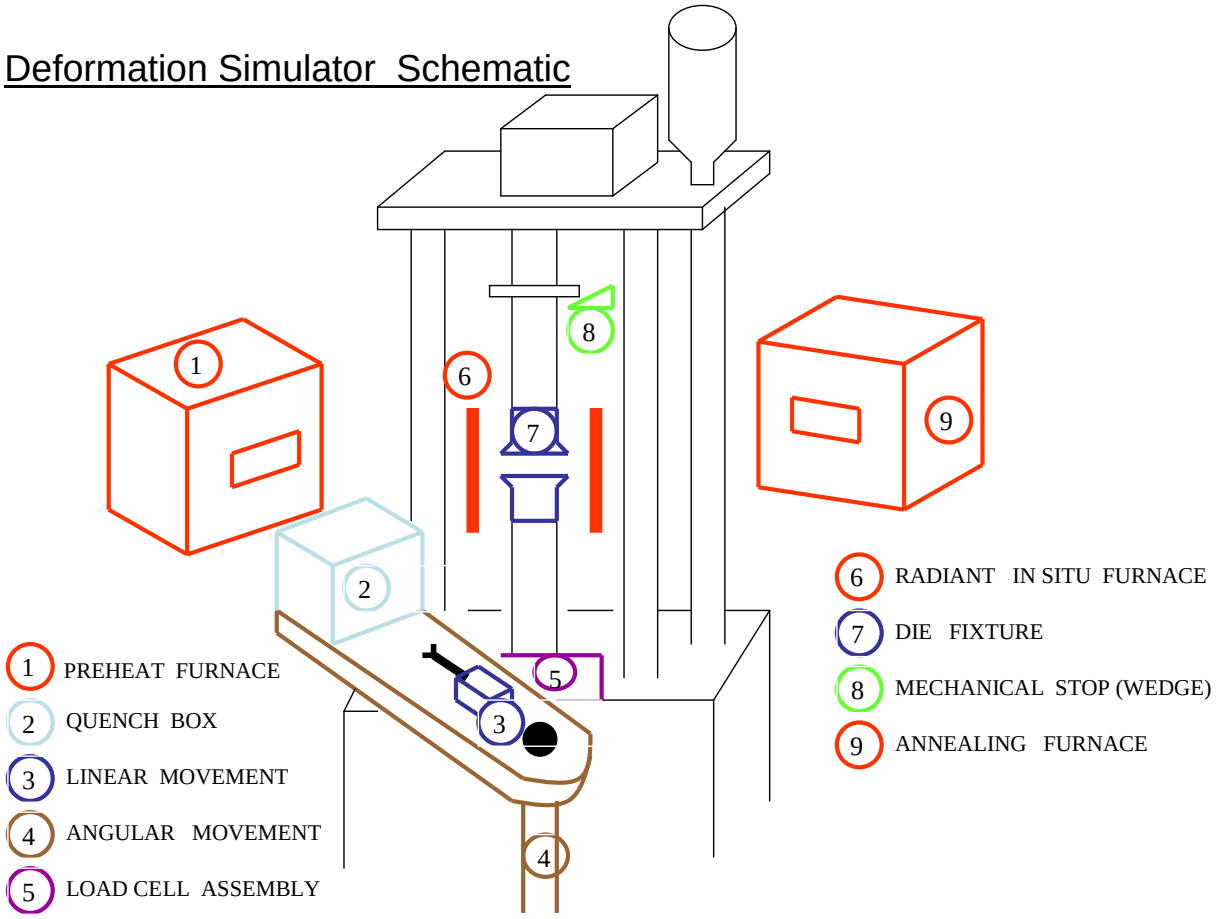

Figure 3.6: Schematic view of the Alcoa deformation simulator used in the current study.

4 Results

The aluminum alloys analyzed in the present study are 1050 and 5005. The kinetics of recrystallization were determined from the variations in microhardness values and the microstructural parameters determined from Orientation Imaging Microscopy (OIM). The parameters of recrystallization kinetics obtained from microhardness values served as the basis against which the parameters obtained from OIM were compared. Different algorithms were developed for determining important microstructural features such as fraction recrystallized (X_V), interfacial area per unit volume between deformed and recrystallized grains (S_V), and contiguity of recrystallized grains (C_r), all from OIM maps. The methods based on intragranular orientation variations were found to be useful for microstructural characterization.

The major portion of the experimental work was carried out on AA1050. A method of analysis was developed which was applied to AA5005 and samples obtained after hot deformation in the deformation simulator. A detailed analysis of recrystallization kinetics was carried out from the microhardness variations including the estimation of activation energy of recrystallization. The Grain Orientation Spread (GOS) method was found useful for partitioning maps into deformed and recrystallized regions. Recrystallization kinetics were obtained from OIM maps by using the Microstructural Path Method (MPM) approach. The results obtained from microhardness and OIM compared well for recrystallization kinetics. The partitioned scans were also analyzed for texture evolution during recrystallization.

4.1 Microhardness Variations

Microhardness values were obtained from the size of indentations and applied load. A typical indent area of $0.1mm^2$ was obtained from each microhardness indent. The microhardness values are directly related to microstructure of the sample. The indentation size is representative of the ease with which plastic flow can occur in the material. This is directly related to dislocation content in the material. An annealed sample with low dislocation content will provide less resistance to plastic flow and yield relatively large indentations (low microhardness values) as compared to a deformed sample, where the prior dislocation content will resist

any further plastic flow and small indentations (high microhardness values) are obtained in this case. The microhardness indentations were obtained on deformed (as-received) and annealed samples. Two important variations were obtained from microhardness tests. The variation of microhardness values with annealing temperatures was used to determine temperatures suitable for isothermal annealing. The microhardness values for isothermally annealed samples with different annealing times were used to determine kinetics of recrystallization.

4.1.1 Microhardness Variation with Annealing Temperature for AA1050

The as-received samples of hot rolled AA1050 were annealed for 1 minute at different annealing temperatures, ranging from 225^oC to 450^oC. The microhardness values obtained for these samples are shown in Fig 4.1. The maximum microhardness value of 378 MPA is obtained for low temperature ($< 300^oC$) annealed samples and the minimum microhardness value of 195 MPA is obtained for completely recrystallized samples at high annealing temperatures ($> 400^oC$). The variation in microhardness values is small at low temperatures, followed by a rapid decline and finally levels off at high annealing temperatures. The microhardness values at low temperature annealing are similar to those obtained from as-received samples, indicating no changes in microstructure during low temperature annealing.

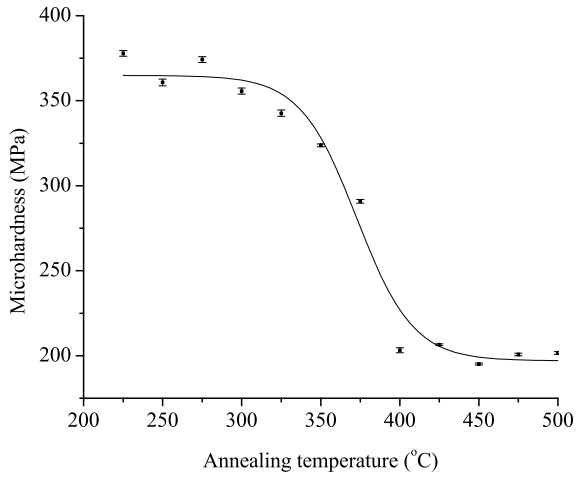

Figure 4.1: Microhardness variations with annealing temperatures for AA1050 samples annealed for 1 minute.

The error bars obtained from the microhardness values are relatively small. A variation of 2MPa was obtained for as-received and partially recrystallized samples and about 0.5MPa for completely recrystallized samples. These values are small compared to the overall changes in microhardness over the entire transformation and are therefore neglected in further analysis. The recrystallized fractions can be obtained from microhardness values by assuming a fraction recrystallized of zero for high microhardness values and one for low microhardness value. Mathematically, it can be expressed as

$$X_i = \frac{H_{max} - H_i}{H_{max} - H_{min}} \tag{4.1}$$

Here, H_{max} is maximum hardness corresponding to deformed samples,

H_{min} is minimum hardness corresponding to completely recrystallized samples,

H_i is hardness value at particular annealing temperature, and

X_i is fraction recrystallized at particular annealing temperature.

The variation of fraction recrystallized for different annealing temperatures is shown in Fig 4.2. An S-type behavior is obtained from the above variation in microhardness. No change in recrystallized fraction is observed for samples annealed at temperatures less than 300^oC and higher than 400^oC, indicating the deformed and completely recrystallized states respectively. The flat regions of the curve during initial and latter parts of annealing reflect no change in microstructure during heating. The middle part of the curve represents a composite microstructure consisting of deformed and recrystallized regions with the fraction gradually approaching one from low initial values. The microstructural heterogeneity is prominent during the early stages of annealing as compared to the latter stages, as shown in Fig. 4.2, indicating a high variation in deformed microstructure and a stable recrystallized microstructure formation during high temperature annealing.

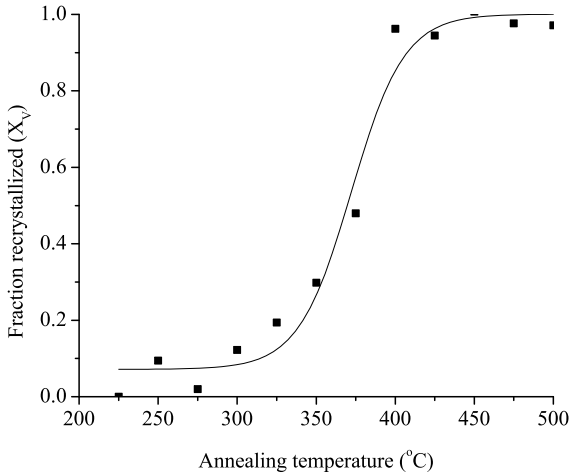

Figure 4.2: Recrystallized fractions for AA1050 samples annealed at different temperatures for 1 minute.

Based on microhardness variations in the samples at different temperatures, four annealing temperatures were selected, $325^oC, 350^oC, 375^oC$ and 400^oC, for isothermal annealing and recrystallization kinetics analysis. The selected temperatures lie in the middle portion of plot in Fig 4.2 and were expected to recrystallize in reasonable time lengths during isothermal annealing.

4.1.2 Recrystallization kinetics from Microhardness Variations

The isothermally annealed samples of hot rolled AA1050 were analyzed for recrystallization kinetics by using the Johnson Mehl Avrami Kolgomorov (JMAK) model. The recrystallized fractions were obtained by using Eq. 4.1. The microhardness values obtained after isothermal annealing at different temperatures included contributions from recovery as well as recrystallization. The determination of recrystallization kinetics would, therefore, involve removal of recovery contributions from the overall microhardness values. Assuming that the isothermal recovery kinetics follow a logarithmic decay relationship, the effect of recovery can

be estimated from the relationship

$$H_{rex} = A - B \ln t \tag{4.2}$$

Where H_{rex} is hardness of an annealed sample if only recovery takes place,

$A = H_1$, the hardness at 1 s annealing time, and

B is the slope of straight line in plot of micro-hardness variation with [41].

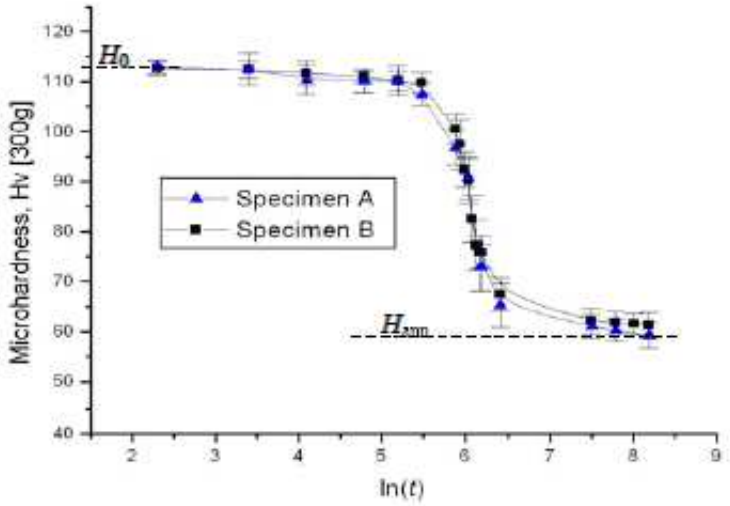

Figure 4.3: Variation of microhardness with during annealing of copper samples [9].

The variation of microhardness with time for OHFC Copper obtained by [9] is shown in Fig. 4.3, indicating that the annealing process can be divided into three stages. During the early stages of annealing, the microhardness values show a very small variation, followed by a significant decrease in a very short time. During the final stages a behavior similar to those obtained at low annealing times is obtained. The three stages observed in Fig. 4.3 are suggestive of recovery, recrystallization and grain growth processes [9]. Plots similar to Fig 4.3 were obtained for samples annealed isothermally at $325^oC, 350^oC, 375^oC$ and 400^oC as shown in Fig 4.4. A linear portion during the early stages, indicative of active recovery, was absent for the annealed AA1050 samples. Thus it was concluded from above analysis that the as-received

hot rolled samples were in a recovered state and the reduction in microhardness values are indicative of recrystallization process alone.

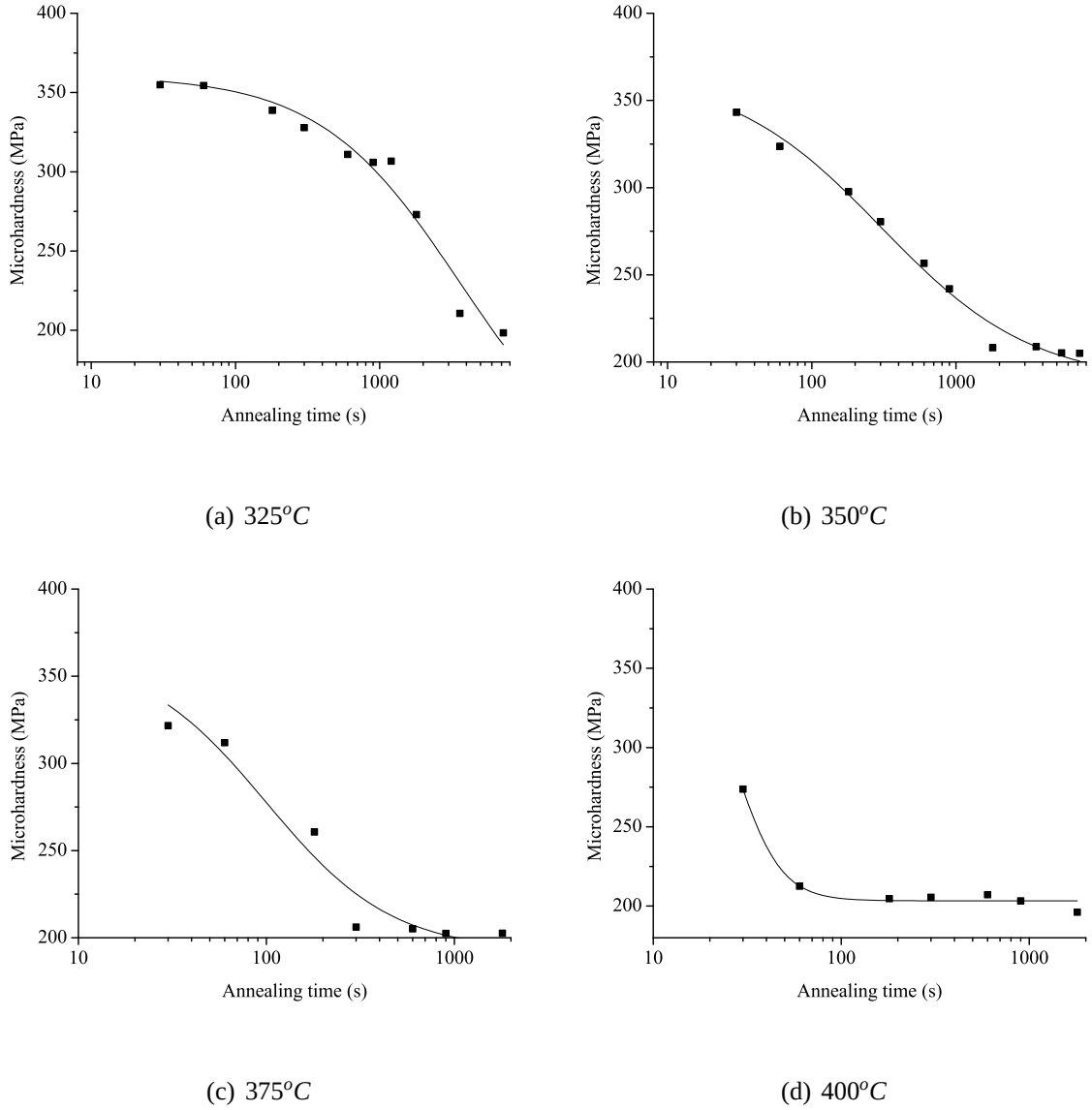

(a) 325^oC (b) 350^oC

(c) 375^oC (d) 400^oC

Figure 4.4: Variation of microhardness with time for isothermal annealing at (a) 325^oC, (b) 350^oC, (c) 375^oC and (d) 400^oC. The flat portion of the curves at long times corresponds to the grain growth process.

The kinetics of recrystallization were obtained from the fraction recrystallized data, determined from microhardness values. The JMAK parameters for recrystallization kinetics were

obtained from non linear curve fitting of experimental values to the JMAK equation given below using the *Origin*© Software. The variation of fraction transformed X_V with annealing time (t) at a given temperature is given as

$$X_V = 1 - \exp\left[-(kt)^n\right] \tag{4.3}$$

Here, n and k are the JMAK exponent and temperature dependent parameter, respectively.

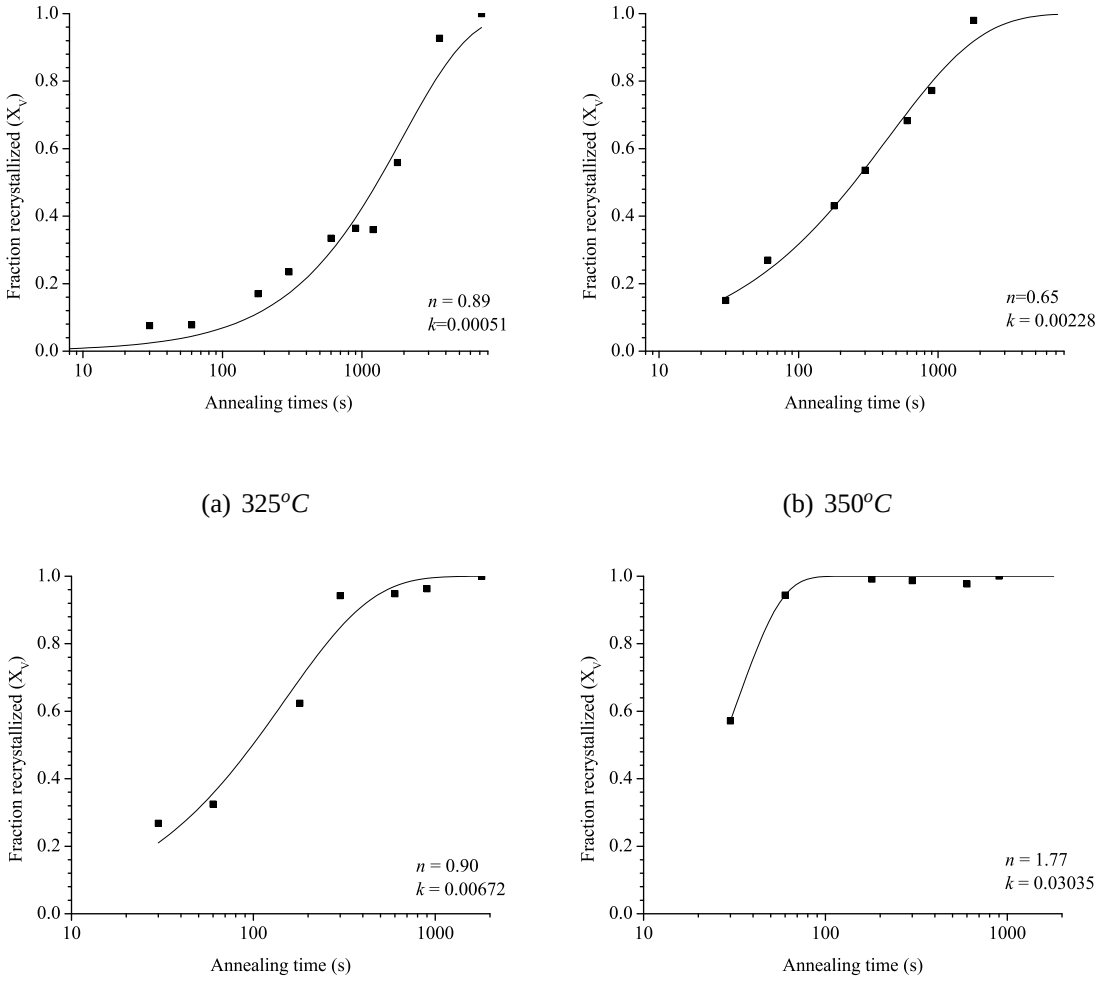

(a) 325^oC (b) 350^oC

(c) 375^oC (d) 400^oC

Figure 4.5: Variation of fraction recrystallized obtained from microhardness values with time for isothermal annealing at (a) 325^oC, (b) 350^oC, (c) 375^oC and (d) 400^oC.

The values of JMAK parameters obtained from recrystallization kinetics analysis from the microhardness data for the four different annealing temperatures are presented in Table 4.1.

Annealing Temperature (^oC)	n	$k(s^{-1})$
325	0.89	0.00051
350	0.65	0.00228
375	0.90	0.00672
400	1.77	0.03035

Table 4.1: JMAK parameters for isothermal annealing of AA1050

The JMAK exponents of annealing temperatures 325^oC, 350^oC and 375^oC are near one. These exponent values, as derived by Cahn [42], represent site saturated grain boundary nucleation. The value of 1.77 at 400^oC, is near 2, is somewhat higher than the others and represents grain edge nucleation. The similarity in n-values is indicative of insensitivity of growth behavior to annealing temperatures. The n values obtained in the present analysis are small compared to the ideal JMAK value of three for three-dimensional growth of recrystallized grains. The observed values are near one and indicate one-dimensional growth of recrystallized grains [6, 42].

The parameter k in JMAK equation is a temperature dependent parameter and its variation with annealing temperature is given with an Arrhenius-type relation

$$k = k_o \exp\left(\frac{-Q}{RT}\right) \tag{4.4}$$

Here, k_o is the pre-exponential factor ,

Q is the activation energy of recrystallization (kJ/mol),

R is the universal gas constant (8.314 J/mol-K), and

T is the annealing temperature (K).

The above expression can be rewritten as a linear expression with logarithmic terms as

$$\ln k = \ln k_o - \frac{Q}{RT} \tag{4.5}$$

Therefore, the slope of a linear fit to a plot between $\ln k$ and 1/T can be used to obtain the activation energy of recrystallization. The activation energy for recrystallization of AA1050 in present analysis was found to be Q = 178 kJ/mol, which similar to an earlier analysis of Vandermeer *et al.* (Q=172kJ/mol) on an AA1050 alloy [29].

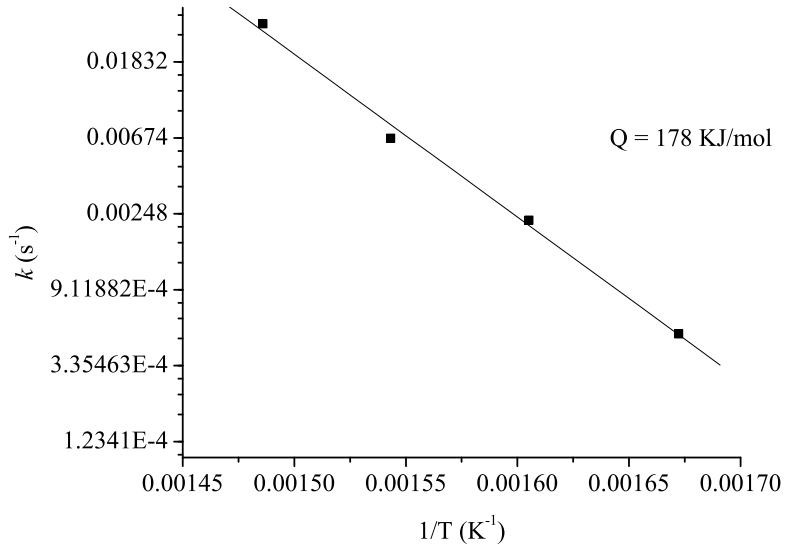

Figure 4.6: Plot between k and 1/T for AA1050 samples isothermally annealed to complete recrystallization. The slope of line is used to obtain the activation energy of recrystallization.

4.1.3 Microhardness Variation with Annealing Temperature for AA5005

The effect of addition of Mg in commercial purity aluminum alloys was determined from the kinetics of recrystallization and texture evolution analysis of AA5005. This analysis was carried out in the same way as for the AA1050. The as-received hot rolled sheet was processed to obtain small samples with dimensions $15mm \times 10mm \times 3mm$. The temperatures for isothermal annealing were determined by annealing the samples at various temperatures in the range $200^oC - 450^oC$. Microhardness indentations were obtained on each sample. The variation of microhardness values with annealing temperatures is shown in Fig. 4.7. The microhardness values for AA5005 are higher than those observed for AA1050. The presence of Mg in solid

solution increases the resistance for plastic flow and therefore, yields higher microhardness values. Almost no change in microhardness and fraction recrystallized is observed with annealing up to 325^oC unlike AA1050, where no change in microhardness is observed till 300^oC. However, recrystallization is complete at 400^oC, thus the kinetics of recrystallization are faster for AA5005 as compared to AA1050. The presence of Mg increased the stored energy of deformation by inhibiting dislocation motion and preventing the formation of recovered dislocation structures. The corresponding variation of fraction recrystallized with annealing temperature is shown in Fig. 4.8. Samples were isothermally annealed at 350^oC, 375^oC and 400^oC for recrystallization kinetics analysis.

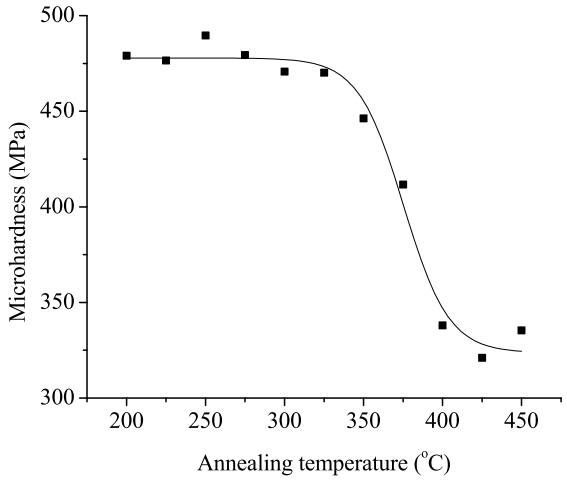

Figure 4.7: Microhardness values of AA5005 samples annealed at different temperature for 1 minute.

Microhardness values were obtained for samples annealed isothermally at 350^oC for recrystallization kinetics analysis. The JMAK parameters were obtained from non-linear least square curve fitting of fraction recrystallized to the JMAK equation, shown in Fig. 4.9. The JMAK exponent (n) obtained from microhardness values is 1.14. This value is similar to that obtained for AA1050 indicating site saturated nucleation on grain boundaries [42].

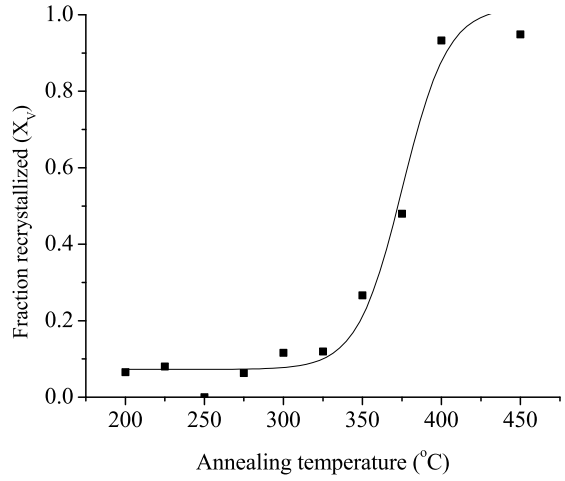

Figure 4.8: Fraction recrystallized variation with annealing temperature obtained from microhardness values for AA5005.

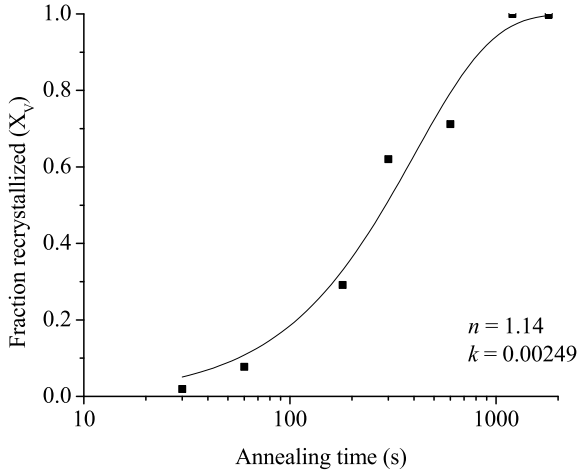

Figure 4.9: Recrystallization kinetics for AA5005 for isothermal annealing at 350^oC from JMAK model.

4.2 Recrystallization kinetics from OIM

The advent of Orientation Imaging Microscopy (OIM) has led to important insights into the characteristics of deformed and recrystallized microstructures. The advantage of obtaining microstructural information along with the orientation information provides an important ability to correlate microstructure with texture and to investigate their effect on each other due to

the thermomechanical treatment. The analysis of recrystallization kinetics from OIM is based on the fact that deformed and recrystallized regions have different characteristics in a scan and these differences can be exploited to partition maps into the deformed and recrystallized regions. The high dislocation content in deformed grains leads to high local misorientation and consequently lower Confidence Indexes (CI) and Image Quality (IQ). The recrystallized grains are however, characterized by low local misorientation and high values of CI and IQ. Different approaches have been developed to analyze the kinetics of recrystallization from OIM. These are mainly based on the intra-granular orientation spread, and the IQ & CI values of the scans. Recrystallization kinetics for AA1050 were first analyzed by the IQ & CI approach and then subsequently with the misorientation approach (GOS and GAM). The details of obtaining fraction recrystallized from IQ & CI values are given in Appendix 1.

The intragranular misorientation variation within deformed and recrystallized grains provides an ideal parameter for distinguishing between deformed and recrystallized grains. The deformed grains are characterized by high long-range and short-range misorientation variations as compared to recrystallized grains, which have low long-range and short-range misorientation variations. Thus both long-range and short-range misorientation variations can be used for determining fraction recrystallized in deformed and annealed samples. The long-range variations are typically represented by Grain Orientation Spread (GOS) whereas for the short-range orientation variations, Grain Average Misorientation (GAM) is used. GOS values are calculated as the average misorientation between all pixel pairs within a grain. GAM values on the other had are determined by averaging the misorientation between the neighboring pixel pairs only. Mathematically, GOS and GAM can be represented as

$$GOS = \frac{1}{N}\sum_{i,j=1}^{N}(g_i g_j^{-1}) \tag{4.6}$$

Where i, j are any two pixel pairs within a grain,

g_i, g_j are the orientations of any two pixel pairs in a grain,

N is the number of pixels in a grain.

$$GAM = \frac{1}{N}\sum_{i=1}^{N}[\sum_{i,j=1}^{nn}(g_i g_j^{-1})] \tag{4.7}$$

where i, j are neighboring pixel pairs within a grain,

nn is the number of nearest neighbor of the i^{th} pixel,

g_i, g_j are the orientations of nearest neighbor pixels in the grain, and

N is the number of pixels in a grain.

Crystal symmetry is implicitly applied to all orientations to find the minimum magnitude of misorientation. An OIM map for a typical partially recrystallized sample is shown in Figure 4.10.

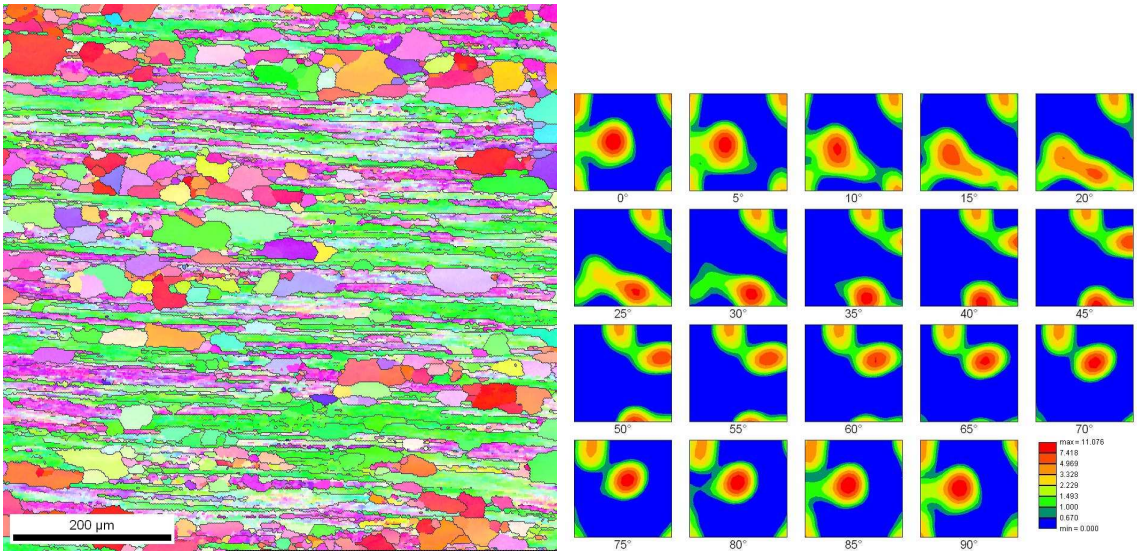

(a) An Inverse Pole Figure (IPF) map for a partially recrystallized sample.

(b) Corresponding Orientation Distribution Function (ODF) indicating contributions from deformed and recrystallized grains.

Figure 4.10: Microstructure and texture of a partially recrystallized sample.

The orientation spread (GOS & GAM) of a grain is a direct indication of the amount of deformation and dislocation content within the grain. A high value of orientation spread indicates a high geometrically necessary dislocation (GND) content and more deformation in the

sample whereas recrystallized samples have lower dislocation densities and are characterized by corresponding lower values of orientation spread as measured by GOS & GAM. Therefore, a suitable orientation spread value can be used to distinguish between deformed and recrystallized grains in a scan. This value will be same for all the scans of a material and will not be impacted by scan settings, an advantage over the methods based on IQ and CI. The partitioned grains can be analyzed for microstructural and textural evolution independently. Fig. 4.11 shows variations in GOS and GAM in a typical partially recrystallized sample. A recrystallized grain is characterized by low GOS and GAM values, indicated by blue color of the grain whereas deformed grains have high GOS and GAM values, shown by yellow and red grains. Histograms of variations in GAM and GOS values with area fractions are shown in Figure 4.12. A bimodal distribution in GAM and GOS values is observed for a partially recrystallized sample. The sharp peaks at the lower values of GAM and GOS represent the contribution from recrystallized grains while the broad peaks at higher values indicate deformed grains.

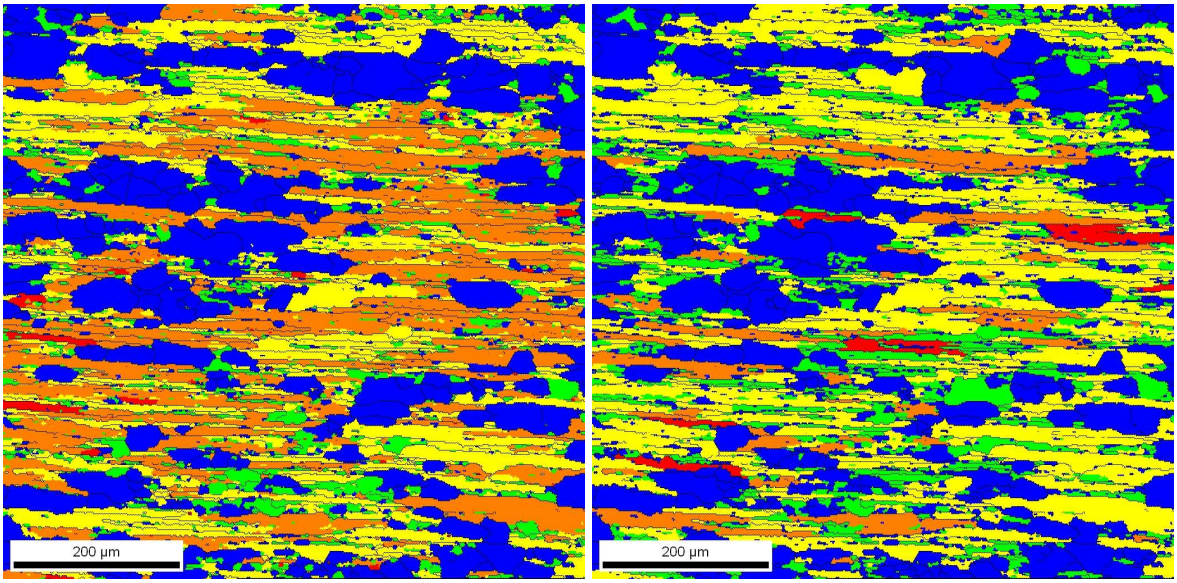

(a) GAM (b) GOS

Figure 4.11: Orientation spread variations in a partially recrystallized sample of AA1050.

The variation in GAM and GOS values with area fraction, as shown in Fig. 4.12, indicates a clear difference between deformed and recrystallized grains. A threshold GAM and

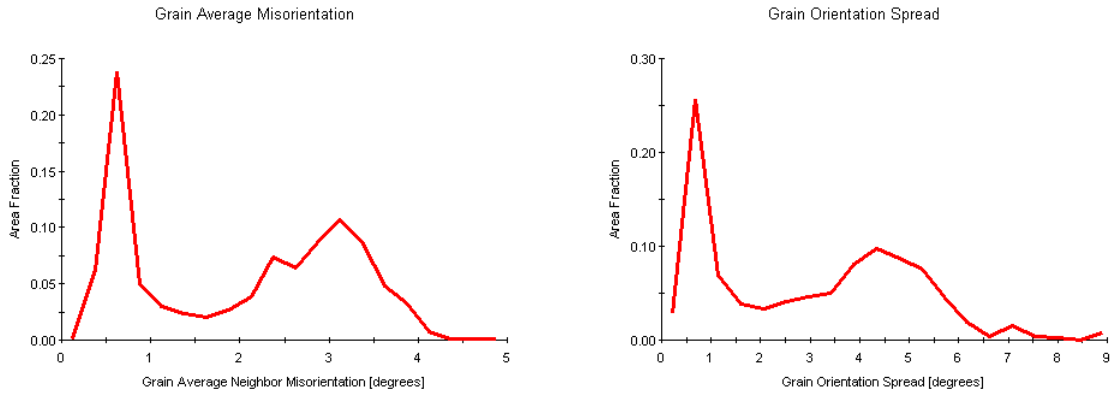

(a) GAM Variation

(b) GOS variation

Figure 4.12: GAM and GOS variation with area fraction

GOS, for identifying the state of recrystallization in each grain, can be used to estimate fraction recrystallized and separate (partition) the two distinct regions of a scan. This also helps in analyzing the texture evolution in deformed and recrystallized grains independently. The estimation of a threshold value suitable for partitioning is difficult or arbitrary from the GAM and GOS variations shown in Fig. 4.12 because some overlap between the recrystallization and deformation peaks exists and the exact location of the threshold GAM and GOS is not self-evident. An alternative approach based on the variation in GOS and GAM with cumulative fraction of points was used. For this analysis, several completely recrystallized samples were scanned. The cumulative variation in fraction of points with GAM and GOS is plotted in Fig. 4.13. Fig. 4.13(b) and (d) give a magnified view of Fig. 4.13 (a) and (c) in the range 0.8-1.0. A threshold GAM was determined from these plots by assuming that any GAM value which includes 95% of points in a completely recrystallized scan is sufficient for characterizing all the recrystallized grains in the material. Since the above analysis includes several completely recrystallized scans (8-10), the threshold GAM determined in this way includes all the effects due to grain orientations and locations. Similar plots for AA5005 are presented in Fig. 4.14.

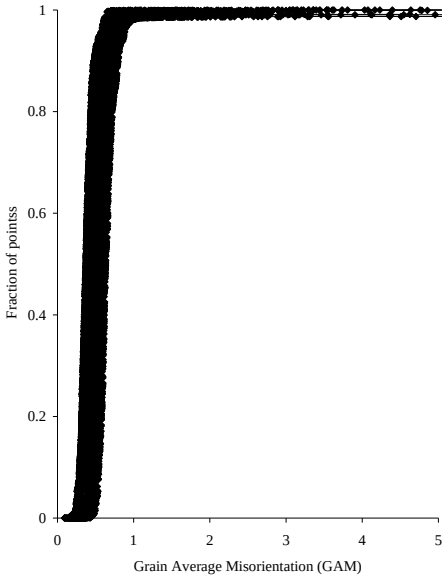

(a) Cumulative GAM Variation

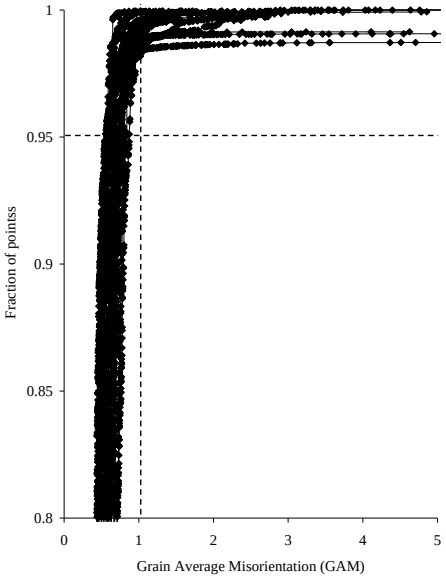

(b) Cumulative GAM variation for points lying between 0.8-1.0

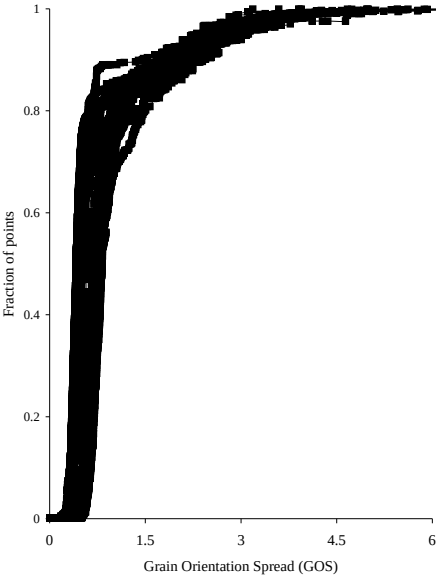

(c) Cumulative GOS Variation

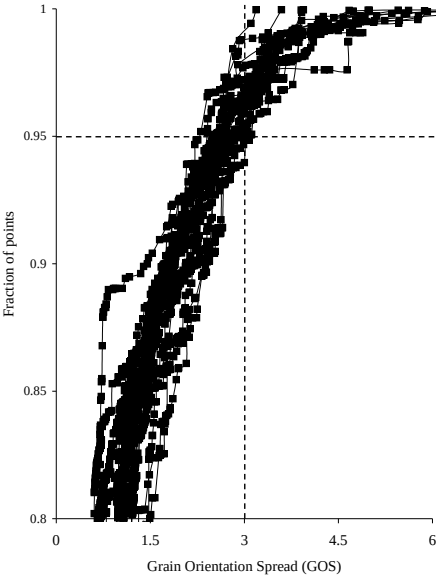

(d) Cumulative GOS variation for points lying between 0.8-1.0

Figure 4.13: Cumulative GAM and GOS variation for AA1050.

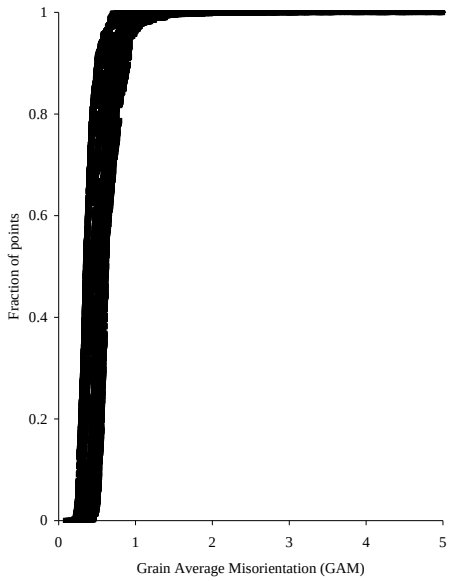

(a) Cumulative GAM Variation

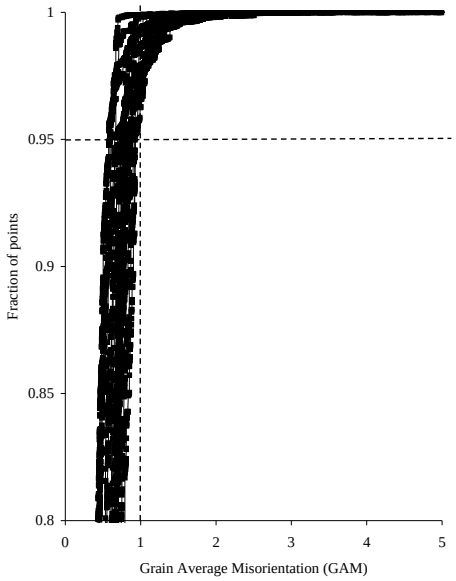

(b) Cumulative GAM variation for points lying between 0.8-1.0

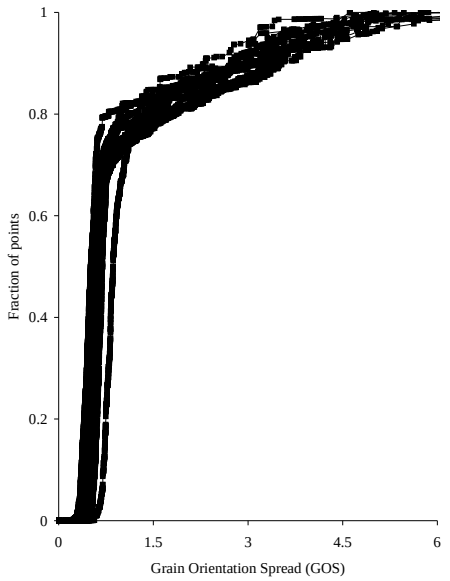

(c) Cumulative GOS Variation

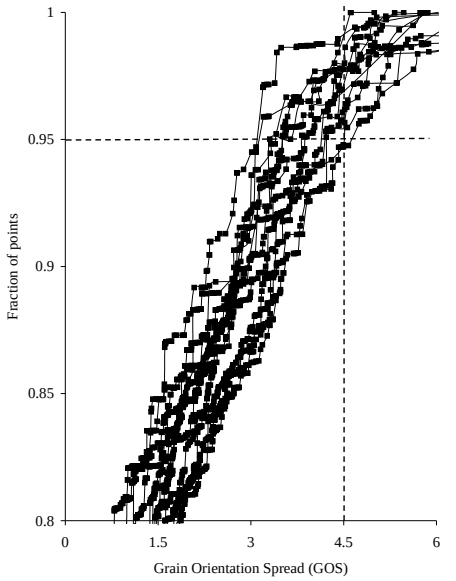

(d) Cumulative GOS variation for points lying between 0.8-1.0

Figure 4.14: Cumulative GAM and GOS variation for AA5005.

Based on the above analysis, threshold values of GAM of 1^o and GOS of 3^o were chosen for distinguishing deformed and recrystallized grains in AA1050. A similar analysis for AA5005 gave corresponding threshold values of GAM and GOS as 1^o and 4.5^o, respectively. These observed threshold values were used to partition a complete scan into deformed and recrystallized regions. The microstructure shown in Fig. 4.10 was partitioned by using the GAM and GOS approaches into deformed and recrystallized grains. The partitioned microstructure and ODF's are shown in Fig. 4.15 and 4.16. The microstructure and texture obtained from the two approaches are very similar. The deformed regions are found to have β-fiber rolling orientations as the main texture components, typically observed in rolled fcc alloys. The recrystallized regions show cube as the dominant texture component. Although some minor differences are observed in the microstructures obtained from the two methods, the similarity in textures for deformed and recrystallized justifies the use of the above mentioned thresholds.

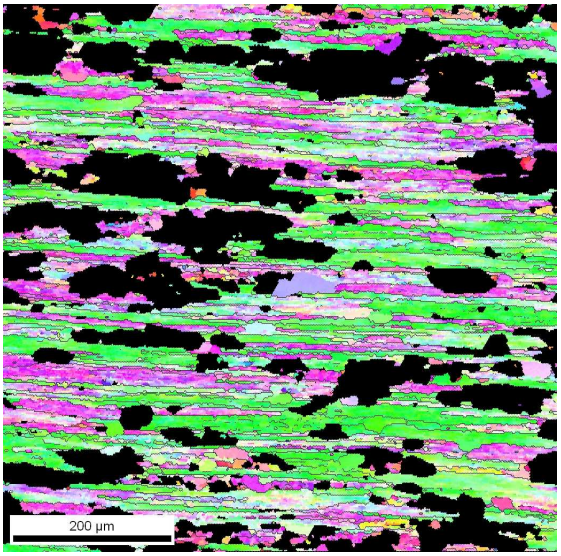

(a) Deformed regions partitioned with a threshold GAM of 1^o.

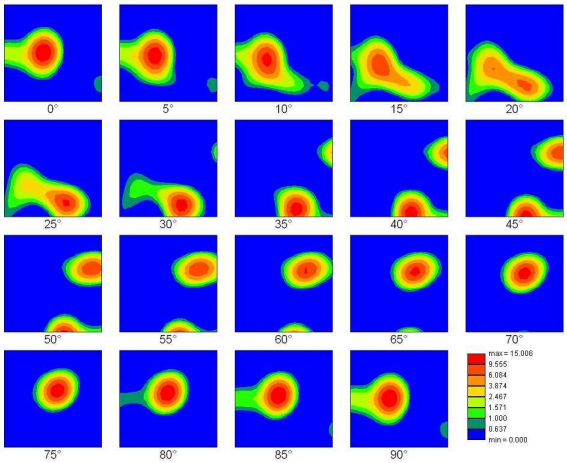

(b) ODF of partitioned deformed regions based on GAM variations indicating rolling texture.

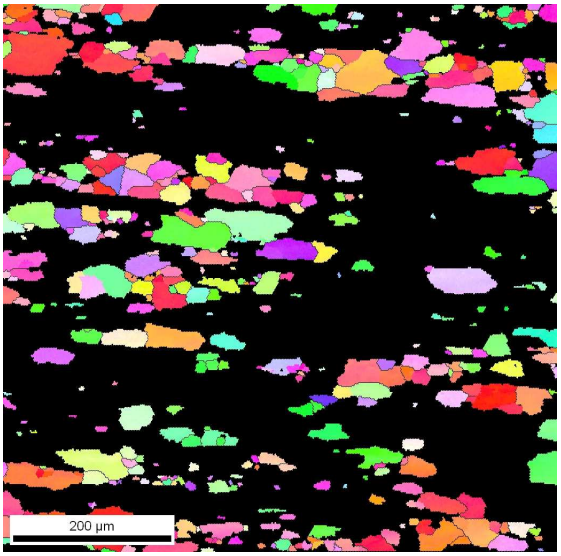

(c) Recrystallized regions partitioned with a threshold GAM of 1^o.

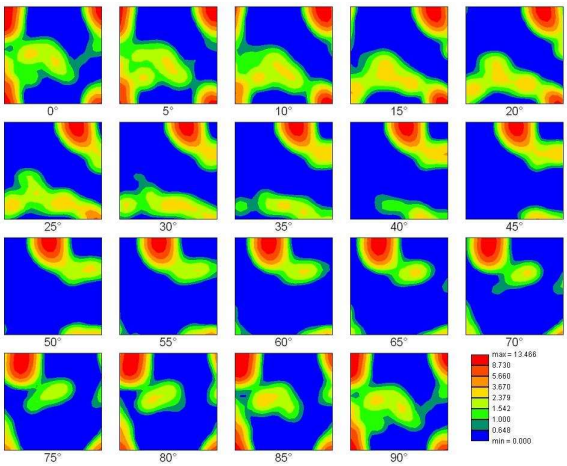

(d) ODF of partitioned recrystallized regions based on GAM variations indicating cube as the dominant texture component for recrystallized grains.

Figure 4.15: Partitioning of a complete scan using a threshold GAM of 1^o.

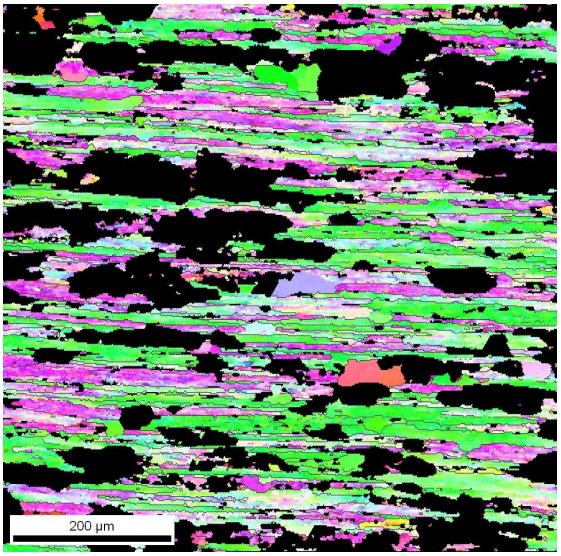

(a) Deformed regions partitioned with a threshold GOS of 3^o.

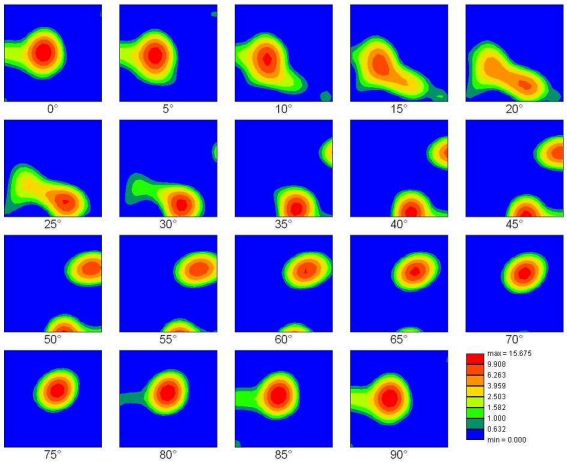

(b) ODF of partitioned deformed regions based on GOS variations indicating rolling texture.

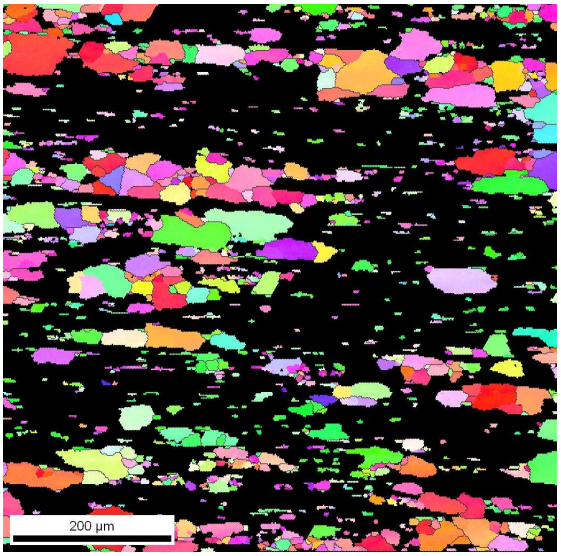

(c) Recrystallized regions partitioned with a threshold GOS of 3^o.

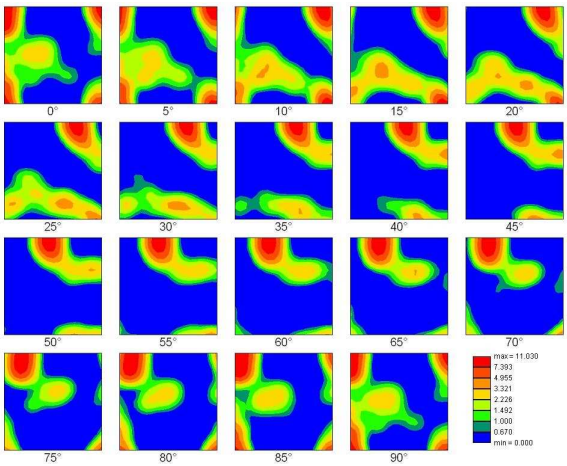

(d) ODF of partitioned recrystallized regions based on GOS variations indicating cube as the dominant texture component for recrystallized grains.

Figure 4.16: Partitioning a complete scan using a threshold GOS of 3^o.

Although GAM and GOS values were the main parameters used to identify deformed and recrystallized grains, certain other criteria were also used for identification of recrystallized grains. An important parameter in the study of deformed and recrystallized samples with GOS

criteria is the step size used in the scan. While a larger step size can be used for fully recrystallized samples, a lower value should be used for deformed and partially recrystallized samples to include more points in the recrystallized nuclei [43]. A step size between $1 - 2\mu m$ was used for partially recrystallized and fully recrystallized samples and between $0.5 - 1\mu m$ was used for deformed samples. The parameters that control the partitioning of deformed and recrystallized regions and eventually for selection of a nucleus among all the subgrains present are:-

1. A minimum grain size of $5\mu m$.

2. The presence of a high angle boundary (15^o boundary misorientation) surrounding a nucleus.

4.2.1 GOS and GAM variation with grain size

Grain Orientation Spread (GOS) and Grain Average Misorientation (GAM) values were compared for deformed and recrystallized grains in the previous section. These parameters were also compared with grain sizes of deformed and recrystallized grains. A study of these parameters aids in understanding the internal dislocation arrangements of deformed and recrystallized grains. Fig. 4.17 and 4.18, show GOS and GAM variations for deformed and recrystallized grains respectively. For deformed regions, only grains with a GOS value greater than 3^o were considered for grain size analysis. For the recrystallized sample in Fig. 4.18, all the grains are considered. An important feature clearly apparent from Fig. 4.17 (a) is that two different types of deformed grains can be identified. There are deformed grains lying near the 1:1 line of GAM-GOS variation. There are also grains which have a high GOS but low GAM. The latter behavior indicates deformed but recovered grains which have large long-range variations but small short-range variations. The recovered & deformed grains were previously confirmed by microhardness variations and are expected in a hot deformed sample.

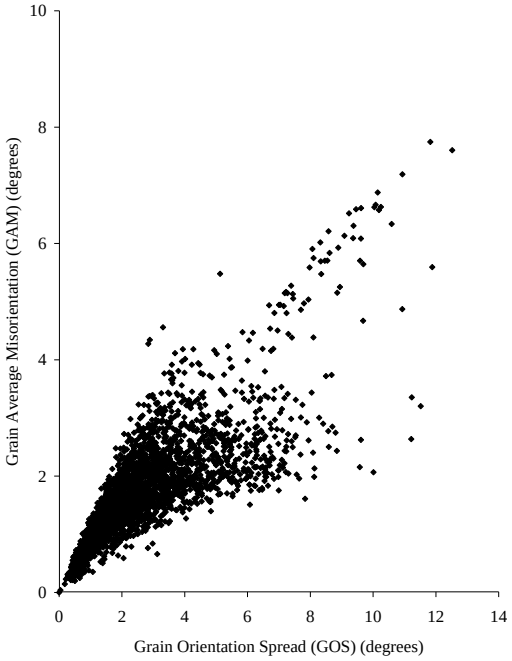

(a) Comparison of GAM and GOS values for a deformed sample.

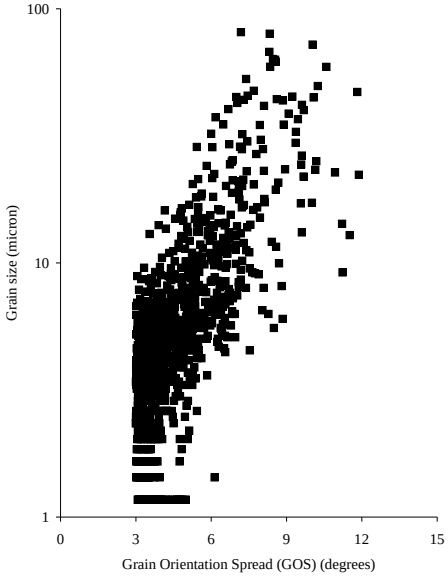

(b) Variation of grain size with GOS

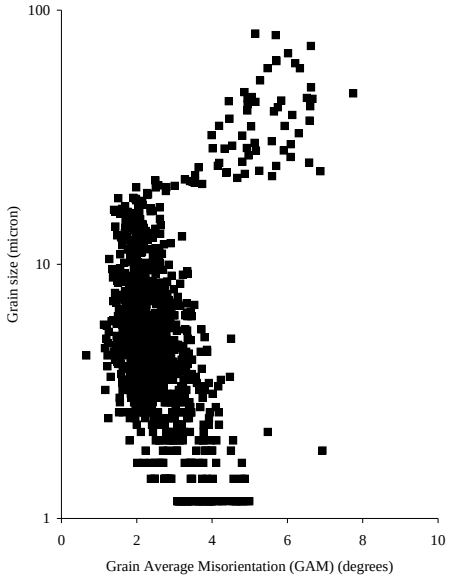

(c) Variation of grain size with GAM

Figure 4.17: GAM and GOS variations in a deformed sample.

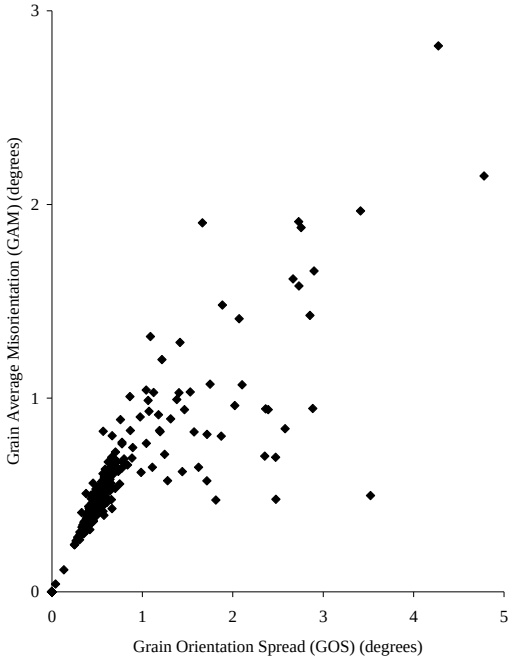

(a) Comparison of GAM and GOS values for a recrystallized sample.

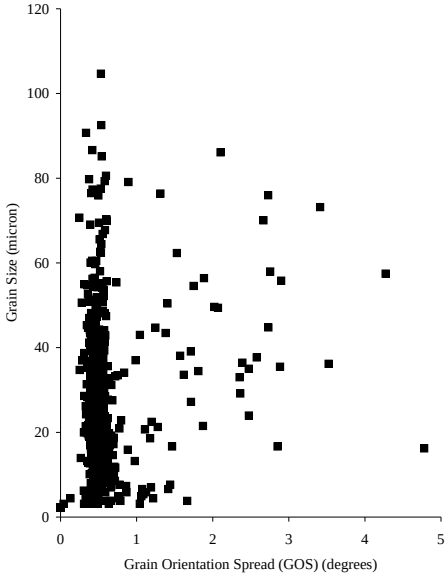

(b) Variation of grain size with GOS

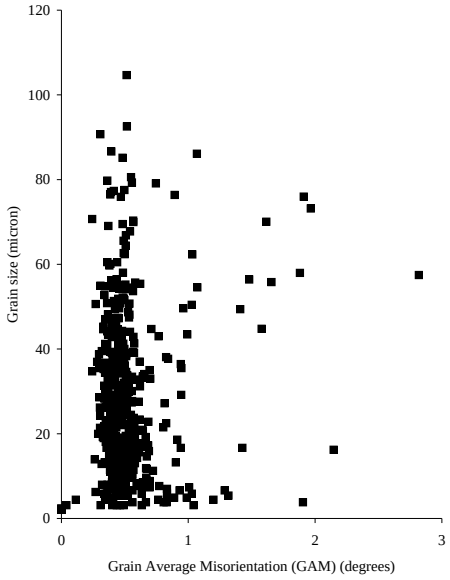

(c) Variation of grain size with GAM

Figure 4.18: GAM and GOS variations in a recrystallized sample.

An analysis of grain size with GOS and GAM values is shown in Fig 4.17 (b) and (c). GOS values are found to follow a linear relationship with grain size. Large deformed grains have high GOS values. GAM, on the other hand, follows a different trend. Here deformed grains form two distinct classes, recovered and unrecovered, as indicated in Fig. 4.17 (c). Recovered deformed grains, which are more numerous, are located near low GAM values and unrecovered deformed grains although few in number are at high GAM values which are also large in size.

The variation between GAM and GOS for recrystallized grains is presented in Fig 4.18 (a). The majority of the recrystallized grains are found near the 1:1 line, indicating similar long-range and short-range orientation variations and a uniform internal dislocation arrangement of recrystallized grains. A few grains with high GOS and low GAM were also observed. This behavior is indicative of the presence of defects due to sample preparation. Any recrystallized grain with a scratch or a pit due to sample preparation will have high GOS value as the bad points are included in calculation for each pixel. On the other hand, in GAM calculations the effect due to these bad points is minimized as they are included in only a small number of neighbor pixels within the grain. An inspection of the GOS and GAM variation with grain size reveals no discernible trend. The majority of grains (small and big) are observed to have low GOS and low GAM values (less than 1^o).

4.2.2 Recovery analysis

The as-received hot rolled samples were obtained in a recovered state and no recovery was indicated by microhardness variation as well as GOS-GAM analysis. The same is not true however, for concurrent recovery occurring during recrystallization annealing of samples. A direct way of observing concurrent recovery is through the variation in hardness of deformed grains. In the estimation of fraction recrystallized from microhardness values, the maximum and minimum hardness values were assumed to be constant. This assumption, although true for recrystallized grains (minimum hardness), is not entirely true for deformed grains (maximum hardness). Annealing of deformed samples will not only cause the recrystallized grains to appear in the the sample but will also cause the simultaneous recovery of deformed grains.

These recovery effects can be estimated from the change in microhardness values of deformed regions. For equation 4.1

$$H_d = \frac{H_i - H_r X_V}{(1 - X_V)} \tag{4.8}$$

Where, H_i is the hardness at any particular time and temperature (measured from microhardness measurements),

H_d is the hardness of deformed regions,

H_r is the hardness of recrystallized regions (constant, estimated from microhardness measurements), and

X_V is the fraction recrystallized (obtained from GOS analysis).

Thus estimating X_V from OIM permits calculation of the variation in H_d from the available values of H_r (constant) and H_i. This variation in deformed hardness (H_d), obtained from combining the two methods, is given in Fig. 4.19 (a). An important aspect revealed from this plot is the variation in deformed grain hardness. A constant value was assumed for H_d in recrystallization kinetics analysis from microhardness. However, it is important to note here that this variation is only analytical and such a large decrease in microhardness values is not expected from recovery alone. The indentation size in microhardness is of the order of $150\mu m$ for deformed samples and might represent an average value over a few layers of deformed grains. It nonetheless, does show analytically that there might be some variations in deformed grains during the annealing. This behavior can be verified by using a nano indentation system providing controlled indentation sizes and loads, allowing measurements in deformed grains of particular orientations.

A similar estimation of concurrent recovery is also obtained from the variation in GOS values of deformed grains with annealing time and temperature. Fig. 4.19 (b) shows the variation in average GOS value of deformed grains for different annealing temperature with fraction recrystallized. The overall behavior of this curve is very similar to the variation obtained from microhardness values of deformed grains in Fig 4.19 (a).

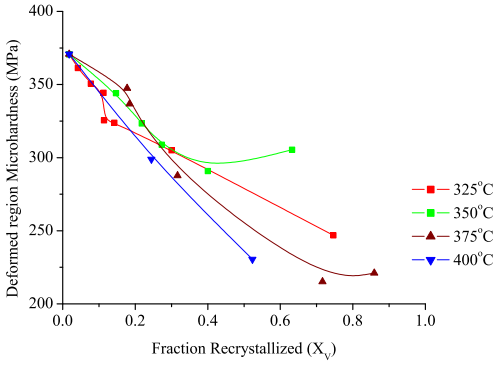

(a) Deformed grains microhardness variation with fraction recrystallized.

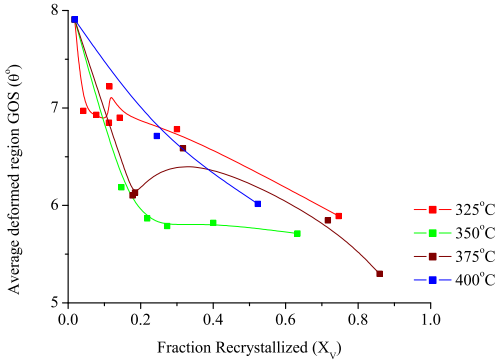

(b) Variation in average GOS value of deformed grains with fraction recrystallized.

Figure 4.19: Estimating concurrent recovery from microhardness and GOS analysis.

4.3 Microstructural Path Modeling (MPM)

The threshold value of 3^o in GOS was used to partition maps into deformed and recrystallized grains in AA1050. The partitioned regions were analyzed for recrystallization kinetics and texture evolution. The kinetics of recrystallization were obtained from Microstructural Path Modeling (MPM). This approach is considered better than the usual JMAK approach as it incorporates more microstructural features than the usual JMAK approach, thus giving a better analysis of microstructural evolution. The parameters used in the MPM approach are fraction recrystallized (X_V), interfacial area per unit volume between deformed and recrystallized grains (S_V) and annealing time (t). The equations used for the MPM approach are

$$X_{VEX} = \ln \frac{1}{1 - X_V} = (kt)^n \tag{4.9}$$

$$\ln X_{VEX} = \ln[\ln \frac{1}{1 - X_V}] = n \ln k + n \ln t \tag{4.10}$$

$$S_{VEX} = \frac{S_V}{(1 - X_V)} = Kt^m \tag{4.11}$$

$$\ln S_{VEX} = \ln \frac{S_V}{(1 - X_V)} = \ln K + m \ln t \tag{4.12}$$

$$S_{VEX} = C(X_{VEX})^q \tag{4.13}$$

$$\ln S_{VEX} = \ln C + q \ln X_{VEX} \tag{4.14}$$

The above equations are solved for exponents *n*, *m* and *q* to obtain information about the nucleation and growth behavior of recrystallized grains. Plots in Fig. 4.20 show the variation of the various parameters. For the case of random nucleation of recrystallized grains growing spherically in 3-dimensions and site saturated nucleation ($N_V = constant$), i.e. JMAK type conditions, the relationship between S_{Vex} and X_{Vex} can be derived as

$$S_{Vex} = 4\pi N_V {R_{Vex}}^2 \tag{4.15}$$

$$X_{Vex} = \frac{4}{3}\pi N_V {R_{Vex}}^3 \tag{4.16}$$

By eliminating R_{Vex} in above equations, a relationship between S_{Vex} and X_{Vex} can be obtained as

$$S_{Vex} = 3\left(\frac{4\pi N_V}{3}\right)^{1/3} (X_{Vex})^{2/3} \tag{4.17}$$

Thus for a JMAK type condition $q = 2/3$. Substituting the real space expressions for S_{Vex} and X_{Vex} in the above expression

$$X_{Vex} = -\ln(1 - X_V) \tag{4.18}$$

$$S_{Vex} = \frac{S_V}{(1 - X_V)} \tag{4.19}$$

$$S_V = 3\left(\frac{4\pi N_V}{3}\right)^{1/3} (1 - X_V)(-\ln(1 - X_V))^{2/3} \tag{4.20}$$

In a general form, equation 4.20 can be written as:

$$S_V = C(1 - X_V)(-\ln(1 - X_V))^q \tag{4.21}$$

Also by eliminating t in equation 4.9 and 4.11, a simplified form for q can be obtained as

$$S_{Vex} = \frac{K}{k^{m/n}}(X_{Vex})^{m/n} \tag{4.22}$$

$$q = \frac{m}{n} \tag{4.23}$$

The nucleation and growth parameters can be obtained by assuming a power-law relationship between nucleation rate ($\dot{N}$) and growth rate *(G)* with time *(t)* is given by

$$\dot{N} = N_1 t^{\delta-1} \tag{4.24}$$

$$G = rPt^{r-1} \tag{4.25}$$

where N_1, δ, r and P are constants.

The volume and interfacial area for a nucleus nucleated at time, τ, and growing for time, t-τ, are given by

$$V(t-\tau) = K_v a(t-\tau)^3 \tag{4.26}$$

$$S(t-\tau) = K_S a(t-\tau)^2 \tag{4.27}$$

where K_V and K_S are shape factors constants and $a(t-\tau)$ is the semi major axis of the spheroid. The relationship between $a(t-\tau)$ and growth rate *(G)* is given by

$$a(t-\tau) = \int_{\tau}^{t} G dt \tag{4.28}$$

The extended space volume fraction, X_{Vex}, and interfacial area per unit volume, S_{Vex}, can be written in terms of the above parameters as

$$X_{Vex} = \int_0^t \dot{N}(\tau)V(t-\tau)d\tau \tag{4.29}$$

$$S_{Vex} = \int_0^t \dot{N}(\tau)S(t-\tau)d\tau \tag{4.30}$$

Substituting the expressions for $\dot{N}$, $V(t-\tau)$, $S(t-\tau)$ and $a(t-\tau)$ in the integrals for X_{Vex} and S_{Vex} and by applying Laplace transforms gives

$$X_{Vex} = K_V N_1 P^3 t^{(3r+\delta)} \frac{\Gamma(3r+1)\Gamma(\delta)}{\Gamma(3r+\delta+1)} \tag{4.31}$$

$$S_{Vex} = K_S N_1 P^2 t^{(2r+\delta)} \frac{\Gamma(2r+1)\Gamma(\delta)}{\Gamma(2r+\delta+1)} \tag{4.32}$$

Comparing the exponents for t in the above equations and equation 4.9 and 4.11 gives

$$n = 3r + \delta \tag{4.33}$$

$$m = 2r + \delta \tag{4.34}$$

Eliminating r in above equations gives $\delta = 3m - 2n$.

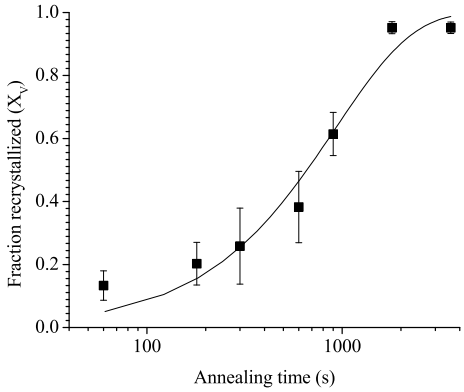

(a) Variation between annealing time and volume fraction recrystallized.

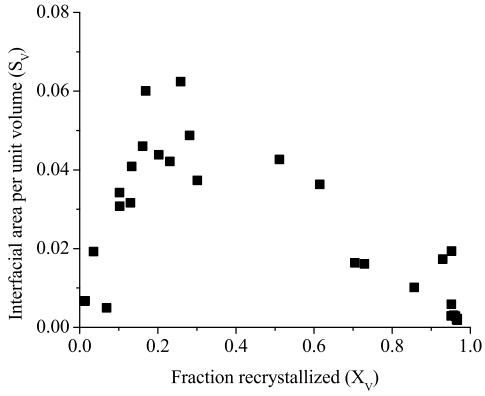

(b) Interfacial area variation with fraction recrystallized; the asymmetry of the curve indicates clustering of recrystallized grains.

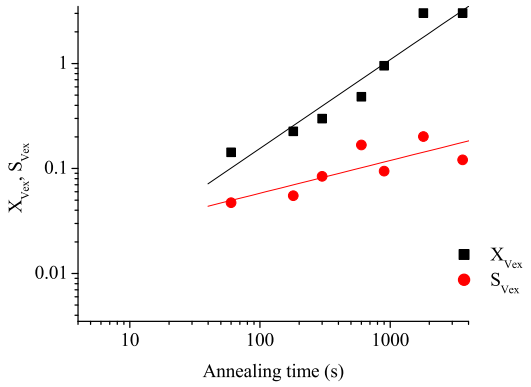

(c) Exponents n and m are obtained from the slope of the lines.

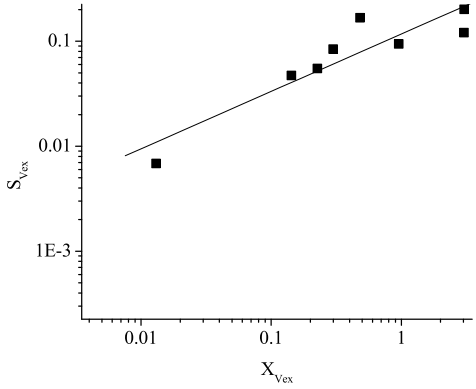

(d) Exponent q is obtained from the slope of $\ln S_{VEX}$ versus $\ln X_{VEX}$

Figure 4.20: Microstructural Path Modeling for AA1050.

A parameter describing nucleation behavior is given by δ, the value which is determined as $\delta = 3m - 2n$ [44]. A value of $\delta = 1$ corresponds to constant nucleation rate and $\delta \leq 0$ corresponds to site saturation. The values obtained from MPM analysis of AA1050 are shown in Table 4.2. The data presented in Table 4.2 clearly shows site saturation during the recrystallization of hot rolled AA1050. The exponent k, which also corresponds to JMAK exponent, is near one, which, according to the rate law derived by Cahn [42], represents grain

boundary nucleation. Another evidence for grain boundary nucleation is presented by the fact that the parameter q lies between 0 and 1/2, which, based on the extension of Cahn's rate laws to Microstructural Path Methods, represents site saturated grain boundary nucleation [45].

Temperature (^oC)	n	m	δ	q
325	1.45	0.71	-0.77	0.49
350	1.09	0.55	-0.05	0.51
375	1.08	0.33	-1.17	0.31
400	1.35	0.62	-0.88	0.47

Table 4.2: MPM exponents for AA1050

A similar analysis carried for AA5005 gave the values of exponents and constants as shown in Table 4.3. The JMAK exponent n increases from 1 to 2.67, indicating grain boundary nucleation at low temperatures to more uniform growth at the higher temperature. The nucleation process as indicated by the values of δ and q still appears to be site saturated.

Temperature ^oC	n	m	δ	q
350	1.09	0.59	-0.41	0.54
375	1.99	0.60	-2.19	0.30
400	2.67	1.73	-1.52	0.64

Table 4.3: MPM exponents for AA5005

4.4 Grain contiguity ratio

The grain contiguity ratio for recrystallized grains is also determined from the recrystallized grains identified with GOS approach. The grain contiguity ratio (C_r) is defined as the fractional interfacial area per unit volume (S_V) that is shared with the other recrystallized grains [46, 47]. Mathematically it is given by the following alternative equations

$$C_r = \frac{2S_{Vrr}}{2S_{Vrr} + S_{Vrd}} \tag{4.35}$$

$$C_r = \frac{a_{rr}}{a_{rr} + a_{rd}} \tag{4.36}$$

where

C_r is the contiguity between recrystallized grains,

S_{Vrr} is the average interfacial area per unit volume between adjacent recrystallized grains,

S_{Vrd} is the average interfacial area per unit volume between a recrystallized grain and an adjacent deformed grain,

a_{rr} is the average area of contact between a recrystallized grain and an adjacent recrystallized grain, and

a_{rd} is the average area of contact between a recrystallized grain and an adjacent deformed grain.

The above two definitions of grain contiguity ratio are equivalent and the mathematical difference can be understood from the differences in the definitions of area of contact per unit volume and interfacial area per unit volume. The area of contact between two recrystallized grains a_{rr} is composed of two surfaces of the adjacent grains thus $a_{rr} = 2S_{Vrr}$. The contiguity ratio (C_r) for a random microstructure with no preference for grains of any particular type can be obtained from the relationships between the interfacial area (S_V) and volume fraction (X_V).

$$S_{Vrd} = 2X_V(1 - X_V) \tag{4.37}$$

$$S_{Vrr} = {X_V}^2 \tag{4.38}$$

Substituting the above relations in Eq. 4.35 yields the expected value of grain contiguity ratio as $C_r = X_V$. The variation of grain contiguity ratio (C_r) with volume fraction recrystallized (X_V) is shown in Fig. 4.21 for AA1050 and Fig. 4.22 for AA5005. The straight line in the middle of the plot corresponds to the case of random nucleation. Any deviation from the line depicts clustering between grains of a particular type (deformed or recrystallized).

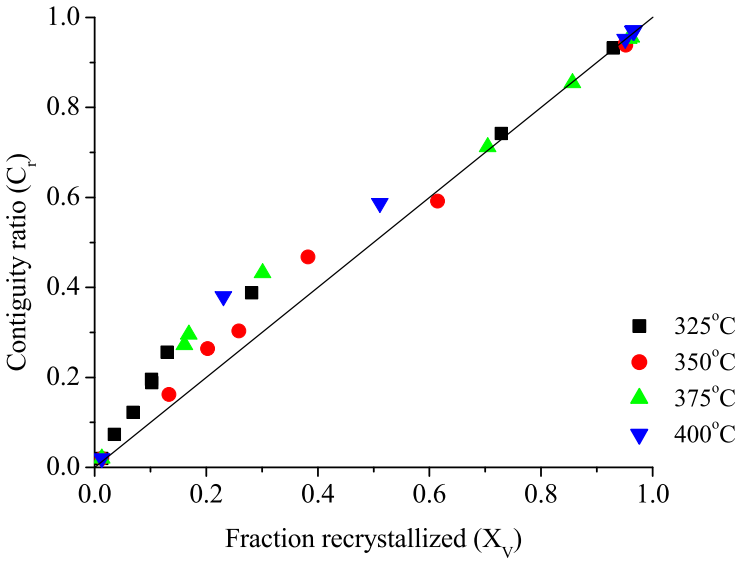

Figure 4.21: Variation of grain contiguity ratio of recrystallized grains with fraction recrystallized for different annealing temperatures for AA1050.

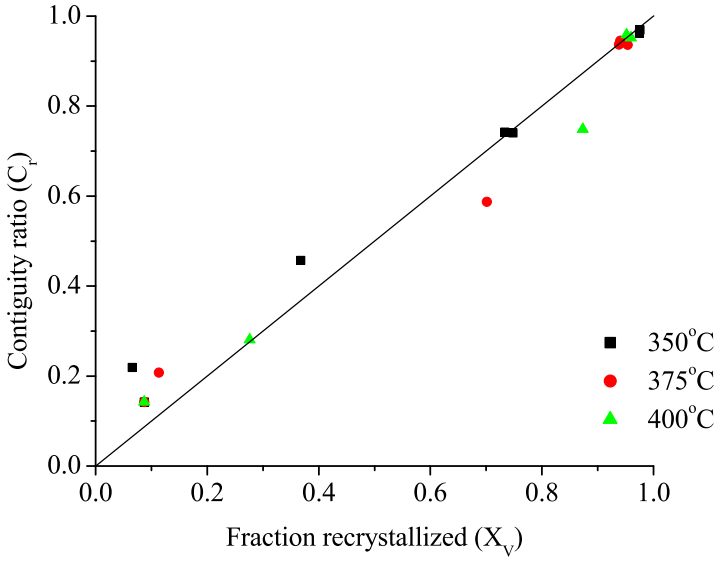

Figure 4.22: Variation of grain contiguity ratio of recrystallized grains with fraction recrystallized for different annealing temperatures for AA5005.

The grain contiguity ratio plots for AA1050 in the present analysis indicate a positive deviation (higher than random contiguity) during the early stages of annealing. This implies a tendency for recrystallized grains to cluster and nucleate in colonies. A similar behavior has been observed by others [48]. However no such behavior is observed in case of AA5005. Almost all the points lie near the 1:1 line for AA5005 indicating no preference for recrystallized grains. Also due to faster kinetics most of the points for AA5005 lie near the higher end of the 1:1 line.

4.5 Recrystallized grains growth rates

The growth rates for recrystallized grains were obtained from the Cahn-Hagel approach [49]. The velocity of a moving interface was derived by Cahn and Hagel as

$$< V >_{CH} = \frac{1}{S_V} \frac{dX_V}{dt} \tag{4.39}$$

This expression can be rewritten by using the JMAK equation for the derivative of the recrystallized fraction with respect to time. Vandermeer *et al.* [50] expressed growth rates of recrystallized grains as

$$< V >_{CH} = -\frac{k}{t} \frac{(1 - X_V)}{S_V} \ln(1 - X_V) \tag{4.40}$$

The main advantage offered by the Cahn-Hagel approach for estimation of growth rates over the JMAK approach is that, in the JMAK approach, a constant growth rate is assumed whereas a time-dependent growth rate can be obtained from the Cahn-Hagel approach. Variations in growth rates for isothermally annealed AA1050 samples are shown in Fig. 4.23 for all annealing temperatures. As shown in Fig. 4.23, decreasing growth rates were obtained for all temperatures. This decrease in growth rates is indicative of a reduction in driving force and concurrent recovery of deformed regions as discussed in Fig. 4.19.

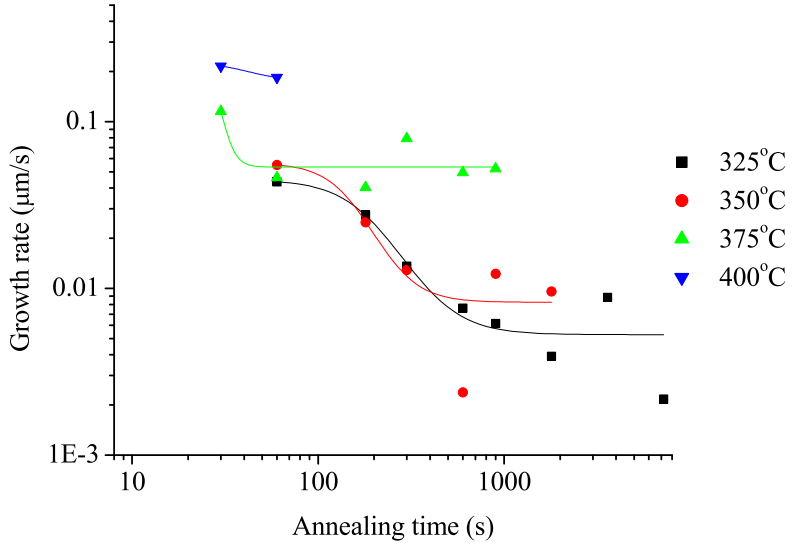

Figure 4.23: Growth rates (Cahn-Hagel) variation with annealing times for isothermally annealed AA1050 samples.

For the comparison of Cahn-Hagel growth rates at different annealing temperatures, the variation in growth rates is also plotted with respect to fraction recrystallized X_V in Fig. 4.24. As indicated, a constant growth rate is obtained at the later stages of annealing at all temperatures. This constant growth rate is temperature dependent and can be used to analyze the activation energy for boundary migration by assuming Arrhenius type behavior of growth rate with temperature for hot rolled AA1050. The activation energy results for AA1050 are shown in Fig. 4.25.

$$G = G_o \exp\left(\frac{-Q}{RT}\right) \tag{4.41}$$

The activation energy for boundary migration rate is obtained as $Q = 168$ kJ/mol and is comparable to the activation energy for recrystallization obtained from microhardness analysis of the JMAK parameter k ($Q = 178$ kJ/mol). These experimental values also compare well with a AA1050 analysis carried out by Vandermeer *et al.* $Q = 172$ kJ/mol [29]. For AA5005, similar plots were also obtained for isothermally annealed samples at $350^oC, 375^oC$ and 400^oC.

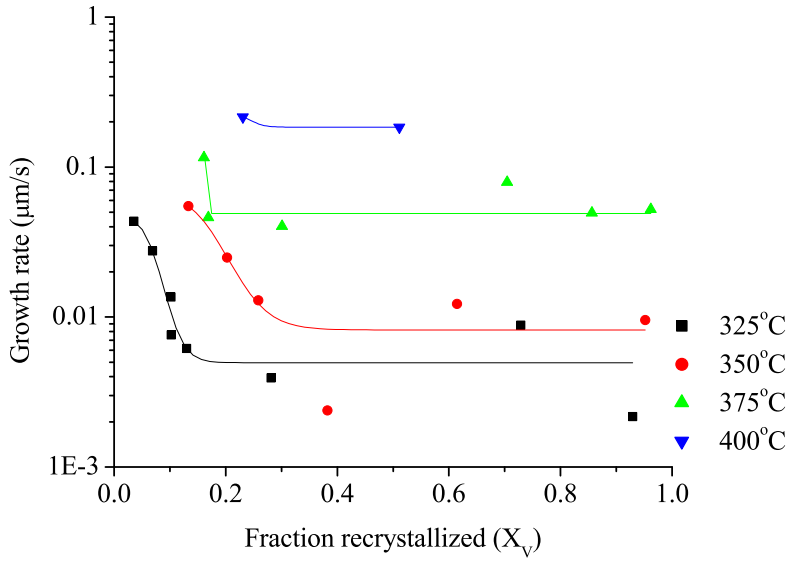

Figure 4.24: Growth rate (Cahn-Hagel) variation with fraction recrystallized X_V for AA1050.

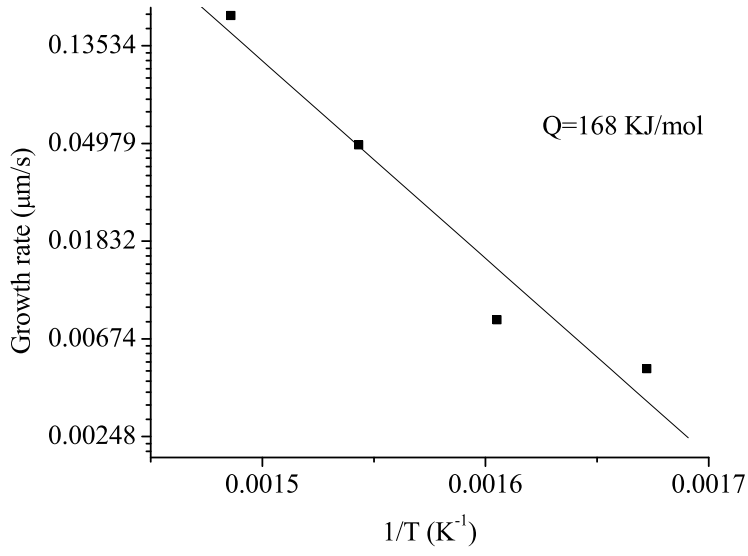

Figure 4.25: Activation energy for boundary migration in hot rolled AA1050.

Fig. 4.26 and 4.27 show the variation of growth rates with annealing times and fraction recrystallized X_V, respectively. The activation energy for boundary migration was determined in a similar manner as for AA1050. The activation energy for the migration of high angle boundaries in 5005 was determined to be 161 kJ/mol as shown in Fig. 4.28, which is slightly lower than the value for AA1050. The smaller decrease in growth rate during recrystallization indicate a smaller degree of recovery in Mg containing 5005.

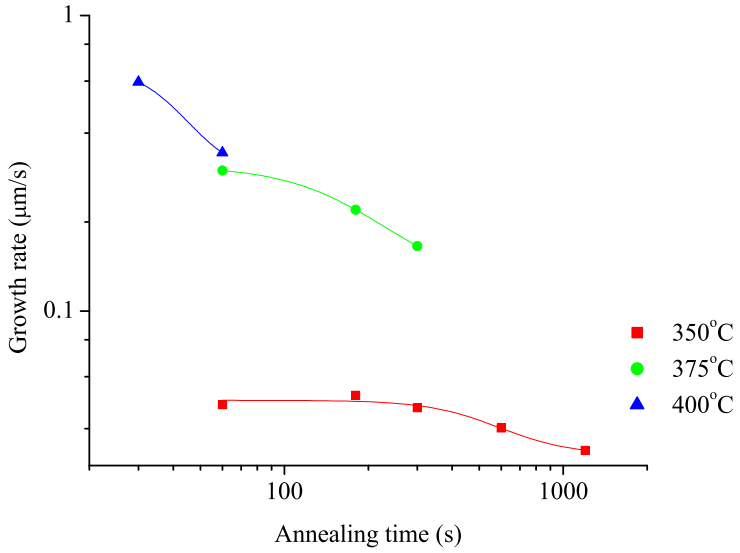

Figure 4.26: Variation of growth rates (Cahn-Hagel) with annealing times for different temperatures for isothermally annealed AA5005.

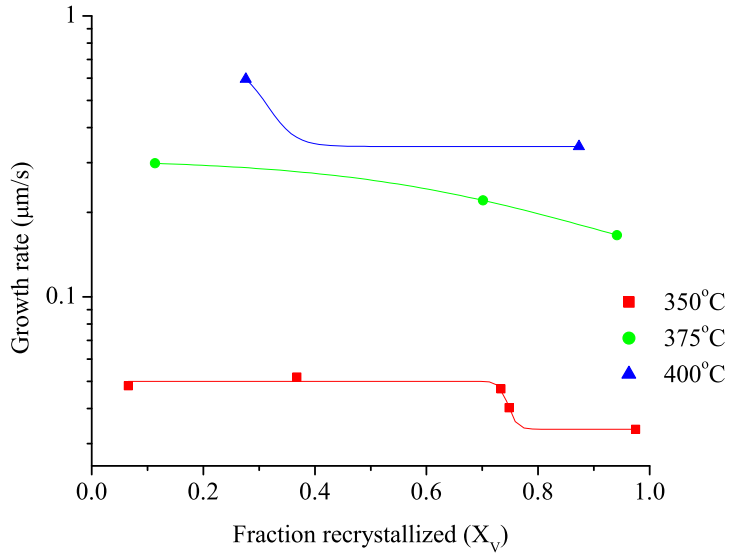

Figure 4.27: Variation of growth rates (Cahn-Hagel) with fraction recrystallized (X_V) for AA5005.

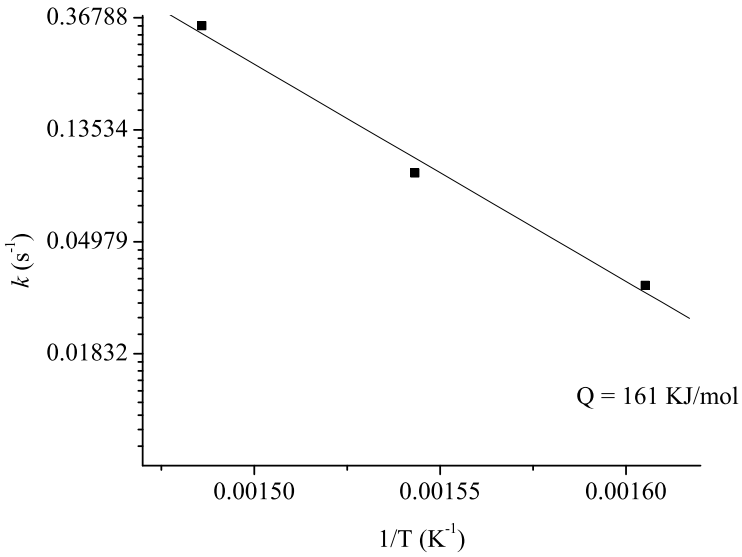

Figure 4.28: Activation energy analysis for boundary migration in hot rolled AA5005.

4.6 Recrystallized Grain Size

The partitioned regions in deformed and annealed samples were also analyzed for grain size of recrystallized grains. Average grain sizes for recrystallized grains in isothermally annealed samples were obtained from the number of pixels and the number density. Figure 4.29 and 4.30 shows the variation for different temperatures for annealed AA1050 and AA5005 samples, respectively. As stated before, a critical nucleus size of $5\mu m$ was used in the present analysis; this is also shown in the figure below as the starting value for all curves. Recrystallized grains follow the same microstructural path for all annealing temperatures for AA1050. The final grain size upon completion of recrystallization is the same for all annealing temperatures. The recrystallized grains size after completition remains constant even after some time has elapsed. This indicates pinning of grain boundaries from particles. Error bars in the Figs. 4.29 and 4.30 indicate the standard deviation about the mean value, obtained from different scans at each annealing condition.

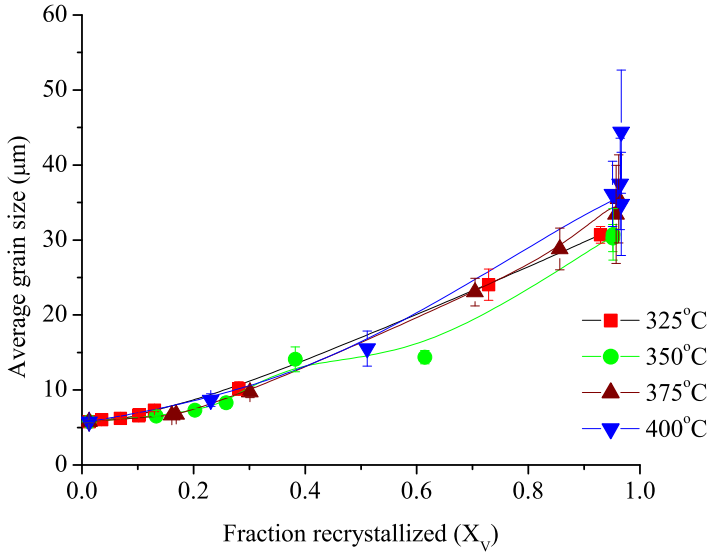

Figure 4.29: Average grain size variation at different annealing temperatures for AA1050

The average recrystallized grain size for AA5005 was higher at 350^oC than at 375^oC and 400^oC, as indicated in Fig. 4.30. The average recrystallized grain size at 350^oC is similar to that

obtained for AA1050 (approximately 40μm). However, the grain size at higher temperatures is smaller. The smaller grain size at higher temperature also points to faster recrystallization at high annealing temperature for AA5005. No grain growth is observed at higher temperatures for AA5005 as well, indicating pinning of grain boundaries from particles.

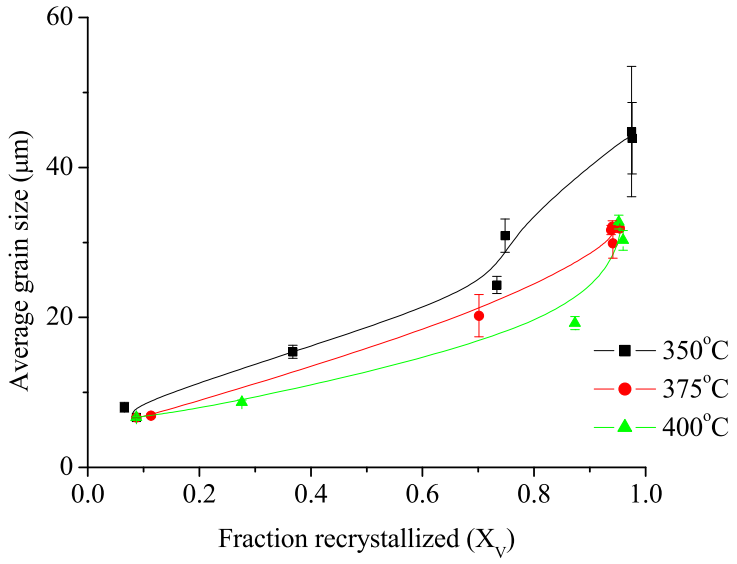

Figure 4.30: Average grain size variation at different annealing temperatures for AA5005

4.7 Texture Evolution

The deformed and recrystallized grains in a scan were partitioned based on their GOS values. An example of a partitioned scan was given in Figs. 4.15 and 4.16 for a sample of AA1050 which is approximately 50% recrystallized. The Inverse Pole Figure (IPF) maps of the partitioned recrystallized regions indicate clustering of recrystallized grains. The behavior is in accordance with the grain contiguity ratio (C_r) plot shown in Fig. 4.21. The overall texture, as well as the texture of the partitioned regions as can be represented with corresponding Orientation Distribution Function (ODF) maps. The texture components used in the present analysis are given in Table 4.4. The texture information available from the above ODF's indicate that cube is the main texture component for recrystallized grains and the deformed grains are concentrated along the β-fiber orientations (brass, copper and S).

The texture evolution in the deformed and recrystallized regions was characterized quantitatively in terms of the volume fractions of the components.

Texture component	Euler angles(degrees)
Cube(Normal & Rotated)	$(0, 0, 0), (0, 10, 0), (0, 20, 0)$ and $(0, 30, 0)$
Brass	$(35, 45, 0)$
Copper	$(90, 35, 45)$
S	$(27, 58, 18)$

Table 4.4: Texture components and their Euler angles used in current study

Volume fractions were calculated based on a 15^o tolerance angle, the average orientation of grains and the number of pixels in each grain. The average orientation for a grain is obtained from an iterative calculation involving the application of 24 cubic crystal symmetry operators to each point and selecting the one with minimum misorientation from the current average orientation. The application of the symmetry operators brings all the pixels in a grain within a single fundamental zone in orientation space. The average orientation is obtained from the arithmetic mean of the quaternions of all the pixels in the zone. A deformation microstructure is shown before and after the application of the average orientation algorithm in Fig. 4.31. No significant changes are observed in the pole figures after the averaging of orientations. This method is similar to previous applications for obtaining average orientation involving unit quaternion calculations [51, 52]. The average orientations are used to determine the texture component of each grain and weighted with the number of pixels of that grain to obtain the corresponding volume fraction.

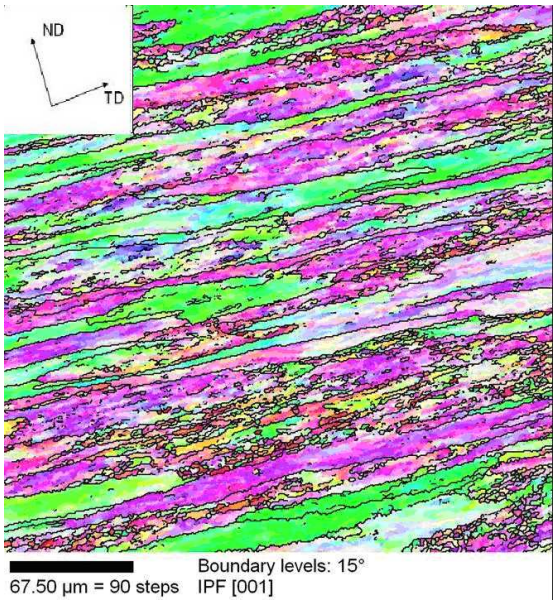

(a) A deformed scan with grains without averaging orientations

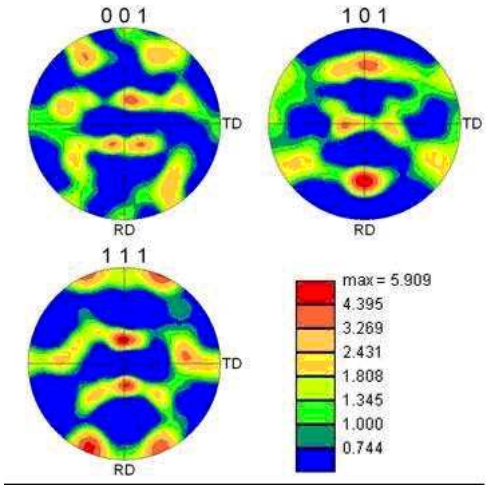

(b) Pole figures for scan (a) without averaging orientations

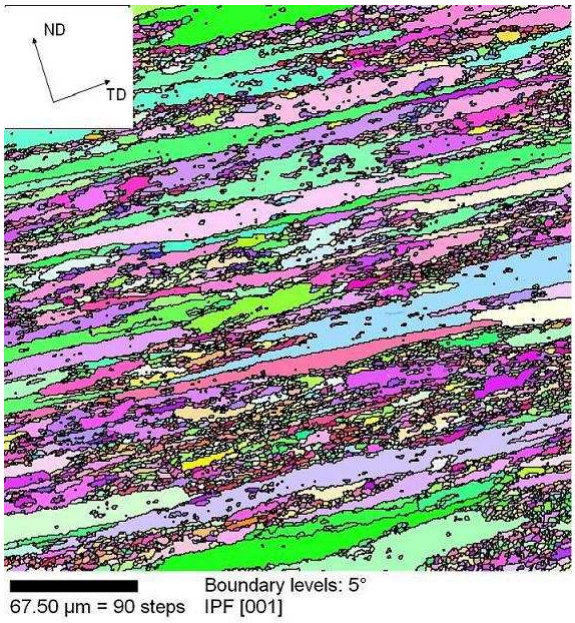

(c) Deformed scan with grains after averaging orientations

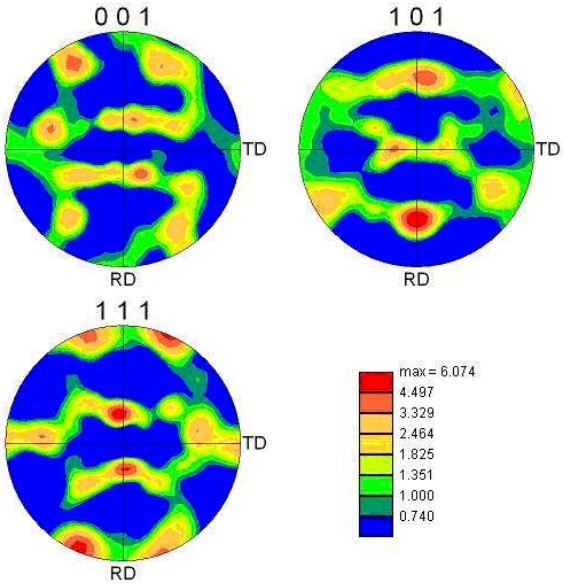

(d) Pole figures for scan (a) after averaging orientations

Figure 4.31: Averaging grain orientations of texture estimation.

A plot of the texture evolution at different annealing temperatures is given in Fig. 4.32 for AA1050 and Fig. 4.33 for AA5005. Similar plots were observed for the other annealing

temperatures ($375^oC, 400^oC$). The evolution of texture in AA1050 and AA5005 is very similar. A few important features of the above plots can be summarized as follows:

1. The volume fractions in each of the deformation and recrystallization texture plots sum to one.

2. The final annealing time on the deformation texture plots corresponds to a time before complete recrystallization, whereas the final annealing time for the recrystallization texture plots corresponds to a time after complete recrystallization of the sample.

3. The local variation in the plots is a result of the heterogeneity of the sample and limited scan areas.

4. During the initial stage of annealing, S is the main texture component for deformed regions while at the later stages, the Brass component dominates the deformation texture.

5. The recrystallization texture is dominated by the Cube texture at the later stages and a composite texture during the initial stages.

6. A comparison of volume fraction of the Cube component in deformed and recrystallized regions shows that even at early stages of recrystallization significantly higher amount of Cube component is present in recrystallized region than in deformed regions. This high fraction of Cube recrystallized grains indicates the presence of Oriented Nucleation (ON).

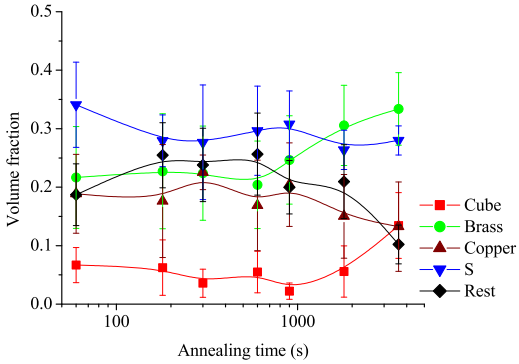

(a) Deformation texture for AA1050 at 325^oC

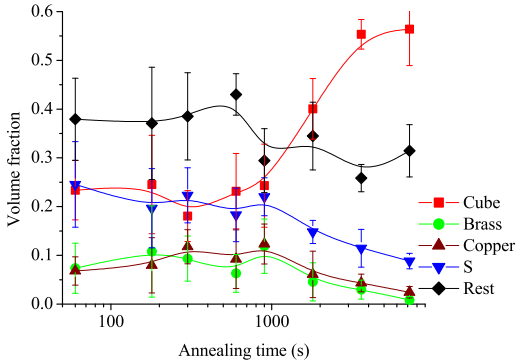

(b) Recrystallization texture for AA1050 at 325^oC

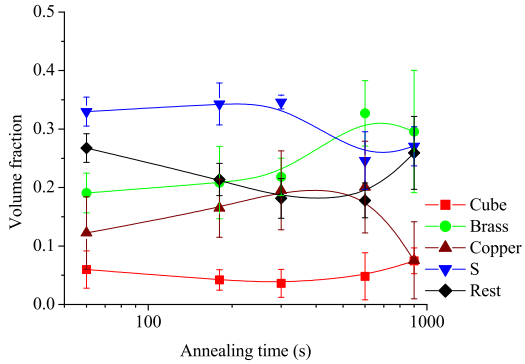

(c) Deformation texture for AA1050 at 350^oC

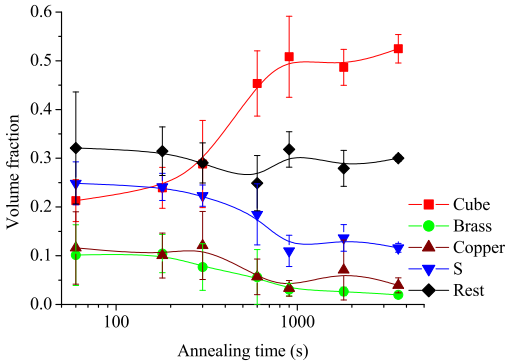

(d) Recrystallization texture for AA1050 at 350^oC

Figure 4.32: Texture evolution at 325^oC and 350^oC for AA1050.

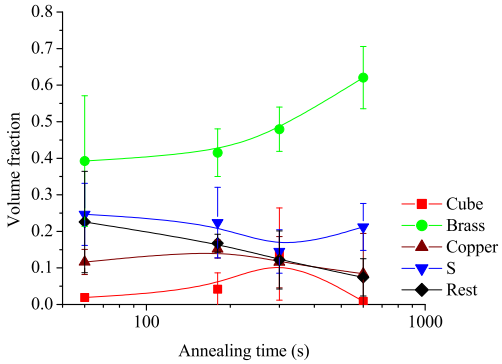

(a) Deformation texture for AA1050 at 350^oC

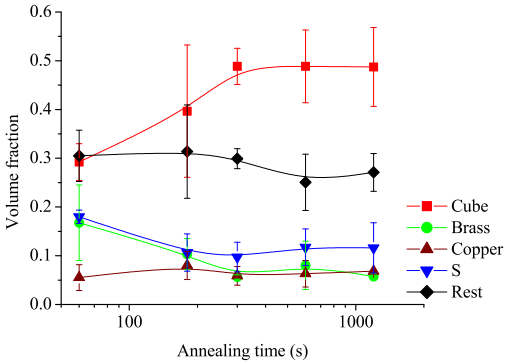

(b) Recrystallization texture for AA1050 at 350^oC

Figure 4.33: Texture evolution at 350^oC for AA5005.

4.8 Nucleation and Growth of Cube Recrystallized Grains

The main texture component for the recrystallized grains is the cube component which grows into a deformed matrix consisting mainly of rolled β-fiber components, accounting for approximately 80% of the deformation texture. The evolution of the recrystallized cube component was analyzed from the interfacial area shared between the recrystallized cube grains and the adjacent deformed grains. The GOS approach was used to partition scans in deformed and recrystallized regions which permited the calculation of interfacial area between neighboring grains. This in turn permited the measurement of the variation in the interfacial area of recrystallized cube grains against different deformation components with the annealing time and temperature. The interfacial areas were obtained by extending the definition of grain contiguity ratio to include different texture components.

$$A_{ij} = \frac{S_{Vij}}{S_{VT,i}} \tag{4.42}$$

where,

A_{ij} is the fractional interfacial area shared between the i^{th} recrystallized component and the j^{th} deformed component

S_{Vij} is the interfacial area shared between the i^{th} recrystallized component and the j^{th} deformed component

$S_{VT,i}$ is the total interfacial area of the i^{th} recrystallized component.

The fractional interfacial areas shared between components do not sum to one because the contribution from recrystallized grains is not included in the above calculations. The plots, Fig. 4.34, show the fraction of interfacial area that the cube recrystallized grains share with different deformation components. The cube component was selected because it is the dominant recrystallization component. The points during the initial stages of recrystallization indicate the nucleation behavior of cube grains whereas the points at later stages represent their growth behavior. The cube recrystallized grains are observed to have a large interfacial contact area with

the deformed S oriented grains during the initial stages of annealing. This behavior is expected as the S component constitutes about 40% of the deformed grains. Although the contribution of deformed cube grains to the overall deformation texture is small, a significant proportion of recrystallized cube grains are found in the vicinity of deformed cube grains during the initial stages of annealing. This indicates a preference for nucleation of cube recrystallized grains inside deformed cube regions. This phenomenon of nucleation from deformed cube bands also known as "Persistent Cube Band (PCB)" nucleation has been reported previously by various authors [31]. The deformed cube bands are formed from the cube grains present before the deformation of material and which have survived the deformation process. The recrystallized cube grains are formed from the subgrains in these deformed bands that have a size advantage [8].

As the fraction recrystallized increases, the fraction of interfacial area shared with deformed grains decreases so that the end point corresponds to completion of recrystallization. While the fractions of boundary pixels shared with S, cube and copper components are observed to decrease, the fraction of boundary pixels neighboring brass oriented deformed grains remains constant or increases during the later stages of annealing. Thus during the final stages of annealing, almost all recrystallized cube grains are adjacent to deformed brass oriented grains. The deformed brass grains are therefore, relatively stable during annealing. All annealing temperatures show a similar behavior.

Another important parameter, along with the actual fractions of boundary pixels shared, are the expected values of these fractions. The expected values are obtained by assuming no preference for a recrystallizing grain in the neighborhood of a deformed grain, i.e. random placement of recrystallizing grains with respect to the matrix. Therefore the expected fractions are simply the volume fractions of texture components scaled by the fraction recrystallized. Mathematically, it can be expressed as

$$E(A_{ir}) = X_V V_r \tag{4.43}$$

$$E(A_{id}) = (1 - X_V) V_d \tag{4.44}$$

Where,

$E(A_{ir}), E(A_{id})$ are the expected interfacial area shared between an i^{th} recrystallized component and an adjacent r^{th} recrystallized component or d^{th} deformed component respectively

V_r is the volume fraction of r^{th} recrystallized component and $\sum_r V_r = 1$

V_d is the volume fraction of d^{th} deformed component and $\sum_d V_d = 1$

X_V is the volume fraction recrystallized in the particular sample.

Fig 4.34b and d and Fig. 4.35b show comparisons of the observed interfacial area shared between cube recrystallized grains and the deformed grains of different orientations and the corresponding expected values at different annealing temperatures. The dashed line along the diagonal on the plot corresponds to a 1:1 ratio between expected and observed fractions. While any point near the dashed line would mean no preference for that component, a point above the line indicates strong preference for nucleation and a point below the line represents a lower probability of nucleation in that component. The different points on the plot indicate the observed and expected values at different annealing times during recrystallization. The points at higher fractions correspond to the initial stages of recrystallization while the points at lower fractions correspond to later stages of recrystallization.

The cube grains are well above the dashed line indicating a strong preference for nucleation from deformed cube grains. S oriented deformed grains are near the dashed line and the brass and copper oriented grains are almost always below the dashed line. Thus the cube recrystallized grains are found to have deformed cube and S grains as neighbors during the early stages of recrystallization and deformed copper and brass oriented grains at the later stages of recrystallization. The boundary area of cube recrystallized grains against deformed grains indicate a high contact area with the S component during the initial stages of recrystallization followed by a monotonic decrease. However, the fraction of boundary pixels against brass remains nearly constant or increases during the later stages of annealing. This behavior points to a favorable growth environment for the growth of cube recrystallized grains in vicinity of deformed S grains during the initial stages. Only after a significant reduction of the S component, do the recrystallized cube grains grow into the deformed brass grains, as revealed by high fraction of

boundary area shared during the later stages of recrystallization. The nucleation and growth behavior of cube recrystallized grains in AA5005 is very similar to that observed in AA1050. This relative stability of brass oriented deformed grains during recrystallization annealing has been observed previously for other aluminum alloys as well [17].

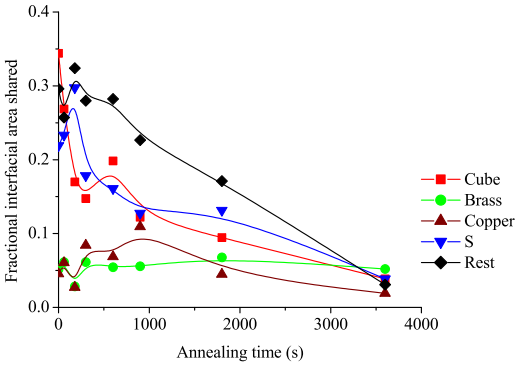

(a) Interfacial area variation for recrystallized cube grains against various deformed components at 325^oC.

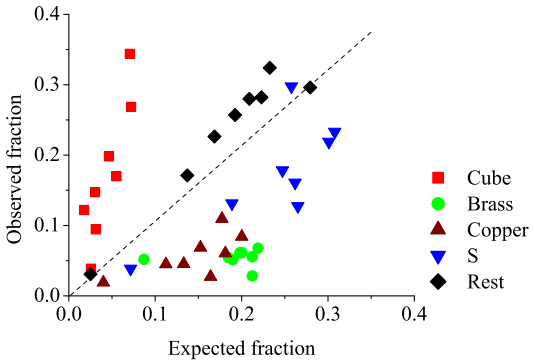

(b) Comparison of observed and expected fractions for recrystallized cube grains against various deformed components at 325^oC.

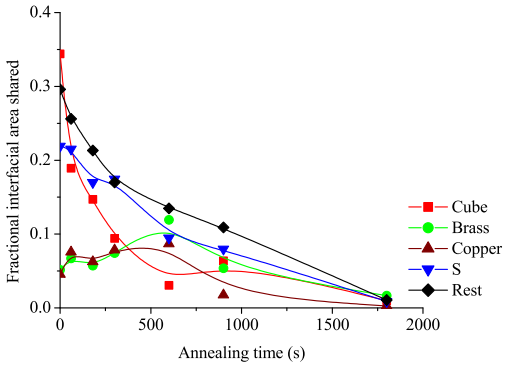

(c) Interfacial area variation for recrystallized cube grains against various deformed components at 350^oC.

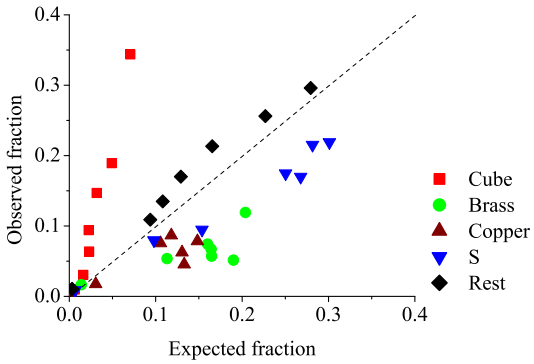

(d) Comparison of observed and expected fractions for recrystallized cube grains against various deformed components at 350^oC.

Figure 4.34: Interfacial area variation for recrystallized cube grains for AA1050. The observed fractional interfacial area shared with deformed grains decreases as the fraction recrystallized increases, (a) and (c).

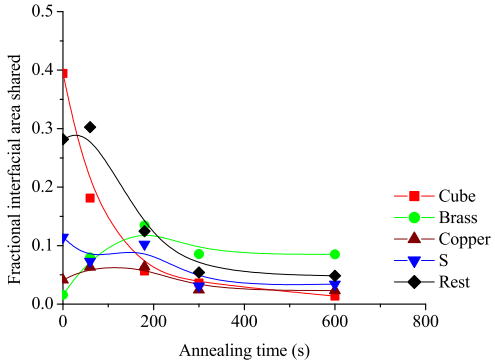

(a) Interfacial area variation for recrystallized cube grains against various deformed components at 350^oC.

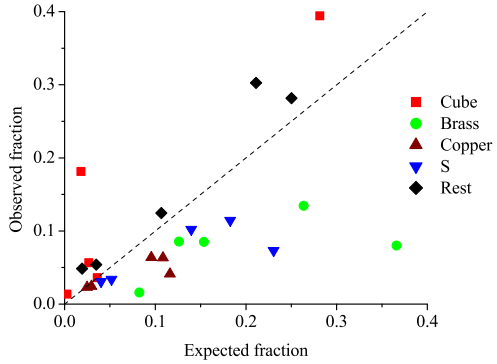

(b) Comparison of observed and expected fractions for recrystallized cube grains against various deformed components at 350^oC.

Figure 4.35: Interfacial area variation for recrystallized cube grains for AA5005. The observed fractional interfacial area shared with deformed grains decreases as the fraction recrystallized increases.

4.9 Growth Rates of Texture Components

The grain size of the recrystallized grains can be used for estimating growth rates of different texture components. Recrystallized grains of all texture components were analyzed at different annealing temperatures and times for grain size. The derivative of grain size with respect to annealing time gives an estimate of growth rate of a particular component. Two different grain sizes were analyzed here. The average recrystallized grain size provides information about the average growth rates for different texture components. The maximum recrystallized grain size helps in estimating the unimpinged growth rate of recrystallized grains. The unimpinged growth rates are important for estimating the maximum possible growth rates. Figs. 4.36 and 4.38 shows the maximum grain size and Figs. 4.37 and 4.39 show average grain size variations for recrystallized grains of all texture components with annealing temperature and times for AA1050 and AA5005, respectively.

At low annealing temperatures in AA1050, cube grains are found to have the largest average and maximum grain size. This indicates a growth advantage for cube recrystallized grains.

This growth advantage however appears to diminish with increase in annealing temperature. At 400^oC, all the recrystallized grains have similar grain sizes at all annealing times. This behavior is also indicative of variation in boundary mobilities with temperature. The above mentioned behavior is also found to be true for the maximum grain size. Another important aspect revealed from grain size analysis is that the growth advantage for cube recrystallized grains is not present during the initial stages of annealing. Only after a considerable fraction (approx. 20%) of material has recrystallized does the growth advantage for recrystallized cube grains become evident. The maximum recrystallized grain size is found to be three times the average recrystallized grain size, which is similar to the ratio found in standard grain size distributions obtained from simulations and experiments [53, 54].

In the case of AA5005, a small growth advantage for cube recrystallized grains is present only at 350^oC, indicated by their larger size. At 375^oC and 400^oC, the average grain sizes for all texture components are nearly the same. The ratio of maximum to average grain size is near three, similar to that observed in AA1050. Just as in AA1050, any growth advantage for Cube disappears at higher annealing temperatures.

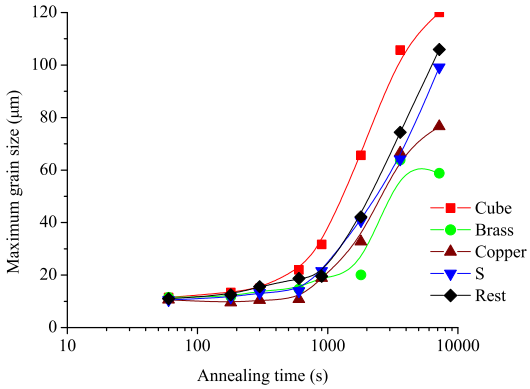

(a) Variation in maximum grain size at 325^oC.

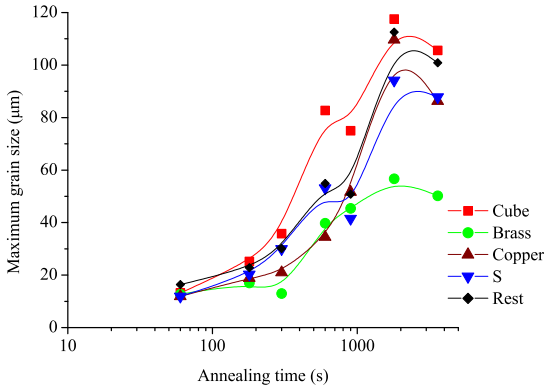

(b) Variation in maximum grain size at 350^oC.

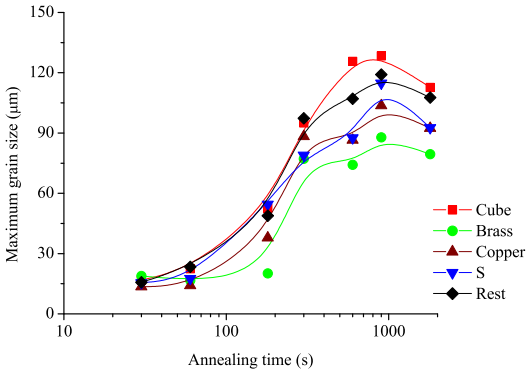

(c) Variation in maximum grain size at 375^oC.

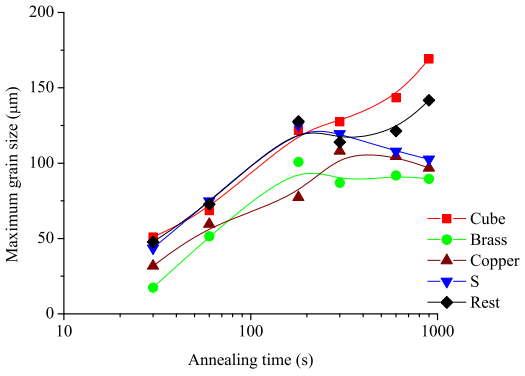

(d) Variation in maximum grain size at 400^oC.

Figure 4.36: Maximum recrystallized grain size for different texture components in AA1050.

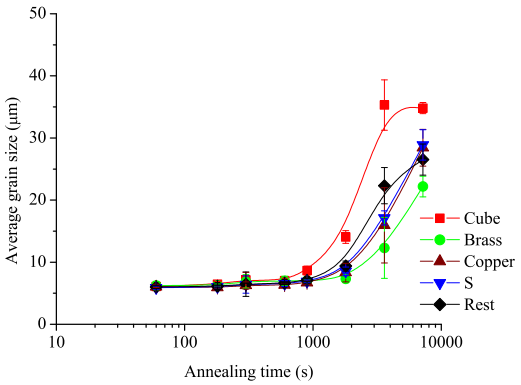

(a) Variation in average grain size at 325^oC.

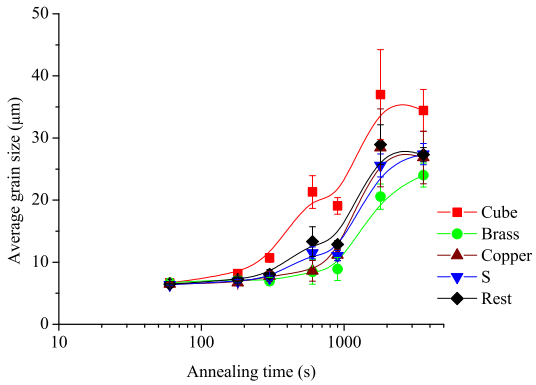

(b) Variation in average grain size at 350^oC.

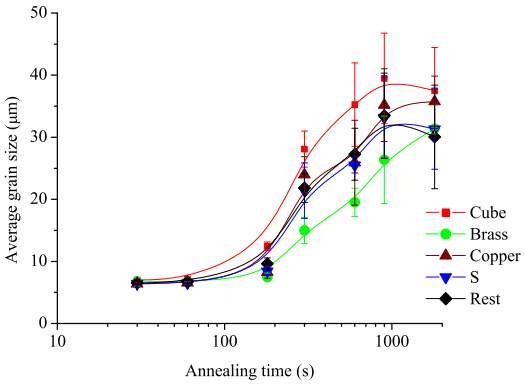

(c) Variation in average grain size at 375^oC.

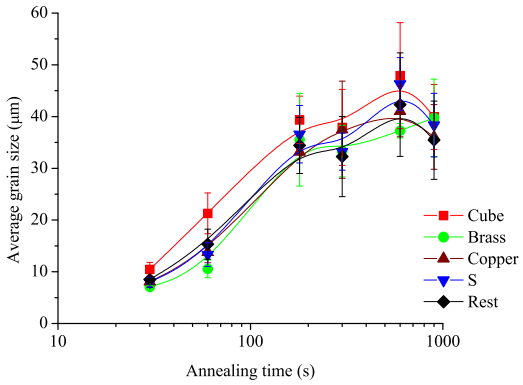

(d) Variation in average grain size at 400^oC.

Figure 4.37: Average recrystallized grain size for different texture components in AA1050.

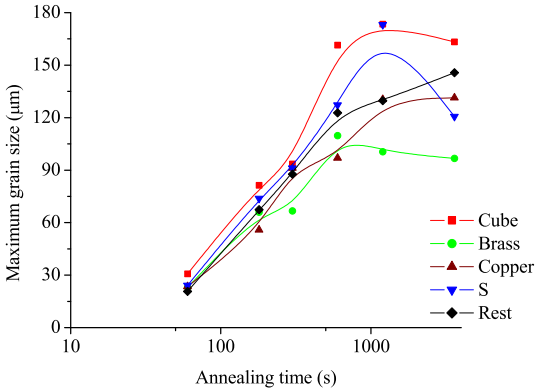

(a) Variation in maximum grain size at 350^oC.

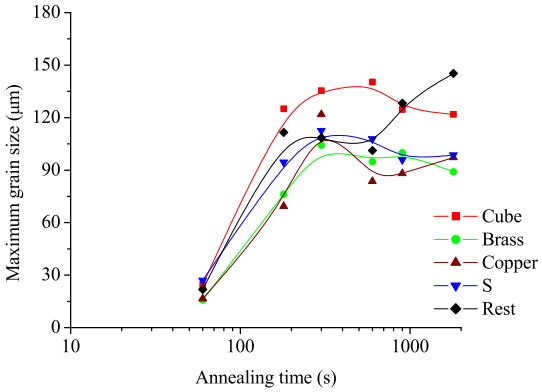

(b) Variation in maximum grain size at 375^oC.

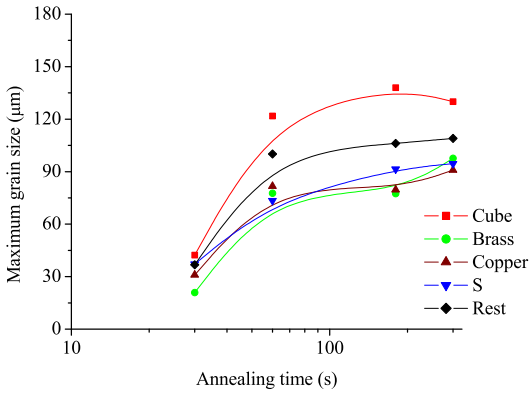

(c) Variation in maximum grain size at 400^oC.

Figure 4.38: Maximum recrystallized grain size for different texture components in AA5005.

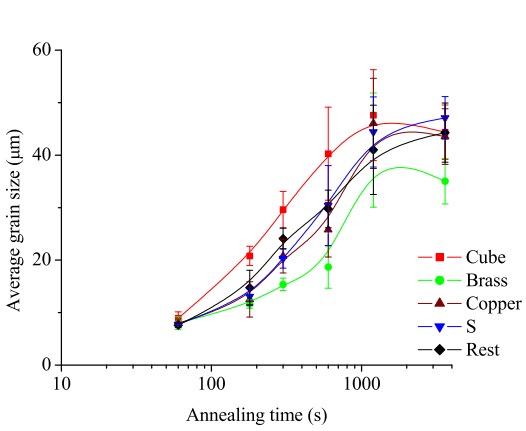

(a) Variation in average grain size at 350^oC.

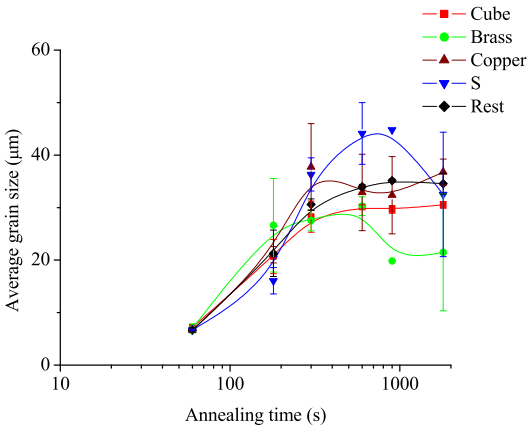

(b) Variation in average grain size at 375^oC.

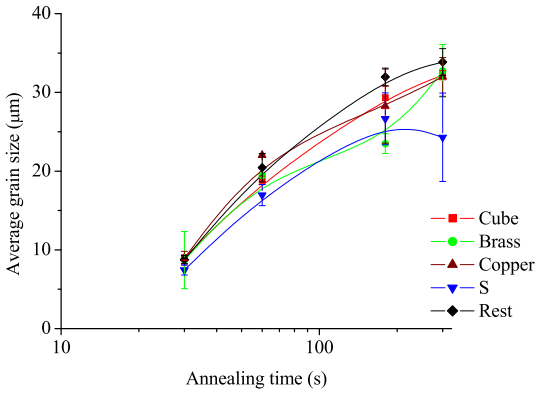

(c) Variation in average grain size at 400^oC.

Figure 4.39: Average recrystallized grain size for different texture components in AA5005.

4.10 GOS variation in different texture components

As pointed out in section 4.2.2, the variation in GOS showed good agreement with the variation in microhardness in the deformed regions. The decrease in the microhardness was attributed to recovery of deformed grains. A similar analysis of the variation in GOS for deformed grains of different texture components aids in understanding the process of recovery in deformation texture components. The partitioned deformed regions were studied for this analysis. Average GOS values for deformed grains of all texture components were obtained at

each annealing time and temperature. These average values are plotted against fraction recrystallized (X_V) for comparison by texture component, as shown in Fig 4.40 for AA1050 and Fig. 4.41 for AA5005.

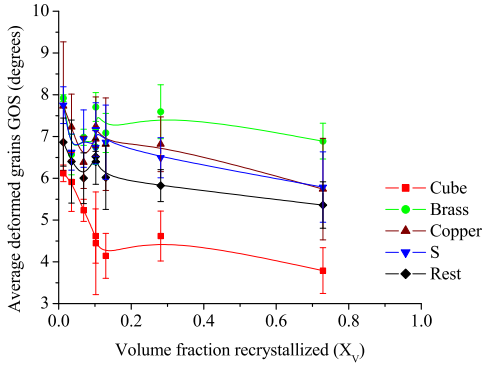

(a) Variation of average deformed GOS with fraction recrystallized (X_V) at 325^oC.

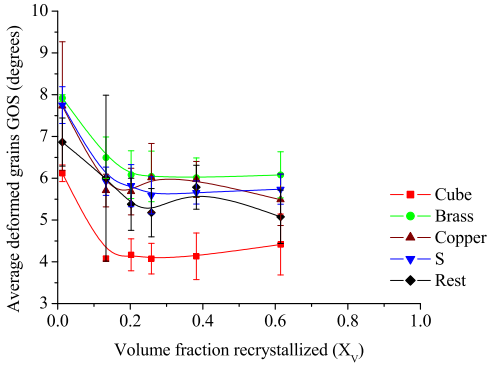

(b) Variation of average deformed GOS with fraction recrystallized (X_V) at 350^oC.

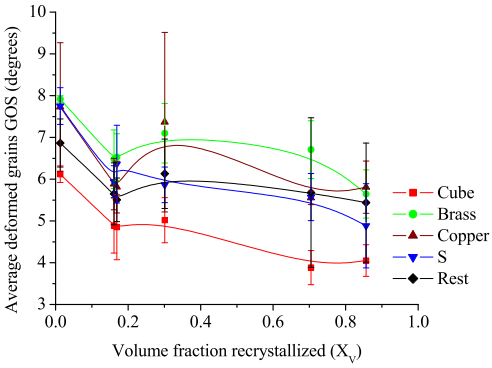

(c) Variation of average deformed GOS with fraction recrystallized (X_V) at 375^oC.

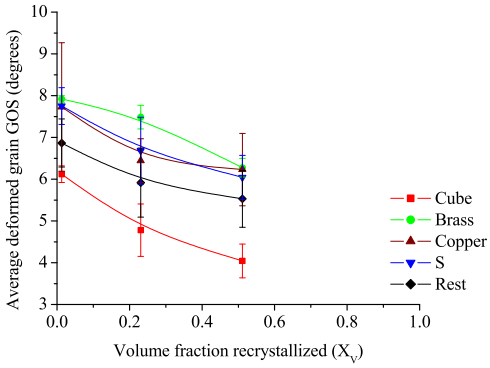

(d) Variation of average deformed GOS with fraction recrystallized (X_V) at 400^oC.

Figure 4.40: Average GOS in deformed grains for AA1050.

A marked difference is observed between the two alloys, AA1050 and AA5005. The average GOS values are found to be lowest for the deformed Cube grains and similar for rolling components (Brass, Copper and S) in AA1050. Components in the "Rest" of the orientation space tend to have GOS values between the deformed Cube component and rolling components. The minimum GOS values are approximately 3.5^o for the Cube grains and about 5^o

for other deformed grains. Therefore, the deformed Cube grains are expected to have higher recovery than the rolling components in AA1050. This behavior has also been observed in commercial purity aluminum alloys by Humphreys *et al.* [10]. A completely different behavior is observed, however, for AA5005. No difference between any texture components is observed in this case. Also the average deformed grain GOS values are higher for AA5005 as compared to AA1050 and exhibit smaller fractional decreases during recrystallization. This indicates less recovery in AA5005 due to the presence of Mg in solid solution.

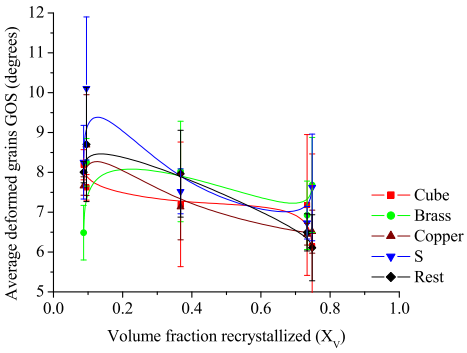

(a) Variation of average deformed GOS with fraction recrystallized (X_V) at 350^oC.

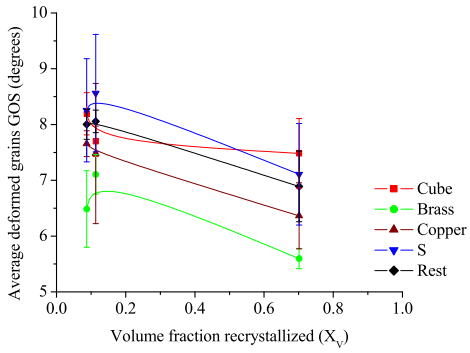

(b) Variation of average deformed GOS with fraction recrystallized (X_V) at 375^oC.

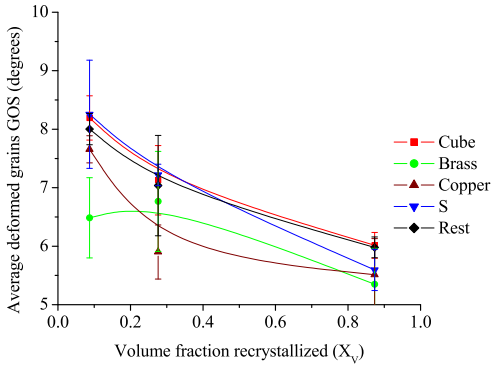

(c) Variation of average deformed GOS with fraction recrystallized (X_V) at 400^oC.

Figure 4.41: Average deformed grains GOS for AA5005.

4.11 Deformation Simulator

The deformation simulator provides an easy way to simulate conditions in rolling (plane strain deformation) on a laboratory scale. Specially machined specimens were deformed under various test conditions to observe the effects of different deformation parameters (i.e. temperature, strain and strain rate) on microstructure and texture evolution. The deformation experiments carried out in present analysis involve 50% deformation at 200^oC and 400^oC at the strain rates of $0.01s^{-1}$ and $1s^{-1}$. These deformation conditions bracket the commonly used deformation conditions for hot rolling in industry. All the experiments were carried on AA1050.

The deformed samples were machined, ground and electropolished on transverse cross-section for OIM analysis. Samples for OIM scans were obtained at the center. The scanned samples were analyzed for microstructure evolution, by observing the variations in GOS and GAM with different deformation conditions and fraction recrystallized, and texture evolution. Microstructures and textures for deformed samples are shown in Figs. 4.42, 4.43, 4.45 and 4.44. The samples deformed at low temperatures clearly show rolling textures and microstructure similar to those of as-received samples. However, for the samples deformed at 400^oC, microstructures and textures very different from the typical rolling textures and microstructures were obtained. A mixed texture comprising mainly Cube and Brass was obtained. Microstructural and textural information for different samples is shown in Table 4.5.

Temperature	200^oC		400^oC	
Strain rates (s^{-1})	0.01	1	0.01	1
Fraction recrystallized (X_V)	0.15	0.10	0.61	0.5
Average deformed grain GOS (degrees)	6.81	7.17	6.21	6.65
Cube fraction	0.083	0.044	0.421	0.248
Brass fraction	0.292	0.263	0.078	0.090
Copper fraction	0.097	0.121	0.039	0.050
S fraction	0.225	0.303	0.074	0.068
Rest fraction	0.302	0.268	0.387	0.541

Table 4.5: Microstructural and textural evolution after hot deformation of AA1050 in the deformation simulator.

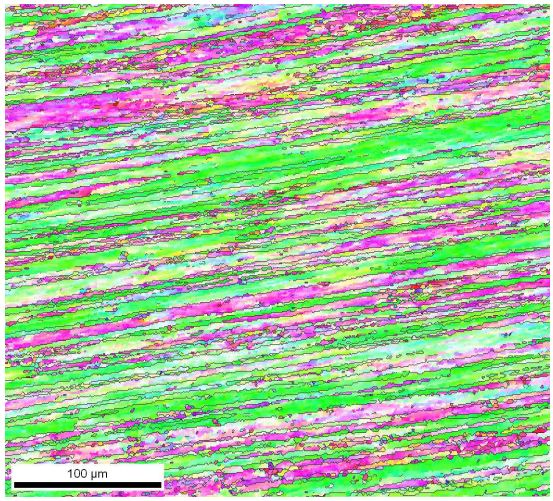

(a) Microstructure of sample deformed at 200^oC and strain rate of $1s^{-1}$.

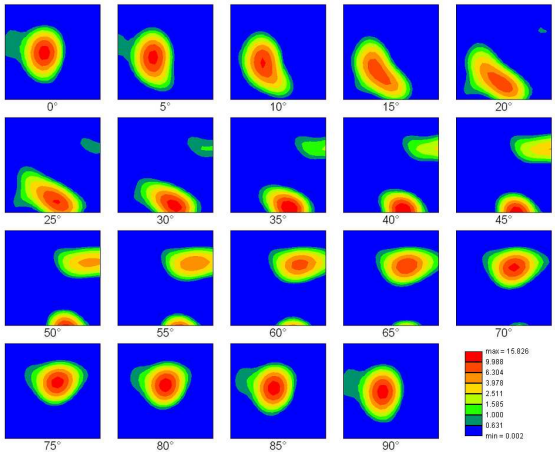

(b) ODF for sample deformed at 200^oC and strain rate of $1s^{-1}$ showing rolling texture.

Figure 4.42: Microstructure and texture for a sample of AA1050 hot deformed at 200^oC and a strain rate of $1s^{-1}$.

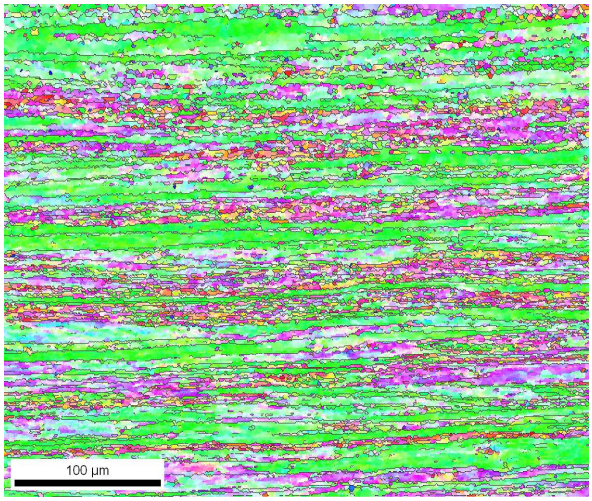

(a) Microstructure of sample deformed at 200^oC and strain rate of $0.01s^{-1}$.

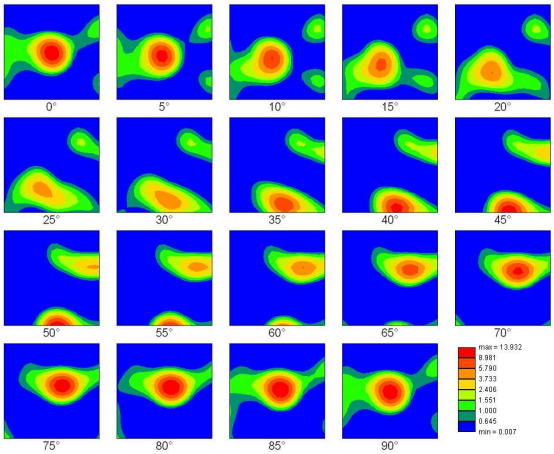

(b) ODF for sample deformed at 200^oC and strain rate of $0.01s^{-1}$ showing rolling texture.

Figure 4.43: Microstructure and texture for a sample of AA1050 hot deformed at 200^oC and a strain rate of $0.01s^{-1}$.

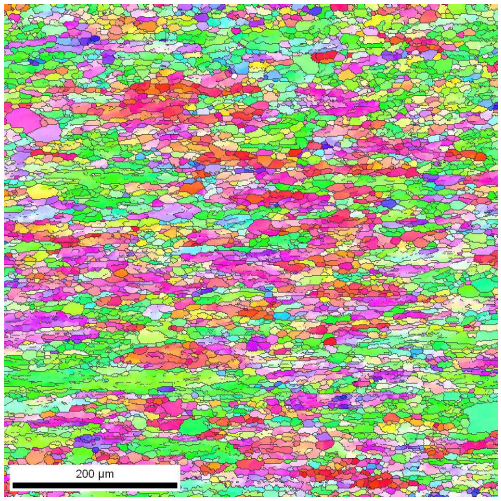

(a) Microstructure of sample deformed at 400^oC and strain rate of $1s^{-1}$.

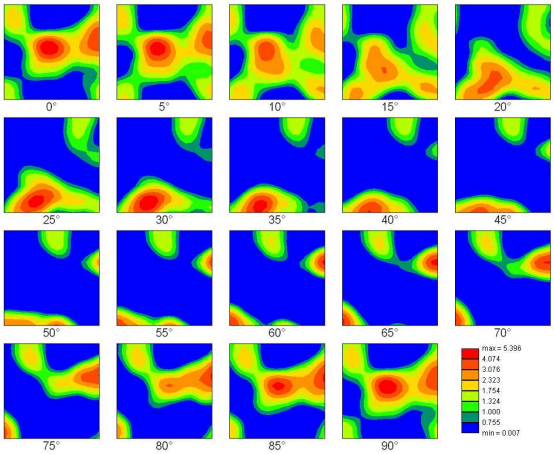

(b) ODF for sample deformed at 400^oC and strain rate of $1s^{-1}$ showing mixed texture.

Figure 4.44: Microstructure and texture for a sample of AA1050 hot deformed at 400^oC and a strain rate of $1s^{-1}$.

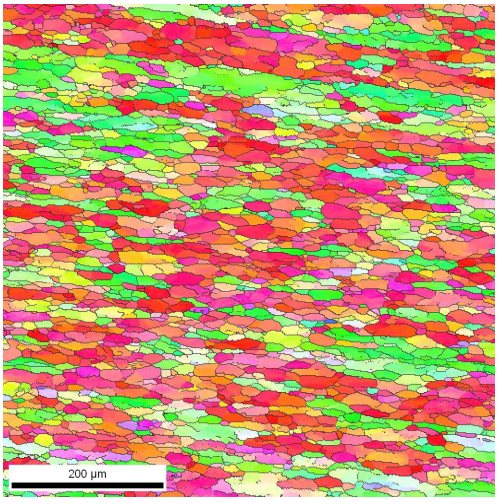

(a) Microstructure of sample deformed at 400^oC and strain rate of $0.01s^{-1}$.

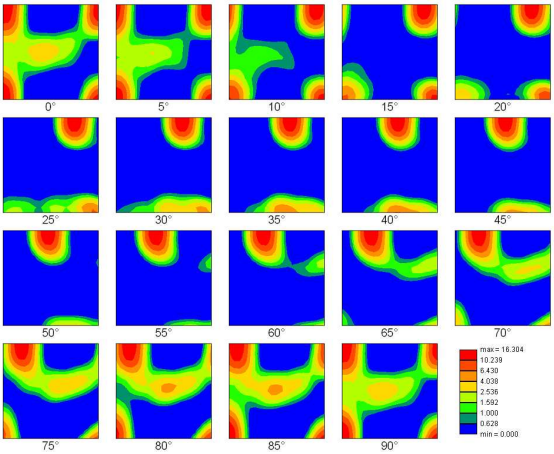

(b) ODF for sample deformed at 400^oC and strain rate of $0.01s^{-1}$ showing mixed texture.

Figure 4.45: Microstructure and texture for a sample of AA1050 hot deformed at 400^oC and a strain rate of $0.01s^{-1}$.

The lower strain rate of $0.01s^{-1}$ at both deformation temperatures resulted in higher fractions recrystallized and lower average GOS values compared to deformation at $1s^{-1}$, indicating a significant contribution from recovery at low strain rate. Comparison of the texture evolution from ODF's in Figs. 4.42, 4.43, 4.45 and 4.44 and Table 4.5 clearly shows that the rolling texture is dominant at low deformation temperature at both strain rates. The microstructural and textural evolution at this temperature is very similar to the as-received samples. Texture evolution at 400^oC indicate a different behavior. Whereas Cube is the dominant texture component at both strain rates, some contribution from Brass is also observed. This indicates a different deformation behavior at 400^oC than that observed at 200^oC.

The effect of different deformation temperatures on recovery can be analyzed by comparing GAM and GOS values on a grain by grain basis. This analysis is shown in Figs. 4.46 and 4.47. Recovery is characterized by local rearrangement of dislocations. This will lead to lower GAM and higher GOS for recovered grains. Thus the recovered grains will have GAM values near recrystallized grains and GOS values near deformed grains. GAM and GOS values for all grains at 400^oC show a significant deviation from the 1:1 line. Also most of the grains are observed to have GAM values of 2^o or less, although GOS extends to 10^o. A similar analysis for deformation at 200^oC shows deviations which are not as large as those observed for 400^oC. In the latter case, most of the grains here have GAM values greater than 2^o, thus indicating significantly less recovery for material deformed at this temperature.

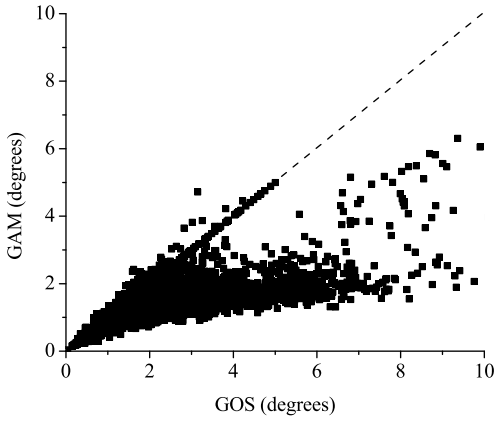

(a) Variation in GAM and GOS values for samples deformed at 400^oC and a strain rate of $0.01s^{-1}$.

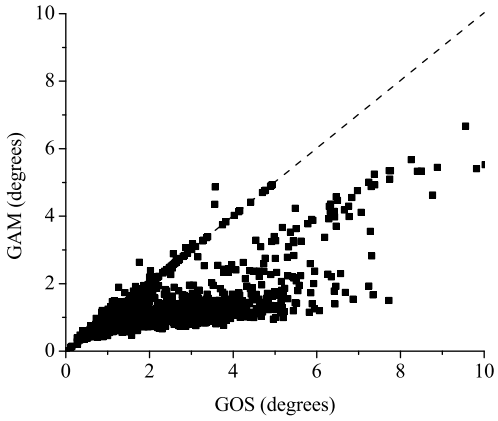

(b) Variation in GAM and GOS values for samples deformed at 400^oC and a strain rate of $1s^{-1}$.

Figure 4.46: GAM and GOS variations at 400^oC for samples deformed in the deformation simulator.

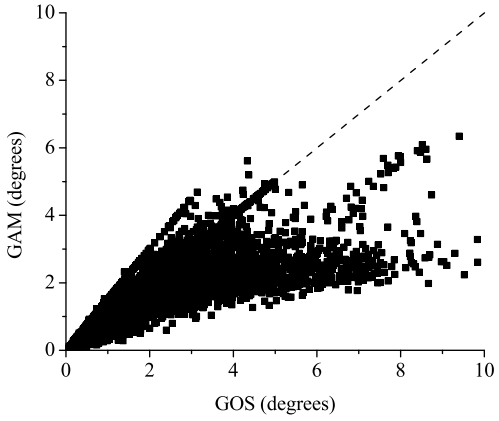

(a) Variation in GAM and GOS values for samples deformed at 200^oC and a strain rate of $0.01s^{-1}$.

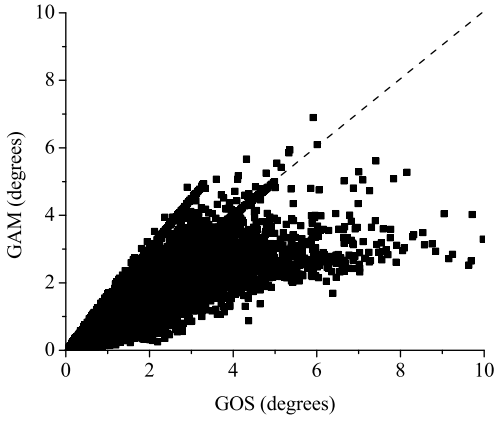

(b) Variation in GAM and GOS values for samples deformed at 200^oC and a strain rate of $1s^{-1}$.

Figure 4.47: GAM and GOS variations at 200^oC for samples deformed in the deformation simulator.

5 Conclusions and Discussions

The kinetics of recrystallization and texture evolution were analyzed for hot rolled Aluminum Alloys 1050 and 5005. The as-received hot rolled samples were isothermally annealed at different temperatures and analyzed by microhardness indentations and Orientation Imaging Microscopy (OIM). The results presented in Chapter 4 clearly indicate the advantages offered by OIM over other methods including microhardness variations. OIM provides the ability to extract parameters such as interfacial area per unit volume between deformed and recrystallized grains, contiguity of texture components, long range and short range orientation variations, etc., whose relevance for the study of recrystallization is clear. The experimental results are compared to a number of current and previous studies on recrystallization of aluminum alloys. This chapter presents some of the comparisons and their relevance to the overall study of recrystallization in hot rolled aluminum alloys.

5.1 Orientation Imaging Microscopy

One of the main aims for the current project was to develop methods based on OIM to characterize microstructural evolution during recrystallization. Although OIM has been used for a long time now, most of the earlier studies were based on one-dimensional line scans [12, 28]. Two-dimensional area scans were used in the current study. OIM scans were analyzed based on Image Quality and Confidence Index and intragranular orientation variations. While most of the previous studies were carried out using orientation variations between neighboring pixels (GAM) [55], an extensive study of long range (GOS) and short range (GAM) orientation variations was carried out in the present study. It was shown that both GOS and GAM can be used independently or in conjunction to obtain fraction recrystallized from OIM.

An important aspect revealed in the current study is the applicability of GOS for recovery analysis. As revealed in section 4.2.2, deformed grain microhardness and average deformed grain GOS showed a similar variation with fraction recrystallized. The reduction in deformed

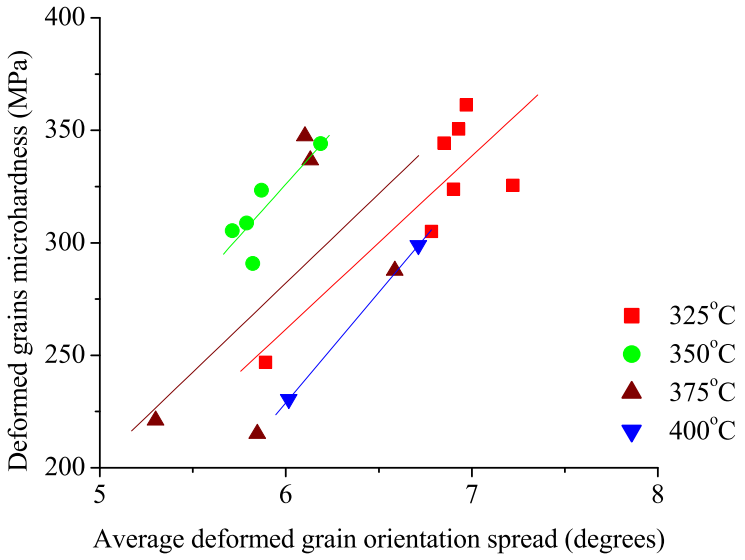

Figure 5.1: Variation between Microhardness and GOS for deformed grains.

grain microhardness was attributed to concurrent recovery of deformed grains. To further understand the relationship between hardness and GOS, a positive correlation between microhardness of deformed grains and their GOS was found, Fig. 5.1. Although the linear fits are not satisfactory at all annealing temperatures, parallel lines representing the linear relationship between recovery and GOS were obtained. These lines demonstrate the applicability of GOS for recovery analysis. An earlier analysis by Humphreys also revealed similar behavior for aluminum alloys, as shown in Fig. 5.2 [10]. The term misorientation spread is equivalent to GOS and mean misorientation refers to GAM in Fig. 5.2.

5.2 Recrystallization Kinetics

Recrystallization kinetics in hot rolled AA1050 were analyzed by using the JMAK approach as well as the Microstructural Path Method (MPM). While the conventional JMAK analysis can be used to obtain the basic information about recrystallization kinetics and nucleation and growth behavior of recrystallized grains, some very important questions remain unanswered. For example, clustering of recrystallized grains, growth rate variations with annealing times and temperatures are of interest. By using more complex models along with JMAK analysis,

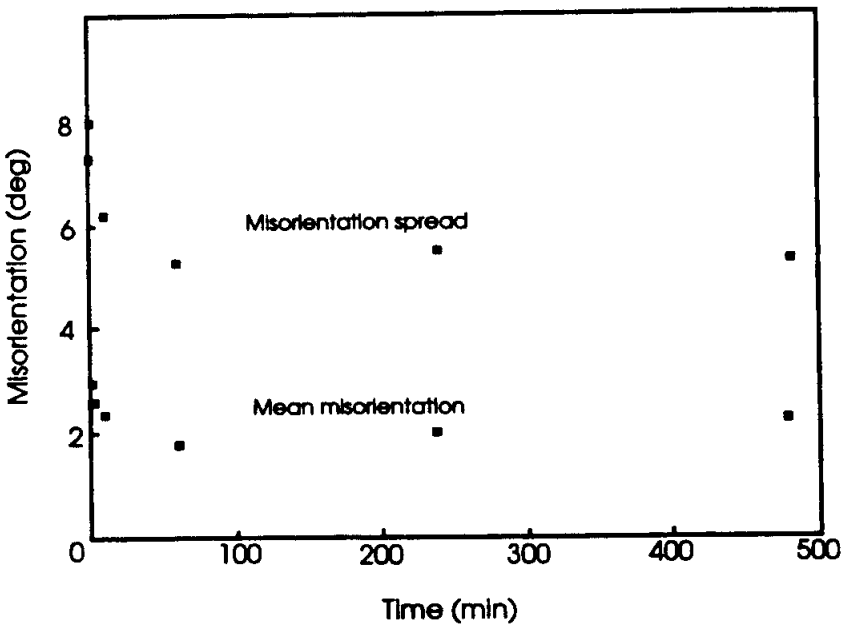

Figure 5.2: Misorientation spread and mean misorientation variation during recovery in 99.998% pure aluminum cold rolled and subsequently annealed at 300^oC. [10]

much more information can be obtained. Table 5.1 gives the JMAK exponents obtained from microhardness variations and OIM analysis using GOS method. The JMAK exponents from the two methods are near one and belong to a similar transformation class, i.e. grain boundary nucleation, as demonstrated by Cahn [42]. Further analytical evidence for grain boundary nucleation is provided by Vandermeer and Masumura [45], who extended Cahn's approach to include interfacial area per unit volume (S_V). The parameter q, directly relates volume fraction recrystallized (X_V) to interfacial area per unit volume (S_V), and lies between 0 and 0.5. Values are shown in Table 5.1 and indicate site saturated grain boundary nucleation. These values are in good agreement with a recent analysis by Vandermeer and Juul Jensen ($q = 0.52$) on a AA1050 type alloy hot deformed under plane strain conditions at 400^oC at a strain rate of $2.5s^{-1}$ followed by isothermal annealing at 400^oC [29]. The microstructure shown in Fig. 5.3 validates the fact that most of the recrystallized grains are present at grain boundaries. Recrystallized grains are evident as small, equiaxed grains that are close to or on grain boundaries in the deformed structure.

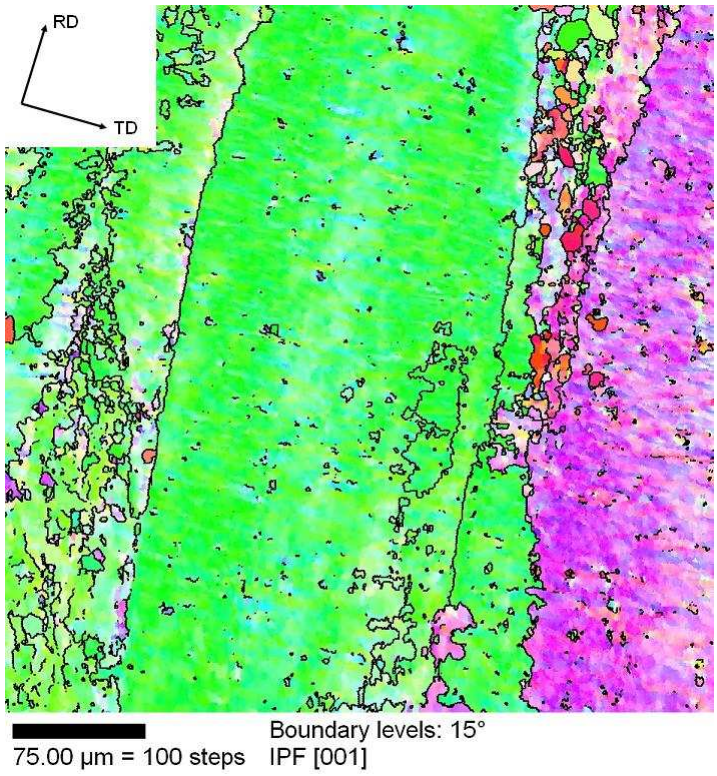

Figure 5.3: Microstructure of an as-received sample showing grain boundary nucleation at prior boundaries.

Temperature^{O}C	Microhardness	OIM	q (MPM analysis)
325	0.89	1.45	0.49
350	0.65	1.09	0.51
375	0.90	1.08	0.31
400	1.77	1.35	0.47

Table 5.1: JMAK exponent (n) obtained from microhardness and OIM and the parameter q obtained from MPM analysis.

Microhardness variations for recrystallization have been used by Waryoba and Kalu [9] for wire drawn Oxygen Free High Conductivity (OFHC) copper wires. However, due to the very high strains (approx. 3.10) imposed, JMAK exponents of the order of 3-4 were observed. This clearly indicates a uniform distribution in stored energy. JMAK exponents near one, can indicate non-uniform distribution of stored energy. The effect of variable stored energy in deformation microstructure was analyzed by Rollett *et al.*, using Monte Carlo simulations

[56]. Inhomogeneous stored energy can lead to JMAK exponents that are much lower than those experimentally predicted for the given nucleation and growth conditions. It also gives rise to nucleation densities that vary from one grain to another. Inhomogeneous stored energies in deformation microstructures of AA1050 and AA5005 were also observed in the present study. This is shown in Fig. 5.4, for an as-received AA5005 sample with boundaries drawn at two different misorientation values. Boundary misorientations at 15^o represent normal high angle boundaries in Fig. 5.4 (a) between different bands. When the boundary misorientation is reduced to 3^o, to show the subgrain structure, different subgrain sizes are observed in different orientations Fig. 5.4 (b). The stored energy of deformation is related to subgrain size (δ) and misorientation (θ) as given by Read-Shockley equation [6]

$$E_S = \frac{3\gamma_o\theta(A - \ln\theta)}{\delta} \tag{5.1}$$

Here,$\gamma_o = \frac{Gb}{4\pi(1-\nu)}$, $A = 1 + \ln\frac{b}{2\pi r_o}$, r_o is radius of the dislocation core, usually taken as between b and 5b.

As Fig. 5.4 shows, the subgrain sizes for different texture components follow the order Cube(red)> Brass(green)> S(pink) which gives the stored energy variations as S>Brass>Cube. A higher stored energy in S deformed grains has been reported by Vatne *et al.* [8] and is also evidenced from the texture evolution in deformed regions, Fig. 4.32(a), 4.32(c) and 4.33(a), which showed relative increase in Brass grains at the later stages of annealing therefore implying stability of this orientation to annealing [57].

The contiguity of recrystallized grains as given in Fig. 4.21 and Fig. 4.22 clearly indicates that recrystallized grains are clustered during the initial stages of annealing. A similar behavior was also obtained in austenite to ferrite transformations and for recrystallization in hot rolled aluminum alloys by Vandermeer [11], Fig. 5.5.

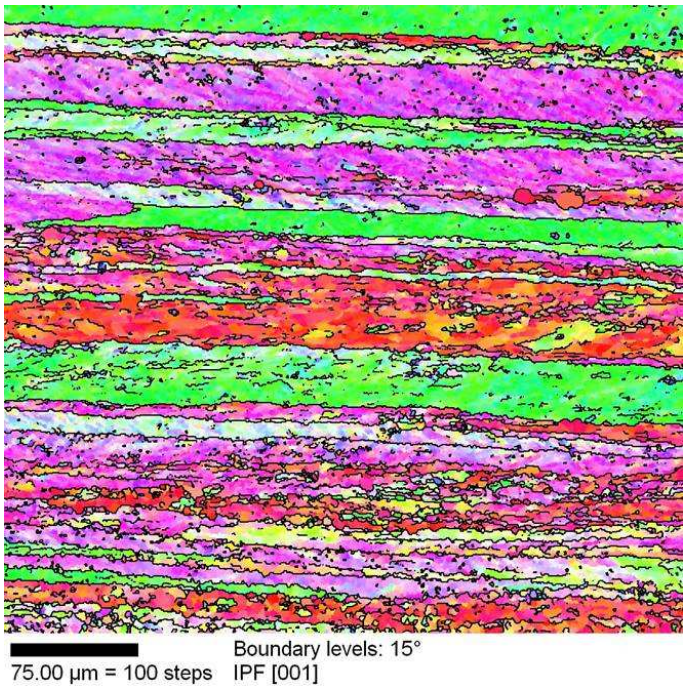

(a) Boundaries drawn at misorientation 15^o

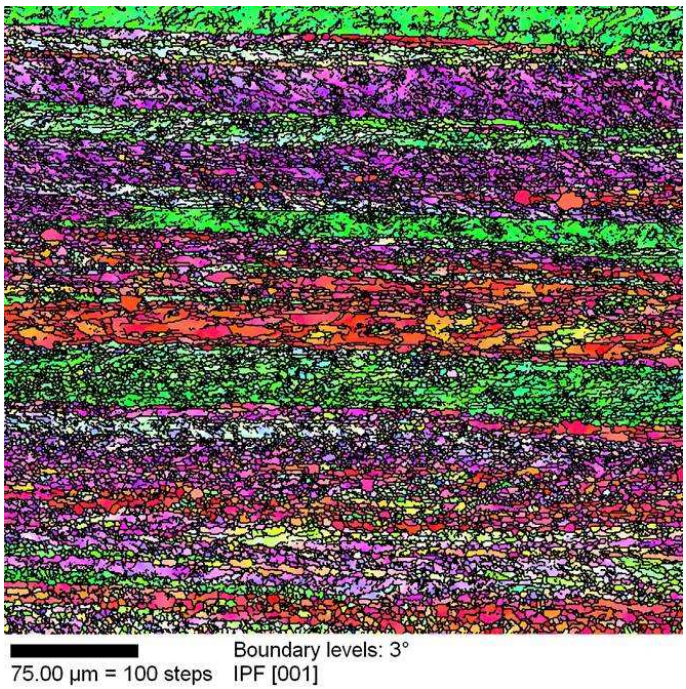

(b) Boundaries drawn at misorientation 3^o

Figure 5.4: As-received AA5005 samples showing different subgrain sizes in texture components. The cube component (red bands) has the largest subgrains, shown in (b), followed by Brass (green bands) and S (pink), which has the smallest subgrains.

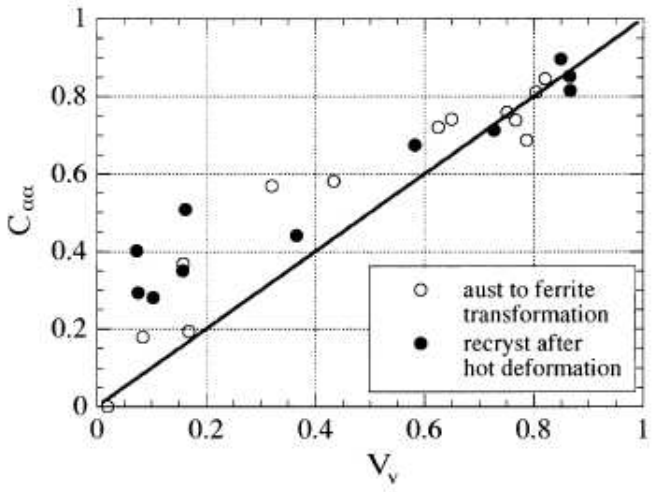

Figure 5.5: Contiguity ratios in steel and hot rolled aluminum [11].

The velocity of the interface between deformed and recrystallized grains as a function of time was obtained from the Cahn-Hagel approach [49]. This represents the average migration rate for high angle boundaries. The growth rate variations shown in Fig. 4.23 and 4.26 show a time dependence of the growth rate. The change in growth rate at low annealing temperatures indicates a more gradual decay in growth rate than at high temperatures, where a rapid decline in growth rates is observed. This variation in growth rates with annealing temperatures is related to the decrease in stored energy. The rate of decrease of stored energy is higher at high annealing temperatures. The growth rate after the initial transient becomes constant and is dependent on annealing temperature. The constant growth rates at long times can be used to determine the activation energy for high angle boundary migration. These activation energies can be compared with the activation energy for recrystallization to determine the dominant mechanism for recrystallization.

The activation energy for recrystallization is obtained from the temperature dependent parameter k in the JMAK equation

$$X = 1 - \exp\left[-(kt)^n\right] \tag{5.2}$$

A variation in k values, obtained from isothermal annealing at different temperatures, was used to obtain the activation energy for recrystallization from the Arrhenius equation

$$k = k_o \exp\left(-\frac{Q}{RT}\right) \tag{5.3}$$

The activation energy for recrystallization, obtained from microhardness variations for samples annealed isothermally at $325^oC, 350^oC, 375^oC$ and 400^oC is 178 kJ/mol. The activation energy for boundary migration obtained from Cahn-Hagel interface migration analysis is 168 kJ/mol. These values are similar to each other and indicate that recrystallization in hot rolled AA1050 is controlled by migration of high angle boundaries as expected. The activation energy for boundary migration obtained in a similar alloy by Vandermeer et al. Q = 172kJ/mol also compares well with the above values [28]. The activation energies of different elements in aluminum are given in Table 5.2.

Element	Activation Energy (kJ/mol)
Al[58]	142
Mg[58]	139
Si[28]	129-154
Fe[59]	58-258

Table 5.2: Activation energies of different elements in Aluminum.

The activation energy for the migration of high angle boundaries is significantly larger than the activation energy for self diffusion in aluminum, indicating that the boundary migration in aluminum is controlled by solute drag of other elements. This activation energy is, however, comparable to the activation energy for diffusion of iron in high purity aluminum Q = 193kJ/mol [60]. The similarity in activation energies of recrystallization, migration of high angle boundaries and the activation energy for diffusion of iron in aluminum provides some evidence that recrystallization in hot rolled aluminum is controlled by migration of high angle boundaries which in turn are controlled by solute by iron in the aluminum matrix.

A comparison of activation energies of recrystallization for AA1050 used in present analysis and other similar alloys reported is given in Table 5.3 along with the concentration of Fe and Si in the alloys.

Alloy	%Fe	%Si	Activation Energy(kJ/mol)
AA1050 (present analysis)	0.31	0.08	168-178
AA1050 (Vandermeer et al.)	0.34	0.15	172
AA1050 (S. P. Chen et al.)	0.185	0.109	225-234
Al-Mg (Sellars et al.)	0.40	0.10	230

Table 5.3: Activation energies of recrystallization obtained in different studies for aluminum alloys

The lower activation energy values in the present analysis can be attributed to the different processing conditions used in the different alloys. As-received hot rolled and recovered samples are used in the present study, whereas tensile specimens were used in the other AA1050 analyses which exhibited JMAK exponent *n* near 2.2 [26]. The Al-Mg alloy was deformed by Plane Strain Compression (PSC) [27]. No contribution of recovery processes was observed in the present analysis, whereas significant recovery contributions were observed in the other analyses [26, 27].

5.3 Texture Evolution

The texture analysis of as-received and annealed samples revealed that deformation and recrystallization textures are qualitatively similar but quantitatively different (consisting of the same components but with different weights) [16]. The main texture components observed in the present analysis are Cube, Brass, Copper and S; these are typically reported for commercial purity aluminum alloys [61, 36, 37]. The partitioning of scanned areas between deformed and recrystallized regions helped in obtaining an independent analysis of texture components in each region. The texture analysis of the deformed regions showed that S and Brass are the main texture components in the deformed regions. A significant amount of the Copper component is also observed along with the small amount of deformed Cube. The variation

of texture components in the deformed regions at different annealing temperatures revealed similar behavior.

The S component is the main texture component during the initial stages of annealing and the Brass component is observed to be dominant at the later stages of annealing. The Copper component is observed to decrease monotonically during the annealing treatment. The increase in the relative volume fraction of the Brass component at the later stages of recrystallization, as shown in Fig. 4.32, indicates relative stability of this component to the annealing treatment. The stability of deformed Brass grains has been observed in other aluminum alloys including AA5182 and other commercial purity aluminum alloys [17, 57]. This stability of Brass grains is attributed to its ability to deform on very few slip systems. They are therefore less likely to nucleate new grains than other deformation orientations during recrystallization of hot rolled samples. The activation of fewer slip systems is thought to also lead to lower stored energy and therefore slower kinetics [57].

The recrystallized regions have Cube as the dominant texture component. The recrystallized grains have similar fractions of Cube and the β-fiber components during the initial stages of annealing. The fraction of Cube component in recrystallized grains is significantly higher than in deformed grains, whereas the fraction of rolling orientations in recrystallized grains is similar to that in deformed grains. Thus Cube recrystallized grains have a nucleation advantage, suggesting the presence of Oriented Nucleation (ON). The texture at latter stages is marked by the presence of higher Cube fractions and smaller fractions of rolling components. The nucleation and growth behavior of recrystallized Cube grains was analyzed by observing the variations in the boundary pixels shared between recrystallized Cube grains and deformed grains of all orientations. A significant fraction of recrystallized Cube grains have deformed Cube grains as their neighbors during the initial stages of annealing, in spite of very low fractions of deformed Cube grains in the overall deformation texture (0.05). The presence of deformed Cube grains has been reported in previous analysis. These are often termed as “Persistent Cube Bands (PCBs)” [31]. In a Transmission Electron Microscopy (TEM) investigation of AA1050 type alloy by Nes *et al.*, the deformed Cube grains were observed to be several hundred micrometers

long in the rolling direction and were found to contain large subgrains which can act as nuclei upon annealing of deformed samples [8]. The presence of a high fraction of deformed Cube grains in the neighborhood of recrystallized Cube grains supports the observations of Nes *et al.*

The recrystallized Cube grains have S as their main deformed neighbor. This is in accordance with the volume fraction of S component in deformed regions, as indicated by the comparison plots in Fig 4.34(b). The points corresponding to S grains are always near the 1:1 line in the plots, indicating similar values for expected and observed fractions. The Brass component points are observed to lie below the 1:1 line at the initial stages (higher fractions) and near the line at final stages (lower fractions). The deformed Cube grains are almost always found above the line, indicating a high probability of nucleation of recrystallized Cube grains from the deformed Cube bands.

A variation similar to that observed by Vatne *et al.* was obtained here. A steep decline in the fraction of boundary pixels shared between deformed Cube grains and deformed S grains was observed during the initial stages whereas the fractions corresponding to Brass components remained constant or showed a small decrease. These observations indicate the relative stability of the different deformation texture components upon annealing of as-received samples. The S grains are found to decline early during upon annealing thus indicating lower stability and higher stored energies. Brass oriented grains have slower recrystallization kinetics and are present until the later stages of recrystallization, indicating higher stability and lower stored energies. The Copper component is found to have intermediate stability and stored energy. The stored energy calculations based on subgrain size and misorientations reported in various studies also revealed a trend similar to that indicated above [19, 18].

A simple view offered by the above observations reveals nucleation of recrystallized Cube grains from the deformed Cube grains, which have relatively large subgrains. The nuclei grow into the deformed matrix which consists of grains of different orientations. The growth of recrystallized Cube grains is fastest in S grains and slowest in Brass grains, in the order of the stored energies of various deformation components.

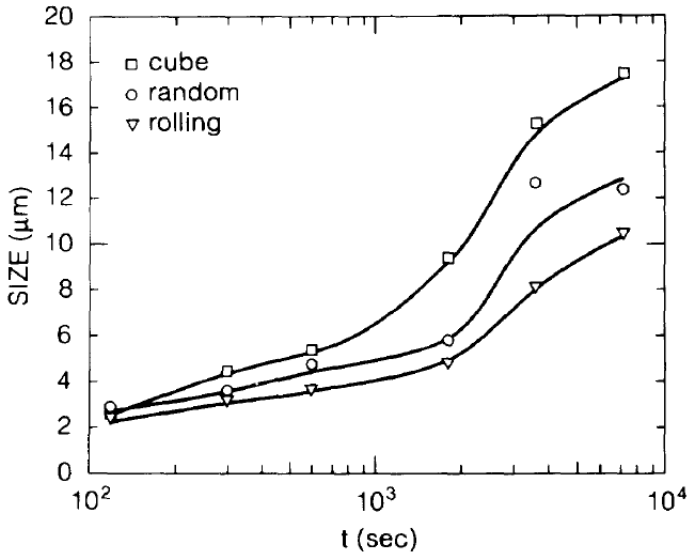

Figure 5.6: Evolution of average grain size for different recrystallization texture components after cold rolling and subsequent annealing of an AA1050(Fe-0.32%, Si-0.15%) type alloy. [12]

The growth rates for different texture components during recrystallization have been analyzed by several researchers [12, 62]. For a cold rolled aluminum alloy, Juul Jensen observed a behavior similar to those presented in Fig. 4.37 , as shown in Fig 5.6. Recrystallized Cube grains exhibit a strong growth preference at low annealing temperatures. However, as the annealing temperature is increased, the growth advantage for recrystallized cube grains is diminished. Thus the overall cube texture in hot rolled AA1050 and AA5005 is in part due to contributions from oriented nucleation (high volume fraction of cube recrystallized grains) and oriented growth (growth advantage to recrystallized cube grains). This growth advantage for cube grains can also be understood in terms of orientation pinning. The overall volume fraction of cube component in the deformed state is very low < 5%. The cube subgrains after reaching a critical size are surrounded by grains of rolling orientations (β-fiber orientations). They have a high angle misorientation with the rolling components and are thus able to grow more than other components. The recrystallized grains of rolling orientations surrounded by deformed matrix of similar orientation, therefore they are pinned by low angle grain boundaries and have smaller size compared to cube recrystallized grains [62]. Further analysis of these issues has been carried out by A. Brahme [63].

A comparison between Oriented Nucleation (ON) and Oriented Growth (OG) indicates that, while OG is present mainly at low annealing temperatures and as the temperatures is increased, the growth advantage for a particular component (Cube) diminishes, ON is present at all annealing temperatures. This behavior suggests that of the two mechanisms ON and OG, ON plays a more important role in the final texture evolution of hot rolled aluminum alloys. An analysis by Brahme [63], using Monte Carlo simulations, on texture evolution in AA1050 also revealed ON to play a more important role than OG.

5.4 AA1050 and AA5005

The main difference between the two hot rolled alloys AA1050 and AA5005 is the higher concentration of Mg in AA5005. The use of AA5005 was therefore, to study the effect of Mg addition on recrystallization kinetics and texture evolution in commercial purity aluminum alloys. Mg is usually present as a solid solution at these concentrations [6]. The presence of Mg in Al increases the overall strain in the Al matrix which hinders the motion of dislocations. This difficulty in dislocation motion is shown by higher microhardness values of deformed and annealed AA5005 samples as compared to AA1050. The microhardness values were typically higher by a factor of 1.5 in AA5005. Another important effect of presence of Mg in Al is that it increases the stored energy in AA5005. A comparison of JMAK exponents for AA1050 and AA5005 is shown in Table 5.4.

Temperature (^oC)	AA1050	AA5005
325	1.45	-
350	1.09	1.09
375	1.08	1.99
400	1.35	2.67

Table 5.4: JMAK exponents in AA1050 and AA5005 obtained from OIM.

The JMAK exponents in Table 5.4 show that while recrystallization in AA1050 remains isokinetic, the mechanism changes from grain boundary nucleation to grain edge nucleation to grain corner nucleation in AA5005, as derived by Cahn [42]. This variation in mechanism can

be understood in terms of stored energy in the two alloys. In AA5005, higher stored energy leads to faster kinetics and the activation of a higher density of nucleation sites. Therefore recrystallization approaches random nucleation conditions. In AA1050, with relatively low stored energy, only grain boundary nucleation is the dominant mechanism, thus low Avrami exponents are obtained. Higher stored energy in AA5005 is also evidenced from the higher average deformed grain GOS values, shown in Fig. 4.40 and 4.41.

Texture evolution in AA1050 and AA5005 is very similar. Cube recrystallized grains are observed to nucleate from deformed cube grains. The growth rate advantage of cube recrystallized grains is only present at 350^oC in AA5005. This indicates oriented nucleation and oriented growth to be simultaneously operative. At higher temperatures, all recrystallized grains have similar growth rates which suggests that ON is more dominant than OG.

6 Future Work

The two most important goals of this project were to develop methods based on Orientation Imaging Microscopy (OIM) for analysis of recrystallization kinetics and texture evolution, and to provide much needed experimental information for simulations of recrystallization kinetics in hot rolled Aluminum Alloys. These goals were successfully achieved by the development Grain Orientation Spread (GOS) and Grain Average Misorientation (GAM) based algorithms. The ability to distinguish and partition deformed and recrystallized grains enabled independent analysis of the regions and provided important insight into the nucleation of Cube oriented grains during recrystallization. The majority of the work was carried out on AA1050 and some analysis was performed for AA5005. The GOS based approach was successfully applied to both alloys to characterize microstructural and textural evolution.

Some of the important results obtained from the current analysis can be summarized as follows:

1. The deformation microstructure consists of elongated grains and the deformation texture is the predominantly the β-fiber.

2. Recrystallization in hot rolled aluminum alloys is controlled by migration of high angle boundaries.

3. Recrystallized grains nucleate at or near grain boundaries between the elongated grains.

4. The recrystallization texture consists mainly of the Cube texture components which nucleates from the deformed bands of Cube orientation that have survived deformation.

5. Of the various orientations present in the deformed regions, the S and copper orientations are found to favor growth of Cube grains while the brass orientation is relatively stable to annealing treatments.

6. No significant differences were observed between AA1050 and AA5005 in terms of texture evolution and nucleation of recrystallized Cube grains.

Based on these results, a few suggestions are presented here for future research projects. Although most of the results for AA1050 and AA5005 were very similar, there were some differences between the two alloys. The differences were predominantly in recrystallization kinetics and the grain size evolution. One of the reasons for these differences might be the different (thicknesses) strains in the two alloys. Therefore, to understand fully the effect of Mg addition in commercial purity alloys, samples with very similar processing conditions should be used. Similarly if the as-received samples at different stages of deformation are studied, they could provide some valuable information about the effect of different deformation parameters such as strain, strain rate and temperature on recrystallization kinetics and texture evolution. It would be most advisable to use samples at the last stages of hot rolling so that grains have undergone sufficient deformation to be captured in a single scan.

Another important area where this method can be immediately applied is the analysis of cold rolled samples. GOS of 3^o and GAM of 1^o were found sufficient in case of hot rolled samples. GOS and GAM values for cold rolled samples are also expected to be the same. An important topic for the analysis of cold rolled samples would be the variation in GOS and GAM on grain by grain basis. Since recovery in as-received samples will be minimal, actual variation in GOS and GAM of deformed grains of different orientation could be followed with annealing time and temperature, thus allowing recovery estimations based on OIM only.

Recovery analysis for hot rolled samples was not very successful in the present analysis. Although an algorithm was proposed and some similarities were obtained in the variation of the hardness of deformed grains and their grains GOS values, the results obtained so far lacked statistical validity. Some experiments could be designed to analyze the variation in recovery from GOS values by using more strained samples and annealing them at very low temperatures. Nano Indentation is expected to provide significantly better results in this regard. The ability to control the load and the size of indentation in nano indentation can be used obtain hardness of a particular orientation in deformed grains. Performing a series of such tests at different annealing times and temperature will provide much more information about recovery than could be obtained from microhardness. This method could also be used for cold rolled materials.

Bibliography

[1] J. Christian, *The theory of transformations in metals and alloys*, p. 542. New York: Pergamon, 2 ed.

[2] R. D. Doherty, D. A. Hughes, F. J. Humphreys, J. J. Jonas, D. J. Jensen, M. E. Kassner, W. E. King, T. R. McNelley, H. J. McQueen and A. D. Rollett, *Materials Science and Engineering*, vol. A238, pp. 219–274, 1997.

[3] I. Samajdar, P. Ratchev, B. Verlinden and E. Aernoudt, *Acta Materialia*, vol. 49(10), pp. 1759–1769, 2001.

[4] K. Lucke and O. Engler, *Materials Science and Technology*, vol. 6, pp. 1113–1130, 1990.

[5] S. Endou and H. Inagaki, *Zeitschrift für Metallkunde*, vol. 93, no. 2, pp. 106–116, 2002.

[6] F. J. Humphreys and M. Hatherly, *Recrystallization and related annealing phenomena*. London: Pergamon Press, 2002.

[7] P. Yang and O. Engler, in *Proceedings of the 16th Riso International Symposium on Materials Science: Microstructural and Crystallographic Aspects of Recrystallization* (Y. L. N. Hansen, D. Juul Jensen and B. Ralph, eds.), pp. 595–602, 1995.

[8] H. E. Vatne, T. Furu and E. Nes, *Materials Science and Technology*, vol. 12, pp. 201–210, 1996.

[9] D. R. Waryoba and P. N. Kalu, "Quantification of recrystallization kinetics in heavily drawn OFHC copper wires by microhardness technique," in *Proc. ASME Int'l Mech. Eng. Congress and Expo. (IMECE'03)*, (Washington D.C.), November 2003.

[10] A. O. Humphreys and F. J. Humphreys, in *International Conference of Aluminum Alloys 4* (T. Sanders and E. Starke, eds.), (Atlanta, Georgia, USA), pp. 222–228, Georgia Inst. of Tech., 1994.

[11] R. A. Vandermeer, *Acta Materialia*, vol. 55, no. 3, pp. 1449–1457, 2005.

[12] D. J. Jensen, *Acta Metallugica et Materialia*, vol. 43(11), pp. 4117–4129, 1995.

[13] H. J. McQueen, *Journal of Materials*, pp. 28–33, 1998.

[14] B. Bay, N. Hansen, D. A. Hughes and D. Kuhlmann-Wilsdorf, *Acta Metallurgica et Materialia*, vol. 40, no. 2, pp. 205–219, 1992.

[15] D. A. Hughes and N. Hansen, in *Advances in Hot deformation Textures and Microstructures* (J. J. Jonas, T. R. Bieler and K. J. Bowman, eds.), pp. 427–444, TMS, Warrendale, 1993.

[16] D. Juul Jensen, M. T. Lyttle and N. Hansen, in *Hot deformation of Aluminum Alloys II* (T. R. Bieler, L. A. Lalli and S. R. MacEwen , eds.), pp. 9–21, 1998.

[17] P. Hollinshead, *Materials Science and Technology*, vol. 8, pp. 57–62, 1992.

[18] A. Bardal, I. Lindseth, H. E. Vatne and E. Nes, in *Proceedings of the 16th Riso International Symposium on Materials Science: Microstructural and Crystallographic Aspects of Recrystallization* (Y. L. N. Hansen, D. Juul Jensen and B. Ralph, eds.), pp. 261–266, 1995.

[19] H. E. Vatne, S. Hofmann, A. Bardal and E. Nes, in *Proceedings of International Conference on Strength of Materials 10* (Oikawa, ed.), pp. 255–258, 1994.

[20] S. Panchanadeeswaran and D. P. Field, *Acta Metallurgica et Materialia*, vol. 43, no. 4, pp. 1683–1692, 1995.

[21] M. Koizumi, S. Kohara and H. Inagaki, *Zeitschrift für Metallkunde*, vol. 91, no. 1, pp. 88–96, 2000.

[22] M. Koizumi, S. Kohara and H. Inagaki, *Zeitschrift für Metallkunde*, vol. 88, no. 7, pp. 576–582, 1997.

[23] M. Koizumi, T. Saitou and H. Inagaki, in *Proceeding of 12th International Conference on Textures of Materials* (J. A. Szpunar, ed.), pp. 848–853, 1999.

[24] H. E. Vatne, O. Daaland and E. Nes, *Materials Science Forum*, vol. 157-162, pp. 1087–1092, 1994.

[25] H. E. Vatne, R. Shahani and E. Nes, *Acta Materialia*, vol. 44, no. 11, pp. 4447–4462, 1996.

[26] S. P. Chen, T. Zuidwijk and S. V. Zwaag, in *Recrystallization and grain growth, Proceedings of the first joint international conference* (G. Gottstein and D. A. Molodov, eds.), pp. 821–830, Springer-Verlag, 2001.

[27] C. M. Sellars, A. M. Irisarri and E. S. Puchi, in *Microstructural Control in Aluminum Alloys: Deformation, Recovery and Recrystallization* (E. H. Chia and H. J. McQueen, eds.), (Warrendale), pp. 179–196, TMS, 1985.

[28] R. A. Vandemeer and D. J. Jensen, *Acta Materialia*, vol. 49, pp. 2083–2094, 2001.

[29] R. A. Vandemeer and D. J. Jensen, *Acta Materialia*, vol. 51, pp. 3005–3018, 2003.

[30] R. A. Vandemeer and D. J. Jensen, *Interface Science*, vol. 6, pp. 95–104, 1998.

[31] H. Weiland, in *Proceedings of the 16th Riso International Symposium on Materials Science: Microstructural and Crystallographic Aspects of Recrystallization* (Y. L. N. Hansen, D. Juul Jensen and B. Ralph, eds.), pp. 215–228, 1995.

[32] O. Engler, H. E. Vatne and E. Nes, *Materials Science and Engineering A*, vol. 205, pp. 187–198, 1996.

[33] R. K. Bolingbroke, G. J. Marshall and R. A. Ricks, in *Proceedings of the 16th Riso International Symposium on Materials Science: Microstructural and Crystallographic Aspects of Recrystallization* (Y. L. N. Hansen, D. Juul Jensen and B. Ralph, eds.), pp. 281–287, 1995.

[34] R. K. Bolingbroke, G. J. Marshall and R. A. Ricks, in *Proceedings of the 10th International Conference on textures of Materials* (H. J. Bunge, ed.), pp. 1145–1152, 1993.

[35] C. I. Maurice and J. H. Driver, *Acta Materialia*, vol. 45, no. 11, pp. 4627–4638, 1997.

[36] K. D. Vernon-Parry, T. Furu, D.J. Jensen and F. J. Humphreys, *Materials Science and Technology*, vol. 12, pp. 889–896, 1996.

[37] C. I. Maurice and J. H. Driver, *Materials Science Forum*, vol. 157-162, pp. 807–812, 1994.

[38] J. H. Driver, M.C. Theyssier and C.I. Maurice, *Materials Science and Technology*, vol. 12, pp. 851–858, 1996.

[39] R. D. Doherty, L. C. Chen and I. Samajdar, *Materials Science and Engineering A*, vol. A257, pp. 18–36, 1998.

[40] I. Samajdar and R. D. Doherty, *Acta Materialia*, vol. 46, no. 9, pp. 3145–3158, 1998.

[41] S. P. Chen. et al., *Journal of Materials Science*, vol. 37, pp. 989–995, 2002.

[42] J. W. Cahn, *Acta Metallurgica*, vol. 4, pp. 449–459, 1956.

[43] V. Randle and O. Engler, *An Introduction to Macrotexture, Microtexture and Orientation Mapping*. Gordon and Breach, London, 2000.

[44] R. A. Vandermeer and B. B. Rath, *Metallurgical Transactions A*, vol. 20A, pp. 391–401, 1989.

[45] R. A. Vandermeer and R. A. Masumura, *Acta Metallurgica et Materialia*, vol. 40, no. 4, pp. 877–886, 1992.

[46] J. Gurland, *Transactions of The Metallurgical Society of AIME*, vol. 228, pp. 452–456, 1958.

[47] J. Gurland, *Transactions of The Metallurgical Society of AIME*, vol. 236, pp. 642–646, 1966.

[48] R. A. Vandermeer and D. J. Jensen, *Materials Science Forum*, vol. 467-470, pp. 193–196, 2004.

[49] J. W. Cahn and W. C. Hagel, ch. Decomposition of Austenite by Diffusional Processes, p. 131. Interscience Publ., 1962.

[50] R. A. Vandermeer and D. J. Jensen, *Scripta Metallurgica et Materialia*, vol. 30, no. 12, p. 15751580, 1994.

[51] J. C. Glez and J. H. Driver, *Journal of Applied crystallography*, vol. 34, pp. 280–288, 2001.

[52] J. M. Humbert, N. Gey and C. Esling, *Journal of Applied Crystallography*, vol. 29, pp. 662–666, 1996.

[53] D. J. Srolovitz, M. P. Anderson, P. S. Sahni and G. S. Grest, *Acta Metallurgica*, vol. 32, no. 5, pp. 793–802, 1984.

[54] S. P. Chen , I. Todd amd S. Van Der Zwagg, *Metallurgical and Materials Transactions A*, vol. 33A, pp. 529–537, 2002.

[55] S. Wright, in 12^{th} *International Conference on Texture of Materials* (J. Szpunar, ed.), pp. 104–110, CRC Press, 1999.

[56] A. D. Rollett, D. J. Srolovitz, R. D. Doherty and M. P. Anderson, *Acta Metallurgica*, vol. 37, no. 2, pp. 627–639, 1989.

[57] J. R. Hirsch, in *Recrystallization '90* (T. Chandra, ed.), (Warrendale), pp. 759–768, TMS, 1990.

[58] O. D. Sherby, A. Goldberg and O. A. Ruano, *Philosophical Magazine*, vol. 84, no. 23, pp. 2417–2434, 2004.

[59] B. S. Bokstein *Materials Science Forum*, vol. 217-222, pp. 685–688, 1996.

[60] S. J. Rothman, N. L. Peterson, L. J. Nowicki, and L. C. Robinson,*Physica Status Solidi B*, vol. 63, p. K29, 1974.

[61] J. Hirsch, *Materials Science and Technology*, vol. 6, pp. 1048–1057, 1990.

[62] O. Engler, *Acta Materialia*, vol. 46, no. 5, pp. 1555–1568, 1998.

[63] A. Brahme. PhD thesis, Carnegie Mellon University, August 2005.

[64] P. Trimby, A. Day, K. Mehnert and N. H. Schmidt, *Journal of Microscopy*, vol. 205, no. 3, pp. 259–269, 2001.

[65] H. Jazaeri and F. J. Humphreys, *Journal of Microscopy*, vol. 213, no. 3, pp. 241–246, 2003.

[66] S. H. Choi and Y. S. Jin, *Materials Science and Engineering A*, vol. 371, pp. 149–159, 2004.

[67] P. Gerber, J. Tarasiuk, T. Chauveau and B. Bacroix, *Acta Materialia*, vol. 51, pp. 6359–6371, 2003.

[68] D. J. Jensen, *Materials Science and Technology*, vol. 16, pp. 1360–1363, 2000.

[69] A. D. Rollett, *Advanced Characterization and Microstructural Analysis: Lecture Notes*. Materials Science and Engineering, CMU, Spring 2003.

[70] A.D. Rollett, M. L. Taheri and B. S. El-Dasher, in *Plasticity'02:The 9th Intl. Symposium on Plasticity and its Current Applications* (A. S. Khan and O. Lopez-Pamies, eds.), (Fulton, MD), pp. 42–46, NEAT Press, Fulton, MD, 2002.

[71] M. H. Alvi, B. S. El-Dasher and A. D. Rollett, in *Hot Deformation of Aluminum Alloys III* (Z. Jin, A. Beaudoin, T. Bieler and B. Radhakrishnan , eds.), (Warrendale), pp. 3–12, TMS, 2003.

Appendix A Orientation Imaging Microscopy

Orientation Imaging Microscopy (OIM) is an advanced microstructural analysis technique which uses the Electron Backscattered Diffraction (EBSD) patterns obtained in a Scanning Electron Microscope (SEM) to obtain crystallographic orientation information from a material. The use of OIM in microstructural characterization and texture analysis of metals and ceramics has increased strongly in the last few decades. This is mainly attributed to the advances in hardware and software development. The speed of data acquisition has increased from 1000-2000 points hr^{-1} in the early EBSD systems to approximately 80000 points hr^{-1} in most modern systems [64]. The use of the Field Emission Gun SEM (FEGSEM) for obtaining EBSD patterns has considerably improved the spatial resolution [65]. The simple sample preparation, ease of use and the possibility to cover large sample areas in shorter times have contributed to the increasing popularity of OIM.

The microstructural and microtextural characterization of metals and alloys has been one of the major application areas of OIM. The changes in microstructures and textures as a result of different transformations (phase transformation and recrystallization) and processing (rolling and extrusion) routes have been successfully analyzed by the use of OIM [66, 67]. A large number of single phase fcc alloys including Aluminum, Copper, Nickel etc. have been studied for microstructural and textural evolution during deformation and recrystallization of the metals. Of the particular interest is the application of OIM in characterizing the deformed state of rolled metals consisting of a cell and subgrain structure and the ability to identify the nucleation and growth mechanisms from the orientations of deformed and recrystallized grains [68].

A.1 Components and working of an EBSD system

A typical EBSD system consists of three major components:-

- A SEM unit for image analysis of sample and for generating the electron backscattered diffraction patterns.
- A Charge Coupled Device (CCD) camera for capturing the diffraction patterns from sample surface.

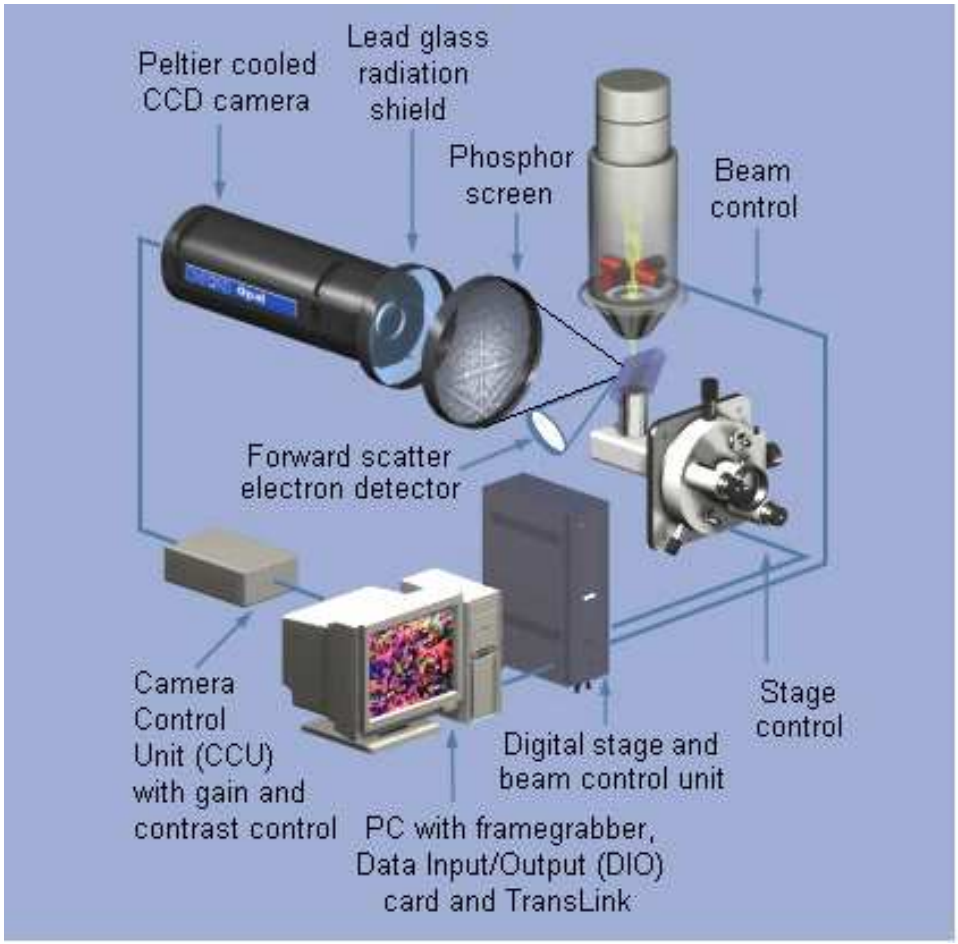

Figure A.1: Schematic view of the major components in an EBSD system

- A work station for analyzing and storing the information generated at each sampling point of the sample surface. A schematic view of the major components of an EBSD system is shown in Fig. A.1 [69].

The working principle of an EBSD system can be described in the following way; as the electron beam strikes the sample surface of a tilted sample ($60 - 70^{o}$), diffraction patterns (similar to Kikuchi patterns in TEM) are generated due to the elastic scattering of electrons from the lattice planes. These patterns are intensified as the scattered electrons undergo further scattering at the other lattice planes, giving a distinct arrangement of parallel lines (bands) for each set of lattice planes. The width and intersection of bands provide all the information needed regarding the crystallographic orientation of the sample volume being analyzed [43]. An EBSD system can be operated in two modes: manual and automatic. The manual method involves the

selection of sampling location on the sample by the operator where as in the automatic mode, sampling locations are pre-programmed and are located by beam or stage control in the microscope. An orientation map of the sample surface can be generated by plotting the orientation of each sampling point obtained from the automated EBSD analysis on a grid of points whose spacing is much finer than the grain size.

A.2 Data analysis

The orientation of each point obtained from the Kikuchi patterns is stored in the form of the Bunge Euler angles (ϕ_1, Φ, ϕ_2) along with the spatial coordinates of the point, the pattern quality and confidence indexes. The Bunge Euler angles represent the rotation necessary for making crystal coordinates coincident with the sample coordinates. The orientation of each point along with its spatial coordinates can be used for further analysis including grain orientation and grain boundary analysis.

Grains in OIM maps are defined as the sets of connected and similarly oriented points. The neighbors of each point in a grain as checked to see if they are within the grain tolerance angle of the given point. If a point is found to be within the tolerance angles, its neighbors are than checked. The procedure is repeated over and over again until all the points in the scan are assigned to different grains. This is known as a "Burn" algorithm. The definition of a grain in an OIM map can be varied by the user by varying the values of the grain tolerance angle and the minimum number of points (pixels) in a grain [69].

A grain boundary in OIM is defined as the line segment separating two measurements points in a scan [69]. Five independent parameters are needed to completely describe a boundary. These are the three parameters for describing the boundary misorientation and two parameters for describing the boundary plane normal. The difference between the orientation of a point and the misorientation between points is that, while an external sample coordinate system is used in describing the orientation of a point, the crystal coordinates of another point are used for describing the misorientation between points. Misorientation calculations are conveniently performed by considering the orientations of the points in matrix form. The matrix form for

orientation or misorientation can be obtained from the Euler angles as:

$$\begin{pmatrix} \cos\phi_1 \cos\phi_2 - \sin\phi_1 \sin\phi_2 \cos\Phi & \sin\phi_1 \cos\phi_2 + \cos\phi_1 \sin\phi_2 \cos\Phi & \sin\phi_2 \sin\Phi \\ -\cos\phi_1 \sin\phi_2 - \sin\phi_1 \cos\phi_2 \cos\Phi & -\sin\phi_1 \sin\phi_2 + \cos\phi_1 \cos\phi_2 \cos\Phi & \cos\phi_2 \sin\Phi \\ \sin\phi_2 \sin\Phi & \cos\phi_2 \sin\Phi & \cos\Phi \end{pmatrix}$$

The misorientation between two points A and B having orientations g_A and g_B can be obtained as:

$$\Delta g = g_B g_A^{-1} = g_B g_A^T \tag{A.1}$$

The symmetry of the crystal lattice will lead to formation of symmetrically equivalent misorientations which can be represented mathematically as :

$$\Delta g = g_B g_A^T = C_i^B g_B (C_j^A g_A)^T = C_i^B g_B g_A^T C_j^{A^T} \tag{A.2}$$

For the case of cubic crystal symmetry having 24 symmetry operators, 1152 symmetrically equivalent misorientations are obtained. A misorientation corresponding to the minimum misorientation angle between the points A and B of the 1152 symmetrically equivalent orientations is chosen as the physically meaningful value. In some cases, the misorientation axis is chosen as the one lying in a particular unit triangle (SST).

Appendix B Recrystallization kinetics from IQ and CI method

This section describes a previous partitioning method, superceded by the GOS approach. The annealed and polished samples were scanned after the micro-hardness test to obtain the orientation information of samples. The orientation information of samples annealed for different time intervals (t) was used to calculate fraction recrystallized (X). In this technique, a focused electron beam is used to scan a sample surface on a regular grid of points. An Electron Backscatter Diffraction Pattern (EBSP) is captured for each point, and this pattern is subsequently indexed to determine the orientation of the crystal at that grid position. The Image Quality (IQ) and Confidence Index (CI), which represent the contrast in the pattern and confidence of the OIM software of indexing the pattern correctly, are also obtained during the scanning of sample surface. The fraction recrystallized of an annealed sample is calculated from criteria based upon CI and IQ values for the scanned sample. The IQ and CI values for determining the candidacy of a particular point for recrystallized or deformed region are selected independently for each scan [70]. The values of fraction recrystallized are significantly affected by the microstructural heterogeneity of scanned regions.

The critical CI value used to get a pattern with sufficient confidence was set at 0.1. This value is obtained from past experience of the transition between well-indexed and poorly-indexed points occuring at 0.1. A second criterion was based on the IQ value for the scanned surfaces. The threshold IQ value was chosen to be the average IQ of all the points with a CI value less than 0.1. The final criterion, based on a neighbor correlation, was applied in order to ensure that the final microstructure was physically reasonable. This allowed a point to be considered recrystallized if it has at least four recrystallized nearest neighbors, or three of its neighbors are within 3^o of the same orientation. This can be expressed as:

$$\forall p \in S, p \in U \; iff \{IQ_p < IQ_{thres}, CI_p < 0.1, n_p < 4\} \tag{B.1}$$

where p is any data point in the set S of all OIM data points, U is the set of all unrecrystallized points, IQ_p is the image quality value of point p, IQ_{thres} is the average IQ of all points with a

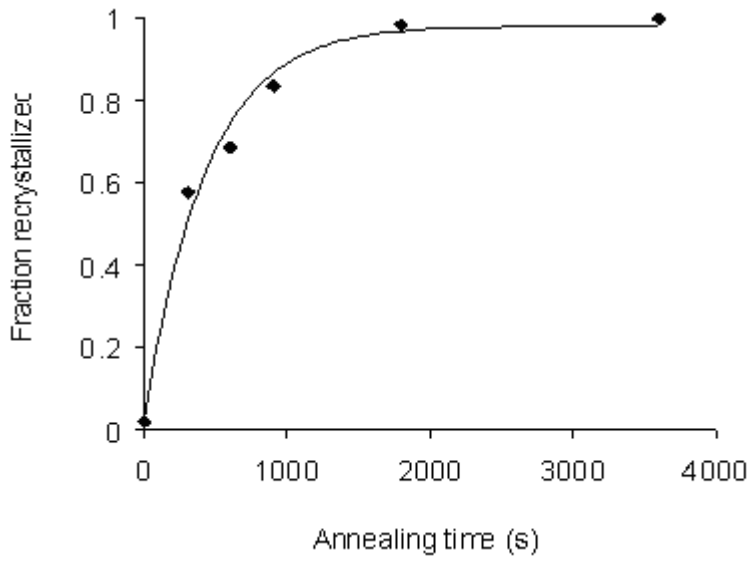

Figure B.1: Variation of fraction recrystallized obtained from critical CI & IQ values for samples annealed isothermally at 350^oC.

$CI < 0.1$, CI_p is the confidence index of point p, n_p is the number of neighbors of p whose IQ and CI are greater than 0.1 and IQ_{thres} respectively [70].

Based on the above criteria, an estimate of the recrystallized fraction was obtained for each scan during the analysis as shown in Fig. 3.10 at 350^oC.

The JMAK exponents obtained for recrystallization kinetics are similar to those obtained from microhardness variations, which suggests that the method based on IQ and CI values of a scan is successful. The small differences can be attributed to the limited scan size of each sample. The micro-hardness data represents an average behavior for recrystallization kinetics, whereas the data obtained from OIM are from limited areas [71]. Although this method yields results that are close to those obtained from other methods, it requires a significant input from the operator as the cut-off value of IQ is different for each scan and is also dependent on the sample preparation technique. These limitations make the application of this approach difficult for an analysis consisting large number of scans and when a number of scans are obtained from each sample. A new method based on intragranular orientation spread overcomes these limitations as described in the body of the thesis.

Appendix C Computer Program

```
program grainsp3
c changes made in the program - date 08/25/2004
c combined copper and dillamore orientations
c the maximum,minimum and average GOS values obtained
c for each component
c deformed neighbors of cube bands looked at
c changed the rotated cube components
c .exe file grainsp7
c changed the ang file to identify the cube rex. grains
c and its deformed neighbors only

c date - 10/29/04
c changes made in the program
c calculated the interfacial area per unit volume -sv
c calculated the grain size of recrystallized grains -gs
c calculated the boundary pixels shared in terms of the
c grain contiguity ratios for recrystallized grains and grains of each texture compo
c grain size is calculated by multiplying the number of pixels
c with step size square and a factor for sqrt(3/2) for hex grid.
c the equivalent diameter is calculated.
c (11/15/04) also calculated the max,ave,min rex. grain size
c and the grainsizes for rex. grain sizes for different texture components
c       02/09/2005 changed the definition of contiguity ratio and included the
c       calculations of the grain size

implicit none
character(50) filein, fileout, top
integer count,grain,id(350000),p,cpix,u,index,n
integer tindex,graintex(12000),tempid,vs(350000)
integer gcur,rg,c,gpix(12000)
real goscut,odf(350000,7),step,sgs,np,phi(3,350000)
real q(4,350000),qq(4,2),thetamin,theta,gg(10000),thetasprd(12000)
real thetasp,phib1,phib,phib2,phic1(12000),phic(12000),rxpix,pix
real phic2(12000),dftex(5),rxtex(5),d(5,5),r(5,5),disormax,dfpix
real disormin,disorav,disor(12000),frarex,texcom(5),aodf(350000,7)
integer bp(12000),ng(12000,12000),rbp(5),ph(350000),rb,inde
integer pdcom(5),prcom(5),i,j,g,td,tr,tex1,gn,texrg,texrg2,texdf
real dgos(5),rgos(5),maxgos(5),mingos(5),x,y,t,infarea(5)
real sv,gs(12000),rv,area,rgc,grpix,pi,gamcut
real maxpix,minpix,avgpix,maxpixtc(5),minpixtc(5),avgpixtc(5)
integer texnrg(5)
real rinfarea(5),dinfarea(5),exinfarea(5),fxa(5,5),fxb(5,5)
real exd(5,5),exr(5,5),dx,dy,dis,ang,th,cgam(12000),bgam,am(10000)
```

```
write(*,*) 'Input  Grain ID file to be analyzed'
read(*,*) filein
c write(*,*) 'Name for the output files'
c read(*,*) fileout

inde=20
do 15, i=20,1,-1
c write(*,*) 'i,fname2(i:i) ',i,fname2(i:i)
if(filein(i:i).eq.' ') inde=i
15 continue
inde=inde-1

pi=3.1416
goscut=3.0
gamcut=1.0
count=0

open(unit=1,file=filein(1:inde)//'.txt',status='old')
101 continue
read(1,*) top
if (top.eq.'#') then
count=count+1
goto 101
end if
close(1)
102 continue
open(unit=1,file=filein(1:inde)//'.txt',status='old')

do i=1,count
read(1,*) top
end do

pix=1
grain=1

103 read(1,*,end=104) odf(pix,1),odf(pix,2),odf(pix,3),odf(pix,4),
     &odf(pix,5),odf(pix,6),odf(pix,7),id(pix)
p=id(pix)
if(p.gt.grain) grain=p
pix=pix+1
goto 103
104 continue
close(1)
```

```
step=odf(2,4)-odf(1,4)

pix=pix-1
write(*,*) 'total pixels in scan', pix
write(*,*) 'total grains in scan', grain
write(*,*) 'step size used in scan', step

sgs=2.5
np=3.63*((sgs*sgs)/(step*step))
cpix=int(np)+1

area=(odf(pix,4)-odf(1,4))*(odf(pix,5)-odf(1,5))

write(*,*) 'number of pixels per grains', cpix

do i=1,grain
gpix(i)=0
end do


do i=1,pix
u=id(i)
if (u.gt.0) then
gpix(u)=gpix(u)+1
end if
end do

do g=1,grain
if(gpix(g).gt.1) then
c write(*,*) 'Grain being analyzed', g
c write(*,*)'number of pixels',gpix(g)
p=1
do i=1,pix
if(id(i).eq.g) then
phi(1,p)=odf(i,1)
phi(2,p)=odf(i,2)
phi(3,p)=odf(i,3)
q(1,p)=sin(phi(2,p)/2)*cos((phi(1,p)-phi(3,p))/2)
q(2,p)=sin(phi(2,p)/2)*sin((phi(1,p)-phi(3,p))/2)
q(3,p)=cos(phi(2,p)/2)*sin((phi(1,p)+phi(3,p))/2)
q(4,p)=cos(phi(2,p)/2)*cos((phi(1,p)+phi(3,p))/2)
if (p.eq.gpix(g)) goto 105
p=p+1
end if
end do
```

```
105 continue

do i=1,gpix(g)-1
theta=0
do j=i+1,gpix(g)
qq(1,1)=q(1,i)
qq(2,1)=q(2,i)
qq(3,1)=q(3,i)
qq(4,1)=q(4,i)
qq(1,2)=q(1,j)
qq(2,2)=q(2,j)
qq(3,2)=q(3,j)
qq(4,2)=q(4,j)

call misquat(qq,thetamin)
theta=theta+thetamin
end do

theta=theta/(gpix(g)-i)
gg(i)= theta
end do

t=0
do i=1,gpix(g)-1
t=gg(i)+t
end do

disor(g)=t/(gpix(g)-1)
c write(*,*)'gos',disor(g)

c       gam calculation
do i=1,p
th=0
n=0
do j=1,p
if(i.ne.j) then
dx=(odf(i,4)-odf(j,4))
dy=(odf(i,5)-odf(j,5))
dis=sqrt(dx*dx+dy*dy)
c write(*,*) dis

if(abs(dis-step).lt.(0.1*step))then
qq(1,1)=q(1,i)
qq(2,1)=q(2,i)
qq(3,1)=q(3,i)
```

```
qq(4,1)=q(4,i)
qq(1,2)=q(1,j)
qq(2,2)=q(2,j)
qq(3,2)=q(3,j)
qq(4,2)=q(4,j)
n=n+1

call misquat(qq,ang)
th=th+ang
end if
end if
end do
am(i)=th/n
end do

do i=1,p
bgam=bgam+am(i)
end do
bgam=bgam/p
cgam(g)=bgam
write(*,*)g,gpix(g),bgam,disor(g)

c average orientation calculation
call averageorientation(q,p,index,thetasp,phib1,phib,phib2)
thetasprd(g)=thetasp
phic1(g)=phib1
phic(g)=phib
phic2(g)=phib2

do
if(phic1(g).le.2*pi) exit
phic1(g)=phic1(g)-2*pi
end do
do
                if(phic(g).le.2*pi) exit
                        phic(g)=phic(g)-2*pi
          end do
do
                if(phic1(g).le.2*pi) exit
                        phic2(g)=phic2(g)-2*pi
          end do

c texture determination
call quattex(phib1,phib,phib2,tindex)
```

```
if(tindex.eq.1.or.tindex.eq.2.or.tindex.eq.3.or.tindex.eq.4)then
graintex(g)=1
end if
if(tindex.eq.5) graintex(g)=2
if(tindex.eq.6) graintex(g)=3
if(tindex.eq.7) graintex(g)=4
if(tindex.eq.8) graintex(g)=5
end if
c main program ends here
end do


c write(*,*)'texture of grain',graintex(i)
do i=1,5
texcom(i)=0
end do

do i=1,grain
do j=1,5
if(graintex(i).eq.j) then
texcom(j)=texcom(j)+gpix(i)
end if
end do
end do

c average,max,min,gos determination
do i=1,5
dgos(i)=0
rgos(i)=0
pdcom(i)=0
prcom(i)=0
maxgos(i)=0
mingos(i)=30
end do

do i=1,grain
if (cgam(i).gt.gamcut)then
do j=1,5
tex1=graintex(i)
if (disor(i).gt.maxgos(tex1)) maxgos(tex1)=disor(i)
          if (disor(i).lt.mingos(tex1)) mingos(tex1)=disor(i)
if (graintex(i).eq.j)then
dgos(j)=dgos(j)+(disor(i)*gpix(i))
pdcom(j)=pdcom(j)+gpix(i)
end if
```

```
end do
elseif (cgam(i).le.gamcut.and.cgam(i).gt.0.and.
     &gpix(i).ge.cpix)then
do j=1,5
                if (graintex(i).eq.j)then
                        rgos(j)=rgos(j)+(disor(i)*gpix(i))
                        prcom(j)=prcom(j)+gpix(i)
                end if
                end do
end if
end do

do i=1,5
dgos(i)=dgos(i)/pdcom(i)
rgos(i)=rgos(i)/prcom(i)
end do

do i=1,grain
do j=1,grain
ng(i,j)=0
end do
end do

do i=1,grain
tempid=0
do j=1,pix
gcur=id(j)
if(gcur.eq.i)then
if(tempid.ne.0.and.tempid.ne.i.and.(odf(j,4)-
     &odf(j-1,4)).eq.step)then
ng(i,tempid)=ng(i,tempid)+1
end if
elseif(gcur.ne.i)then
if(tempid.eq.i.and.(odf(j,4)-odf(j-1,4)).eq.step)then
ng(i,gcur)=ng(i,gcur)+1
end if
end if
tempid=gcur
end do
end do

do i=1,grain
bp(i)=0
end do
```

```
do i=1,grain
do j=1,grain
bp(i)=bp(i)+ng(i,j)
end do
end do

do i=1,5
dftex(i)=0
rxtex(i)=0
end do

do i=1,grain
   if(cgam(i).le.gamcut.and.cgam(i).gt.0.and.
     &gpix(i).ge.cpix)then
tr=graintex(i)
rxtex(tr)=rxtex(tr)+gpix(i)
   else
if(gpix(i).gt.1) then
td=graintex(i)
dftex(td)=dftex(td)+gpix(i)
end if
end if
end do

do i=1,5
do j=1,5
d(i,j)=0
r(i,j)=0
end do
infarea(i)=0
end do

c determining the interfacial area/vol for recrystallized grains
c sv-interfacial area in contact with deformed grains
c rv-interfacial area in contact with rex grains
c rbp-total boundary pixels for that rex component
sv=0
rv=0
do i=1,grain
if (cgam(i).le.gamcut.and.cgam(i).gt.0.and.gpix(i).ge.cpix)then
texrg=graintex(i)
do j=1,grain
if (ng(i,j).ne.0) then
if (gpix(j).gt.1) then
if (cgam(j).gt.0.and.cgam(j).le.gamcut.and.gpix(j).ge.cpix)then
```

```
rv=rv+ng(i,j)
texrg2=graintex(j)
r(texrg,texrg2)=r(texrg,texrg2)+ng(i,j)
else
sv=sv+ng(i,j)
texdf=graintex(j)
d(texrg,texdf)=d(texrg,texdf)+ng(i,j)
end if
end if
end if
end do
rbp(texrg)=rbp(texrg)+bp(i)
end if
end do

do i=1,5
do j=1,5
infarea(i)=infarea(i)+r(i,j)+d(i,j)
end do
end do

do i=1,5
do j=1,5
r(i,j)=r(i,j)/infarea(i)
d(i,j)=d(i,j)/infarea(i)
end do
end do

c       obtain max and min gos values
disormax=0.0
do i=1,grain
if (disor(i).gt.disormax)then
disormax=disor(i)
end if
end do

disormin=180.0
do i=1,grain
if(disor(i).lt.disormin)then
disormin=disor(i)
end if
end do

disorav=0.0
do i=1,grain
```

```
if (disor(i).ge.0) then
disorav=disorav+(disor(i)*gpix(i))
end if
end do
disorav=disorav/pix

rg=0
maxpix=0
minpix=100000
rxpix=0
dfpix=0
do i=1,grain
if (cgam(i).le.gamcut.and.cgam(i).gt.0.and.gpix(i).ge.cpix)then
rg=rg+1
if(gpix(i).gt.maxpix) maxpix=gpix(i)
if(gpix(i).lt.minpix) minpix=gpix(i)
rxpix=rxpix+gpix(i)
else
dfpix=dfpix+gpix(i)
end if
end do
frarex=rxpix/pix
write(*,*) "fraction recrystallized", frarex
avgpix=rxpix/rg

maxpix=1.05*step*sqrt(maxpix)
minpix=1.05*step*sqrt(minpix)
avgpix=1.05*step*sqrt(avgpix)

sv=(sv*step)/area
rv=(rv*step)/area
rgc=(rv)/(rv+sv)

c rex. grain size

do i=1,5
texnrg(i)=0
maxpixtc(i)=0
minpixtc(i)=100000
avgpixtc(i)=0
end do
do i=1,grain
if(cgam(i).gt.0.and.cgam(i).le.gamcut.and.gpix(i).ge.cpix)then
texrg=graintex(i)
texnrg(texrg)=texnrg(texrg)+1
```

```
avgpixtc(texrg)=avgpixtc(texrg)+gpix(i)
if(gpix(i).gt.maxpixtc(i)) maxpixtc(i)=gpix(i)
if(gpix(i).lt.minpixtc(i)) minpixtc(i)=gpix(i)
end if
end do

do i=1,6
avgpixtc(i)=avgpixtc(i)/texnrg(i)
end do

do i=1,5
maxpixtc(i)=1.05*step*sqrt(maxpixtc(i))
minpixtc(i)=1.05*step*sqrt(minpixtc(i))
avgpixtc(i)=1.05*step*sqrt(avgpixtc(i))
end do

do i=1,5
dftex(i)=dftex(i)/dfpix
rxtex(i)=rxtex(i)/rxpix
end do

c expected values of grain contiguity ratios for the components
do i=1,5
   do j=1,5
      exr(i,j)=0
      exd(i,j)=0
   end do
end do

do i=1,5
do j=1,5
exd(i,j)=(1-frarex)*dftex(j)
exr(i,j)=rxtex(j)*frarex
end do
end do

c do i=1,pix
c gn=id(i)
c aodf(i,1)=odf(i,1)
c aodf(i,2)=odf(i,2)
c aodf(i,3)=odf(i,3)
c aodf(i,4)=odf(i,4)
c aodf(i,5)=odf(i,5)
c aodf(i,6)=odf(i,6)
c aodf(i,7)=odf(i,7)
```

```
c ph(i)=0
c if(disor(gn).gt.0.and.disor(gn).le.goscut.and.gpix(gn).ge.cpix)then
c if(graintex(gn).eq.1)then
c vs(i)=3001
c else
c vs(i)=3000
c end if
c else
c vs(i)=1000
c do j=1,grain
c if(ng(gn,j).ne.0)then
c if(disor(j).gt.0.and.disor(j).le.goscut.and.gpix(j).ge.cpix)then
c if(graintex(j).eq.1)then
c vs(i)=1001
c end if
c end if
c end if
c end do
c
c end if
c end do

open(unit=2,file=filein(1:inde)//'.gra',status='new')
open(unit=3,file=filein(1:inde)//'.tex',status='new')
c open(unit=4,file=filein(1:inde)//'.ang',status='new')

c do i=1,pix
c write(4,4) aodf(i,1),aodf(i,2),aodf(i,3),aodf(i,4),
c    &aodf(i,5),aodf(i,6),aodf(i,7),ph(i),vs(i)
c end do

write(3,*)'scan analyzed;',filein
write(3,*)'fraction recrystallized;',frarex
write(3,*)'interfacial def;',sv
write(3,*)'interfacial rex;',rv
write(3,*)'nucleation density;',rg/area
write(3,*)'rgrain contig;',rgc
write(3,*)'max grsize;',maxpix
write(3,*)'avg grsize;',avgpix
write(3,*)'min grsize;',minpix
write(3,*)
write(3,*)'total texture'
write(3,*)'cube tex;',texcom(1)/pix
write(3,*)'brass tex;',texcom(2)/pix
write(3,*)'copper tex;',texcom(3)/pix
```

```
write(3,*)'S tex;',texcom(4)/pix
write(3,*)'rest tex;',texcom(5)/pix
write(3,*)
write(3,*)'deformation texture'
write(3,*)'cube tex;',dftex(1)
write(3,*)'brass tex;',dftex(2)
write(3,*)'copper tex;',dftex(3)
write(3,*)'S tex;',dftex(4)
write(3,*)'rest tex;',dftex(5)
write(3,*)
write(3,*)'recrystallization texture'
write(3,*)'cube tex;',rxtex(1)
write(3,*)'brass tex;',rxtex(2)
write(3,*)'copper tex;',rxtex(3)
write(3,*)'S tex;',rxtex(4)
write(3,*)'rest tex;',rxtex(5)
write(3,*)
write(3,*)'deformed grains GOS'
write(3,*)'maximum; average; minimum'
write(3,*)'Cube;',maxgos(1),dgos(1),mingos(1)
      write(3,*)'Brass;',maxgos(2),dgos(2),mingos(2)
      write(3,*)'Copper;',maxgos(3),dgos(3),mingos(3)
      write(3,*)'S;',maxgos(4),dgos(4),mingos(4)
      write(3,*)'Rest;',maxgos(5),dgos(5),mingos(5)
      write(3,*)
write(3,*)'obs cont ratio between rex. grains deformed grains'
do i=1,5
write(3,3)d(i,1),d(i,2),d(i,3),d(i,4),d(i,5)
end do
write(3,*)
write(3,*)'obs cont ratio between rex. other rex. grains'
do i=1,5
write(3,3)r(i,1),r(i,2),r(i,3),r(i,4),r(i,5)
end do
write(3,*)
write(3,*)'exp cont ratio between rex. and  deformed grains'
do i=1,5
write(3,3)exd(i,1),exd(i,2),exd(i,3),exd(i,4),exd(i,5)
end do
write(3,*)
write(3,*)'expt cont ratio between rex. and rex. grains'
do i=1,5
write(3,3)exr(i,1),exr(i,2),exr(i,3),exr(i,4),exr(i,5)
end do
```

```
write(2,*)'scan analyzed',filein
write(2,*)'recrystallized fraction',frarex
write(2,*)'total number of grains', grain
write(2,*)'total number of pixels',pix
c write(2,*)'area scanned',area
c write(2,*)'nucleation density',rg/area
c write(2,*)'maximum gos',disormax
c write(2,*)'minimum gos',disormin
c write(2,*)'average gos',disorav

c c=0
do i=1,grain
c if (gpix(i).gt.cpix)then
grpix=gpix(i)
c c=c+1
write(2,2) i,cgam(i),disor(i),gpix(i),step*1.1026*sqrt(grpix)
c end if
end do


2 format (i5,f10.3,f10.3,i5,f10.3)
3 format (7f7.4)
4 format (f8.3,2f9.3,2f10.3,f7.1,f7.3,i3,i8)
c5 format (a9,3f7.4)

end
c     ------------------------------------------------------------

subroutine quattex(phi1,phic,phi2,texindex)

real eulphi(7,3),qt(4),qtex(4,7),qav(4),phi1,phic,phi2,qunit(4)
real qend(4),quatsymm(4,24),quatsamp(4,4),dismin(7),d1,d2,d3
real thetamin,t,qmis(4,2),qresult(4),qresult1(4),qq(4)
integer numsymm,numsamp,texindex
common/a1/ quatsymm,numsymm,quatsamp,numsamp
logical result

eulphi(1,1)=0.0
eulphi(1,2)=0.0
eulphi(1,3)=0.0

eulphi(2,1)=0.0
eulphi(2,2)=10.0
eulphi(2,3)=0.0
```

```
eulphi(3,1)=0.0
eulphi(3,2)=20.0
eulphi(3,3)=0.0

eulphi(4,1)=0.0
eulphi(4,2)=30.0
eulphi(4,3)=0.0

eulphi(5,1)=35.0
eulphi(5,2)=45.0
eulphi(5,3)=0.0

eulphi(6,1)=40.0
eulphi(6,2)=65.0
eulphi(6,3)=26.0

eulphi(7,1)=64.934
eulphi(7,2)=74.499
eulphi(7,3)=33.69

degrad=57.29578
pi=3.14159265
twopi=2*pi

do i=1,7
call quatB(eulphi(i,1)/degrad,eulphi(i,2)/degrad,
     & eulphi(i,3)/degrad,qt)
do j=1,4
qtex(j,i)=qt(j)
end do
end do

call quatB(phi1,phic,phi2,qq)

open(unit=4,file='quat.symm.cubic',status='old')
read(4,*)
read(4,*) numsymm
c write(*,*)numsymm
do i=1,numsymm
read(4,*) (quatsymm(j,i),j=1,4)
end do
close(4)

open(unit=5,file='quat.symm.ort',status='old')
read(5,*)
```

```
read(5,*) numsamp

do i=1,numsamp
read(5,*) (quatsamp(j,i),j=1,4)
end do
close(5)


disorientmin=15.
do j=1,7
dismin(j)=999999.
enddo
c write(*,*)'hi'

do i=1,numsymm
c call postsymm(qav,i,quint)
qresult(1)=quatsymm(4,i)*qq(1)+quatsymm(1,i)*qq(4)
     &  +quatsymm(3,i)*qq(2)-quatsymm(2,i)*qq(3)
      qresult(2)=quatsymm(4,i)*qq(2)+quatsymm(2,i)*qq(4)
     &  +quatsymm(1,i)*qq(3)-quatsymm(3,i)*qq(1)
      qresult(3)=quatsymm(4,i)*qq(3)+quatsymm(3,i)*qq(4)
     &  +quatsymm(2,i)*qq(1)-quatsymm(1,i)*qq(2)
      qresult(4)=quatsymm(4,i)*qq(4)-quatsymm(1,i)*qq(1)
     &  -quatsymm(2,i)*qq(2)-quatsymm(3,i)*qq(3)

do j=1,numsamp
c call presamp(qunit,j,qend)
qresult1(1)=qresult(1)*quatsamp(4,j)+qresult(4)*quatsamp(1,j)
     & -qresult(2)*quatsamp(3,j)+qresult(3)*quatsamp(2,j)
qresult1(2)=qresult(2)*quatsamp(4,j)+qresult(4)*quatsamp(2,j)
     & -qresult(3)*quatsamp(1,j)+qresult(1)*quatsamp(3,j)
qresult1(3)=qresult(3)*quatsamp(4,j)+qresult(4)*quatsamp(3,j)
     & -qresult(1)*quatsamp(2,j)+qresult(2)*quatsamp(1,j)
qresult1(4)=qresult(4)*quatsamp(4,j)-qresult(1)*quatsamp(1,j)
     & -qresult(2)*quatsamp(2,j)-qresult(3)*quatsamp(3,j)

call q2eulB(d1,d2,d3,qresult1)
   if(d1.lt.0.0) d1=d1+twopi
   if(d2.lt.0.0) d2=d2+twopi
   if(d3.lt.0.0) d3=d3+twopi
   d1=d1*degrad
   d2=d2*degrad
   d3=d3*degrad
call testangs(d1,d2,d3,result)
if(result) then
```

```
do ijk=1,9
do jk=1,4
qmis(jk,1)=qresult1(jk)    ! gets the current orient
qmis(jk,2)=qtex(jk,ijk) ! gets the component
enddo  !
call misquat(qmis,thetamin)
c write (*,*) thetamin
if(thetamin.lt.dismin(ijk)) then
dismin(ijk)=thetamin
endif
enddo  ! ijk loop on components
endif
end do
end do

t=360.0
do i=1,7
if(dismin(i).lt.t) then
t=dismin(i)
texindex=i
end if
end do

if (t.gt.15.0) texindex=8

c write(*,*) (dismin(j),j=1,9)
end

c
c _____________________________
c
c
        subroutine postsymm(qq,lindex,qresult)
        real qq(4),qresult(4)
        integer lindex
c
c        include 'common.f'
        common/a1/ quatsymm(4,24),numsymm,quatsamp(4,4),numsamp
c       PI=3.14159265
c
c  algorithm for forming resultant quaternion/rotation
c  from applying a symmetry operator, QUATSYMM(n,lindex)
c  to the first quaternion/rotation, QQ
c
```

```
c  If the symm oper == O, and the input quaternion, QQ, is an active
c  rotation, then Qresult = (QQ x O)
c  the "POST" in the name refers to writing the operator after the
c  rotation/orientation in vector/tensor notation:  Q' = Q x O
c  or in conventional quaternion notation, Qresult = Qsymm ? QQ
c
c  Thus, for active rotations (standard definition of orientation in
c  mechanics) this is suitable for applying CRYSTAL symmetry
c
        if(lindex.gt.numsymm) stop 'error in presymm, lindex>numsymm'
        if(lindex.lt.1) stop 'error in presymm, lindex<1'
        qresult(1)=quatsymm(4,lindex)*qq(1)+quatsymm(1,lindex)*qq(4)
     &  +quatsymm(3,lindex)*qq(2)-quatsymm(2,lindex)*qq(3)
        qresult(2)=quatsymm(4,lindex)*qq(2)+quatsymm(2,lindex)*qq(4)
     &  +quatsymm(1,lindex)*qq(3)-quatsymm(3,lindex)*qq(1)
        qresult(3)=quatsymm(4,lindex)*qq(3)+quatsymm(3,lindex)*qq(4)
     &  +quatsymm(2,lindex)*qq(1)-quatsymm(1,lindex)*qq(2)
        qresult(4)=quatsymm(4,lindex)*qq(4)-quatsymm(1,lindex)*qq(1)
     &  -quatsymm(2,lindex)*qq(2)-quatsymm(3,lindex)*qq(3)
c
c       write(*,*) 'qresult ',qresult
c
        return
end
c
c
c _____________________________
c
c
subroutine presamp(qq,lindex,qresult)
real qq(4),qresult(4)
integer lindex
c
common/a1/ quatsymm(4,24),numsymm,quatsamp(4,4),numsamp
c       PI=3.14159265
c
c  algorithm for forming resultant quaternion
c  from applying a symmetry operator, QUATSYMM(n,lindex)
c  to the first quaternion/rotation
c
c  If the symm oper == O, and the input quaternion, QQ, is an active
c  rotation, then Qresult = (O x QQ)
c  the "PRE" in the name refers to writing the operator before the
c  rotation/orientation in vector/tensor notation:  Q' = O x Q
c  or in conventional quaternion notation, Qresult = QQ ? Qsymm
```

```
c
c  Thus, for active rotations (standard definition of orientation in
c  mechanics) this is suitable for applying SAMPLE symmetry
c
if(lindex.gt.numsamp) stop 'error in PRESAMP, lindex>numsamp'
if(lindex.lt.1) stop 'error in presamp, lindex<1'
qresult(1)=qq(1)*quatsamp(4,lindex)+qq(4)*quatsamp(1,lindex)
     & -qq(2)*quatsamp(3,lindex)+qq(3)*quatsamp(2,lindex)
qresult(2)=qq(2)*quatsamp(4,lindex)+qq(4)*quatsamp(2,lindex)
     & -qq(3)*quatsamp(1,lindex)+qq(1)*quatsamp(3,lindex)
qresult(3)=qq(3)*quatsamp(4,lindex)+qq(4)*quatsamp(3,lindex)
     & -qq(1)*quatsamp(2,lindex)+qq(2)*quatsamp(1,lindex)
qresult(4)=qq(4)*quatsamp(4,lindex)-qq(1)*quatsamp(1,lindex)
     & -qq(2)*quatsamp(2,lindex)-qq(3)*quatsamp(3,lindex)
c
c write(*,*) 'qresult ',qresult
c
return
end
c
c
c  ------------------
c
subroutine testangs(phi1, capphi, phi2,result)
c  tests to see if the angles fall within the specified range
c  which for now is just 0<angle<=90
c
c  LOCAL VARIABLES
integer i
real phi1,capphi,phi2
logical result
c
result=.true.
if(phi1.le.0.0) result=.false.
if(phi1.gt.90.0) result=.false.
if(capphi.le.0.0) result=.false.
if(capphi.gt.90.0) result=.false.
if(phi2.le.0.0) result=.false.
if(phi2.gt.90.0) result=.false.
return
end
c
c
```

```
c _____________________________________
c
subroutine quatB(p1,p,p2,q)
c  convert Bunge Euler angles (radians) to quaternion;
c  direct conversion from angles, see Altmann's book
c  the rotation is a vector transformation (active rotation)
c
real p1,p,p2,q(4)
double precision c1,c,c2,s1,s,s2,d(3,3),tmp(4),sin2,cos2,rtmp,rnorm
c
c
       PI=3.14159265
c  form cosine, sine of Phi, and sum & diff of phi1, phi2
       S=DSIN(0.5d0*P)
       C=DCOS(0.5d0*P)
       S1=DSIN(0.5d0*(P1-P2))
       C1=DCOS(0.5d0*(P1-P2))
       S2=DSIN(0.5d0*(P1+P2))
       C2=Dcos(0.5d0*(P1+P2))
c      write(*,*) 's1,c1,s,c,s2,c2'
c      write(*,*) s1,c1
c      write(*,*) s,c
c      write(*,*) s2,c2
q(1)=s*c1
q(2)=s*s1
q(3)=c*s2
q(4)=c*c2
return
end
c
c _____________________________________
c

subroutine averageorientation(q,n,ind,thetas,phia1,phia,phia2)

real qc(4,24),qmf(4),qm(220000,4,24),qav(4,24),Qa(4,2),theta(24)
real thetsmin,ang,phia1,phia,phia2,qnorml,qnorm(4),q(4,300000)
real qn(4),qnr(4),qnrml, symm(300000)
real thetaav,thetas,Qb(4,2)
integer ind,nsym

open (unit=3,file='quat.symm.cubic',status='old')

read (3,*)
read (3,*) nsym
```

```
do i=1,nsym
read(3,*) (qc(j,i),j=1,4)
end do


symm(1)=1
do i=1,4
qmf(i)=q(i,1)
end do


qm(1,1,1)=qc(1,1)*q(4,1)+qc(4,1)*q(1,1)-qc(2,1)*q(3,1)
     &+qc(3,1)*q(2,1)
qm(1,2,1)=qc(2,1)*q(4,1)+qc(4,1)*q(2,1)-qc(3,1)*q(1,1)
     &+qc(1,1)*q(3,1)
qm(1,3,1)=qc(3,1)*q(4,1)+qc(4,1)*q(3,1)-qc(1,1)*q(2,1)
     &+qc(2,1)*q(1,1)
qm(1,4,1)=qc(4,1)*q(4,1)-qc(1,1)*q(1,1)-qc(2,1)*q(2,1)
     &-qc(3,1)*q(3,1)

do k=2,n
do j=1,24
qm(k,1,j)=qc(1,j)*q(4,k)+qc(4,j)*q(1,k)-qc(2,j)*q(3,k)
     &+qc(3,j)*q(2,k)
qm(k,2,j)=qc(2,j)*q(4,k)+qc(4,j)*q(2,k)-qc(3,j)*q(1,k)
     &+qc(1,j)*q(3,k)
qm(k,3,j)=qc(3,j)*q(4,k)+qc(4,j)*q(3,k)-qc(1,j)*q(2,k)
     &+qc(2,j)*q(1,k)
qm(k,4,j)=qc(4,j)*q(4,k)-qc(1,j)*q(1,k)-qc(2,j)*q(2,k)
     &-qc(3,j)*q(3,k)
end do

do j=1,24
qav(1,j)=qm(k,1,j)+qmf(1)
qav(2,j)=qm(k,2,j)+qmf(2)
qav(3,j)=qm(k,3,j)+qmf(3)
qav(4,j)=qm(k,4,j)+qmf(4)
end do

do j=1,24
qnorml=0
do i=1,4
```

```
qnorml=qnorml+qav(i,j)*qav(i,j)
end do
qnorml=sqrt(qnorml)
do i=1,4
qav(i,j)=qav(i,j)/qnorml
end do


Qa(1,1)=qmf(1)
Qa(2,1)=qmf(2)
Qa(3,1)=qmf(3)
Qa(4,1)=qmf(4)
Qa(1,2)=qav(1,j)
Qa(2,2)=qav(2,j)
Qa(3,2)=qav(3,j)
Qa(4,2)=qav(4,j)

call misquat(Qa,thetsmin)
theta(j)=thetsmin
c write(*,*)thetsmin
c pause
end do

ind=0
ang=360
do m=1,24
if (ang.gt.theta(m))then
ang=theta(m)
ind=m
end if
end do
symm(k)=ind

do i=1,4
qmf(i)=qav(i,ind)
end do

call norm(qmf,qnrml)
do i=1,4
qmf(i)=qmf(i)/qnrml
end do
end do
close(3)

c pause
```

```
thetas=0
do k=1,n
i=symm(k)
Qb(1,2)=qmf(1)
Qb(2,2)=qmf(2)
Qb(3,2)=qmf(3)
Qb(4,2)=qmf(4)
Qb(1,1)=qm(k,1,i)
Qb(2,1)=qm(k,2,i)
Qb(3,1)=qm(k,3,i)
Qb(4,1)=qm(k,4,i)
call misquat(Qb,thetaav)
thetas=thetas+thetaav
c write(*,*) thetaav
end do
thetas=thetas/n


c write(*,*) (qc(i,ind),i=1,4)
c pause
call q2eulB(phia1,phia,phia2,qmf)

if (phia1.lt.0) phia1=2*3.14159+phia1
if (phia.lt.0) phia=2*3.14159+phia
if (phia2.lt.0) phia2=2*3.14159+phia2
c write(*,*)'average orientation',phia1,phia,phia2

end
c _____________________________________
c
c
c ______________________________
c
c
subroutine misquat(qq,thetamin)
real qq(4,2),thetamin,qresult(4),tmp(2),rquat(4)
real disor,pi
real qmax,q1max,q2max
c
       PI=3.14159265
c
c  algorithm for forming resultant quaternion
c  and determining minimum angle taken from Sutton & Baluffi
c
c  note that the resultant quaternion is not returned
```

```
c  because it is not in the fundamental zone
c
c  note change of signs to get inverse of second orientation
c
qresult(1)=qq(1,1)*qq(4,2)-qq(4,1)*qq(1,2)
     & +qq(2,1)*qq(3,2)-qq(3,1)*qq(2,2)
qresult(2)=qq(2,1)*qq(4,2)-qq(4,1)*qq(2,2)
     & +qq(3,1)*qq(1,2)-qq(1,1)*qq(3,2)
qresult(3)=qq(3,1)*qq(4,2)-qq(4,1)*qq(3,2)
     & +qq(1,1)*qq(2,2)-qq(2,1)*qq(1,2)
qresult(4)=qq(4,1)*qq(4,2)+qq(1,1)*qq(1,2)
     & +qq(2,1)*qq(2,2)+qq(3,1)*qq(3,2)
c
c write(*,*) 'qresult ',qresult
qmax=0.
iqindex=0
do 10, i=1,4
qresult(i)=abs(qresult(i))
if(qresult(i).gt.qmax) then
qmax=qresult(i)
iqindex=i
endif
10 continue
c
q1max=0.
iq1index=0
c  find the next highest q component
do 20, i=1,4
if(i.eq.iqindex) goto 20
if(qresult(i).gt.q1max) then
q1max=qresult(i)
iq1index=i
endif
20 continue
c
disor=amax1(qmax,(qmax+q1max)/sqrt(2.),
     & (qresult(1)+qresult(2)+qresult(3)+qresult(4))/2.)
if(disor.gt.1.0) disor=1.0
if(disor.lt.-1.0) disor=-1.0
thetamin=acos(disor)*360./pi
c write(*,*) 'thetamin ',thetamin
c
q2max=0.
iq2index=0
c  find the next highest q component
```

```
do 30, i=1,4
if(i.eq.iqindex.or.i.eq.iq1index) goto 30
if(qresult(i).gt.q2max) then
q2max=qresult(i)
iq2index=i
endif
30 continue
c
rquat(4)=qmax
rquat(3)=q1max
rquat(2)=q2max
do 40, i=1,4
if(i.ne.iqindex.and.
     & i.ne.iq1index.and.
     & i.ne.iq2index)  rquat(1)=qresult(i)
40 continue
c  supply the sorted quaternion
c  CAUTION:  note that q1<q2<q3<q4
c  whereas typical Rodrigues sorting is R1>R2>R3
c
return
end
c
c _____________________________
c
subroutine norm(q ,qnorm)

real :: q(4),qnorm

qnorm=0
do i=1,4
qnorm=qnorm+q(i)*q(i)
end do

qnorm=sqrt(qnorm)

end




c
c  ______________________
c
subroutine q2eulB(p1,p,p2,qq)
c
```

```
c  converts quaternion to Bunge Euler angles
c  based on Altmann's solution for Euler->quat
c
real qq(4),p1,p,p2
real sum,diff
c
       PI=3.14159265
c
diff=atan2(qq(2),qq(1))
sum=atan2(qq(3),qq(4))
p1=(diff+sum)
p2=(sum-diff)
tmp=sqrt(qq(3)**2+qq(4)**2)
if(tmp.gt.1.0) tmp=1.0
p=2.*acos(tmp)
c write(*,*) ' quaternion input= ',qq
c write(*,*) 'Bunge angles output= ',p1,p,p2
c write(*,*) ' angles [degrees]= ',180.*p1/pi,180.*p/pi,180.*p2/pi
return
end
c
c  _____________________
c
```

Modelling Microstructure Evolution during Recrystallization

Abhijit P. Brahme

Submitted in partial fulfillment of the requirements

for the degree of

Doctor of Philosophy

in the field of

Physics

September 12, 2005

Abstract

The main aim of this work was to model microstructural evolution during recrystallization. This was achieved by characterizing it in terms of recrystallization kinetics and texture development and by identifying factors that exert the greatest effect on the recrystallization process.

To achieve the above, geometric and crystallographic observations from two orthogonal sections through a polycrystal were used. Using these as input to the computer simulations, a statistically representative three dimensional model was created. Assignment of orientations to the grains was done such that nearest neighbor relationships match the observed distributions. The microstructures thus obtained were allowed to evolve using a Monte-Carlo simulation. A parametric study was done to study the effects of various factors on recrystallization kinetics and texture development during microstructural evolution.

A set of software tools (*Microstructure builder*) were developed to generate the microstructures. The process involved the use of a ellipsoidal packing method combined with a voxel-based tessellation technique to create a 3 di-

mensional digital microstructure having the desired set of grain aspect ratios. Orientation assignment to the grains in the microstructure was done using a simulated annealing method that minimized the error between the orientation distribution function (ODF) and misorientation distribution function (MDF) of the measured and simulated materials.

The effect of grain geometry and placement of nuclei on recrystallization kinetics was studied. A close match in the recrystallization kinetics as measured in the experiments and the simulations was found to be most sensitive to the accuracy with which the geometry of the simulated microstructure matched that observed in experiments.

Also the effects of anisotropy, both in energy and in mobility, stored energy and oriented nucleation on overall texture development were studied in the light of various established competing theories of oriented nucleation (**ON**), oriented growth (**OG**) and orientation pinning (**OP**). The results from the simulations suggested that all of oriented nucleation, mobility anisotropy, stored energy and energy anisotropy (listed in order of their relative importance) influence texture development.

Acknowledgments

I would like to thank my advisor, Professor Anthony D. Rollett for his support, guidance, motivation and expressing confidence in my abilities.

I would like to acknowledge David Saylor and Joseph Fridy as their work formed the basis of this study. In particular I have had number of stimulating discussions with Joseph Fridy at ALCOA which always helped me clear my ideas. I have had extensive help from Mohammed Haroon Alvi in getting experimental data and input to the project.

I also thank Professors Robert Suter and Michael Widom for agreeing to be on my dissertation committee.

I thank Programming, Environment and Training program, US DoD, and MRSEC program of the National Science Foundation under Award Number DMR-0079996 for supporting the work on this project. Support from the Pennsylvania Technology Investment Authority (PTIA) is also acknowledged.

My parents and family have always supported me for all these years and have been there for me. I am grateful to them for instilling all the values and morals without which I would not have made it so far. Last but not the least

I am thankful to all my friends who made my years in Pittsburgh enjoyable.

Contents

List of Figures

List of Tables

List of Symbols

$\boldsymbol{\theta}$ Disorientaion across boundary

$\boldsymbol{\gamma}$ Grain boundary Energy

$\boldsymbol{\mu}$ Grain Boundary Mobility

$\boldsymbol{\Sigma} = \mathrm{n}$ Coincidence Site Lattice

$\mathbf{E}$ Energy

$\mathbf{D}$ Grain diameter

$\mathbf{t}$ Time

$\mathbf{T}$ Temperature

$\mathbf{R}$ Rodrigues vector

$\mathbf{q}$ Quaternion

$\mathbf{V}$ Volume

$\boldsymbol{\lambda}$ System error (texture matching)

$\boldsymbol{\phi_1, \Phi, \phi_2}$ Euler angles

$\mathbf{X}$ Recrystallized volume fraction

$\boldsymbol{\beta}$ Boltzman constant

$\boldsymbol{\alpha}$ Ovelap penalty

$\boldsymbol{\omega}$ Overlap encouragement

$\boldsymbol{\zeta}$ Zero penalty

$\boldsymbol{\beta}$ Cost decrease (Microstructure Builder)

Chapter 1

Introduction

The mechanical properties and the behavior of a metal are determined by the dislocation content, the grain size, phase structure and the grain orientation distribution. Many of these state variables are determined by the thermo-mechanical processing. The amount and condition of plastic deformation determines the dislocation content and its distribution in the microstructure as well as the deformation texture. The grain size and texture are determined during the process of recrystallization. As the density of dislocations increases the strength increases and the ductility decreases. Smaller grain sizes have been shown to increase the strength in steels. Texture, for example, determines the earing behavior in beverage cans in deep drawing of aluminum.

Parametric experimental studies to identify the important processing parameters are prohibitively costly and time consuming. Some of the param-

eters such as grain boundary properties, are not normally considered to be controllable hence there is a need to build quantitative models that have predictive capability. The lack of sound knowledge about the important parameters is a hindrance in constructing such models. Also the existing analytical models have a very simplistic view while computer simulations are capable of handling more complex problems that are not yet (or may never be) analytically tractable. Also the use of simulation can deepen our understanding by pointing us toward doing more experimental work in important areas.

The main objective of this work is to identify the parameters that influence the microstructural evolution during the process of recrystallization. This is done by constructing a computer model to build a microstructure, chapter 3, and studying its evolution during recrystallization (4, 5). The main focus is on matching the kinetics and the texture evolution. The outline of the thesis is as follows. The background and the introduction to the Monte Carlo model, which is the backbone of the work, is discussed in chapter 2. In chapter 3 the various tools that were used to to generate a statistically representative microstructure are discussed. Chapter 4 presents kinetics results of the model and chapter 5 presents the results of texture evolution. Chapter 6 discusses results obtained in the previous chapters and some suggestions for future work are discussed in the last chapter.

No model, whether analytical or computational, can be complete if it can not describe the expected or observed, properties. Hence we tested our

model against commercial purity aluminum (Al-1050) obtained from the ALCOA Technical Center. The 1050 sample was hot rolled at 326°C to a final thickness of 6.3mm. Mohammed Haroon Alvi (a fellow student) provided essential experimental data and advice (EBSD scans, measurement of texture evolution, recrystallization kinetics) for this work.

Chapter 2

Background

2.1 Recrystallization

The annealing process can be thought of as consisting of recovery, recrystallization and subsequent grain growth. All materials undergoing plastic deformation contain defects and interfaces. During the process of **recovery**, annihilation and rearrangements of dislocations takes place. Normally the microstructural changes due to the recovery process occur homogeneously in the material. There is only partial restoration of the properties and negligible effects on the boundaries between deformed grains. In **recrystallization** new grains are formed in the deformed/recovered microstructure. These new grains have a low dislocation density. The "new" grains (*nuclei*) grow to consume the old grains thereby creating a new structure with a low dislocation density. Although this new structure has a lower dislocation density it still

has high internal surface area (many grain boundaries). The grain boundaries are unstable, in the sense of excess free energy, and some of them are eliminated if annealed further. This process of **grain growth** eliminates the smaller grains in favor of the large ones. The grain boundaries thus assume a lower energy configuration. The process of **recrystallization** is stored energy driven whereas the **grain growth** is driven primarily by curvature. Figure 2.1[1] shows the schematic of the annealing process. Panel (a) shows the

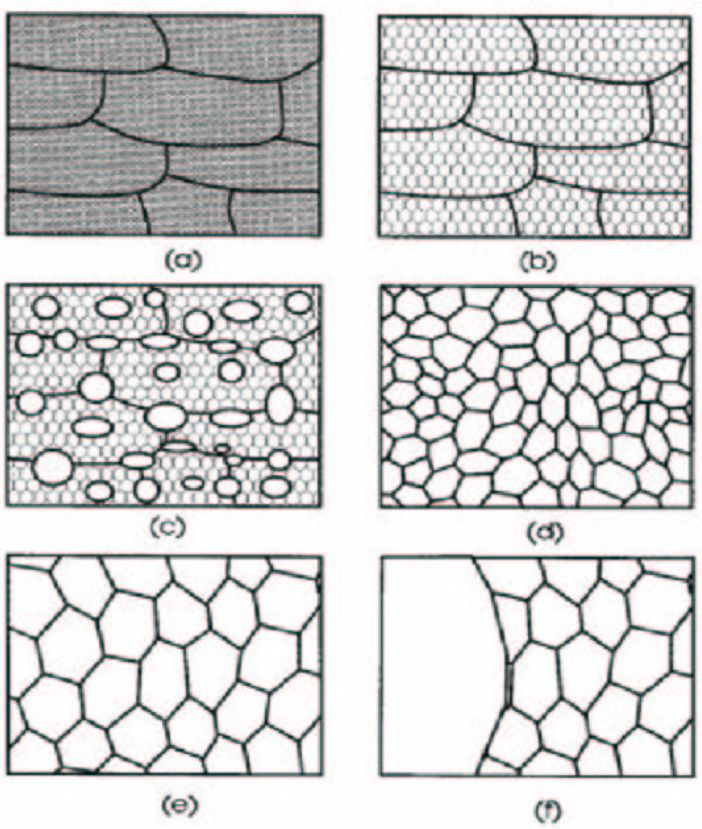

Figure 2.1: Schematic of the Annealing processing [4]

[1] taken from [4] p. 2

deformed grain structure with a high density of dislocations along with grain boundaries. Panel (b) shows the grain structure after recovery and hence a lower density of dislocations but the grain boundaries have not moved. Panel (c) shows the formation of new grains and the onset of recrystallization. Panel (d) shows the fully recrystallized structure with low dislocation density grains. Panel (e) is a snapshot in time during grain growth. Notice that the overall grain size is bigger and there are fewer grains as compared to panel (d). Panel (f) shows abnormal grain growth (sometimes referred to as secondary recrystallization) where a few grains grow larger than the rest.

2.2 Texture

Essentially all naturally occurring and man made materials show preferred crystallographic orientation or **textures**[2]. It is one of the important properties governing the behavior of anisotropic polycrystalline materials. There are various ways of representing the texture in materials. The macrotexture can be represented by:

- **Pole figures**
- **Inverse Pole figures**
- **Orientation distribution functions (ODF) in Euler space**
- **ODF Rodrigues-Frank space**

[2]Only certain types of castings and powder products are texture free

- **3×3 orthogonal rotation matrices**

To represent the "microtexture"[3] we need three independent parameters which specify the orientation of the crystal with respect to a fixed reference frame (generally the sample frame). The orientation of a crystal can be described by a set of Euler angles $(\phi_1,\ \Phi,\ \phi_2)$ which take the crystal coordinate axes to coincide with the sample frame coordinate axes. An alternate description of the orientation can be done in terms of an axis angle combination using either **Rodrigues vectors** or **quaternions**. If θ is the rotation angle about axis $\hat{r}$ having direction cosines (u, v, w) then the Rodrigues vector is given by:

$$\vec{R} = \hat{r}\tan(\frac{\theta}{2}) \tag{2.1}$$

while the unit quaternion is given by

$$\mathbf{q} = \left(u\sin\left(\frac{\theta}{2}\right), v\sin\left(\frac{\theta}{2}\right), w\sin\left(\frac{\theta}{2}\right), \cos\left(\frac{\theta}{2}\right)\right) \tag{2.2}$$

Even though it might appear that the above representations have four independent parameters, one has to remember that the axis triplet (u, v, w) has only two independent parameters as they form the unit normal and hence have an additional constraint.

$$u^2 + v^2 + w^2 = 1$$

[3] generally taken to include spatial information as in the contraction of "microstructure" and "texture"

It is much easier to work with either the unit quaternions or the Rodrigues-vectors in computations since the algebra for combining rotations is much simpler.

Most cold worked materials develop particularly strong textures. Figure 2.2 shows the pole figures and the ODF for a cold rolled FCC metal. Some of the components which occur frequently in rolled FCC metals are presented in table 2.1[4] along with the Euler angles and the Miller indices ({hkl}<uvw>)[5]. Copper, Brass and S form most of the rolling texture while there may be small traces of the others present. Many FCC metals show a growth in the cube component during annealing .

Table 2.1: Common Texture components in FCC metals

Component	**Euler angles** (ϕ_1, Φ, ϕ_2)	**{hkl} <uvw>**
Cube	(0,0,0)	{001}<100>
Copper	(0,35,45)	{112}<111>
S	(64.93,74.50,33.69)	{231}<124>
Goss	(0,45,0)	{011}<100>
Brass	(35,45,0)	{011}<211>
Dillamore	(0,27,45)	{4,4,11}<11,11,8>

The growth of the cube component as the main recrystallized component has been a hotly debated issue. It appears in aluminum, copper as well as gold, nickel and some iron alloys. The remarkable fact is that the deformed microstructure shows only very small amounts of cube component. There

[4]The exact location of some of the important texture components is depicted in appendix A

[5]{hkl} is the crystal direction parallel to the sample Z axis and <uvw> is the crystal direction parallel to sample X axis.

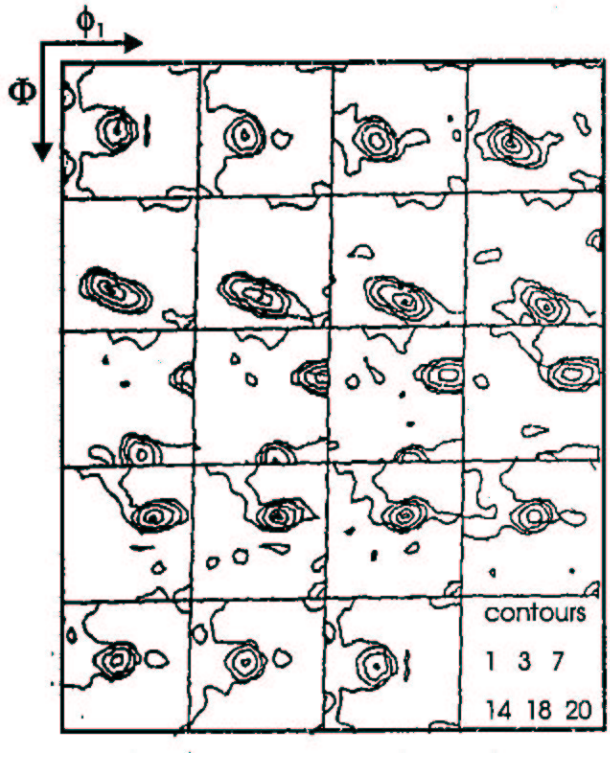

(a) ODF for typical FCC rolling texture [4]

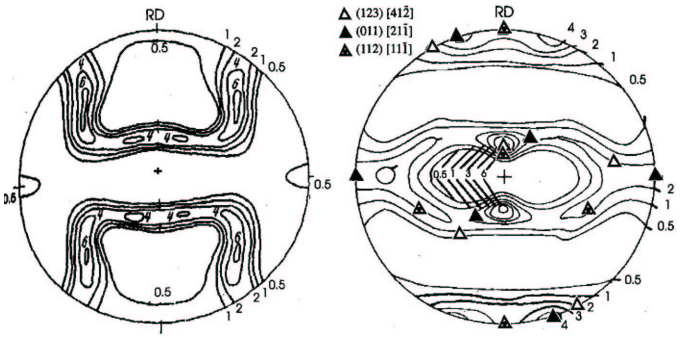

(b) 001 and 111 Pole figures for typical FCC rolling texture [4]

Figure 2.2: FCC rolling Texture

have been many conflicting experimental results supporting different theories that try to explain the origin and growth of cube component. The two main theories, **Oriented Nucleation** and **Oriented Growth**, will be discussed in sections 2.5.1 and 2.5.2 respectively.

2.3 Grain Boundary

What is a grain boundary? A grain boundary can be defined as an array of continuous dislocations separating two crystals. We will look only at those properties of grain boundaries that play an important role in recrystallization and grain growth. Since a grain boundary is the interface between two grains (crystals) it can be described by the misorientation between the two grains and the grain boundary inclination. The grain boundary inclination can be expressed in terms of the grain boundary normal. It might seem that we have **6 independent degrees** of freedom, three from the misorientation and three more from the grain boundary normal. However the grain boundary normal has only two independent parameters since the length of the normal is constrained to be unity. The figure 2.3 shows a grain boundary between two grains. The two crystals (grains) have a 20° disorientation between them. In this study we will adopt the three parameter description (misorientation) of grain boundaries instead of the full five parameter description. The method used to generate the 3-D microstructures, as described in chapter 3, is by using two 2-D slices. To obtain the full five parameter grain boundary char-

acter one needs a technique such as serial sectioning or statistical stereology. Furthermore to obtain a reasonable texture assignment one would also need more grains in the final microstructure. With a resolution of 5° one would need data on 10^5 boundary segments to get a 5 parameter description[13]. The misorientation description of grain boundaries, as will be clear in the following chapters, is sufficient to get an approximate solution, given the system constraints. Grain boundaries can be loosely classified in terms of the disorientation (θ) between the two grains by distinguishing between a **low angle grain boundary (LAGB)** and a **high angle grain boundary (HAGB)**. The cutoff angle for this distinction is $\sim$ 10° to 15°. So we will classify any boundary more than 15° as a high angle grain boundary

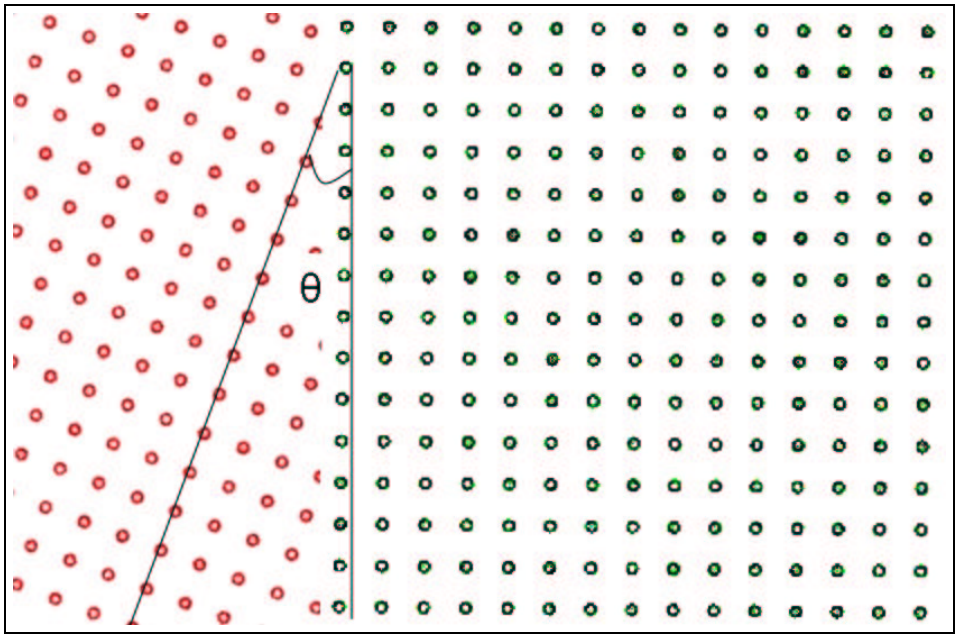

Figure 2.3: Grain Boundary

as explained below. The classification of grain boundaries into LAGB and HAGB will be discussed in the following sections. This classification helps us to get an insight in making some estimations of the anisotropy in the system based on just the disorientation. Grain boundaries can also be divided into tilt and twist boundaries. **Tilt boundaries** are those boundaries for which the crystals on either side of the boundary are related by an disorientation about an axis which lies in the plane of the boundary. **Twist boundaries** by contrast have the axis perpendicular to the plane of the grain boundary.

2.3.1 Low angle grain boundary

A low angle boundary is an represented an array of discrete dislocations. One of the reasons for having this distinction between LAGBs and HAGBs based on the disorientation angles is related to the proximity of the dislocation cores. As stated above we can represent the boundary by an array of dislocations; as the disorientation angle approaches 15°, however, the dislocation cores begin to overlap and separate dislocations can not be identified.

The energies of low angle boundaries are given by equation 2.3 [1].

$$\gamma_s = \gamma_0 \theta \big(\mathrm{A} - \ln(\theta) \big) \tag{2.3}$$

where γ_0 and A constants. It is more convenient to express the above equation

in the following form:

$$\gamma_s = \gamma_m \frac{\theta}{\theta_m}\Big(1 - \ln\big(\frac{\theta}{\theta_m}\big)\Big) \tag{2.4}$$

where γ_m and θ_m are the values at the cutoff ($\sim 15°$) for the energy and disorientation angle respectively. The experimental results agree well with the calculated values for low angle grain boundary energies [2].

Even today there are no conclusive quantitative results which give a clear verdict on the shape of the mobility function with respect to the disorientation. There are only qualitative results indicating the nature of the curve. It is generally believed that for very LAGB ($\theta \to 0$) the mobility of the boundary decreases with increase in disorientation till it goes through a minimum and then the mobility increases with disorientation (θ) till $\theta \sim$ 15-20° after which it is independent of θ. Recent work by Winning and Rollett [61] showed a clear transition between the low angle to high angle regime closer to 15°.

2.3.2 High angle grain boundary

A general high angle grain boundary can be treated as a generic interface since its structure and properties are essentially independent of disorientation. There are, however, certain "special" high angle boundaries which are of interest since they exhibit "special" properties. Most times these boundaries also have "special" geometric configurations associated with these . The

concept of a coincidence site lattice (**CSL**) was introduced first by Kronberg and Wilson [3] in 1949. There have been many extensive studies on the CSL relationship since then. Figure 2.4 (taken from Humphrey's book [4]) shows two interpenetrating simple cubic lattices, corresponding to shaded and open circles. The points where the two lattices coincide, shown by solid circles, form the coincidence site lattice. The $\mathbf{\Sigma}$ value, calculated as the ratio of volume of the unit CSL cell to the volume of the standard unit cell, for the

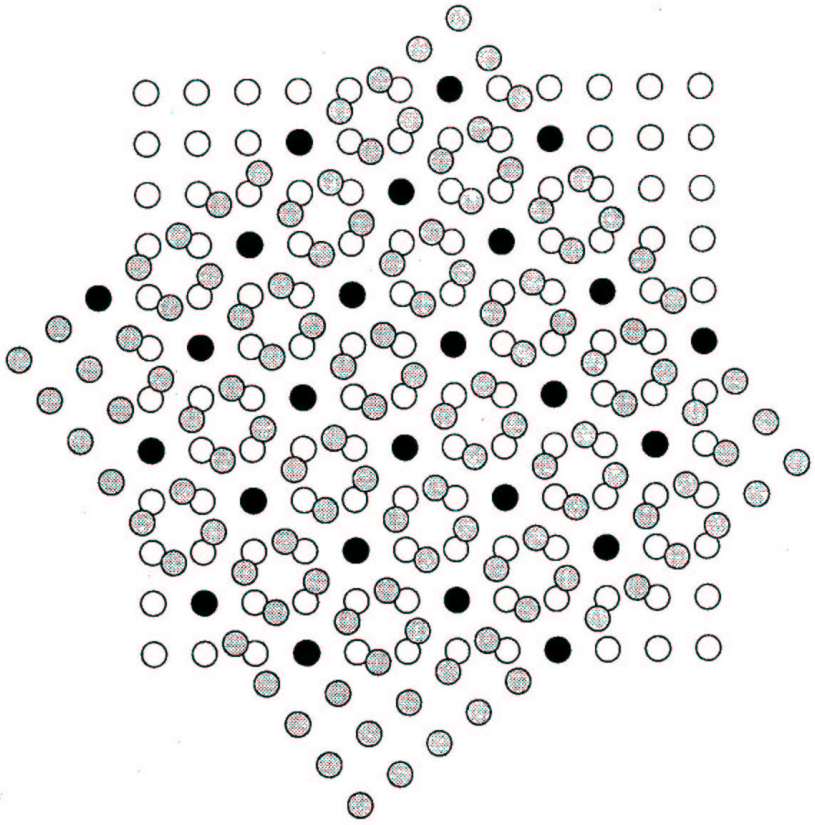

Figure 2.4: A coincidence site lattice formed by two simple cubic lattices [4] illustrated for the case of $\Sigma 5$ case

CSL shown in fig. 2.4 is **Σ5**. A list of **Σ** values and the associated axis-angle values are summarized in table 2.2 (from Mykura 1980[5]). It is assumed by many researchers that, if a boundary contains a high density of points in a CSL then it will have low energy. Hasson and Goux [6] showed the correlation between calculated and experimentally measured values for grain boundary energy in symmetrical $< 100 >$ and $< 110 >$ tilt boundaries in Aluminum. Some of these special boundaries show up as cusps in the grain boundary energy against disorientation curve. A completely opposite picture is seen for grain boundary mobility. Some of the CSL boundaries have been shown to be highly mobile. That is they show up as peaks in the mobility against disorientation curve. The presence of peaks in the mobility function does not have a one to one correspondence with the presence of cusps in the energy function. For example, the **Σ7** boundary has high mobility and low energy as against the **Σ3** boundary which has only low energy. In general the mobility anisotropy has been shown to have higher anisotropy than the grain boundary energy. The specific values of mobility used for this work will be discussed in section 5.3.3.

2.4 Recrystallization + Texture evolution

The texture of the recrystallized material depends mainly on:

1. Orientation of the nuclei or new grains

2. The growth rate of the new grains

Table 2.2: Coincident site lattices

Sigma	Rotation	Axis
Σ3	60.00	< 111 >
Σ5	36.87	< 100 >
Σ7	38.21	< 111 >
Σ9	38.94	< 110 >
Σ11	50.48	< 110 >
Σ13a	22.62	< 100 >
Σ13b	27.80	< 111 >
Σ15	48.19	< 210 >
Σ17a	28.07	< 100 >
Σ17b	61.93	< 221 >
Σ19a	26.53	< 110 >
Σ19b	46.83	< 111 >
Σ21a	21.79	< 111 >
Σ21b	44.40	< 211 >
Σ23	40.45	< 311 >
Σ25a	16.25	< 100 >
Σ25b	51.68	< 331 >
Σ27a	31.58	< 110 >
Σ27b	35.42	< 210 >
Σ29a	43.61	< 100 >
Σ29b	46.39	< 221 >

For example, assume that new grains have a random texture and further that there is no particular component favored to grow. Then one can safely expect that the final texture, after recrystallization is complete, will have the same distribution as that of the nuclei (new grains). Whereas if any particular component has a higher growth rate then it will become the dominant component. In general it is the combination of these two effects that governs the recrystallization texture. The next section deals in detail with the factors

influencing texture and the various theories.

2.5 Factors influencing texture evolution

The most popular theories that have emerged in the past few decades favor one or the other of the two views mentioned previously. The **oriented nucleation** theory claims that the origin of the recrystallized texture is in the preferred nucleation of preferred nuclei. The **oriented growth** theory, however, claims that the origin of the final texture lies in preferred growth of particular nuclei from a more or less random initial distribution.[6]

2.5.1 Oriented Nucleation

The most important work for the support of this argument was done by Dillamore and Katoh [14]. It is now widely accepted that the new grains are generated from the original deformed matrix by subgrain coarsening. The main contention of the oriented nucleation theory is that not all regions in the matrix are deformed "equally". Some of the regions are found to be deformed more than others. These regions are more likely to "seed" the new grains. Dillamore and Katoh calculated the rotation paths of individual grains during the compression of polycrystalline bcc iron. They showed that bands with particular orientations have a higher tendency to form nuclei which was supported by the experimental observation of those orientations

[6]The discussion is only applicable to FCC metals

being dominant after recrystallization. Similar experiments in copper by Ridha and Hutchinson [15] show the emergence of cube texture from the precisely predicted regions.

Vatne et al. in their recent work [16] have shown that that cube nuclei from deformed cube bands. They argued that the cube grains are metastable during the process of hot deformation and serve as nucleation sites for the new grains. They also concluded that these recrystallizing grains have a size advantage over the other orientations. Inagaki et al. in a recent paper[17] have reported that for high purity Aluminum rolled to high reduction (98%) the formation of the cube nuclei was not restricted to the cube bands. On the contrary they occurred as isolated equiaxed grains.

2.5.2 Oriented Growth

The alternate hypothesis of Oriented growth (OG) was proposed by Barrett in 1940[18]. The theory of oriented growth is centered around the experimental observations of specific rotational relationships. Early experiments by Beck[19, 20] on artificially nucleated deformed single crystals showed evidence of oriented growth in the form of rapid growth of new grains having a 40° misorientation about $< 111 >$ with deformed grains. There also have been several experiments on polycrystals which favor the oriented growth theory. There is considerable evidence that certain grain boundaries having specific orientation relationships have high mobilities. The table 2.3 lists a few of these "special" orientations for Aluminum. The most important of

Table 2.3: Orientations with higher mobility and/or lower energy

Sigma	Rotation	Axis
$\Sigma = 3$	60	$< 111 >$
$\Sigma = 7$	38.2	$< 111 >$
$\Sigma = 13b$	27.8	$< 111 >$
$\Sigma = 19b$	46.8	$< 111 >$
$\Sigma = 37c$	19	$< 100 >$

these is the $\Sigma 7$ boundary which has been to shown to be the most mobile. By contrast the $\Sigma 3$ boundary, which is a low energy configuration, is relatively immobile.

The $40° < 111 >$ boundary has attracted much attention since the relation between the S component $\{231\}< 124 >$ which is a dominant component in FCC rolling texture is related by this to the cube component $\{001\}< 100 >$ which is the dominant recrystallized component.

2.5.3 Other Theories

Both the above mentioned theories have notable exceptions and they alone can not explain the wide range of experimental results. Most notably Juul Jensen [21] showed that the growth rate for the cube grains was about 1.5 times higher than the rest, however, there was wide range of possible misorientation between the recrystallized grains and the deformed matrix. Imagine a nucleus growing in a deformed matrix. As this nucleus grows, at the expense of surrounding material, its neighborhood changes constantly. As a result it samples many different orientations during its growth and there is

can not be a special orientation relationship between the growing cube grains and the matrix grains.

One of the recent theories on the selection of cube texture as a major recrystallization texture component is "orientation pinning". Proposed by Juul Jensen [21] it has been substantiated by Doherty et al. [23]. The theory relies on presence of LAGB to slow the growth rate of the non-cube grains. Assuming that the cube nuclei originate from cube bands and that the cube bands are well separated from each other one can deduce that the cube nuclei will impinge on other less frequently. By contrast, new grains forming in the dominant texture component will impinge on like oriented grains more frequently and hence will be slowed down or blocked. This theory can thus explain the presence of stronger cube texture if the recrystallized grain size is comparable or more than the band spacing in the deformed microstructure. Engler[22], though, showed that "orientation pinning" alone is insufficient to explain the growth of cube component. This conclusion is reinforced by this work.

One can also not overlook the effect of **stored energy**, i.e the effect of heterogeneity on the final texture of the microstructure. Godfrey et al. [24] showed that the recrystallization proceeds much faster, 2 orders of magnitude, in a region with higher stored energy. Hence if cube nuclei occur in the region between cube and S bands then we can expect to observe rapid growth of these nuclei since S bands have been shown to have more stored energy [16].

2.6 Monte Carlo

All the references to the Monte Carlo technique in this work are actually what statisticians like to refer to as MCMC (Markov chain Monte Carlo) models. The Monte Carlo method encompasses any technique that involves using random number sequences to approximate solutions to problems. The name Monte Carlo was coined by Ulam and Metropolis [26], inspired by the card games Ulam enjoyed playing. Monte Carlo methods have been used to solve a variety of problems such as numerical integration to simulating a system of interacting particles such as ferromagnetic materials. The particular method of most interest in this context is the Potts model.

2.6.1 Potts model

The Potts model [28] is an natural extension of the the Ising Model. The Ising model [27] is system of spins on a lattice where each spin can take either of the two possible values +1 or -1 (up and down). The energy of the model is derived from the interaction between the spins. The system forms a canonical ensemble and hence if one can determine the partition function (Z) then all the other properties such as free energy etc. can be expressed in terms of the partition function. The PDF of a canonical distribution is given by equation 2.5

$$P = \frac{1}{Z} e^{\frac{-E}{\beta T}} \tag{2.5}$$

where Z is the partition function given by

$$Z = \sum_{\{\sigma\}} exp(-\beta E(\{\sigma\})) \tag{2.6}$$

β is the Boltzmann factor and $\{\sigma\}$ is the combination of all the spins (possible configurations) in the system. The partition function may or may not be solvable in analytic form hence one needs to use a Monte Carlo technique to approximate the solution.

In the Potts model [28] the spins are allowed to, unlike in the Ising model, take more than two discrete values. In a q state Potts model, the spin σ_i can take values ranging from $1 \ldots$ q. For $q = 2$ the system reduces to an Ising model. The energy of the system in the Potts model is calculated using equation 2.7.

$$E = \frac{J}{2} \sum_i \sum_j (1 - \delta_{ij}) \tag{2.7}$$

where J is the interaction energy between two unlike spins. The factor of 2 is needed in the denominator to avoid double counting. Equation 2.7 holds true only for the isotropic case with no external field applied. In general the system energy is given by:

$$E = \frac{1}{2} \sum_i^N \sum_j^n \left\{ \gamma(s_i, s_j) \left(1 - \delta_{s_i s_j} \right) \right\} + \sum_i^N H(s_i) \tag{2.8}$$

where $\gamma(s_i s_j)$ is the interaction energy and $H(s_i)$ is the contribution to the energy due to an external field. The first summation, on j, is over the nearest

neighbors (This is the distance over which the interactions between various lattice spins are considered to be significant). In the simple cubic three dimensional lattice the count extends to the 26 nearest neighbors. The second summation is over all the lattice sites in the system. One can easily see that by setting the external term $H(s_i)$ to zero and making $\gamma(s_i, s_j)$ a constant we recover equation 2.7. We will be using the term $H(s_i)$ to represent the stored energy.

2.6.2 Metropolis Algorithm

Metropolis et al. [29] introduced an algorithm, which carries his name, to solve equation 2.8 using the Monte Carlo method. The steps in the Metropolis Algorithm are outlined below

1. Pick a site, i, and a new spin value, s_i', at random.
2. Calculate the energy change ΔE associated with changing the spin of the i^{th} site to s_i'.
3. Generate a random number r such that $0 < r < 1$.
4. if $r < e^{\frac{-\Delta E}{\beta T}}$ then accept this change
5. increment the time by 1/N.

Thus the transition probability P is given by

$$P = \begin{cases} 1 & \Delta E \leq 0 \\ \exp\Big(- \frac{\Delta E}{\beta \mathrm{T}} \Big) & \Delta E > 0 \end{cases} \tag{2.9}$$

Thus all moves which reduce the total energy of the system are always accepted while the ones which increase the system energy are accepted with probability $\exp\Big(- \frac{\Delta E}{\beta \mathrm{T}} \Big)$. For the zero temperature case the probability reduces to:

$$P = \begin{cases} 1 & \Delta E \leq 0 \\ 0 & \Delta E > 0 \end{cases} \tag{2.10}$$

The above procedure is not the exact Metropolis algorithm but an adaptation for the Potts model. For the Ising model a lattice site can only take two values of spin hence the probability given by 2.9 represents the probability of spin flip.

2.6.3 n-fold Way

The basic, or "brute force", Monte Carlo is very inefficient when dealing with large and sparse datasets. After a considerable amount of coarsening has taken place the probability of a successful transition is very low since many of the lattice sites are surrounded by sites having the same spin. Bortz et al.[30] first proposed an algorithm to eliminate unsuccessful attempts *a priori*, so that all the attempts are accepted. The basic idea of the scheme is

to calculate all the spin flip probabilities beforehand. To do this the lattice sites are sorted by spin-flip probability classes. Each site having a similar environment will have the same transition energy for a flip. Once all the classes are known the sum of all spin-flip probabilities is calculated in the following fashion:

$$Q_n = \sum_{j}^{n} n_j p_j \tag{2.11}$$

where the sum is over all the possible classes and the probability of each class is given by 2.9 and n_j is the number of sites belonging to j^{th} class. The NFW algorithm then proceeds in the following manner.

1. Pick a random number r and increment time by an amount Δt.
2. Choose a class k such that

$$Q_{k-1} \leq rQ_n \leq Q_k$$

3. Randomly choose one of the sites in the k^{th} class
4. flip the spin of the site
5. Update the class of the chosen spin and its neighbors
6. Calculate Q_n

In the conventional Potts model, the time is incremented after every attempted flip whether it is successful or not. In the NFW approach, however,

only the flips that are successful are allowed. Hence the time increment in the NFW has to be scaled accordingly. Novotny [31] provides a detailed discussion about the time increment in NFW (effectively treated as a Poisson process). In essence the time increment is given by

$$\Delta t = -\frac{Q-1}{A}\ln(r) \tag{2.12}$$

where Q is the total number of spins allowed in the system and A is system level activity given by

$$A = \sum_{i}^{N} P(\Delta E_i) \tag{2.13}$$

2.6.4 Grain Growth and Recrystallization

The use of Monte Carlo methods have been discussed in detail in many publications. Anderson, Srolovitz, Grest and Sahani put together a set of papers [48, 49, 50, 51, 52] verifying the behavior of the MC model for simulating grain growth. The first step is to map a continuum grain structure onto a discrete lattice. Each lattice point is assigned a spin value depending on which grain the site is embedded within. The initialization of the systems to get the correct properties is one of the most important parts of the MC simulations. We will discuss the approach to depict the three dimensional microstructure used for this work in chapter 3. Shown below is an example of a 2-D microstructure.

```
  1    1   18   18   18   18   18   18   18   18
 18   18   18   18   18   18   18   18   18   18
856  856   18   18   18   18   18   18   18   18
595   18   18   18   18   18   18   18   18   18
 18    6  618  618  831    6    6    6    6    6
  6    6    6    6    6    6    6    6    6  628
628    6    6    6    6    6    6    6    6  779
779    6    6    6    6    1    1    1    1    1
  1    1    1    1    1    1    1    1    1    1
  1    1    1    1    1    1    1    1    1    1
```

Each lattice site is assigned a spin value. The spin value is identical to the grain number. Thus the limit on the number spins allowed, $\mathbf{q}_{max}$, in the microstructure is decided by the number of grains in the system. The nuclei are assigned spins greater than $\mathbf{q}_{max}$. This structure shows nuclei (having spin value >500) embedded in a matrix. The total energy of the system is given by the Potts Hamiltonian, equation 2.8 [28]. Each lattice site contributes $H(s_i)$ bulk energy to the system; this can be thought of as being analogous to the density of dislocations. For the simulation of recrystallization this value of bulk energy, for the nuclei, can be set to a low value similar to a dislocation free nucleus. The basic merit of the MC model is the inherent simplicity of the model. It is very easy to input the energy and mobility, discussed in detail in 5.3, for the system. To incorporate mobility

the transition probability in equation 2.9 is modified as follows

$$P = \begin{cases} \frac{\gamma(s_i,s_j)}{\gamma_{max}} \frac{\mu(s_i,s_j)}{\mu_{max}} & \Delta E \leq 0 \\ \frac{\gamma(s_i,s_j)}{\gamma_{max}} \frac{\mu(s_i,s_j)}{\mu_{max}} \exp\Big(- \frac{\Delta E}{\beta \mathrm{T}} \Big) & \Delta E > 0 \end{cases} \tag{2.14}$$

By varying the coordination number n in equation 2.8 one can include as many nearest neighbors as desired in the interaction term. However in 3-D Anderson et al. showed that it is necessary and sufficient to include the contributions up to the third nearest neighbors. Anderson[48] showed the effect of using a square lattice in 2D Monte Carlo simulations. In the longer time configurations the grains seemed to be "frozen" and most of the boundaries met at either 90° or 180°. Holm in her 1991 Phy. Rev. paper [32] showed that, by increasing the lattice temperature or by including longer range interactions, the "lattice pinning" can be eliminated. The interaction energy is also dependent on the the orientation of the sites. Thus one can control or limit effect of the anisotropy on the system. Also since there are only a finite number of spins allowed, it is possible to calculate the interaction between various terms beforehand and shorten the running time of the code. Like any other model this model is not free of short-comings and the most notable among them is the inherent lattice anisotropy. Holm [33] has analyzed (in both 2D and 3D) the lattice effects on grain growth.

Chapter 3

Microstructure Builder

3.1 Introduction

This chapter describes methods for generating a three dimensional polycrystalline microstructure that is representative of an experimentally characterized sample. The input is from two orthogonal observations in the form of EBSD maps of cross sections of the polycrystalline sample. Approximating the grains as ellipsoids and combining with a Voronoi tessellation technique, a microstructure was generated. The emphasis was on generating a microstructure which was statistically similar to the experimentally observed rather than reproducing an exact match to a specific volume, which would require 3D X-ray method or serial sectioning. These methods need expertise in the particular field, which are still under development, and are very time consuming. Using the orientation distribution and misorientation dis-

tribution between nearest neighbor grains, the generated microstructure was overlaid with texture.

3.2 Experimental Input

3.2.1 EBSD maps

The input to the Microstructure Builder was in the form of **E**lectron **B**ack-**S**catter **D**iffraction (EBSD) maps. An EBSD map is a list of pixels containing information about location x, y coordinates, from a reference point, and the crystallographic orientation at each point. Using this information the pixels aggregated into grains using a predetermined threshold misorientation between neighboring pixels. The EBSD maps provide information not only about the geometry, size and shape, of the experimental microstructure, but also of the crystallographic orientation (texture).

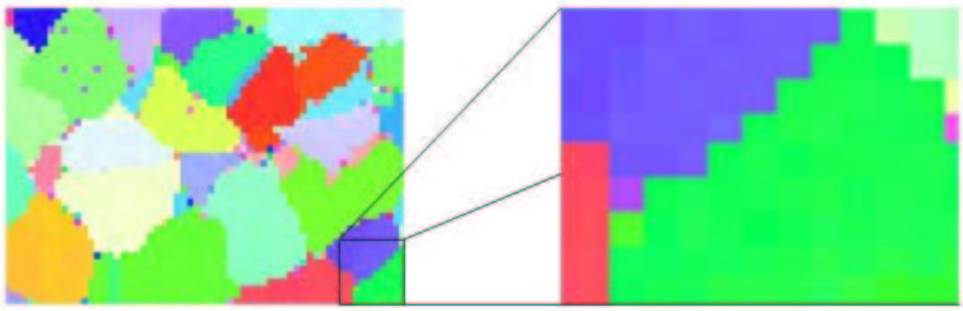

Figure 3.1: A typical EBSD map

Figure 3.1 shows a typical EBSD map with an enlarged small portion of

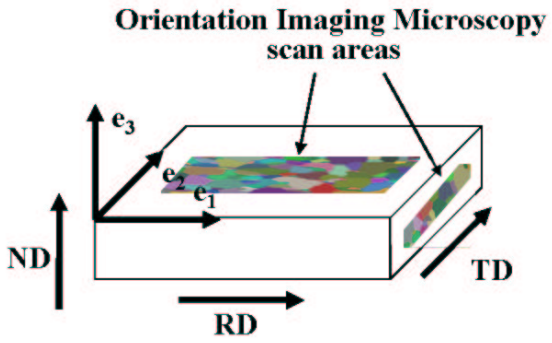

Figure 3.2: EBSD observation areas

it. The enlarged portion shows the resolution of the scan, indicating that the scan was done on a square grid. The grains are distinguished by colors assigned based on the crystallographic orientations. Grain boundaries are drawn between a pair of pixels if the disorientation (angle only) was larger than 15 degrees.

Figure 3.2 shows the observation planes of a polycrystalline sample. The scans are obtained from two orthogonal planes, one perpendicular to the sample normal direction (**ND**) and the other perpendicular to the sample rolling direction (**RD**). The two scans must be on orthogonal planes to get the full form of distribution on the ellipsoid shape distribution function. The sample axis 1, X, (e_1) is $\|$ to **RD** sample axis 2, Y, (e_2) is $\|$ to **TD** and sample axis 3, Z, (e_3) is $\|$ to **ND**. A third section would provide information that could be used to check the size distribution. The ellipsoids used here are assumed to have their semi-axes aligned with the specimen axes although the method allows for the ellipsoid orientations to vary (an untested option).

3.3 Ellipsoid Shape Distribution

The basic assumption, as stated earlier, is that the grains can be approximated as ellipsoids. This assumption holds true for the aluminum samples discussed in this thesis. Figure 3.3 shows the three semi-axes as a along X axis, b along Y and c along Z axis respectively. Each ellipsoid can be completely described by its semi-axes, eq. 3.1.

$$\left(\frac{x}{a}\right)^2 + \left(\frac{y}{b}\right)^2 + \left(\frac{z}{c}\right)^2 \leqslant 1 \tag{3.1}$$

Assuming that there is no gradient in grain size through the sample and that the ellipsoids have the same orientation, then a homogeneous distribution of ellipsoids $f(a,\ b,\ c)$ is sufficient to represent the grain size and shape distribution. Even though the full form of $f(a,\ b,\ c)$ is impossible to calculate, one can approximate or estimate it by eq. 3.2.

$$f\,(a,\ b,\ c) = f\,(a,\ b) \cdot f\,(c|b) \tag{3.2}$$

Both $f(a,\ b)$ and $f(c|b)$ can be obtained from the set of orthogonal orientation scans. The procedure to obtain these is described in detail elsewhere.[7]

3.4 Population of Ellipsoids

3.4.1 Sampling from distribution

The simulation domain is in the form of a cubical box whose dimensions are 1×1×1. This box is populated with a sampling of ellipsoids drawn from the distribution $f(a,\ b,\ c)$. For this purpose the distribution function $f(a,\ b,\ c)$ must be scaled appropriately. The values of the semi-axes a, b and c must be expressed in terms of fractions of the box size, in this case 1. The scaling factor is determined by the total number of grains desired in the final microstructure. For example, consider a microstructure with 1000 monodispersed equiaxed grains, that is $a = b = c$ and $f(a,\ b,\ c)$ is the delta function. The values of a, hence b and c, are picked such that;

$$1000 \times (volume\ of\ a\ ellipsoid) = 1$$

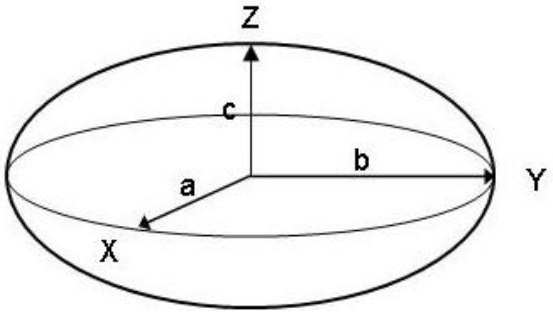

Figure 3.3: Ellipsoid

$$(volume\ of\ a\ ellipsoid) = \frac{4}{3} \times \pi \times a^3$$

giving $a \sim 0.05$.

For each ellipsoid generated the semi-axes are chosen from the given distribution function. This can be done by generating values for a', b' and c' such that, $0 > a' \geq a_{max}$, $0 > b' \geq b_{max}$ and $0 > c' \geq c_{max}$ respectively. Next a random number, say r_1, is generated. The choice of a', b' and c' is accepted if $f(a',\ b',\ c') \leq\ r_1$. If the choice is accepted the ellipsoid is placed inside the simulation box by randomly choosing coordinates as its center.

Thus a set of overlapping ellipsoids is generated. The exact scheme used in this study will be discussed in a later section 3.9.3. The total number of ellipsoids generated is many times the target number of grains (by a factor of about 10-100).

3.4.2 Minimal subset

Out of this set of ellipsoids only a minimal subset is retained such that it optimally fills the simulation box. An optimal filling is defined as a system having minimal overlap and maximum space filling. This could be achieved by solving a many-body dynamics problem as in [8]. Since there is no theory to indicate a unique solution to this problem, however, the approach discussed here uses Monte Carlo integration to approximate the packing.

The Simulation box is populated by Monte Carlo integration points. In the present case we use the ellipsoid centers as integration points. The system

cost for each point is evaluated by calculating the number of ellipsoids that a given point is contained within. Consuming a point decreases the system cost by a fixed amount, say β. If another ellipsoid tries to engulf a point contained in another ellipsoid, the system cost increases by another amount, say α.

Even though we do not want the ellipsoids to overlap, the penalty assessed for engulfing a Monte Carlo point should not be same throughout. For example a point well within the engulfing ellipsoid should have a higher penalty than a point near its periphery. The following function is used to quantify α.

$$\alpha = \frac{-\omega}{1 - \frac{1}{\zeta^2}} \left(1 - \frac{E^2}{\zeta^2} \right) \tag{3.3}$$

where, ω is the overlap encouragement factor, ζ is the zero penalty and E is the ellipsoid function. Given a point $(i,\ j,\ k)$, an ellipsoid with semi-axes $(a,\ b,\ c)$ and an ellipsoid center $(x,\ y,\ z)$, then the *ellipsoid function* is defined by equation 3.4. Since a given integration point might be contained in more than one ellipsoids the total penalty is just the sum of individual penalties.

$$E = \left(\frac{i - x}{a} \right)^2 + \left(\frac{j - y}{b} \right)^2 + \left(\frac{k - z}{c} \right)^2 \tag{3.4}$$

The values of ω and ζ are chosen empirically to achieve maximum space filling and minimum overlap. For example, for the work described in the

later sections we used values of 1.00 and 0.95 for ω and ζ respectively. Using these to calculate the cost decrease, β, for removing a point and overlap penalty, α, the system energy can be calculated. Numerical experiments suggest that these values are near optimal and that the packing algorithm will only generate small deviations from these values.

A simulated annealing algorithm is used to choose a subset of the ellipsoids by minimizing the system energy. The algorithm proceeds in the following manner. A random subset of the ellipsoids is chosen from the original set such that the total volume contained in the subset is about the same as the box volume. The total energy of the system is evaluated. This energy is then minimized by a series of add, subtract, swap and jog transactions. Any transaction that reduces the energy is accepted. If a transaction increases the energy then it is accepted with a certain probability depending on the amount of increase (which is a user input). The transactions allowed are *addition* where a randomly chosen ellipsoid is added to the existing set; *subtraction* is where a randomly chosen ellipsoid is taken out of the set; *swap* is where a randomly chosen ellipsoid in the set is replaced by another randomly chosen ellipsoid not in the set; and *jog* is where a randomly chosen ellipsoid is replaced by another ellipsoid contained in it.

The procedure discussed above generates an optimal set, $\mathcal{E}$, of ellipsoids which forms the grain structure in the final microstructure. There might be regions, in the simulation box, that are contained in more than one ellipsoid and others that are not contained in any. To overcome this difficulty, the

***C**ellular **A**utomaton* (CA) approach[7] can be used. In the *CA* the centroids of the ellipses are used as nucleation sites and the grains are allowed to grow until they impinge and the total space is filled. Even though this automatically eliminates overlaps and empty space in the box, the output is not a periodic structure but , it can easily be made to be so. The approach discussed in the next few sections uses a Voronoi tessellation based approach to generate a non overlapping and space filling microstructure.

3.5 Voronoi Diagram

Voronoi Diagrams have been known for more than century. They have been studied since middle of the 19^{th} century, first by Dirichlet[1850] and by Voronoi[1908]. The concept finds uses in the natural sciences, mathematics and computer science. Some of the applications are *Wigner-Seitz zones, Johnson-Mehl and Apollonius Model, Thiessen Polygons, nearest neighbor clustering, facility location, path planning, medial axis* etc. Given a set of points in a region, the *Voronoi diagram* divides the region based on a nearest neighbor rule [9]. Let $P = \{p_1, p_2, \ldots, p_n\}$ be a set of points, sites, in Euclidean plane. The Voronoi regions are calculated by partitioning the plane by assigning every point in the plane to its closest site. The *Voronoi region* $V(p_i)$ consists of points at least as close to p_i as to any other site:

$$V(p_i) = \left\{x : |p_i - x| \quad \leq \quad |p_j - x| \;\; \forall j \neq i\right\} \tag{3.5}$$

Some points do not have a unique site as a nearest neighbor. The set of all the points that have more than one nearest neighbor form the *Voronoi diagram* $\mathcal{V}(P)$ [10]. In other words: "The Voronoi diagram of a finite set of S points in the plane is a partition of the plane so that each region of the partition is the locus of points which are closer to *one member* of S than to any other member. [11]"

3.5.1 Properties of Voronoi Diagrams

Some of the important properties of the Voronoi diagrams are listed as follows:

V1. Each Voronoi region $V(p_i)$ is convex

V2. $V(p_i)$ is unbounded iff p_i is on the convex hull of the point set S.

V3. Every nearest neighbor of p_i in S defines an edge of the Voronoi region $V(p_i)$.

V4. Every vertex, v, of the Voronoi Diagram, $\mathcal{V}(P)$, is the circumcenter of a facet of the Delaunay triangle associated with v.

3.6 Tessellation

As stated previously we are interested in generating a non-overlapping space filling structure. The idea here is to do so by utilizing the properties of

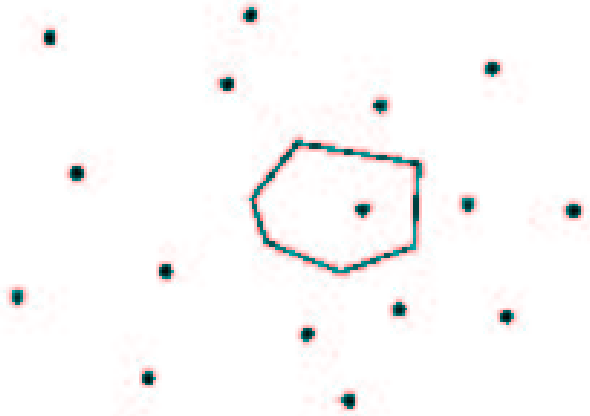

(a) Voronoi region

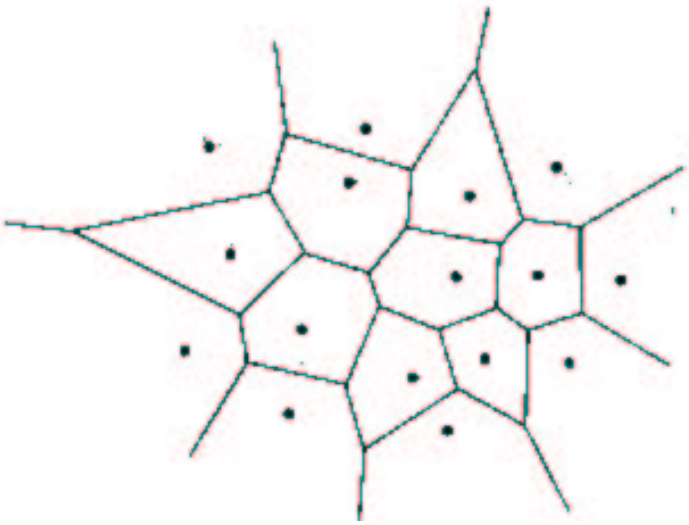

(b) Voronoi Diagram of the same set

Figure 3.4: (a)Voronoi region (b)Voronoi diagram [9] on a set of points

Voronoi diagram $\mathcal{V}(P)$. The Voronoi diagram divides the space into Voronoi regions, which by definition is a non- overlapping set. The method used to compute the Voronoi diagram utilizes Delaunay triangulation, which is a straight line dual of $\mathcal{V}(P)$. To generate the Voronoi regions the space[1] is sampled randomly with points, so call this set $\mathcal{S}$. For each of the sampled points in $\mathcal{S}$, the number of ellipsoids, from the set $\mathcal{E}$ (as defined in 3.4.2), that it is contained in can be calculated. Out of these sampled points, only those contained in one and only one ellipsoid are retained. That is, if a point is contained by more than one ellipsoid, or is contained in neither, it is eliminated from $\mathcal{S}$. Using this set $\mathcal{S}$ we construct the Voronoi diagram $\mathcal{V}(P)$. According to the property **V2** of the Voronoi diagram as stated 3.5.1 all the Voronoi regions associated with the points in the input set $\mathcal{S}$ which do not lie on the convex-hull of $\mathcal{S}$ are bounded. This implies, however, that the points on the convex-hull of $\mathcal{S}$ are unbounded. To overcome this problem and also to generate a periodic structure the input set $\mathcal{S}$ is modified as described below. As described earlier to generate the set $\mathcal{S}$ we sample the space, which we will call $\mathcal{R}$. $\mathcal{R}$ is a bounded box as defined by user. For purpose of outlining the method say it is a box bounded by $x = 0; x = X; y = 0; y = Y; z = 0$ and $z = Z$ planes. Hence the points in $\mathcal{S}$ are bounded by $(0, 0, 0)$ and $(x1, y1, z1)$. For every point p_i in $\mathcal{S}$, 26 copies are generated by adding or subtracting X or Y or Z to the coordinates of p_i. That is, if the coordinates of p_i are $(x1, y1, z1)$ then the copies of p_i are $(x1 - X, y1 - Y, z1 - Z)$, $(x1 - X, y1 - Y, z1)$,

[1] not the entire space but only a subspace. For example $1 \times 1 \times 1$ box.

$(x1 - X, y1 - Y, z1 + Z)$, $(x1 - X, y1, z1 - Z)$ $\ldots$ $(x1 + X, y1 + Y, z1 + Z)$. As a result the points which were on the convex hull of $\mathcal{V}(P)$ are now interior points and hence the Voronoi regions associated with them are all bounded.

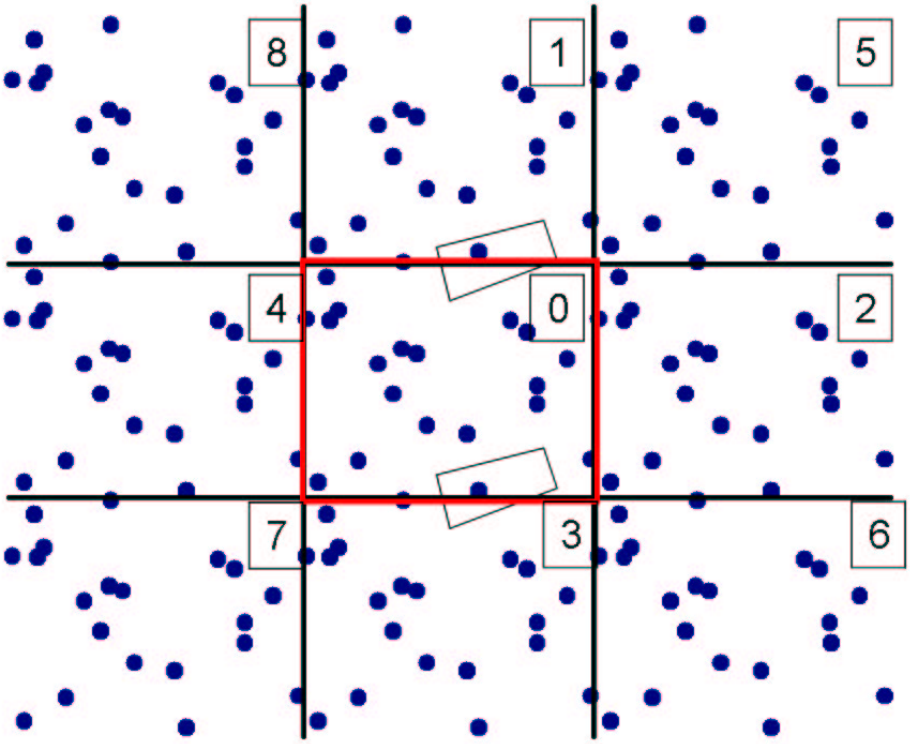

Figure 3.5: Periodic Structure

The figure 3.5 illustrates this in 2 dimensions. The original space from which 20 points are chosen randomly is the central highlighted square. This square is padded from all the sides with its eight nearest, first and second, neighbors. These are populated by making copies of the points, already selected, displaced in one or both the orthogonal directions by the size of the box. To demonstrate the effect on the points on the convex hull and the

periodicity, consider the point, p, bounded by the box and contained in the central square. The box around it is the Voronoi region associated with it, obtained by drawing the perpendicular bisectors between p and its nearest neighbors. This would have been unbounded if p were on the convex hull. Now corresponding to p there are eight more copies. The one of the most interest, however, is the one contained in square directly above it, that is in square "1", label it p'. The Voronoi region associated with p is clearly not contained in the bounding box, square "0". At the same time the Voronoi region $V(p')$ is not contained entirely in "1" and some of it "leaks" into "0". This is an exact replica of the part of $V(p)$ which lies outside the box "0" but is displaced by the box height. Thus it appears as if the Voronoi region associated with p is continued at the top of the box. It is easy to see that the same would hold true for any other point on the convex hull. Now if only the original square, "0", is retained (after constructing $\mathcal{V}(P)$ on the extended space) then we obtain a network of Voronoi cells (regions) which are periodic in the box length.

3.7 Grain Assignment

As stated in section 3.6 the space is sampled and only points which lie inside one and only one ellipsoid are retained. Hence it is possible to assign every point in $\mathcal{S}$ to an ellipsoid. After constructing the Voronoi diagram on the extended set $\mathcal{S}'$ the resulting Voronoi regions have a one to one correspon-

dence to the points in $\mathcal{S}$. That is for every Voronoi region $V(p_i)$ there is a unique point $p_i \in \mathcal{S}$. Hence the Voronoi regions/cells can also be assigned to ellipsoids in $\mathcal{E}$.[2] These Voronoi regions can be aggregated into grains by assigning them to an ellipsoid. For example if ellipsoid $E_m \in \mathcal{E}$ contains points $p_i, p_j, \ldots p_k$ and hence the Voronoi regions $V(p_i),\ V(p_j), \ldots,\ V(p_k)$ are aggregated to form a single grain, with grain id m. Thus all the Voronoi cells can be aggregated to form a set of grains.

As the cells themselves are non-overlapping and space filling, the grains are just collections of cells, are also non-overlapping and are space filling. Also, since the grains are roughly similar to the ellipsoids in the set $\mathcal{E}$, they have a similar shape and size distribution as dictated by distribution function $f(a,\ b,\ c)$. The detailed quantitative relationship between these distributions has, however, yet to be determined. The output microstructure obtained is in terms of Voronoi vertexes, edges, and patches. If desired one can convert it to a regular grid in the following manner:

1. Sample the box on a regular grid. For example, insert points along the X axis with a step size of 1.

2. For every point find the Voronoi region and hence the grain that it is contained within.

3. Assign each point the grain id.

[2]Even though the point p_i is contained in ellipsoid E_m, the associated Voronoi region $V(p_i)$ need not be entirely contained in E_m.

3.8 Texture

Once the microstructure is generated, texture can be added to it using the approach discussed by Miodownik *et al.* [12] and Saylor *et al.* [7]. The assumption made is that the crystallographic texture for the entire polycrystalline material can be sufficiently summarized in terms of the orientation distribution (ODF) and the misorientation distribution (MDF) across grain boundaries. Also any effects of long distance correlations, if present, are negligible.

3.8.1 Texture input

As stated in section 3.2.1 the input is in the form of EBSD maps having orientation and grain shape/size information. The observations have the orientation information, for each pixel of the scan, in terms of Euler angles ($\phi_1,\ \Phi,\ \phi_2$) with respect to the sample axes. Since the measurements on EBSD do not take into account the symmetry, the observed angles have to be rotated so that they are brought into the *fundamental zone*. These Euler angles are converted into vectors in homochoric space and binned (as decided by the user, but a typical discretization uses 1000 cells in the ODF and 1000 cells in the MDF). Using this orientation information a discrete form of the ODF, $f_{exp}(g)$, can be calculated. Similarly a discrete form of the MDF, $f_{exp}(\Delta g)$, can be calculated by using a pair of orientations. The pair is chosen such that each observation is across a grain boundary segment. A

grain boundary segment is defined by pixels having a misorientation θ greater than a value θ_0, which is decided by the user.

3.8.2 Texture Assignment

To assign texture to the generated microstructure another assumption, in addition to the ones stated at the beginning of this section, is made. We assume that each entire grain has one single orientation. That is, there is no spread in orientation inside each grain. Every voxel has the same value for the set of quaternions or Euler angles describing the orientation. This assumption though is not entirely accurate. The assumption is that the average behavior of the macroscopic system does not depend on the spread of orientation inside each grain but depends only on the average orientation of grain. The effect of orientation spread or the presence of dislocations in the grains is expressed through the stored energy in each grain.

Initially each grain is assigned a orientation chosen randomly. One could also make an educated guess based on prior knowledge of the material and its history to chose the set of initial assignments. When the grains are aggregated to form the microstructure (as described in section 3.7) a list of volumes contained in each grain and the boundary areas between different grains is also generated. Using these the ODF and the MDF for the generated microstructure are calculated; we call them $f^{sim}(g)$ and $f^{sim}(\Delta g)$ respectively. Once we have the values of $f^{sim}(g)$ and $f^{sim}(\Delta g)$ the error value, λ , between the experimental and the assigned values is calculated using equation 3.6,

$$\lambda = \sum_{i}^{i_{max}} \left(f^{sim}(g)_i - f^{exp}(g)_i\right)^2 + \sum_{j}^{j_{max}} \left(f^{sim}(\Delta g)_j - f^{exp}(\Delta g)_j\right)^2, \quad (3.6)$$

where index i is over all the orientation categories and index j is over all the misorientation categories. Once the system error is calculated the goal is to reduce it by orientation change and orientation swap operations. An orientation change will changes the orientation of a randomly chosen grain to a random orientation. An orientation swap choses two grains and swaps their orientations. After each operation, chosen randomly from the two described above, the new system error (λ^{new}) and the change in the error ($\Delta\lambda$) are calculated, where $\Delta\lambda = \lambda^{new} - \lambda$. An operation is either accepted or rejected based on the probability given by equation 3.7 (which is similar to 2.9).

$$P = \begin{cases} 1 & \Delta\lambda \leq 0 \\ \exp\left(\frac{-\Delta\lambda}{\mathrm{T}}\right) & \Delta\lambda > 0 \end{cases} \quad (3.7)$$

Hence every operation which reduces the system error is always accepted and the probability of accepting the operation, if the system error increases, determined by the value T, is less than one. The iteration procedure is repeated until the error is reduced below a predetermined limit or after a certain predetermined number of iterations (~ 50).

3.9 Application to commercial purity Aluminum

3.9.1 Experimental Observations

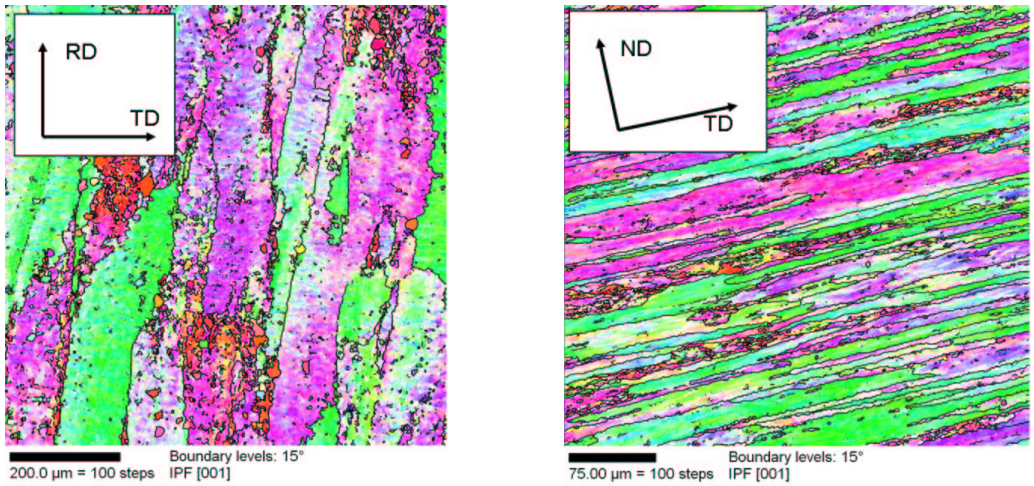

(a) Planar view

(b) Transverse view

Figure 3.6: Deformed Micro structure (experimental observation on the Al-1050 sample)

The figure 3.6 shows two orthogonal views of the commercial purity Aluminum sample that was to be modeled. The planar view is a of section perpendicular to the sample normal direction (**ND**) and the transverse view is of a section perpendicular to the sample rolling direction (**RD**). The EBSD maps were obtained in a Phillips FEI XL40 Field Emission Gun scanning electron microscope using the TSL^{TM} EBSD software. The first conclusion one can draw by visually inspecting the microstructure is that the grains are extremely elongated along the rolling direction. After analyzing the mi-

crostructure the grains were shown to have semi-axes ratios of approximately >20:4:1. The material also shows the expected rolling texture components, S, brass and Copper, along with some amount of cube component. About 32% of the texture could not be resolved into any of the standard texture components for Aluminum.[3]

3.9.2 Geometrical Stretching

Due to the memory constraints on a serial machine and the design of the algorithm there is a limit on how many grains can be included when generating a microstructure. Also, if the experimentally observed microstructure has elongated grains then it puts additional constraints on the Microstructure builder. One could solve this problem while still working within the framework of the Microstructure builder by parallelizing the code. This, however, would have been a time intensive solution. The other way is to get around it is by generating a slightly non-equiaxed structure and then subject it to an affine expansion. The Microstructure Builder can be broken down into 4 parts. These are summarized in table 3.1. The first three steps are carried out the same way as described earlier. The output of step three (tessellation) gives the Voronoi cells which are then aggregated to from the grain structure in step four. We expand the Voronoi cells by scaling the vertexes forming the cell appropriately. For example let the desired stretching by $5\times2\times1$ along

[3]We used a 15 ° disorientation from the exact location of a component as the criteria for binning

RD, TD and ND respectively. To achieve this stretch each set of vertex coordinates of each cell are multiplied by a (5,2,1 stretch), assuming that RD is along X axis, TD is along Y axis and ND is along Z axis.

Table 3.1: M S Builder

step no.	brief description
1	Extraction grain geometry from the EBSD maps
2	Generation of a optimal set of ellipsoids
3	Tessellation
4	Grain aggregation from the tessellation

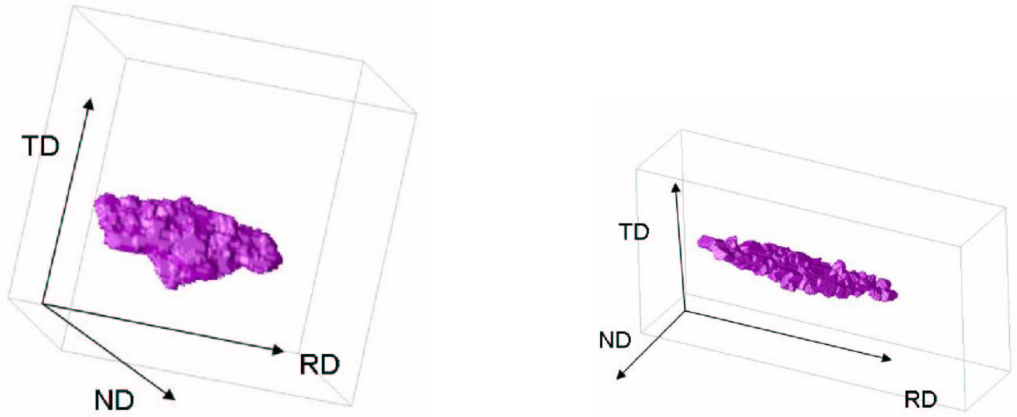

(a) before stretching (b) after stretching

Figure 3.7: Affine stretching

Figure 3.7 shows the effect of stretching on one grain in the microstructure. The grain is stretched along the RD by a factor of 5, along the TD by a factor of 2 and no stretching is applied along ND. The volume of the grain as a result of this stretching is increased by a factor of 10.

3.9.3 Simulated Microstructure

We will present the results here and a detailed discussion will follow in chapter 6. The initial input to the microstructure builder was a list of ellipsoid centers sampled from a $1\times1\times1$ box. Even though the observed semi-axes ratio was >20:4:1, it was not possible to generate a microstructure with a large number of grains having a distribution with an average semi-axes ratio of >20:4:1. Hence initially a microstructure with semi-axes with a ratio of $3 \times 2 \times 1$ was generated which was then subjected to an expansion of $5 \times 2 \times 1$.

Each ellipsoid was assigned values for the semi-axes drawn from a flat distribution centered around an average value of (0.09,0.06,0.03). The center coordinates are chosen using following scheme. Choose an arbitrary point in the box as the coordinates of the center of an ellipsoid. Compare the box size with the minimum of the semi-axes lengths of said ellipsoid. If the box size is greater than twice the minimal semi axis then divide the box into 8 quadrants and re-sample, that is add another, new, ellipsoid (for each quadrant) to the list. This procedure is repeated by subdividing each of the boxes recursively until the box size is less than or equal to a user input fraction (default value set at 0.333) times the minimal semi axis length. Figure 3.8 illustrates the above with the means of a flow diagram.

Using the above set of ellipsoid centers as input we selected a subset which had maximal space filling and minimal overlap. The set of ellipsoids thus generated was then padded from all sides by half the box size, following

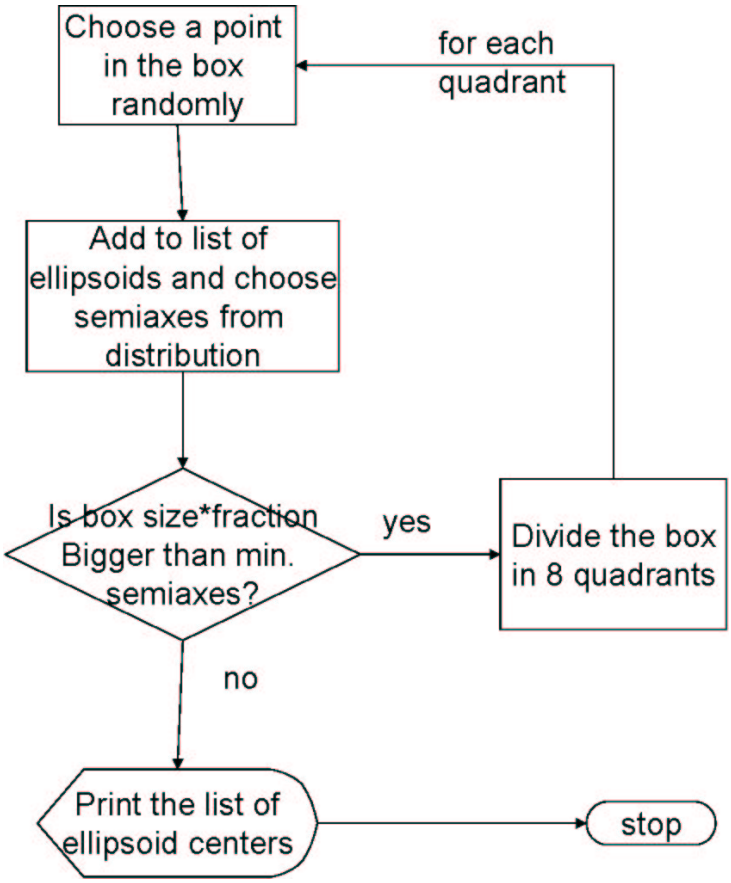

Figure 3.8: Flow diagram illustrating the the process of population of ellipsoids

the scheme as discussed in 3.6, to form an input to the tessellation. The Voronoi cells are then grouped to form the final microstructure.

Figure 3.9 shows the simulated microstructure after the stretching. The microstructure depicted in figure 3.9 has ~800 grains. Using the procedure discussed in section 3.8 texture is added to the microstructure. Figure 3.10 shows the texture fitting. The error (λ) at the start of the texture assignment

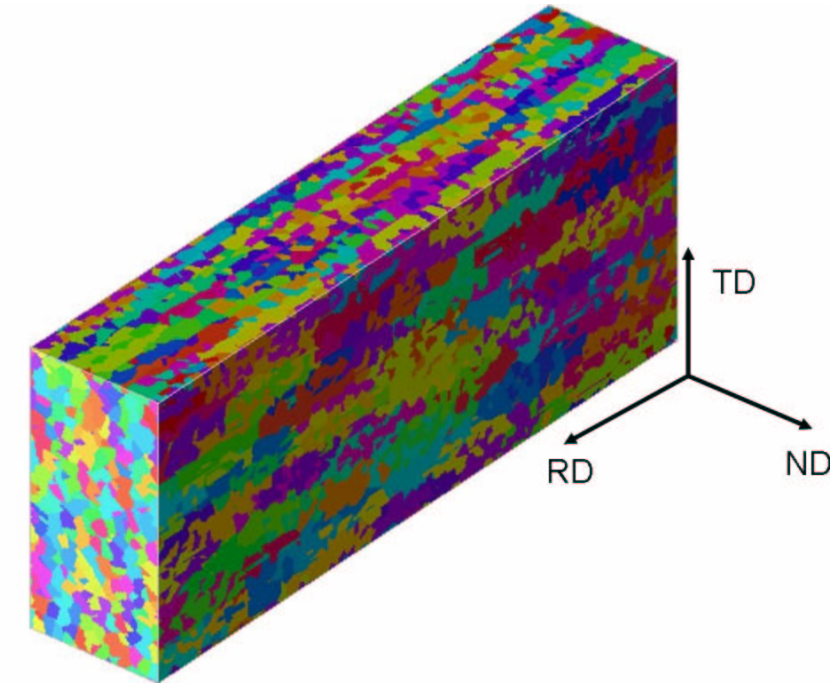

Figure 3.9: Simulated Microstructure (output of the Microstructure Builder)

was 0.0086 and at the end was 8.7×10^{-5}.

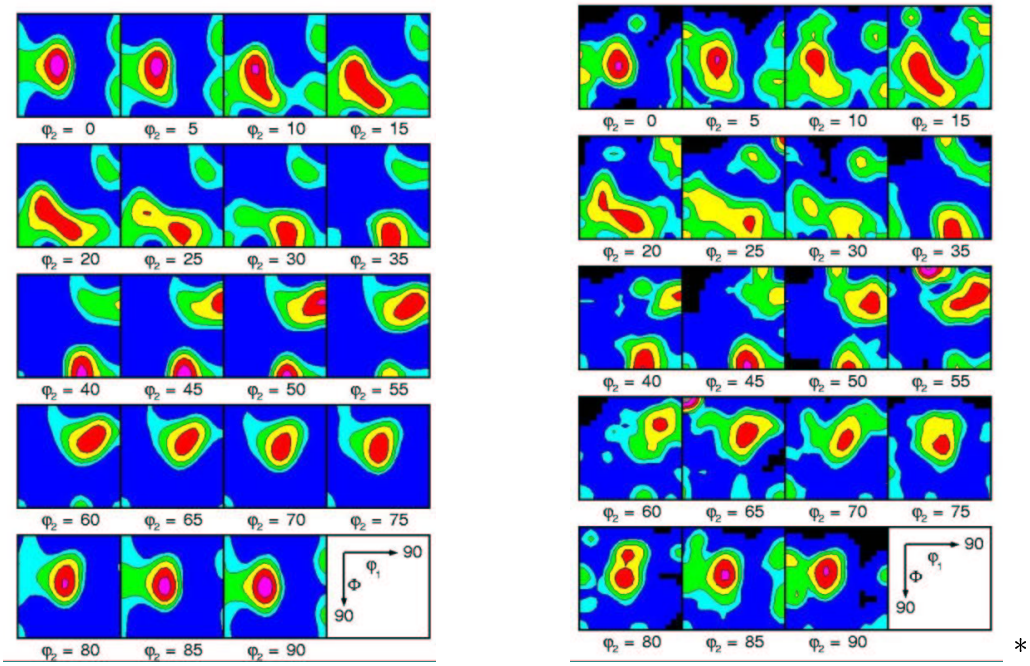

(a) Input Texture (b) Fitted Texture

Figure 3.10: Texture Fitting (average value is 100)

Chapter 4

Recrystallization Kinetics

4.1 Recrystallization

The process of recrystallization can be broadly divided into **nucleation** of new grains and **growth** of these new grains. Figure 4.1 shows a typical recrystallization behavior. It shows a plot of fraction recrystallized of the deformed material as a function of time. At early times there are nucleation events. This is then followed by subsequent growth of the new grains until the growing grains impinge each other. Even though for any given (recrystallizing) grain the events of nucleation and grain growth occur in the given order, in general these process can occur simultaneously in various parts of the material. These and other important topics concerning the kinetics of recrystallization will be discussed in the following sections of this chapter.

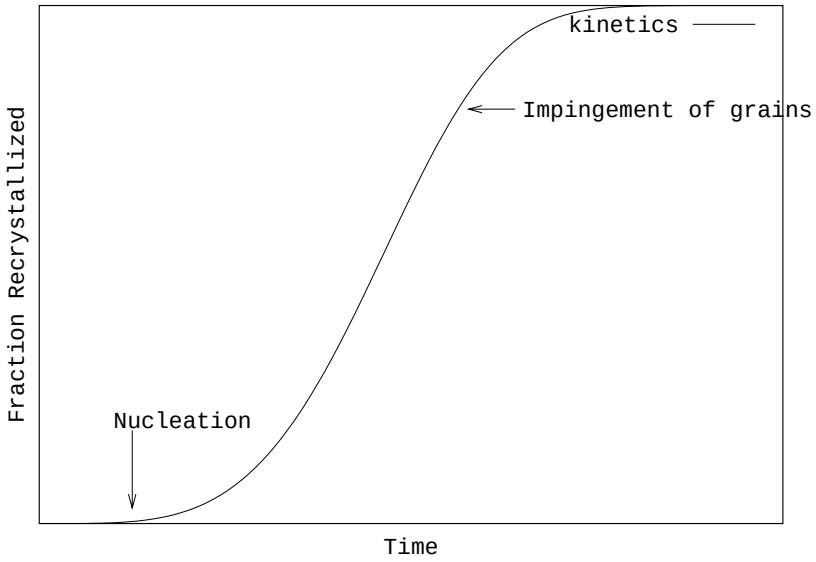

Figure 4.1: Typical recrystallization Kinetics

4.2 Nucleation

We begin by defining, for at least this discussion, what we mean by a nucleus. A **nucleus** is a small grain or crystal having a relatively dislocation free interior growing into the deformed matrix. As a result, the stored energy for the nucleus is small and the difference in the stored energy between nucleus and the deformed matrix constitutes the driving force for the process of recrystallization. The nuclei are separated from the surrounding deformed matrix (grains) by high angle grain boundaries. As stated in the previous section, nuclei can be formed at any time during the process of recrystallization. This makes nucleation a complex phenomenon to model. Since there is so much variability in the nucleation rate it is also an important factor influencing

the rate of recrystallization. The rate at which nuclei are generated in the deformed structure, in general, will be a function of time.

$$\begin{aligned} I(t) &= N_0 + N_1 t^n \\ \dot{I} &= N_1 n t^{n-1} \end{aligned}$$

where I(t) is the number of nuclei at any given time t. N_1 and n are constants. $\dot{I}$ is the rate at which new nuclei are formed. Clearly if n = 0 then the system has a fixed number of nuclei present at time $t = 0$. This special case is called *site saturated nucleation*. When n = 1 we get a constant rate for nucleation; this case is called the *constant nucleation rate* case.

Apart from the nucleation rates there can also be variability in the occurrence of nuclei in the microstructure. Cahn[40] has made a detailed analysis from the perspective of occurrence of nuclei at specific sites. The nuclei can be formed at grain boundaries (where two grains meet) or at edges (where three grains meet) or corners (where four grains meet). The effect of occurrence of nuclei at specific sites will be discussed further in 4.4.

4.3 Factors affecting recrystallization kinetics

Here we list the major factors of interest.

F1. **The deformed structure.** The amount of deformation and the mode[1] of deformation affect the rate of recrystallization. Deformation affects the amount of stored energy and the number of nuclei as well as their neighborhood in the microstructure. Anderson and Mehl [25] showed that with an increase in tensile strain the rate of recrystallization increases in aluminum. Also for most materials there is a minimum strain below which recrystallization will not take place. Above this threshold the rate of recrystallization increases steadily until it hits a plateau and does not increase further.

F2. **The deformation texture.** Different grains in the same microstructure have a difference in the stored energy due to the differing activities of the active slip systems present. This in turn depends on the initial orientations of the grains. Hibbard and Tully [37] showed that single crystals having different orientations showed different recrystallization kinetics.

F3. **The deformed grain size.** Fine grained material is generally found to recrystallize much faster than a coarse grain material. This is due to more nucleation sites being available since there is more grain boundary area available for smaller grain sized material than in a material with coarse grains. Hutchinson et al. [38] showed the effect of initial grain size on kinetics in copper.

[1] only plane strain compression considered

F4. **Solutes.** The primary effect of solutes is to slow down the recrystallization front through solute drag [39]. Therefore recrystallization temperatures rise with increasing solute content.

F5. **The annealing conditions.** Annealing conditions such as annealing temperature and heating rate have a great effect on the kinetics. The rate of recrystallization has a Arrhenius relationship with the annealing temperature, given by equation 4.1.

$$\text{Rate} = \frac{1}{t_{0.5}} = Cexp\Big(-\frac{Q}{\beta T}\Big) \tag{4.1}$$

where $t_{0.5}$ is the time it takes for 50% of the material to recrystallize, Q is the activation energy, T is the annealing temperature and β is the Boltzmann constant. This is a direct consequence of the thermally activated nature of both the nucleation and growth stages.

4.4 The JMAK model

The **J**ohnson-**M**ehl-**A**vrami-**K**olmogorov or the JMAK model is the basic theory of recrystallization kinetics and transformation kinetics in general. Even though Kolmogorov (1937), Johnson and Mehl (1939) and Avrami (1939) developed their theories independently around the same time, we shall treat them as one single model. The model makes some fairly simple assumptions to arrive at a relationship between the fraction of recrystallized material

as a function of annealing time, depicted in equation 4.2:

$$\mathrm{X} = 1 - exp(-kt^n) \tag{4.2}$$

where X is the volume fraction of the recrystallized material

$$X = \frac{Volume\ rex.}{total\ Volume}$$

t is the time and k and n are constants. The model assumes that the nucleation sites are randomly distributed in space. It also assumes an isotropic growth rate. Although the model is simplistic it gives us a useful tool to study the kinetics of recrystallization because the microstructure and the spatial characteristics of nucleation dictate the exponents one gets from the Avrami plots. The details of the model can be found in the original papers of Kolmogorov [41], Johnson and Mehl [42] and Avrami [43, 44, 45]. The article by Christian has a good discussion about the relation between nucleation and growth rates and the exponents[46].

From Avrami [44] we have the following relation between the extended volume (V_{ex})[2] and the volume (V), where the assumption of random distributions of nuclei is critical;

$$dV = dV_{ex}(1 - V) \tag{4.3}$$

[2]volume of the material that would have recrystallized in absence of impingement of nuclei on each other

$$V = 1 - e^{-V_{ex}} \tag{4.4}$$

A similar equation can be derived for the extended volume fraction.

$$X = 1 - e^{-X_{ex}} \tag{4.5}$$

where X_{ex} is the extended volume fraction given by equation 4.6

$$X_{ex} = \int_0^t V dN \tag{4.6}$$

$$dN = \dot{N} dt \tag{4.7}$$

$$\therefore \quad X_{ex} = \int_0^t V \dot{N} dt \tag{4.8}$$

Depending on the rate of nucleation and the spatial characteristics of nucleation[3] the value of the extended volume fraction will change. As an example, for continuous nucleation ($\dot{N} = N_0$, constant) with random placement and sufficiently low volume fraction of nuclei[4] we get $X_{ex} = C_1 N_0 t^4$ where C_1 is a geometrical factor.

One can make Avrami plots, plot log(log(1/(1-X))) as a function of log(t), to obtain the JMAK exponents (slope of the plots). Cahn [40] discusses the effect of non random nucleation in the case of site saturated nucleation. He also gave master curves for the various nucleation schemes. Table 4.1 summarizes the theoretical exponents one can obtain using the JMAK approach.

[3] grain boundary nucleation or edge nucleation or corner nucleation

[4] so that we can ignore the effect of impingement effects. Normally, JMAK assumes infinitely small (point) nuclei.

Experimental observations of Rosen *et al.* [34] have shown the presence of a transition point in exponents between the short times and long times. This transition is presumably due to the impingement of growing grains.

4.5 Experimental exponents

There were several early experiments, for example Anderson and Mehl [25], showing good agreement with the theoretically expected value for JMAK exponent of n$\sim$4. These experiments had very low amounts of deformation so that the nucleation truly approached random distribution. Yet, experiments involving larger deformations rarely show good agreement with the expected exponents. Often the JMAK plots are nonlinear or have a slope of less than 3, for a site saturation assumption, or both. These departures from the theoretical predictions can be attributed to the effect of the following factors

1. **Non-Random distribution of the nuclei:** There is evidence of non-random nucleation in almost all materials including a particular study presented with this work in later chapters. Examples of non-random nucleation in literature include the works of Rosen et al.[34] in iron,

Table 4.1: Theoretical JMAK exponents

Nucleation type	Continuous nucleation	Site saturated nucleation
Corner	4	3
Grain Edge	3	2
Grain Boundary	2	1

Hutchinson et al.[38] in in copper and Hjelen et al. [35] in aluminum.

2. **Recovery during recrystallization:** Vandermeer and Gordon[36] showed that the lower exponents can be explained using loss of driving pressure due to simultaneous recovery.

3. **Stored energy:** Hutchinson et al.[38] showed that the regions with higher stored energy recrystallized first. Rollett et al.[47] showed using Monte-Carlo simulations the effect of non-uniform stored energy on the lowering of JMAK exponent.

In short, the variation in the JMAK exponent from the theoretical values has been well studied and is mostly attributed to the inhomogeneity in the microstructure giving rise to non-random nucleation or non-random distribution of the stored energy.

4.6 Simulation

All the simulations were carried out by using the Monte Carlo model [48, 49, 50, 51, 52]. The input microstructure was in form of a regular lattice structure on a cubic grid. All the simulations assumed site saturated conditions for nucleation based on experimental evidence[56]. All the nuclei were added to the microstructure at time $t = 0$ and the system was allowed to evolve. The values of JMAK exponents were obtained by plotting ln(ln(1/(1-X))) against ln(t). These exponents were compared with the ex-

perimentally obtained exponents from the recrystallization kinetics of Al1050 samples annealed isothermally. The JMAK exponents were obtained for different temperatures. It was found that for the different temperatures the JMAK exponents remained unchanged[56].

4.6.1 Results

Table 4.2: Comparison of the time scaling to obtain the JMAK exponents for the experimental and simulated cases

Simulation conditions	δt experimental in sec.	δt simulations in MCS
Randomly placed nuclei	50	300
3% nuclei placed only at grain boundaries	50	150
10% nuclei placed only at grain boundaries	50	100
6% nuclei semi-axes ratio 3:2:1	50	1000
6% nuclei semi-axes ratio 15:4:1	50	500

For each set of conditions, Avrami plots are presented alongside the experimental results. The slopes, JMAK exponents in each case, are also included in the plots. Since the time is arbitrary and the "real" initial time point ($t = 0$) can not be determined, an arbitrary fixed value δt was added to all the time values. In both, the as-received sample and the simulated microstructure, there is a fixed initial volume fraction of nuclei. That is, it is assumed, in both cases, that the nucleation has already taken place and that the system has reached a state where there are no further nucleation

events. This implies that a finite time has already elapsed. The value δt was determined so that the JMAK curves were most straight lines. The value of δt was different for different conditions. The values of δt are reported in table 4.2.

Effect of nucleation sites

The following simulations were carried out on a system whose size was a $100 \times 100 \times 100$ box. Figure 4.2 shows the Avrami plot for the case of a low volume fraction, 3%, of nuclei spread randomly throughout the microstructure. A standard linear regression was applied to each dataset and the coefficients in $y = mx + a$ are displayed in the plot.

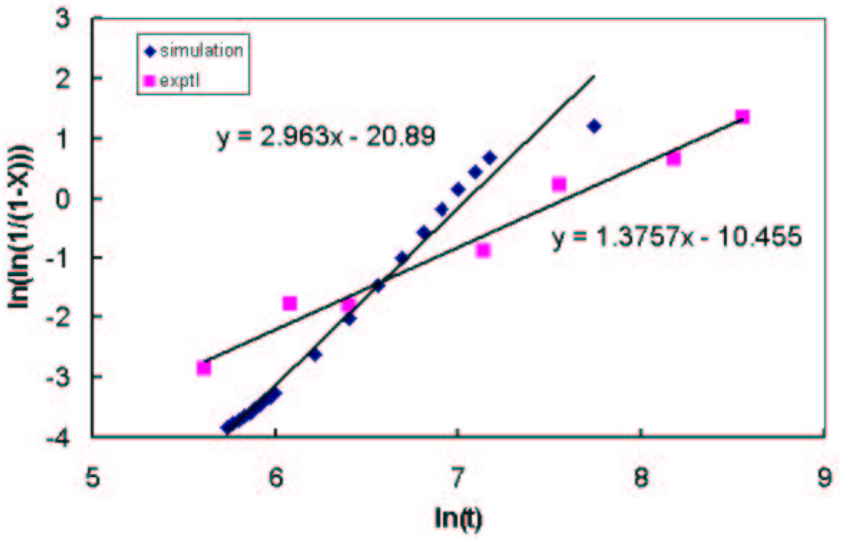

Figure 4.2: Recrystallization Kinetics with randomly placed nuclei

Figure 4.3 shows the results of having the same number of initial nuclei

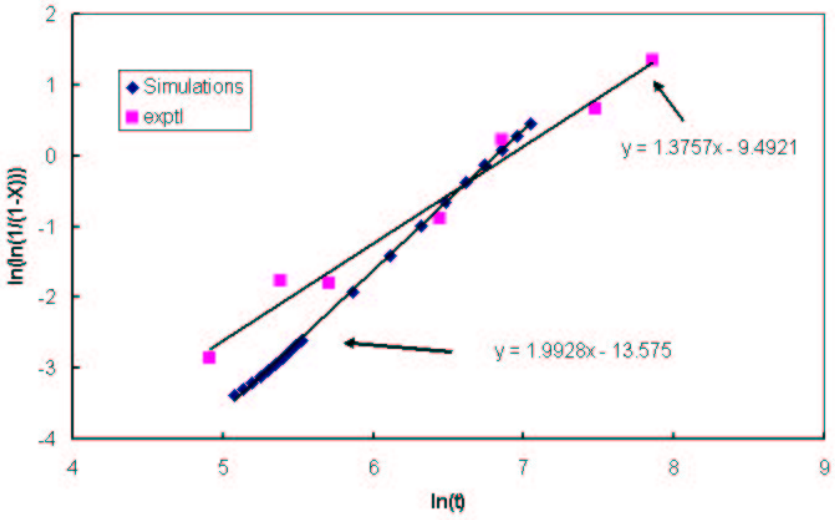

Figure 4.3: Kinetics with 3% nuclei placed only at grain boundaries

in the system, namely 3%, but where the nuclei are placed only at the grain boundaries.

Figure 4.4 displays the result of increasing the number of nuclei put into the system from 3% to 10% while still maintaining the nuclei placement at grain boundaries. Clearly this latter approach leads to the best agreement.

Effect of Grain geometry

For the following results the box size was varied and as a result the ratio of semi-axes was also varied. Figure 4.5 shows a JMAK plot for a nearly equiaxed grain structure. The grains had semi axes ratios of 3:2:1 in RD, TD and ND respectively.

Figure 4.6 shows JMAK plot with a pancake like grain structure. The

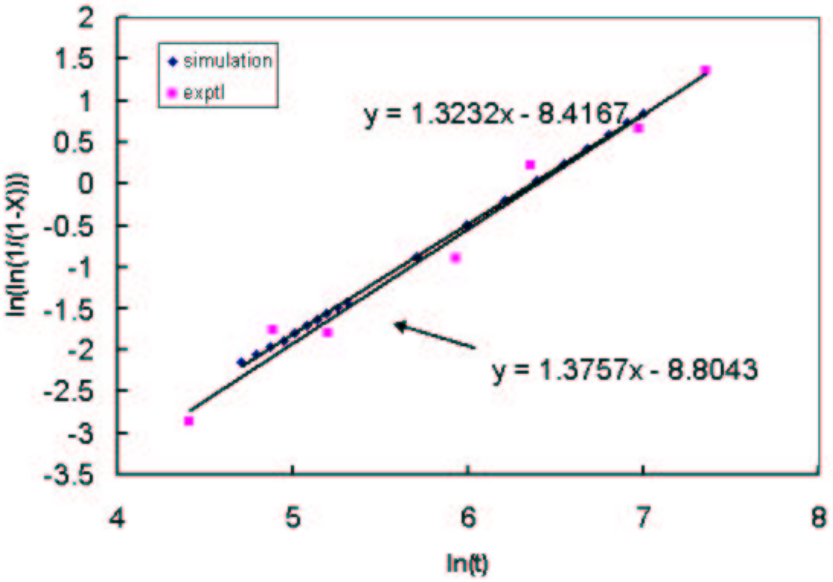

Figure 4.4: Kinetics with 10% nuclei placed only at grain boundaries

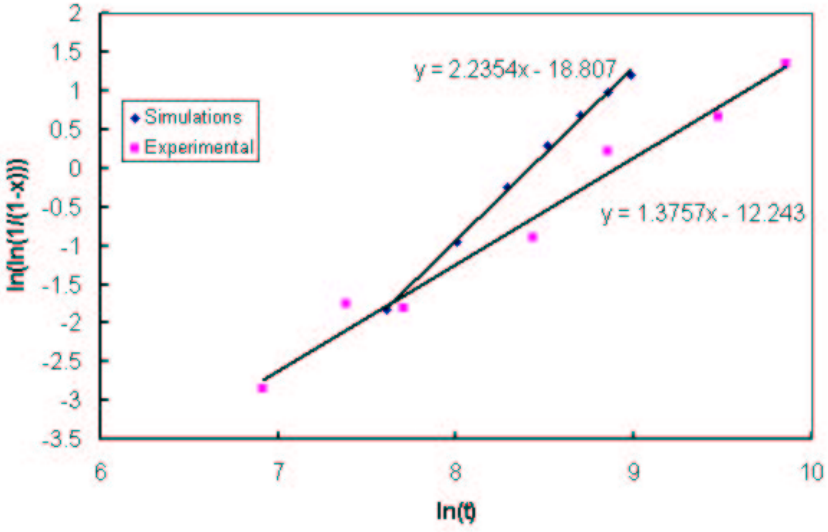

Figure 4.5: Kinetics for a microstructure having semi-axes ratios 3:2:1

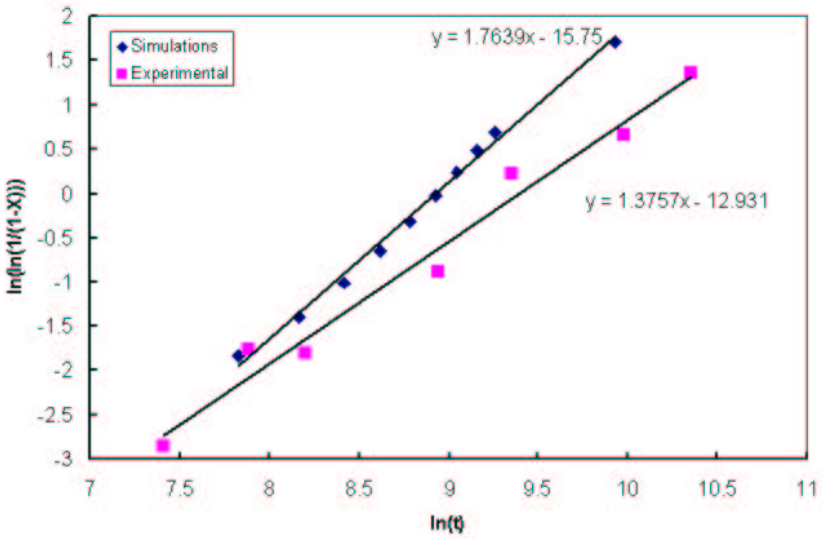

Figure 4.6: Kinetics for a microstructure having semi-axes ratios 15:4:1

Table 4.3: Grain geometry effect on JMAK exponents

Semi-axes ratio	nuclei fraction	JMAK exponent
15:4:1	3%	2.07
15:4:1	6%	1.76
3:2:1	6%	2.24

grains had a semi axes ratios of 15:4:1 in RD, TD and ND respectively. Again the elongated grain shape in the deformed structure resulted in better agreement.

We will discuss the results in more detail in chapter 6. Briefly one can conclude that the grain geometry, nuclei placement and nuclei fraction all affect the recrystallization kinetics.

Chapter 5

Texture Evolution

This chapter primarily discusses the texture evolution during the process of recrystallization. The first part highlights the experimental results and shows the emergence of cube as a dominant texture component. The important factors influencing texture development are also identified. The next part discusses the simulation procedures. Lastly, simulation results for the various cases are presented.

Cube Component

As discussed in section 2.4 the Cube component emerges as the dominant texture component after recrystallization in most FCC rolled materials. The details of the evolution and the other components present will be discussed in the following section. The main intention of the work presented here is to have a model which matches as closely as possible the experimental results in

all aspects including texture development. Hence it is necessary to identify the important factors.

5.1 Experimental texture evolution

The experimental results discussed are obtained from an isothermally annealed Al1050 sample at 375°C. The data was extracted from EBSD maps. To optimize the statistics, data from multiple scans was pooled together. All the scans were obtained from a plane perpendicular to the Rolling direction (RD).

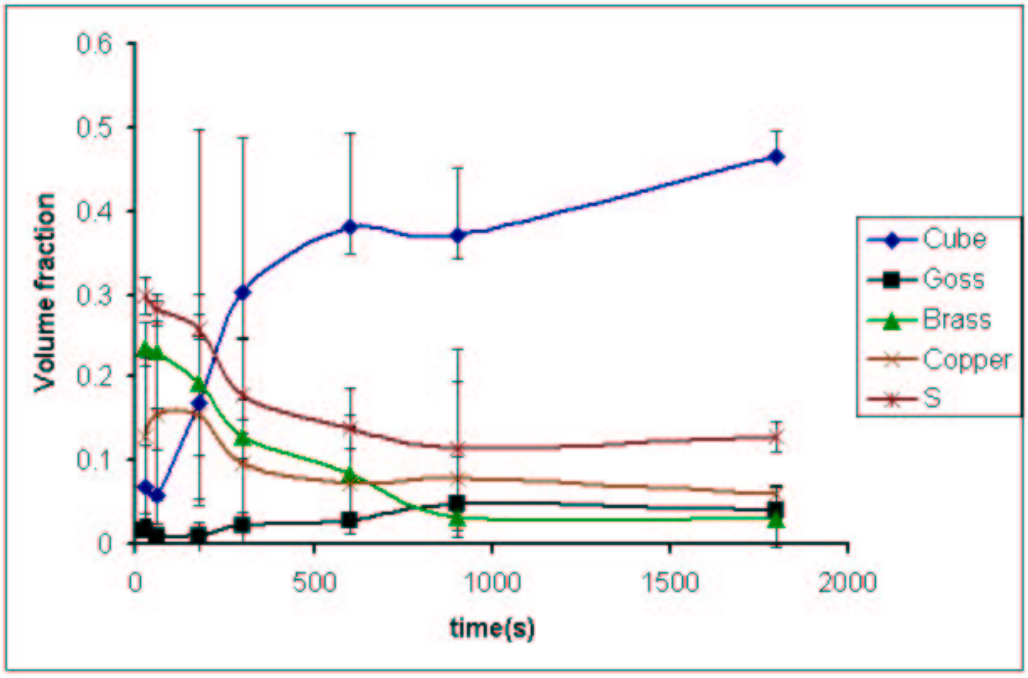

Figure 5.1: Experimental Texture evolution

Figure 5.1 shows the texture evolution as a function of time in terms of volume fractions of components. The texture components at each time step, or observation point, are calculated by binning the orientation data. The binning criterion is decided by the disorientation. Each Euler angle triplet in the scan is converted to quaternions, say q_1. The disorientation between this q_1 and the various components[1], q_{comp} is calculated and binning is done by the smallest disorientation angle within 15° of the component.

The texture evolution of each component is reported in terms of volume fraction of that particular component at any given time step. For example the volume fraction of the cube component at time t = 900 s is 0.37. The volume fraction, f, at any time, t, is calculated by

$$f = \frac{\text{Volume of the component}(t)}{\text{total Volume}(t)}$$

The S component ($\{231\}< 124 >$) is the dominant component at the initial time as expected in a rolled aluminum sample. Along with S, other major rolling texture components, copper and brass, make up most of the initial texture. There is a certain amount, though very small, ∼5%, of cube present initially. But at later times the recrystallizing cube component ($\{001\} < 100 >$)grows to be the dominant texture. In both the deformed state as well as the completely recrystallized state there was a significant amount of texture which could not be categorized into any of the known

[1]The list of texture components used is the same as the one presented in table2.1

components for Aluminum. This will be referred to as the "rest".

5.2 Factors influencing Texture Evolution

As noted in section 2.5 the factors controlling texture evolution are:

- Oriented Nucleation
- Oriented Growth
- Stored Energy

One of the aims of this study is to identify the relative importance of these factors. To achieve this objective, Monte Carlo simulations were performed while varying the system parameters (factors) stated above. The **Oriented Growth** theory is centered around the specific rotational relationships that may exist between different grains. This is due to either lower grain boundary energy and/or higher mobility associated with special boundaries. Hence to gain a better understanding, this study looked at the anisotropy by treating mobility and energy anisotropy separately. Thus we have the following factors *oriented nucleation, energy anisotropy, mobility anisotropy* and *stored energy.*

5.3 System Setup

Recrystallization is carried out using the Monte Carlo simulation technique as described in the section 2.6.1. The setup involves generating a representative

microstructure, adding nuclei to the microstructure, adding anisotropy to the system (both energy and mobility) and calculating stored energy for each deformed grain.

5.3.1 Microstructure

The microstructure is generated using the Microstructure Builder as discussed in ch. 3. We begin by extracting the geometry and the orientation data from the experimental EBSD maps. Using the geometry data we build a distribution of ellipsoids which will eventually describe the grains in the microstructure. Using a random set of points we make a Voronoi diagram. Each of the Voronoi cells are assigned to the ellipsoids thus make a space filling grain structure. Areas of grain boundaries and volumes of the grains are calculated. Each grain is assigned a crystallographic orientation such that the difference between both the orientation distribution function (ODF) and the misorientation distribution function (MDF) of the assigned orientations and target distribution is minimized. This microstructure is then fed as an input to the Monte Carlo codes to simulate recrystallization.

To have a good match of initial texture assignment the initial microstructure should at least have a few thousand grains [54]. The experimental observations, as depicted in figure 3.6, indicate that the grains are elongated along the rolling direction and can be approximated as ellipsoids. These ellipsoids have the longest semi-axes length in the rolling direction and the smallest in the normal direction. To have a statistically similar microstructure, an initial

set of slightly equiaxed ellipsoids was generated which was then stretched to get the desired grain shape. The final microstructure was in form of a cubical lattice of size $500 \times 200 \times 100$. Each of the lattice points was labeled by the grain number/id which can serve as the spin number, q, in the Monte Carlo simulations.

5.3.2 Nucleation

Once we have the microstructure, the next step is to add nuclei to the system. Here the assumption is made that system exhibits site saturated nucleation. This assumption is made since the system being modeled showed site saturation type nucleation. In general it is fairly straightforward to model any other type of nucleation scheme. Also all the nuclei are given a fixed size of three voxels. The nucleation itself can be broken down into two different components.

i. nuclei placement

ii. nuclei orientation

These two components can either be treated separately or as a combination depending on the problem at hand. For example if one is trying to model a system having absolutely no or very little correlation between the nuclei placement and the nuclei texture then one can have two separate algorithms to mimic the process of nucleation. Whereas, if one believes that the two are highly correlated, as in the present case, then one has to design an algorithm

to address both the issues at the same time. The following is the algorithm to add nuclei to the microstructure employed for this study.

Two important assumptions are made in this implementation. The first of these, as already stated, is the site saturation condition. The other assumption is that the nuclei (new grains) occur only at sites which are adjacent to or on interfaces between two grains. This second assumption is justified in present case since the experimental observations support the claim [56].

Algorithm

We will first present the algorithm and then study it in more detail with the help of an example.

1. Read the data (microstructure, $\mathcal{M}$, and probability matrix, $\mathcal{P}$[2]);
2. Build a list of sites on grain boundaries, say $\mathcal{L}$;
3. Pick a site from $\mathcal{L}$, say s_i;
4. If s_i is recrystallized remove from $\mathcal{L}$ and go to 3;
5. if s_i has two or more deformed neighbors proceed, else, go to 3;
6. Read the texture of this s_i, say o_i;
7. Pick a nucleus texture (equivalent to picking a q value), say o_n;

[2]The probability matrix $\mathcal{P}$ is more properly termed a frequency matrix since we multiply each entry of the probability matrix with the total number of nuclei needed to make the required volume fraction

8. If $\mathcal{P}(o_n, o_i)$ is greater than 0 accept the assignment remove s_i from $\mathcal{L}$ and go to 10;

9. Else go to 10;

10. Repeat above till required number of nuclei generated.

The probability matrix is generated from the experimental observations. Since it is impracticable to have a probability matrix associated with every orientation even in the reduced fundamental zone, the orientations were binned into the major texture components. For the present study the components chosen were **Cube**, **Brass**, **Copper**, **S** and **rest** (for both deformed as well as recrystallized). Thus the probability matrix $\mathcal{P}$ is a 5×5 matrix whose $(i, j)^{th}$ entry is the probability of finding a nucleus with orientation close to C_i next to a deformed grain with orientation close to C_j. C_i and C_j both belong to the above mentioned component list. To speed up the (numerical) process of nucleation, each entry in $\mathcal{P}$ was multiplied by the total number of nuclei to be added to give, in effect, a frequency matrix. Every time there is a successful assignment we mark off the $(i, j)^{th}$ entry by one.

Example: Assume we happen to choose a site, from $\mathcal{L}$, in the deformed grain having an orientation close **S**; if this site does not have two or more deformed neighbors then we reject this as a possible nucleation site. On the other hand, if it meets the criteria, then we randomly choose an orientation for the nucleus from a preexisting list of possible orientations (generated from experimental observations). The nucleus orientation we happen to chose is,

say, brass. If the entry in $\mathcal{P}$ corresponding to a brass nucleus next to a deformed S grain is less than or equal to 0 then we discard both nucleus and the location and choose the site again. If the entry is positive then we accept this particular location for placing the nucleus with the particular orientation. The entry $\mathcal{P}(brass, S)$ is reduced by one and the site is removed from the list of possible sites for nucleation. Table 5.1 shows the probabilities used in the simulations. To get $\mathcal{P}$, each entry in the matrix is be multiplied by the number of nuclei to be included in the simulations. Example, for a microstructure of size $500 \times 200 \times 100$ and having 6% volume fraction of nuclei each entry is be multiplied by 200000[3].

Table 5.1: Probability matrix used in the simulations

	Cube	Brass	Copper	S	Rest
Cube	0.344	0.0515	0.0454	0.219	0.296
Brass	0.0727	0.355	0.0417	0.298	0.232
Copper	0.0155	0.0636	0.324	0.184	0.388
S	0.156	0.0987	0.102	0.353	0.274
Rest	0.122	0.0753	0.0548	0.203	0.522

5.3.3 Energy-Mobility

The anisotropy in the system is expressed via anisotropy in energy and anisotropy in mobility. In this simulation scheme, only the sites adjacent to an interface of two grains are allowed to change state (flip spin). Hence

[3]Assuming that each nuclei has a volume of 3 voxels hence total number of nuclei are: $N_{nuclei} = V_{total} \times$ fraction / 3

only the grain boundary energy and mobility are important.

Energy Anisotropy

The energy anisotropy is characterized by the misorientation between the two neighboring grains. We divide the boundaries into low angle boundaries (disorientation $\theta \leq 15°$) and high angle boundaries ($\theta > 15°$). The energy of grain boundaries in the low angle regime is expressed by equation 5.1.

$$\gamma = \gamma^* \theta^* (1 - \ln(\theta^*) \tag{5.1}$$

where θ^* is $\frac{\theta}{15°}$ and γ^* is a normalizing factor. For the high angle boundaries the energy associated is constant at γ^*. The only exceptions are certain "special" boundaries. There has been considerable experimental work to investigate the exact nature of the grain boundary energy curve as function of misorientation as well as the full five parameter description (misorientation and boundary normal). For this study, though, only misorientation is considered. Figure 5.2 shows the variation of grain boundary energy as a function of misorientation angle (θ). The value of energy increases as the misorientation angle increases till the high angle value ($\sim 15°$). The cusps in the energy value shown in the figure are associated with only special boundaries and not all boundaries having those misorientation angles. The special boundaries considered here are $\Sigma 3$, $\Sigma 7$, $\Sigma 13b$ and $\Sigma 19b$. The rotation axis and angles are presented in table 2.3.

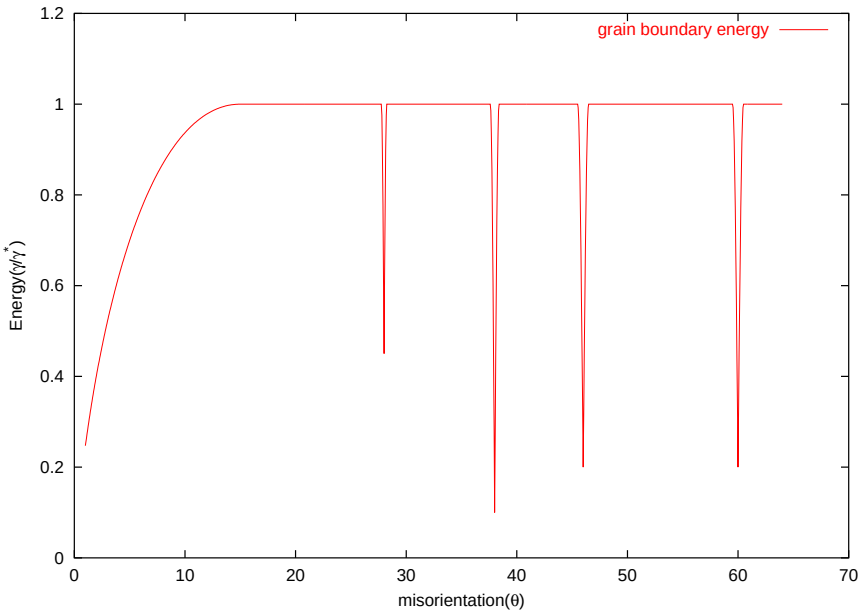

Figure 5.2: Grain boundary energy

Mobility Anisotropy

Similar to energy, the mobility anisotropy is also characterized by the grain boundary misorientation. Unlike the grain boundary energy which has cusps, or valleys for the special boundary configurations, the mobility plot shows peaks corresponding to the highly mobile boundaries. Figure 5.3 shows the plot of mobility as a function of the misorientation angle. The peaks in plot correspond to $\Sigma 37c$, $\Sigma 7$ and $\Sigma 19b$ boundaries. These CSL values have been noted to have higher mobilities in both experimental and atomistic simulation results [57, 58, 59, 60]. Note all these are in the $< 111 >$ misorientation axis series. Thus the peaks shown in figure 5.3 are unique points in the 3 dimensional misorientation space

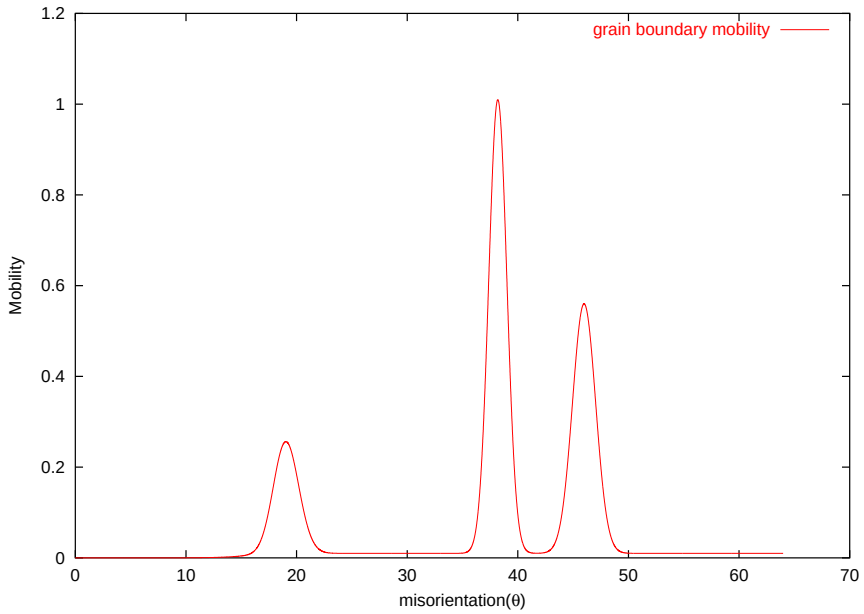

Figure 5.3: Grain boundary Mobility as a function of misorientation angle

5.3.4 Stored Energy

Each grain in the system is assigned a single value for the stored energy. It is assumed that there is no local variation of stored energy inside each grain. Further, all the grains having a similar orientation are given the same stored energy. For example, two grains having an orientation close to copper are assigned the same value for stored energy. This assumption, though simplistic, is a good first order approximation. Thus all sites in all grains having similar orientation are assigned the same value for stored energy. The method for determining the stored energy values associated with each component is discussed elsewhere (sec. 6.2). Table 5.2 gives the values of

stored energy used for the various components. [4]

Table 5.2: Stored Energy assignment

Component	Stored Energy	Vatne values
Cube	1.0	1.0
Brass	1.23	0.75
Copper	1.24	0.9
S	1.27	1.3
rest	0.96	1.0

All the rolling components (Brass, Copper and S) have a higher stored energy as compared to Cube. These data agree well with those obtained by Vatne et al. [16][5] for a similar system.

5.4 Simulation Conditions

Once the microstructure is generated, with the texture assignment, and nuclei, grain boundary properties and the stored energy have been specified, Monte Carlo simulations can be run. This study looked at the effect of oriented nucleation, energy and mobility anisotropy and stored energy on texture evolution. Since the objective of the study is to identify the relative importance of the above mentioned factors, the simulations examined the effect of turning each of the factors on or off. The table 5.3 summarizes the different conditions for which the simulations were done. An $\times$ in a column

[4] All values relative to the cube component

[5] The values published in the paper used $\bar{\theta}/\bar{\delta}$ as stored energy estimator instead of the Read Shockley relationship

implies a factor being turned OFF (its effect not included). A $\surd$ in a column implies a factor being turned ON.

Table 5.3: Simulation Conditions

Oriented Nucleation	Mobility Anisotropy	Energy Anisotropy	Stored Energy	Fig. number
×	$\surd$	$\surd$	$\surd$	5.4
$\surd$	×	×	$\surd$	5.5
$\surd$	×	$\surd$	×	5.6
$\surd$	×	$\surd$	$\surd$	5.7
$\surd$	$\surd$	×	×	5.8
$\surd$	$\surd$	×	$\surd$	5.9
$\surd$	$\surd$	$\surd$	×	5.10
$\surd$	$\surd$	$\surd$	$\surd$	5.11

5.5 Results

The results are presented as plots depicting texture evolution of two of the components (Cube and S). These were chosen since the S is the dominant deformation texture component and Cube is the dominant texture component after the recrystallization is complete. Each of the plots shows a comparison between the experimental and the simulation results. The error bars on the experimental results are based on compiling the data from various scan areas (using the max/min values), while the error bars for the simulations are from different runs (typically 3-4 runs per set of conditions and using standard deviations). The initial volume fractions of the S component shows a discrepancy between the experimental and the simulated values. There can

be two possible explanations for this. First, as stated earlier, one needs a few thousand grains to completely describe the orientation/misorientation space whereas the simulated structure has approximately 800 grains. Second, even though the volume fraction and hence the ODF might not be an exact match, this mismatch can be compensated by a better match in the MDF, thereby reducing the overall error in the system in the fitting process.

Figure 5.4 shows the result of drawing the nuclei from a random distribution. The nuclei placement and the nuclei texture assignment were carried out randomly. Stored energy and anisotropy effects were included. The simulated texture development is sharply different from the experimental one.

Figure 5.5 shows the result of turning the oriented nucleation and the stored energy ON. Figure 5.6 shows the result of turning the oriented nucleation and the energy anisotropy ON.

Figure 5.8 shows the result of turning the oriented nucleation and the mobility anisotropy ON. Figure 5.7 shows the result of turning the oriented nucleation, stored energy and the energy anisotropy ON. Figure 5.9 shows the result of turning the oriented nucleation, stored energy and the mobility anisotropy ON. Figure 5.10 shows the result of turning the oriented nucleation and both mobility and energy anisotropy on. Figure 5.11 shows the result of turning ON all the factors.

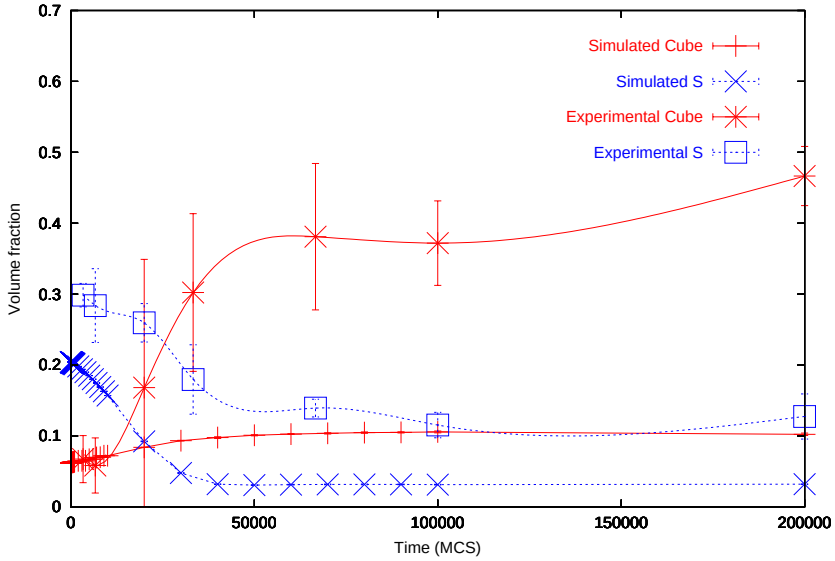

Figure 5.4: Random Nucleation

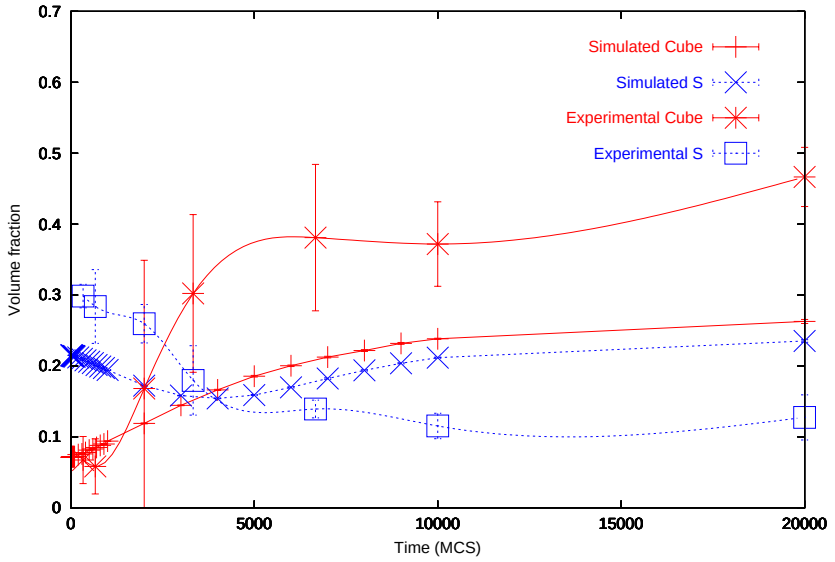

Figure 5.5: Effect of Stored Energy

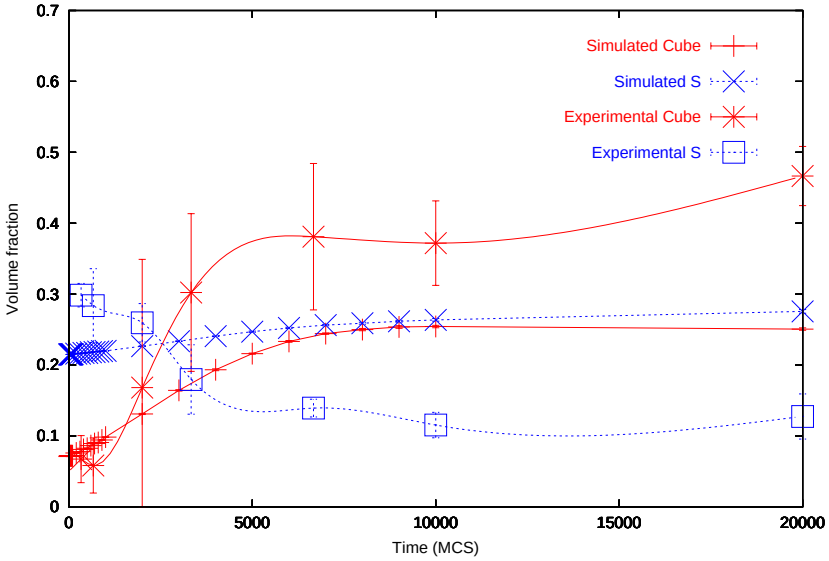

Figure 5.6: Effect of Energy Anisotropy

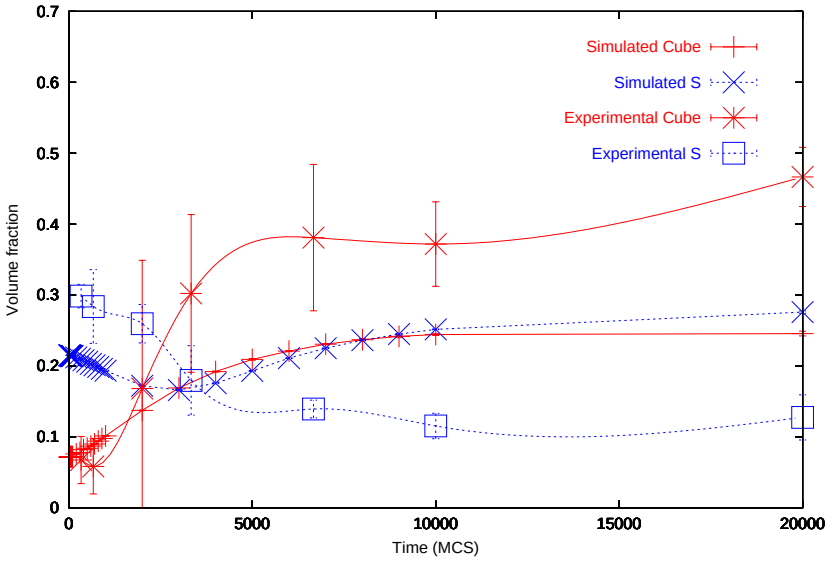

Figure 5.7: Effect of Energy Anisotropy and Stored Energy

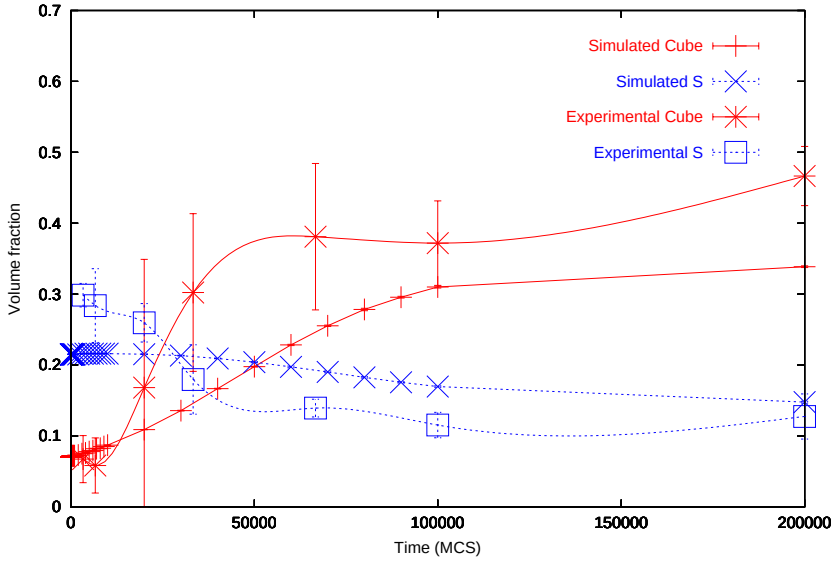

Figure 5.8: Effect of Mobility Anisotropy

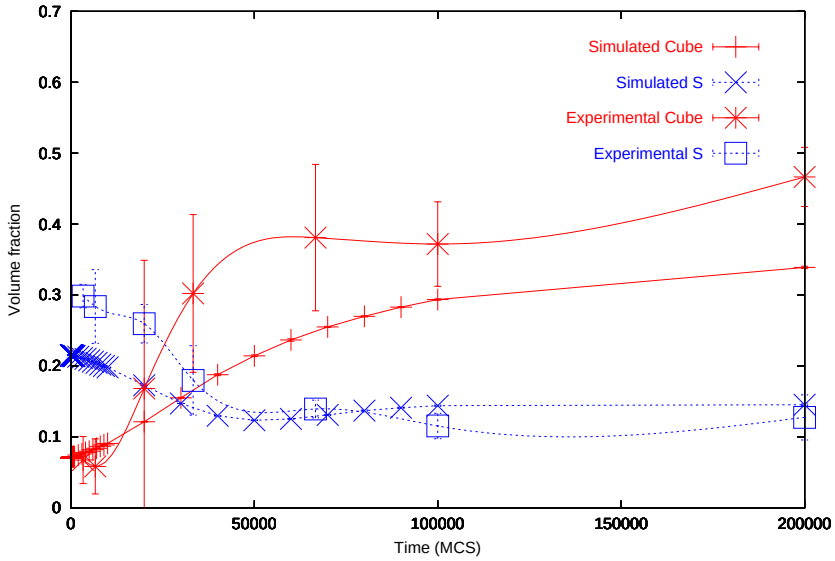

Figure 5.9: Effect of Mobility Anisotropy and Stored Energy ON

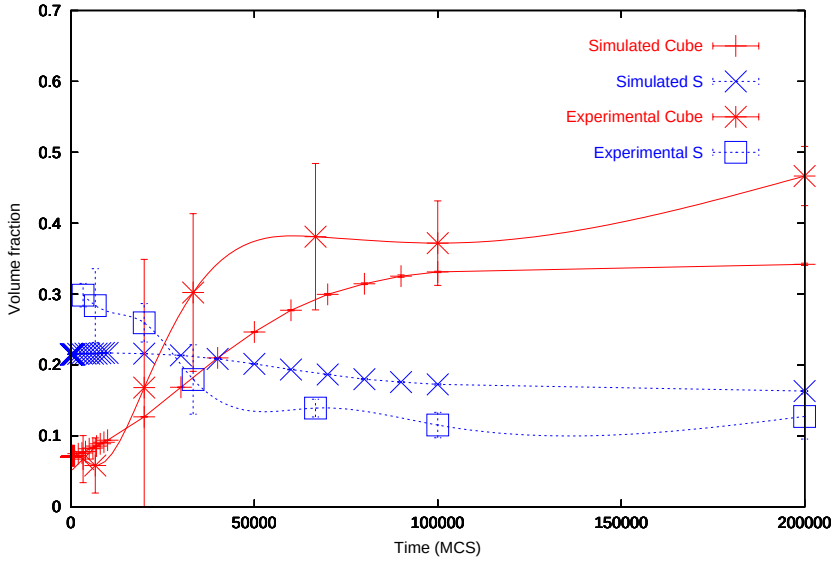

Figure 5.10: Oriented nucleation and Total Anisotropy

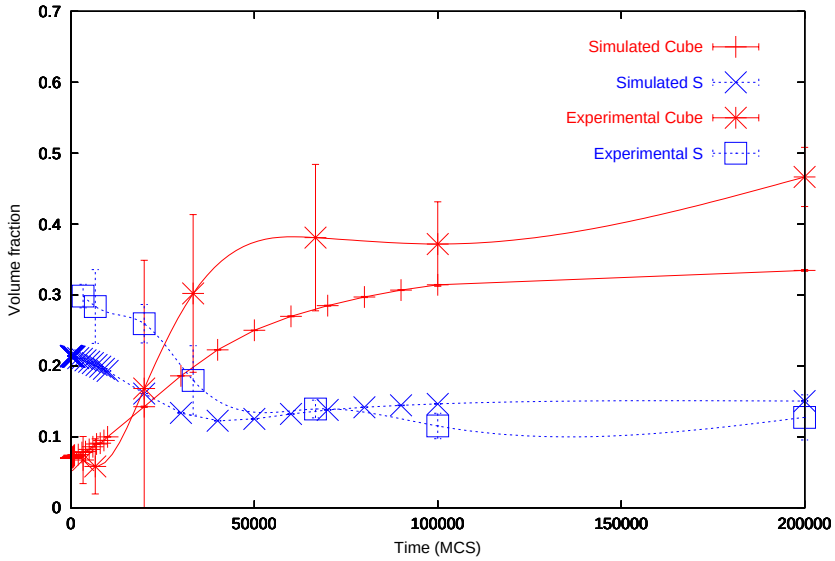

Figure 5.11: Oriented Nucleation, Total Anisotropy and Stored Energy

Figure 5.12 shows all the texture evolution of all the relevant texture components for the case which includes the effect of all the factors. Most of the components show a steady decrease in the volume fraction as time increases. Only "cube", which is the dominant component at the end of recrystallization, and "Goss" show an increase volume fraction as the time increase. Overall, the texture evolution of the various components in the simulations follow the experimentally measured trends.

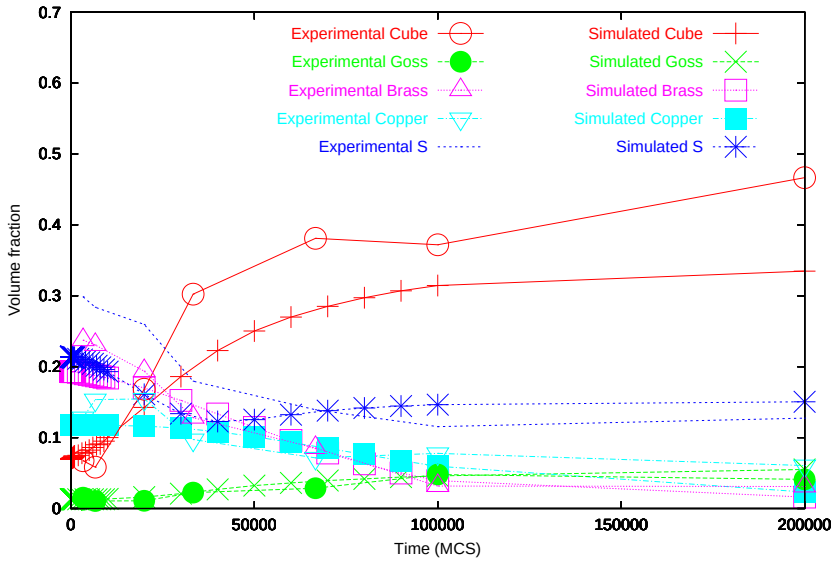

Figure 5.12: Comparing texture evolution of all the relevant components

Chapter 6

Discussion

6.1 Microstructure Builder

The output of the microstructure builder is shown in figure 3.9. A visual comparison with the simulated microstructure in the figure 3.6 shows that we have been successful in generating a representative microstructure geometry. The aim is not to generate an exact reproduction of the specific microstructure but to generate one which is statistically similar to the experimental input. The central idea is to capture the overall microstructural geometry of the sample rather than the details. The microstructure generated used ellipsoids centered around (15,4,1) as the semi-axes ratio set. This value for the ratio was chosen empirically while trying to stay as close as possible to the experimentally observed geometry. The biggest constraint on generating an elongated geometry, like the one seen in the experimental observation of

the Al-1050, is the number of grains in the final microstructure. One would ideally like to have $\sim$ 1000 grains in the generated microstructure to get good statistics. The limitations on the computer memory prevented us from generating a large system with many grains. The microstructure generated here has $\sim$800 grains. Although this is not as many grains as one would like to have, it is the closest match in geometry that could be generated while still maximizing the number of grains. All the grains are assumed to have their semi-axes parallel to the sample axes.

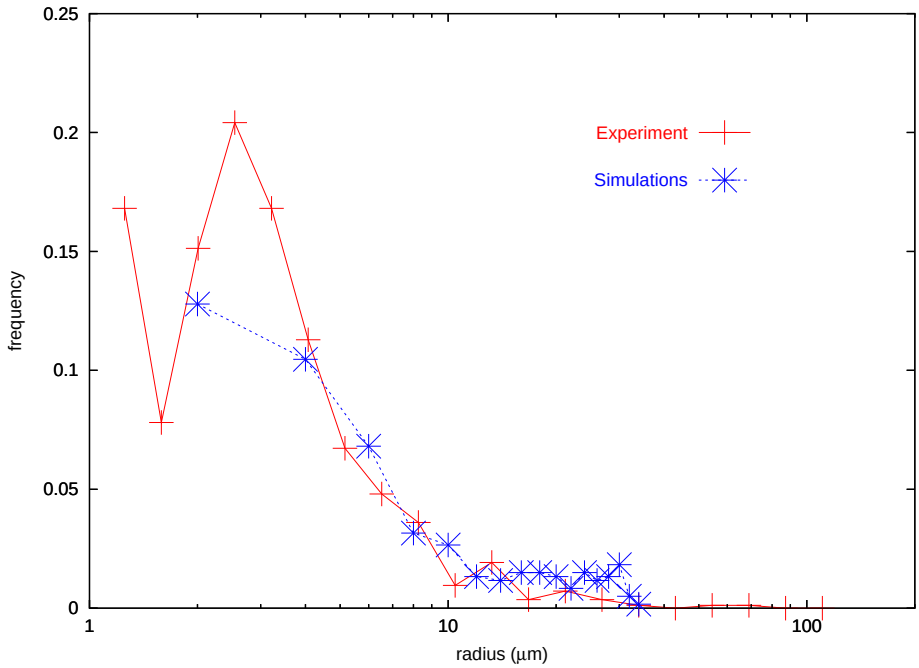

Figure 6.1: Grain Size Comparison

The plot in figure 6.1 shows grain size distributions from experiments and from simulations. The grain size distribution for the experiments was

obtained from multiple sections from a plane perpendicular to the Rolling Direction. For the simulations the microstructure was sliced perpendicular to one of the sample axis. The axis chosen was the one along which the ellipsoids had the longest semi-axis, which can be thought of as being the Rolling Direction in the simulated microstructure. To calculate grain size the grains were first fitted with ellipses and the semi-axes were calculated. Once we have the semi-axes the sphere equivalent radius was calculated. If a particular grain is approximated by an ellipse with a and b as semi-axes length then the grain size, s is given by:

$$s = \sqrt{a^2 + b^2}$$

The scaling in the simulations was done by setting the average grain size in the simulations equal to the average grain size in the experiments. An additional issue in the comparison of the distributions was that the experimental data for the distribution was binned with variable bins, i.e. not all the bins were of the same width, and the total number of bins was different in the simulations and the experimental dataset. Hence to compare the distribution, we normalized both the distributions by the total area under the curve. Even with only $\sim$800 grains in the simulated microstructure, the distributions are very close. Note how the flat distribution used to generate the initial ellipsoid set has been converted into a realistic distribution by the packing and selection process section (3.4.2).

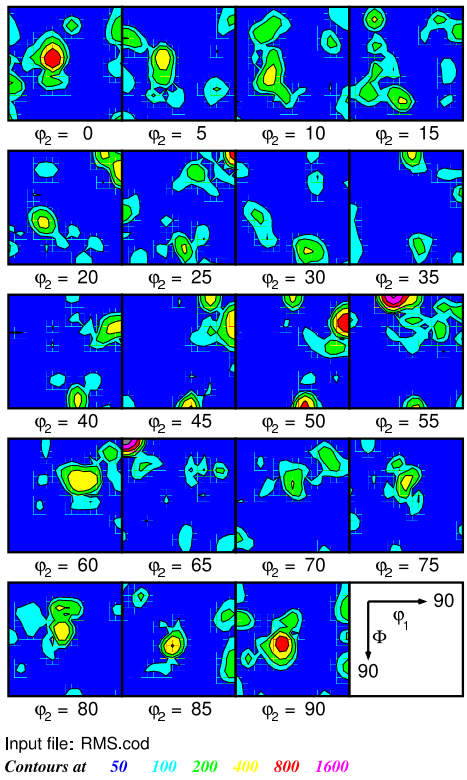

Figure 6.2: ODF difference between the experimentally observed distribution and the one obtained from texture fitting

Figure 6.2 shows the difference orientation distribution function (ODF). The ODF is calculated by dividing the $90 \times 90 \times 90$ euler space into bins with a width of 5° along each Euler angle (ϕ_1, Φ, ϕ_2). The difference ODF is calculated by taking the absolute difference between the experimental and the simulated intensities in each of the bins. A higher value in any of the bins implies a larger difference between the fitted and experimentally observed texture. In fig. 6.2, contours are drawn at 0.5, 1.0, 2.0, 4.0, 8.0 and 16.0 times average intensity. The difference ODF suggests that for most of the

bins the fitting procedure does a good job in assigning orientation. There still are a few locations which show differences. This can be due to two factors. First is the limited number of grains in the system. If the ODF is divided the way mentioned above then there a total of 19^3 bins whereas there are only 800 grains in the system and so only a limited number of orientations possible. The other factor is that the fitting procedure forces both the ODF and the misorientation distribution function (MDF) to match. The error is calculated using eqn. 3.6 and only moves that reduce the total error are permitted. Any new assignment of orientations changes both the ODF and MDF and hence the error associated with each distribution. A particular orientation assignment might worsen the error in the ODF but improve the total error. Hence the final orientation assignment might not be the most ideal fit for the ODF but the total error will be the least.

6.2 Stored Energy Calculation

There have been various methods in the literature proposed to estimate the stored energy. The stored energy can be characterized by direct measurement methods like calorimetry or indirect methods like hardness measurement. **Calorimetry** involves the measurement of energy change during annealing and includes both the geometrically necessary and free dislocations. Other methods of calculating the stored energy are **X-Ray** line broadening, subgrain analysis in both TEM and EBSD and the aforementioned hardness

measurements (Vicker's Microhardness and Nano-indentation). It is not possible to get the stored energy in individual components using Calorimetry. Using the hardness measurements, careful experimental setup of where the indents are made, and then measuring the the neighborhood of the indents, one can obtain the stored energy of different components. Borbély et al. [53] recently reported a stored energy calculation of different components using an X-Ray broadening technique. Vatne et al. [16] reported use of a subgrain analysis method with EBSD measurements to arrive at the stored energy for individual components. The subgrain analysis method in EBSD will be discussed in more detail in the next subsection along with the relevant theory.

6.2.1 Sub-Grain Analysis

The subgrain analysis relies on identifying the subgrain structure in the material. Hence it can be used with any technique capable of resolving the microstructure to that level for example TEM measurements that include orientation measurement. We shall, however, restrict this discussion to only EBSD measurements. The basic requirement for this type of measurement is to clearly partition the subgrains. This a very important point and we will revisit this again. A **subgrain** is defined as a region which has low dislocation density and is surrounded by a walls of high dislocation density. These "walls" of high dislocation densities can be regarded as low angle boundaries (having low grain boundary disorientation). Thus any method capable of showing these low angle boundaries can be employed to use this analysis.

Using the EBSD measurements one can achieve this objective. The method to calculate the stored energy is based on the estimation of the area of a low angle grain boundary and the specific energy of the low angle grain boundary (γ_s). γ_s can be estimated by using dislocation theory as developed by Read and Shockley [1] and summarized by equation 2.4. The area of the low angle grain boundary can be estimated as $\sim$ 3/D (D is the subgrain diameter). Thus the stored energy per unit volume (E_D) is given by equation 6.1.

$$E_D = \frac{3\gamma_s}{D} \tag{6.1}$$

Substituting equation 2.4 we get:

$$E_D = \frac{3\gamma_m \frac{\theta}{\theta_m}\left(1 - \ln\left(\frac{\theta}{\theta_m}\right)\right)}{D} \tag{6.2}$$

Both θ and D, the subgrain diameter, can be determined experimentally and thus the stored energy can be determined using subgrain analysis. Additionally one can determine the average orientation of the subgrains and thus classify the grains by the component it is closest to. Using this one can determine the stored energy based on the component. Vatne et al. [16] used this approach to calculate stored energy based on the texture component.

This method only counts the dislocations which form the subgrain boundary and ignores all other contributions to the stored energy such as "statistically stored" dislocations. Also it requires that the dislocations form a continuous piece of boundary to be included in the counting. The figure

6.3 is a cartoon which illustrates this point. The original grain has been divided by the subgrain boundary denoted by **b1** into subgrains **A** and **B**. The boundary **b1** is an intermediate disorientation boundary. The grain **B** shows a piece of "hanging" boundary contained within it. The boundary **b2** starts off as a relatively low angle boundary after which it may split up in two or more even lower angle boundaries which go undetected since they are below the detection threshold. The subgrain analysis does not include the dislocations forming boundary **b1** because it does not enclose any part of the grain. As a result the stored energy calculated using the subgrain analysis method will not reflect all the dislocations. Of course in principle, EBSD at a fine enough resolution should be able to capture all the GND content but this is impracticable in the SEM.

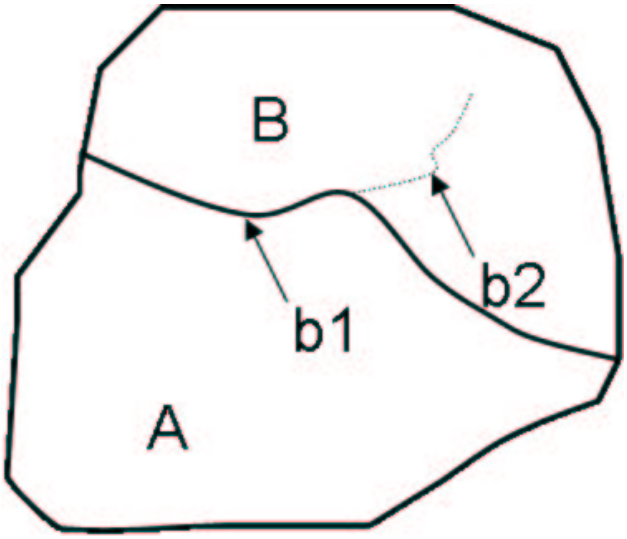

Figure 6.3: "Hanging" sub-boundary

6.2.2 Boundary Segment Analysis

Boundary Segment Analysis uses a similar idea as discussed previously about counting subgrains. Instead, however, of finding a continuous line of dislocations forming a subgrain boundary, this method looks at all LAGB segments which may or may not be a part of a subgrain boundary. This LAGB segment shall be referred to as a boundary segment. For every boundary segment, the disorientation associated with it is calculated. Once the disorientation is calculated we use equation 6.2 to estimate the stored energy associated with it. Since we are not looking at a subgrain there is no subgrain diameter, **D**. Equation 6.2 therefore needs to be modified. The proposed equation is given by

$$\epsilon_{\mathrm{i}} = \gamma_m \frac{\theta_i}{\theta_m}\left(1 - \ln\left(\frac{\theta_i}{\theta_m}\right)\right)\left(\frac{\lambda}{\mathrm{A}}\right)\left(\frac{\pi}{4}\right) \tag{6.3}$$

where ϵ_i is the energy associated with the i^{th} boundary segment, θ_i is the disorientation, **A** is the area and λ is the step size. The factor $\frac{\lambda}{\mathrm{A}}$ gives the line length per unit area and also the right dimension. $\frac{\pi}{4}$ [55] is the steriological factor to convert from line length per unit area to surface per unit volume. It follows from equation 6.3 that all boundary segments having same disorientation value will have the same stored energy. Thus to calculate the total stored energy, the entire observational area is binned by boundary segments having same disorientation and then the number in each bin is

convoluted with the stored energy associated with the center of each bin.

$$\begin{aligned} \mathrm{E_V} &= \sum_j \left(f_j \epsilon_j\right) \\ &= \sum_j f_j \left\{ \gamma_m \frac{\theta_j}{\theta_m} \left(1 - \ln\left(\frac{\theta_j}{\theta_m}\right)\right) \left(\frac{\lambda}{\mathrm{A}}\right) \left(\frac{\pi}{4}\right) \right\} \end{aligned} \tag{6.4}$$

Equation 6.4 is the final equation to calculate the total stored energy based on boundary segments. θ_j is the center of the j^{th} bin and f_j is the frequency associated with the j^{th} bin. To calculate the stored energy in each component the following equation can be used

$$\mathrm{E_V^c} = \sum_j f_j^c \left\{ \gamma_m \frac{\theta_j^c}{\theta_m} \left(1 - \ln\left(\frac{\theta_j^c}{\theta_m}\right)\right) \left(\frac{\lambda}{\mathrm{A}}\right) \left(\frac{\pi}{4}\right) \right\} \tag{6.5}$$

where $\mathrm{E_V^c}$, θ_j^c and f_j^c are the stored energy, disorientation of the center of j^{th} bin and frequency j^{th} bin associated with component c respectively. Table 5.2 sums the result of using the above analysis on the Al-1050 sample.

6.3 Recrystallization Kinetics

Figures 4.2 to 4.6 show JMAK plots for the various simulation conditions. As noted earlier the plots contain both the experimental and the simulated results. The experimental results (indicated by black squares) were obtained from the Al-1050 system. The JMAK exponent obtained from the experimental results is $\sim$ 1.38. This value, which is far from the value of "3"

expected for the theoretical case of randomly placed site saturated nuclei and isotropic 3D growth, indicates that the system does not exhibit random nucleation. A close inspection of the EBSD scans indicates that most of the nuclei occur along the grain boundaries and in clusters. Figure 6.4 shows nuclei occurring at grain boundaries. They appear in clusters and are not spread uniformly along the all the boundaries. The region marked in red shows the presence of nuclei on grain boundary, whereas the region marked in blue shows a piece of grain boundary without any nuclei on it. The dia-

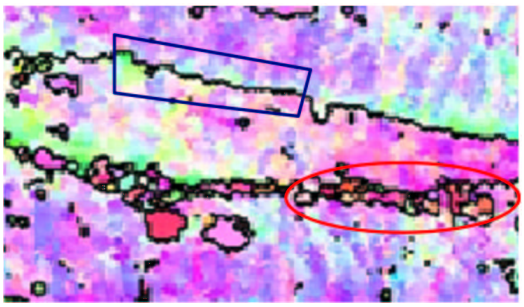

Figure 6.4: Nuclei on grain boundaries

monds in each plot show the data points for the simulations. Since we are interested only in the slopes of the JMAK curves, no time scaling was done but it is assumed that the scaling would be linear. The experimental curves were shifted so that the two plots lie in the same region.

In the case of randomly placed nuclei we recover the slope of the simulation JMAK plot close to the theoretically expected value of "3". Contrast this to the case of placing the nuclei at grain boundaries, where one recovers a slope of ~ 2. As we increase the total number of nuclei in the system we

can see a gradual change in the slope of the JMAK curve from the value of ~ 2, at 3% volume fraction of nuclei, to ~ 1.33, at 10% volume fraction of nuclei. The figures 4.5 and 4.6 compare the effect of changing the geometry from slightly equiaxed grains to a rolled structure with elongated grains while keeping the same volume fraction (6%) of nuclei. To explain this, let us revisit Cahn's analysis. Cahn in his '56 paper proposed a master curve governing a transformation which nucleates at grain boundaries, edges and corners. All of these curves had a JMAK slope of 4 at the beginning and depending on the type of nucleation, the slope changes at later times. For the case of the grain boundary surface nucleation the slope decreases from a value of 4 to a value of 1. His analysis was for the case of constant nucleation. For site saturated nucleation the slope changes from an initial value of 3 to a final value of 1. The change in slope occurs when the "growing grains" begin to impinge on each other. He also assumed that the nucleation sites are distributed randomly along the boundary surface, resulting in almost all the grains impinging at about the same time, hence giving a well-marked transition in the master curve. This point of transition in the curve depends on the total number of nuclei present.

In all the simulations discussed earlier, the nuclei were placed on the grain boundaries only, thus one would expect that they would follow the master curve for grain boundary nucleation. The plots (both the experimental and simulated) show that there is no transition point in the curves where the slope changes from 3 to 1. The reason for the deviation from this expected

behavior can be explained by taking into account the fact that, even though the nucleation sites are at grain boundaries, they are non-uniformly distributed. Hence, once these "new" grains start growing, impingement does not occur at the same time for all the grains. As a result the transition point is smeared out and the slope is higher than the expected value of "1". At any given time the system has some grains which have already impinged on other grains while others are growing without having yet impinged. The final slope of the JMAK plot is hence a function of the number of (volume fraction) nuclei in the system. If the system contains a smaller initial volume fraction of recrystallizing grains then there will be more grains growing without impingement which will increase the slope to a higher value. This is seen in the simulations when we vary the volume fraction of the nuclei in the system from 3% to 10% and the slope changes from 1.96 to 1.33. The impingement also depends on the effective volume available for the nuclei. If the effective volume available is smaller then more nuclei will experience the impingement. This can be seen by varying the grain geometry. In the nearly equiaxed grains the total volume available for nucleation is $\sim 27\%$ where as in the case of the elongated grains it is $\sim 17\%$. [1]

[1] The total system size is not the same in these two cases. The system with the elongated grains has 10 times the size. Also the stretching does not conserve the volume of the grains; if it were to conserve the volume while elongating the grains the boundary area would increase.

6.4 Texture Evolution

The objective of the study is to determine the parameters controlling the process of recrystallization. Table 5.3 lists the simulation conditions for studying the effects on texture evolution. The results are presented in the texture evolution plots in figures 5.4 to 5.11. The rationale behind showing just two components has been already explained earlier. The blue lines show the Cube component and the red lines show the evolution of the S component during recrystallization. The results are presented as the time evolution of the volume fraction of components and not the error between the simulated and experimental values because we only have six experimental observations. These observations are sufficient to give us a qualitative idea of texture evolution but one would have to interpolate between observations to extract a quantitative behavior. Let us first present the factors in the order of their importance and then we will look at the rationale behind this summary.

1. Oriented nucleation
2. Mobility Anisotropy
3. Stored Energy
4. Energy Anisotropy

When the nuclei orientation are selected randomly, even though Cube is the dominant component at the end of recrystallization, the final volume fraction is still far away from the experimentally observed value between 40-50%.

When the results, shown in figure 5.4, are compared with the results shown in figure 5.11, where all the other conditions are identical and the nuclei orientations are selected according to the earlier mentioned scheme, it can be concluded that oriented nucleation plays a very important role. Table 6.1 shows the initial volume fractions of the different components in the case of random nucleation and the experimentally observed distribution. Oriented

Table 6.1: Comparison of initial texture (all numbers reported as percentage of the total volume)

Component	Experimental	Random Nucleation
Cube	24	13
Brass	2.4	3.4
Copper	5.3	5.2
S	24	6.0

nucleation is the most important factor but by no means the only factor required, as is evident by examining the evolution for the other cases. It is fairly clear that a combination of other factors is necessary if not all. Figures 5.6, 5.5 and 5.8 show that including energy anisotropy, stored energy and mobility anisotropy separately with oriented nucleation, can not provide the desired result. In all the three cases, the cube component shows reasonable growth but either it is not the dominant component and/or the S component does not follow the experimental pattern. For the case of including only the stored energy, the Cube component is dominant but at late times the S component increases again. For the case of including only the energy anisotropy, S never decreases. Including only the mobility anisotropy gives

the closest result but the S component does not fall fast enough. Thus one can conclude that the next most important factor governing the texture evolution is the mobility anisotropy. Comparing figures 5.5 and 5.7 it appears that including the energy anisotropy helps the growth of S component. Similarly by comparing the figures 5.8 and 5.10, one can draw a similar conclusion. If stored energy and the anisotropy due to mobility are included then the texture of the final microstructure has the best match with the experimental results.

Thus the factors in the order of their relative importance are oriented nucleation, mobility anisotropy, stored energy and grain boundary energy anisotropy. The initial rise of Cube and the fall of the S component can be attributed to the effect of stored energy which can be inferred by comparing figures 5.8 and 5.9. The difference between these two figures is that figure 5.9 also includes the effect of stored energy in addition to the oriented nucleation and mobility anisotropy. The stored energy of all the nuclei is the same "zero" which is in accordance with the fact that the new grains are relatively dislocation free and hence have lower stored energy. The stored energy of the deformed grains is determined by the orientation of the grains and the values shown in table 5.2. Hence stored energy will dominate the early part of the texture evolution since all the nuclei are surrounded by deformed grains. Once the nuclei impinge on each other, however, the anisotropy starts playing an important role. As noted earlier it appears that including the energy anisotropy seems to help the growth of the S component at later

times. Figure 5.2 shows the energy anisotropy as a function of disorientation angle. A general high angle boundary has high mobility and also high energy other than the special CSL boundaries. The energy anisotropy has cusps for the special boundaries while the mobility anisotropy has peaks. The cube component is related to S by having a misorientation of 40° about the $< 111 >$ axis, which happens to be close to the $\Sigma 7$ type of boundary. The mobility curve has a peak at the $\Sigma 7$ position (figure 5.3) implying that this boundary is highly mobile. Thus the anisotropy in mobility can help the growth of the cube component when the cube and the S nuclei impinge on each other. On the other hand the $\Sigma 7$ position in the energy curve has a cusp implying that the boundary has lower energy. Hence if the effect of energy anisotropy is included and if the cube and S nuclei impinge, then the boundary is going to be a stable boundary and cube component can not grow at the expense of S. Hence it appears that overall growth of S component is aided by the energy anisotropy.

6.5 Scaling

The initial length scale for the simulated microstructure was set by equating the grain size to the experimentally observed deformed grain size. The grain size was obtained using the line intercept method. We only considered the grain size (thickness) along the normal direction. The size of the EBSD scans was not same for the initial and the final time points. Also the number of

recrystallizing nuclei was not the same in simulations and the experiments, hence to compare the final grain size, the average increase in the volume of each grain was used. The average initial grain size in the real material was ~ 5.55 μm, while the average final grain size, obtained by sphere equivalent radius, was ~ 29.15 μm. That is, the average increase in grain size was ~ 3.8. The average initial grain size in simulations was ~ 0.89 voxels and the final grain size ~ 3.2 voxels giving a value of factor 3.6 for the increase in grain size, which is very similar to the experimental value.

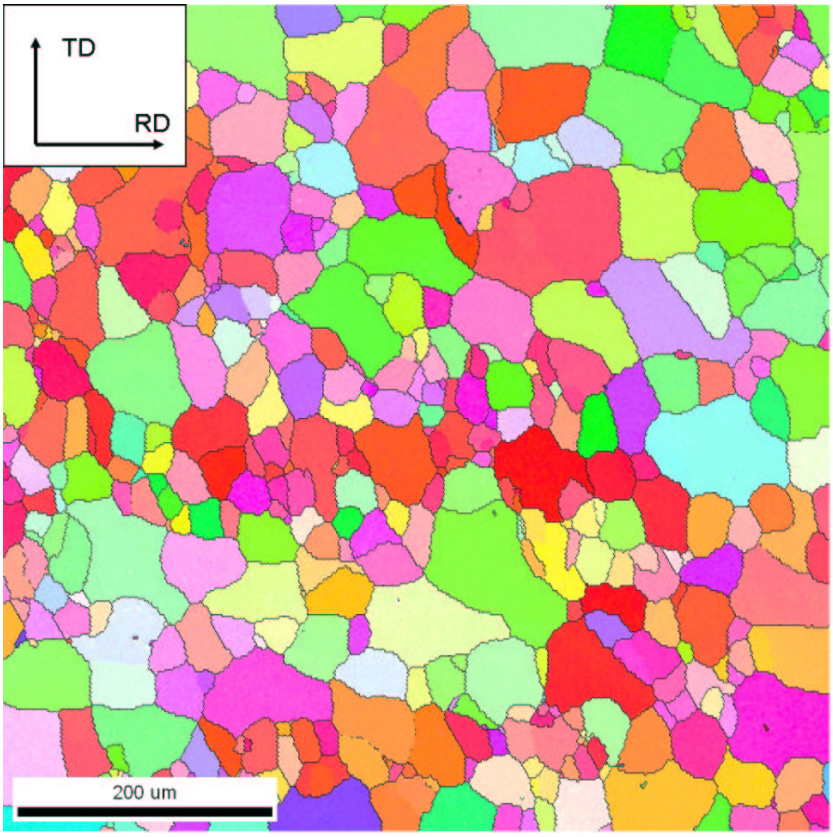

Figure 6.5: IPF map of microstructure after recrystallization

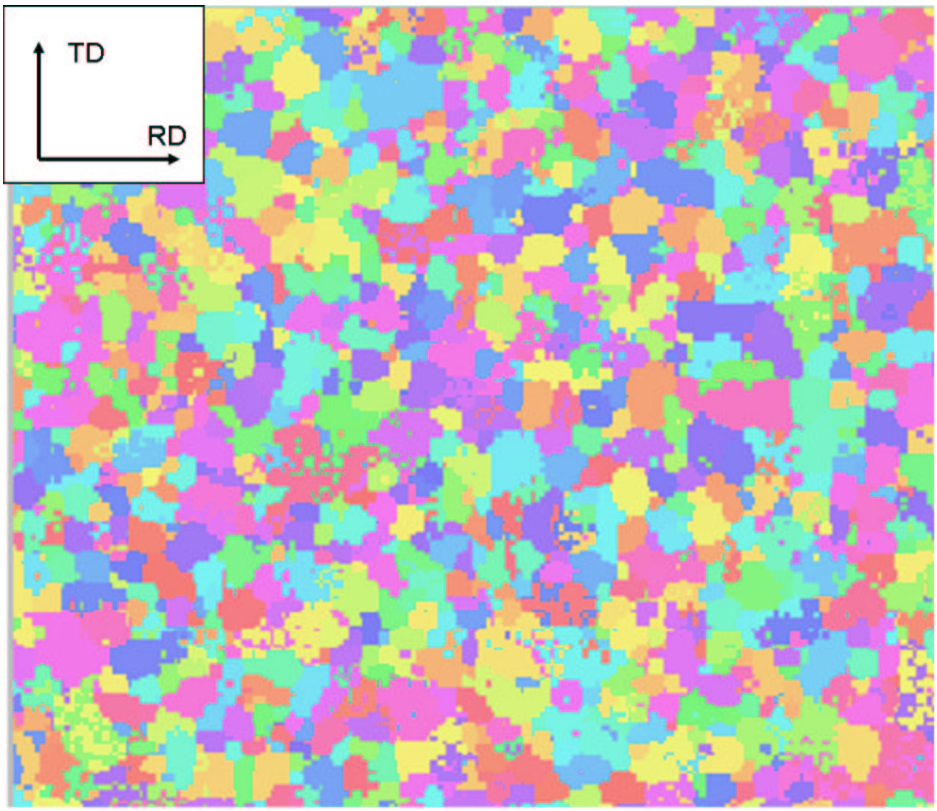

Figure 6.6: Microstructure after recrystallization in simulations (colors assigned randomly)

Figures 6.5 and 6.6 shows typical microstructures after recrystallization in experiment and simulation respectively.

It was assumed that the time in the simulation scales linearly with the real time. The initial and the final time, the time at which recrystallization is complete, in the simulations is set equal to the corresponding experimental times. For the different simulation conditions the final time was different. Instead of equating the initial time (t=0) one could as well do the scaling at

t=δt, which gives a straight line for the JMAK plot. This value of δt was found to be about 100 times smaller than the final time and hence would not change the scaling factor by much.

Chapter 7

Summary and Future work

We summarize the main objectives of this work and then see how well they have been achieved.

- Build a computer model which simulates the process of recrystallization
- Identify important parameters governing recrystallization

We have a set of tools now assembled to generate statistically representative 3-D microstructures using 2-D inputs in the form of EBSD maps. Even with a small number of grains ($\sim$800) we have shown that the resultant microstructure is a close match to the experimentally observed one in terms of geometry as well as crystallographic orientation. The next step is to build bigger structures capable of having $\sim$1000-10000 grains in it. We are limited in this endeavor by the available computing power. The natural extension of this would be to have MS builder run on a parallel platform, which would,

however, require significant additional programming mainly for the selection of the optimally packed set of ellipsoids.

The simulated recrystallization kinetics follow the experimental observations very well when the nuclei placement and the geometry is correct. The combined effect of oriented nucleation, stored energy and anisotropy is required to get the best possible agreement with the experimental results for texture evolution. Orientation dependent stored energy gives the correct behavior of the texture evolution for the initial times when the nuclei are growing freely without impinging on each other. The anisotropy gives the correct behavior for texture evolution at later times when the nuclei impinge on each other. Thus the following parameters all affect the microstructural evolution to varying degrees.

- Geometry
- Nuclei placement
- Oriented nucleation
- Mobility anisotropy
- Stored energy
- Energy anisotropy

Thus we have addressed the objectives that we set out with, while gathering valuable insight on the effect of each parameter on the overall behavior

of the system. The work has also helped to give some direction to the experiments by requiring the determination of the neighborhood of the nuclei and the stored energy in each component.

7.1 Future Direction

The study has examined certain aspects and properties which were thought of as being important to the understanding of recrystallization kinetics and texture evolution. Even though we have answered some of the questions we still are far away from a complete understanding of the system. A more detailed investigation has to be carried out before the last word in this matter is said. Here we would like to identify some of the questions which might addressed.

First, and the most straightforward idea to follow up, is to study the effect of nucleus size on both the kinetics of recrystallization and texture evolution. We believe that texture evolution would be independent of the nuclei size though the time scaling would have to be modified appropriately. The reason for this claim is that the size of the recrystallizing grains does not appear explicitly, as long as volume fraction of nuclei is constant, in any of the factors governing texture. The kinetics of recrystallization, on the other hand, may change. Consider two nuclei separated by a distance $\mathbf{D}$. Assume that the nuclei are spread uniformly throughout the entire simulation domain.

Further assume that each nucleus grows at a constant rate given by **c**.

$$\begin{aligned} c &= \frac{\mathrm{d}r}{\mathrm{d}t} \\ r(t) &= c * t + r_0 \end{aligned}$$

Let t_1 be the time when these two nuclei impinge. At this time $\mathrm{r}(\mathrm{t}_1) = \mathrm{D}/2$. Hence,

$$\begin{aligned} \frac{D}{2} &= ct_1 + r_0 \\ \Rightarrow t_1 &= \frac{D/2 - r_0}{c} \end{aligned}$$

But

$$D = \frac{\left((4/3)\pi r_0^3\right)^{\frac{1}{3}}}{f}$$

where $(4/3)\pi r_0^3$ is the initial volume of each nucleus and f is the initial volume fraction of nuclei. This leads us to,

$$\begin{aligned} t_1 &= \frac{Ar_0 - r_0}{c} \\ A &= \frac{(4\pi/3)^{\frac{1}{3}}}{f} \end{aligned}$$

Now $\mathrm{A} > 1$. Hence,

$$t_1 \propto r_0$$

Using this simplistic approach we can argue that if the initial nucleus size is larger, then impingement will take place later in time. As noted earlier this will in turn affect the slope of the JMAK curve.

The effect of system size (simulation domain) also needs to be studied. The simulation box is assumed to be the fundamental building block of a representative volume element. This implies that we have a balanced sample of all the constituents that play an important role, present in this box. This assumption can be tested. As we have described all the properties in terms of either grain volume/areas or grain boundaries it is the most natural way to probe the effect of the above assumption. We have already seen the effect of available grain boundary area for nucleation on recrystallization kinetics. By increasing the system size we can include more grains in the system and hence have more samples for various properties. As noted earlier the current major limitation is the availability of computing power. Since we are interested in recrystallization and the new grains are only going to sample their immediate neighborhood, including more grains may not be a critical factor.

The effect of various parameters was studied by either including them in the model or by excluding them from the model. One could do a detailed study of sensitivity of each of these parameters and arrive at a quantitative estimate of the dependencies.

Figure 5.3 shows the mobility profile used in this work. This function was built from disparate data obtained from various sources. There is a lack of constitutive relationship of mobility as a function of grain boundary

character. The present study showed that mobility is one of the major factors that influences texture development. Hence there is a need to do more focused experiments to obtain the exact nature of the dependence of mobility on grain boundary properties. Each of the peaks in the mobility curve corresponds to a CSL type. One could see the effect of each CSL by changing the mobility function appropriately. We are presently assuming that one can describe each peak by a Gaussian function centered around particular misorientation. One could in principle also vary the height and the standard deviation (spread) of each Gaussian and study its effects on the system evolution. Increasing the height of each peak can be thought of as the level of anisotropy associated with that CSL boundary while increasing the spread can be thought of as increasing the range of misorientations over which the increased mobility is active.

One could, in a similar manner, study the effects of changing the energy function. This will enable us to identify the relative importance of the various boundary types and the role they may play in controlling the process of recrystallization. Lastly a similar study can be carried out on a completely different material system or a similar system with different properties like deformation etc., thereby testing the robustness and predictive behavior of the model.

Bibliography

[1] W. T. Read and W. Shockley, *Phys. Rev.* **78** p 275 (1950).

[2] W. T. Read, *Dislocations in Crystals* McGraw Hill (1953).

[3] M. L. Kronberg and F. H. Wilson, *Trans. Metall. Soc. A.I.M.E.* **185** p 501 (1949).

[4] F. J. Humphreys and M. Hatherly, *Recrystallization and Related Annealing Phenomena* Pergamon (2002).

[5] H. Mykura, *Grain Boundary Structure and Kinetics* ed. Balluffi, ASM Ohio p 445 (1980).

[6] G. C. Hasson and C. Goux, *Scripta Metall.* **5** p 889 (1971).

[7] D.M. Saylor, J. Fridy, B.S. El-Dasher, K-Y Jung and A.D. Rollett, *Metall. Mater. Trans A* **35A** p 1969 (2004).

[8] K. Shimada and D. Gossard, *ACM Third Symposium on Solid Modeling and Applications* p 409 (1995).

[9] F. Aurenhammer, *ACM Computing Surveys* **23** p 345 (1991).

[10] J O'Rourke, *Computational Geometry in C* Cambridge University Press (1994).

[11] F.P. Preparata and M.I. Shamos, *Computational Geometry* Springer-Verlag (1990).

[12] M. Miodownik, A.W. Godfrey, E.A. Holm and D.A. Hughes, *Acta Mater.* **47** p 2661 (1999).

[13] D. M. Saylor, A. Morawiec, B. L. Adams and G. S. Rohrer, *Interface Science* **8** p 131 (2000).

[14] I.L. Dillamore and H. Katoh, *Met. Sci.* **8** p 151 (1974).

[15] A. A. Ridha and W. B. Hutchinson, *Acta Met.* **30** p 1929 (1982).

[16] H. E. Vatne, R. Sahani and E. Nes, *Acta Mater.* **44** p 4447 (1996).

[17] H. Inagaki and A Umezawa, *14th International Conference on Textures of Materials* p 1273 (2005).

[18] C. S. Barrett, *Trans. Metall. Soc.* A.I.M.E. **137** p 128 (1940).

[19] P. A. Beck, *Advances in Physics* **3** p 245 (1954).

[20] P. A. Beck and H. Hu, *Recrystallization, Grain Growth and Textures* ed Margolin, ASM p 393 (1966).

[21] D. Juul Jensen, *Acta Met.* **43**, 11 p 4117 (1995).

[22] O. Engler, *Acta Mater.* **46** p 1555 (1998).

[23] R. D. Doherty, L-C. Chen and I. Samajdar, *Mat. Sci. and Eng.* **A257** p 18 (1998).

[24] A. Godfrey, D. Juul Jensen and N. Hansen, *Acta Mater.* **49** p 2429 (2001).

[25] W.A. Anderson and R.F. Mehl, *Trans. Metall. Soc.* A.I.M.E. **161** p 140 (1945).

[26] N. Metropolis and S. Ulam, *J. Amer. Stat. Assoc.* **44** p 335 (1949).

[27] E. Ising, *Zeitschrift für Physik* **31** p 253 (1925).

[28] R. B. Potts, *Proc. Cambridge Philosphical Soc.* **48** p 106 (1952).

[29] N. Metropolis, A.W. Rosenbluth, M.N. Rosenbluth, A.H. Teller, and E. Teller, *J. Chem. Physics* **21** p 1087 (1953).

[30] A. B. Bortz, M. H. Kalos, J. L. Lebowitz, *J. Computational Physics* **17** p 10 (1975).

[31] M. A. Novotny, *Computers in Physics* **9(1)** p 46 (1995).

[32] E. A. Holm, J.A. Glazier, D.J. Srolovitz and G. Grest, *Phys. Rev. A* **43** p 2662 (1991).

[33] E. A. Holm, *Ph.D. Thesis* U. Michigan 1992.

[34] A. Rosen, M. S. Burton and G. V. Smith, *Trans. Metall. Soc. A.I.M.E.* **230** p 205 (1964).

[35] J. Hjelen, R. Orsund and E. Nes, *Acta Met.* **39** p 1377 (1991).

[36] P. Gordon and R. A. Vandermeer, *Trans. Metall. Soc.* A.I.M.E. **224** p 917 (1962).

[37] W. R. Hibbard and W. R. Tully, *Trans. Metall. Soc.* A.I.M.E. **221** p 335 (1961).

[38] B. Hutchinson, S Jonsson and L Ryde, *Scripta. Met.* 37, 1047 (1989).

[39] O. Dimitrov, R. Fromageau and C. Dimitrov, *Recrystallization of Metallic Materials* ed. Haessner. Dr. Rieder-Verlag GMBH, Stuttgert p 137 (1978).

[40] J. W. Cahn, *Acta Met.* **4** p 449 (1956).

[41] A. E. Kolmogorov, *Akad. nauk SSSR, Ivz., sr. Mat.* **1** p 335 (1937).

[42] W. A. Johnson and R. F. Mehl, *Trans. Am. Inst. Min. Engrs.* **135** p 416 (1939).

[43] M. Avrami, *J. chem. Phys.* **7** p 1103 (1939).

[44] M. Avrami, *J. chem. Phys.* **8** p 212 (1940).

[45] M. Avrami, *J. chem. Phys.* **9** p 177 (1941).

[46] J. W. Christian, *Theory of Transformation in Metals and Alloys.*

[47] A. D. Rollett, D. J. Sorolovitz, R. D. Doherty and M. P. Anderson, *Acta Met.* **37** p 627 (1989).

[48] M. P. Anderson et al. *Acta Met.* **32** p 783 (1984).

[49] D. J. Srolovitz et al. *Acta Met.* **32** p 793 (1984).

[50] D. J. Srolovitz et al. *Acta Met.* **32** p 1429 (1984).

[51] G. S. Grest et al. *Acta Met.* **33** p 509 (1985).

[52] D. J. Srolovitz et al. *Acta Met.* **33** p 2233 (1985).

[53] A. Borbély, J. H. Driver and T. Ungar, *Acta Mater.* **48** p 2005 (2000).

[54] S. Matthies and F. Wagner , *12th International Conference on Textures of Materials* p 40 (1999).

[55] E. E. Underwood, *Quantitative Stereology* Addison Wesley, Reading, Massachusetts (1970).

[56] M. H. Alvi, S. Cheong, H. Weiland, A. D. Rollett, *Materials Science Forum* **467-470** p 357 (2004).

[57] Y. Huang and F. J. Humphreys, *Acta Mater.* **47** (1999).

[58] M. Upmanyu et al. *Acta Mater.* **46** (1999).

[59] M. Winning. *Acta. Mater.* **51** p 6465 (2003).

[60] M.L. Taheri, A.D. Rollett and H. Weiland, *Material Science Forum* **467-470** p 997 (2004).

[61] M. Winning, A.D. Rollett, *Acta Mater.* **53** p 2901 (2005).

[62] J-H. Cho, A. D. Rollett and K.H. Oh, *Metallurgical and Materials Transactions A* **35A** p 1075 (2004).

Appendix A

Figure A.1 shows location of various components in the 3-D Euler space summarized in the following table. Figure A.1 shows Brass, located in the

Table A.1: Common Texture components in FCC metals

Component	**Euler angles** (ϕ_1, Φ, ϕ_2)	**{hkl} <uvw>**
Cube	(0,0,0)	{001}<100>
Copper	(0,35,45)	{112}<111>
S	(64.93,74.50,33.69)	{231}<124>
Goss	(0,45,0)	{011}<100>
Brass	(35,45,0)	{011}<211>
Dillamore	(0,27,45)	{4,4,11}<11,11,8>

top left corner, Copper, located in the top right corner, S, located on the left in the middle row, Goss, located on the right in the middle row, and Cube, in the bottom left corner. The bottom right shows all of the above components together along with rotated cube (45, 0, 0). The cube component forms a continuous line from $\phi_1 = 90^\circ$ to $\phi_2 = 90^\circ$ because the first and the third Euler angles are linearly dependent when $\Phi = 0^\circ$;

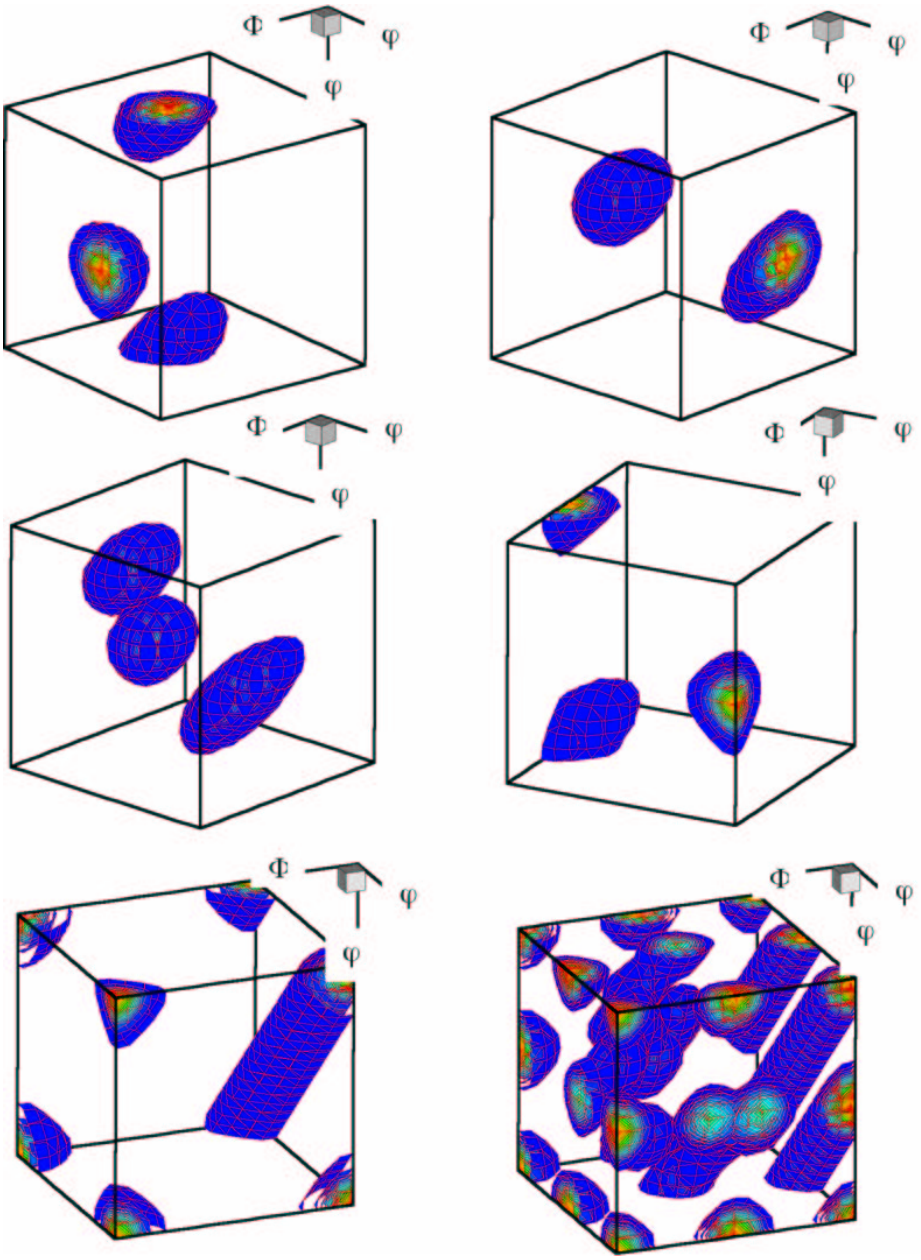

Figure A.1: Location of common FCC texture components in Euler space [62]

Appendix B

Representation of textures

B.1 Pole Figures

A pole figure is a stereographic projection showing the distribution of a particular crystallographic direction in the assembly of grains.

B.2 Inverse Pole Figures

An inverse pole figure shows the position of a sample direction relative to the crystal reference frame.

B.3 Fundamental zone

A crystal having proper rotation symmetries can be rotated to multiple positions, from a reference orientation, which are physically indistinguishable

from each other. The idea of a *fundamental zone* is to limit the orientation space such that the physically indistinguishable rotations are represented only once. Depending on the point group to which the crystal belongs the shape and the extent of the fundamental zone change. The fundamental zone is typically created by including only the orientations having the smallest disorientation value, with respect to the origin, from the set of the physically indistinguishable sets.

The fundamental zone may or may not be bounded depending on the symmetry of the point group. When it is bounded, each point lying outside the fundamental zone has exactly one equivalent point inside the zone. Figure B.1 shows the fundamental zone of the **RF** space for cubic crystals. The volume OACBDE contains all the **RF** vectors defining the misorientation distribution function (MDF). The distance OB $= \sqrt{2} - 1$, and the distance OA $= \frac{1}{3}$

B.4 Euler Angles

One can also use Euler angles to represent textures. A set of three angles is required to represent the texture. The first two Euler Angles ϕ_1 and Φ determine the position of the crystal [001] direction relative to the specimen axes while the third Euler angle ϕ_2 describes the amount of rotation about the crystal [001] direction.

Figure B.2(a) shows the typical Euler space used to represent textures.

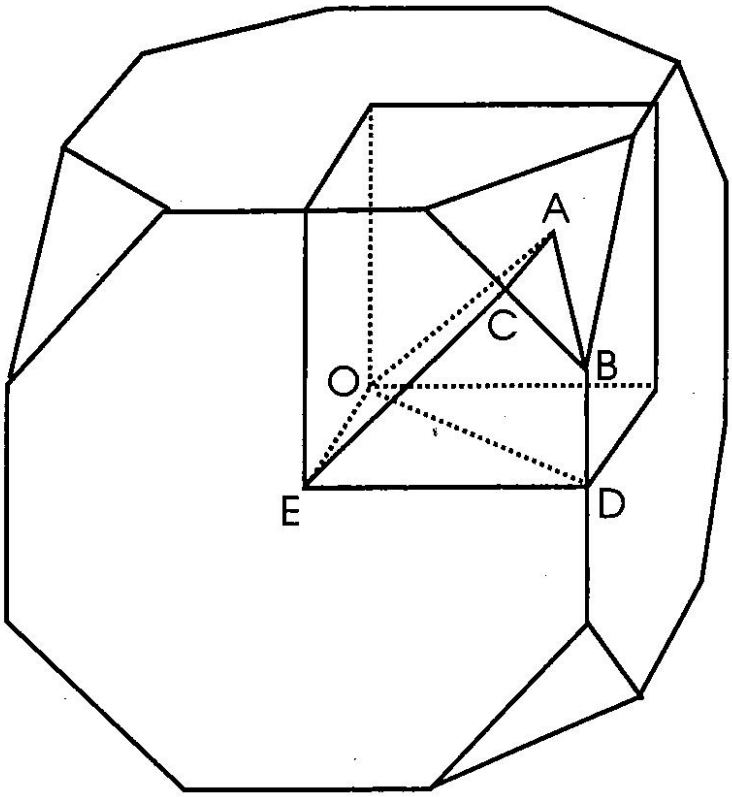

Figure B.1: Fundamental zone of the Rodrigues-Frank space for cubic crystals. Volume OACBDE represents the fundamental zone for the misorientation sapce [4]

Most of the typical FCC components show up at more than one place in the $90 \times 90 \times 90$ Euler space as depicted in figure B.2(a).

The orientation distribution function (ODF) is typically represented in form of slices through the Euler space. Figure B.2(b) shows a representation of the ODF. Each slice through the space has a constant value of ϕ_2.

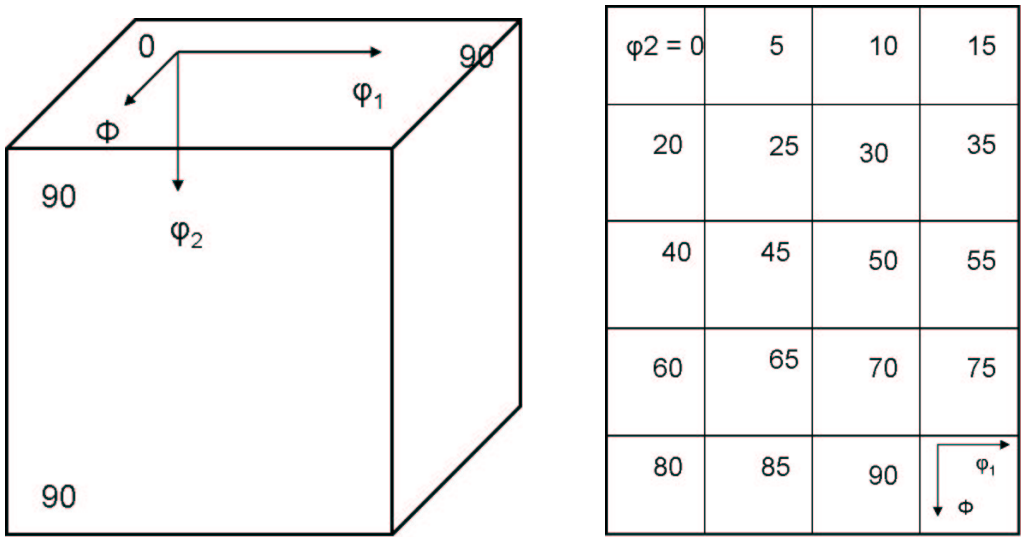

(a) Euler Space

(b) ODF

Figure B.2: $90 \times 90 \times 90$ Euler space and $\phi_2 = const$ slices through the space

Appendix C

Code to calculate stored energy

```
#include <iostream>
#include <fstream>
#include <string>
#include <math.h>
#include <stdio.h>
#include <stdlib.h>
#include <algorithm>
#include <iomanip>

using namespace std;

typedef double quat[4];
typedef double vector[3];

void VectToQ(vector v, quat q);
void QuatToV(quat q, vector v);
double CompTayF(quat, int [], quat [], quat []);
void Rotate(quat, quat, quat);
void NormalizeQ( quat);

int main(){
```

```
  //<variables>
  char inname[50];
  vector v1,v2;
  quat q1;
  int hlines;
  char dummy[300];
  float wt, dumm, tayf;
  int comp[7];
  int optno;
  quat soperators[24];
  quat saperators[4];

  //</variables>

  //read the symmetry operators
  //<crystal symmetry>
  ifstream symmopt("quat.symm.cubic", ios::in);

  if(!symmopt){
    cout<<"Could not open file quat.symm.cubic."<<endl
    <<"This program needs a file with all symmetry operators."
    <<endl;
    exit(1);
  }

  symmopt.getline(dummy,100);
  symmopt>>optno;
  cout<<"optno "<<optno<<endl;
  int i = 0;

  while(symmopt>>soperators[i][0]>>soperators[i][1]>>
soperators[i][2]>>soperators[i][3]){
    i++;
  }
  //</crystal symmetry>

  //<sampl symmetry>
  ifstream samopt("quat.symm.ort", ios::in);
```

```
  if(!samopt){
    cout<<"Could not open file quat.symm.ort."<<endl
    <<"This program needs a file with all symmetry operators."
    <<endl;
    exit(1);
  }

  samopt.getline(dummy,100);
  samopt>>optno;
  cout<<"optno "<<optno<<endl;
  int k = 0;

  while(samopt>>saperators[k][0]>>saperators[k][1]>>
saperators[k][2]>>saperators[k][3]){
    k++;
  }
  //</sample symmetry>

  //-------------

  //output file
  FILE *outf;
  outf = fopen("rexstored.wts","w");

  //the array comp stores the various component counts
  for( int i = 0; i < 7; i++){
    comp[i] = 0;
  }


  //<open the input file and skip over the header>
  cout<<"what is the input file name?\n";
  cin>>inname;
  ifstream inf( inname, ios::in);
  if(!inf){
    cerr<<"could not open file "<<inname<<endl;
    exit(1);
```

```
  }

  cout<<"how many header lines?"<<endl;
  cin>>hlines;
  for( int i = 0; i < hlines; i++){
    inf.getline(dummy,250);
    fprintf(outf, "%s\n",dummy);
  }

  //</open the input file and skip over the header>

  //read data
  while(inf>>v1[0]>>v1[1]>>v1[2]>>wt>>dumm){
  //while(inf>>v1[0]>>v1[1]>>v1[2]>>wt){
   v2 = v1;
    VectToQ(v2, q1);

    tayf = CompTayF(q1,comp, soperators, saperators);

    fprintf(outf, "%1.3f  %1.3f  %1.3f  %3.3f  %3.3f\n",
v1[0], v1[1], v1[2], wt, tayf);

  }
  fstream cfile("comps.txt", ios::out);
  cfile<<"cube \ts \tcopper \tbrass \tgoss \trest"<<endl;
  for( int i = 0; i < 6; i++){
    float temp = (float) comp[i]/comp[6];
    cfile<<setw(3)<<setprecision(3)<<temp<<"\t";
  }
  cerr<<comp[6]<<endl;
  cfile<<endl;
  inf.close();
  fclose(outf);
  return 0;
}

//-----------------------------------
//function declerations
```

```
void VectToQ(vector v, quat q){
  double pi = 4*atan(1);
  for( int i = 0; i < 3; i++){
    v[i] *=(pi/180);
    v[i] = fmod(v[i] + 2*pi, 2*pi);
  }
  q[0] = sin(v[1]/2)*cos((v[0] - v[2])/2);
  q[1] = sin(v[1]/2)*sin((v[0] - v[2])/2);
  q[2] = cos(v[1]/2)*sin((v[0] + v[2])/2);
  q[3] = cos(v[1]/2)*cos((v[0] + v[2])/2);
  NormalizeQ(q);
}

void QuatToV(quat q, vector v){

  double sum;
  double diff;
  double tmp = sqrt(q[2]*q[2] + q[3]*q[3]);
  if(tmp > 1){cerr<<"tmp > 1 "<<tmp<<endl;}
  v[1] = 2*acos(tmp);
  if(q[3] != 0){sum = atan2(q[2],q[3]);}
  else{ sum = 2*atan(1);}
  if(q[0] != 0){diff = atan2(q[1],q[0]);}
  else{ diff = 2*atan(1);}

  v[0] = sum + diff;
  v[2] = sum - diff;
}

void Rotate( quat qrot, quat qin, quat qout){

  //quat qtmp;
  NormalizeQ(qin);
  NormalizeQ(qrot);
  qout[0] = (qrot[0]*qin[3] + qrot[3]*qin[0] -
qrot[1]*qin[2] + qrot[2]*qin[1]);
  qout[1] = (qrot[1]*qin[3] + qrot[3]*qin[1] -
```

```
qrot[2]*qin[0] + qrot[0]*qin[2]);
  qout[2] = (qrot[2]*qin[3] + qrot[3]*qin[2] -
qrot[0]*qin[1] + qrot[1]*qin[0]);
  qout[3] = (qrot[3]*qin[3] - qrot[0]*qin[0] -
qrot[1]*qin[1] - qrot[2]*qin[2]);

  NormalizeQ(qout);

}


void invQuat(double a[], double ainv[]){
  for(int i = 0; i < 3; i++){
    ainv[i] = a[i];
  }
  ainv[3] = (-1)*a[3];
}

void pickAxisAngle(double a[], double b[]){
  sort(a, a + 4);
  double temp1 = a[3];
  double temp2 = (a[2] + a[3])/sqrt(2.0);
  double temp3 = (a[0] + a[1] + a[2] + a[3])/2;
  if( temp1 >= temp2 && temp1 >= temp3){
    for( int i = 0; i < 4; i++){
      b[i] = a[i];
    }
  }
  else if(temp2 > temp3){
    b[0] = (a[0] - a[1])/sqrt(2.0);
    b[1] = (a[0] + a[1])/sqrt(2.0);
    b[2] = (a[2] - a[3])/sqrt(2.0);
    b[3] = (a[2] + a[3])/sqrt(2.0);
  }
  else{
    b[0] = (a[0] -a[1] + a[2] -a[3])/2;
    b[1] = (a[0] + a[1] -a[2] -a[3])/2;
    b[2] = (-a[0] + a[1] + a[2] -a[3])/2;
```

```
    b[3] = (a[0] +a[1] + a[2] + a[3])/2;
  }
}

 void combineQuat(double a[], double b[], double c[]){
   c[0] = (a[0]*b[3] + a[3]*b[0] - a[1]*b[2] + a[2]*b[1]);
   c[1] = (a[1]*b[3] + a[3]*b[1] - a[2]*b[0] + a[0]*b[2]);
   c[2] = (a[2]*b[3] + a[3]*b[2] - a[0]*b[1] + a[1]*b[0]);
   c[3] = (a[3]*b[3] - a[0]*b[0] - a[1]*b[1] - a[2]*b[2]);
 }

void deltaQ( double q1[], double q2[], double dq[]){

  NormalizeQ(q1);
  NormalizeQ(q2);

  double q2inv[4];
  double tempq[4];

  invQuat( q2 , q2inv);
  combineQuat( q1, q2inv, tempq);
  //Rotate(q1, q2inv, tempq);
  for( int i = 0; i < 4; i++){
    tempq[i] = fabs(tempq[i]);
  }
  pickAxisAngle(tempq, dq);
}


int closeTo(quat q1, quat sop[], quat sap[]){

  double pi = 4*atan(1);
  quat tsquat, mquat;
  float temp = 360;
  int rvalue = 15;
  float disort = 360;
  //float qm = 0;
  quat qr1;
```

```
int compno = 8;
vector vcomp[compno];
quat qcomp[compno];


//<components>
//cube
vcomp[0][0] = 0;
vcomp[0][1] = 0;
vcomp[0][2] = 0;

//RDcube10
vcomp[1][0] = 0;
vcomp[1][1] = 10;
vcomp[1][2] = 0;

//RDcube20
vcomp[2][0] = 0;
vcomp[2][1] = 20;
vcomp[2][2] = 0;

//RDcube30
vcomp[3][0] = 0;
vcomp[3][1] = 30;
vcomp[3][2] = 0;

//S
vcomp[4][0] = 64.9339981;
vcomp[4][1] = 74.4990005;
vcomp[4][2] = 33.6899986;

//copper
vcomp[5][0] = 40;
vcomp[5][1] = 65;
vcomp[5][2] = 26;

//brass
vcomp[6][0] = 35;
```

```
  vcomp[6][1] = 45;
  vcomp[6][2] = 0;

  //goss
  vcomp[7][0] = 0;
  vcomp[7][1] = 45;
  vcomp[7][2] = 0;

  for( int i = 0; i < compno; i++){
    VectToQ(vcomp[i], qcomp[i]);
  }

  //</components>

  //<new>

  for( int i = 0; i < 4; i++){
    Rotate(q1, sap[i], tsquat);
    for(int j = 0; j < 24; j++){
      Rotate( sop[j], tsquat, qr1);
    for( int k = 0; k < compno; k++){
  deltaQ(qr1, qcomp[k], mquat);
disort = acos(fabs(mquat[3]))*360/pi;
if(disort < temp){
  temp = disort;
  rvalue = k;
}
      }
    }
  }
  if(temp > 15){
    rvalue  = 15;
  }

  //</new>

  return rvalue;
}
```

```
//--------------


double CompTayF(quat q, int comp[], quat sop[], quat sap[]){
  double tayf = 0;
  int ctype;
  ctype = closeTo(q, sop, sap);

  if(ctype == 0 || ctype == 1 || ctype == 2 || ctype == 3){
    tayf = 1.0;
    comp[0]++;
    comp[6]++;
  }
  else if(ctype == 4){
    tayf = 1.27;
    comp[1]++;
    comp[6]++;
  }
  else if(ctype == 5){
    tayf = 1.24;
    comp[2]++;
    comp[6]++;
  }
  else if(ctype == 6){
    tayf = 1.23;
    comp[3]++;
    comp[6]++;
  }
  else if(ctype == 7){
    tayf = 1.0;
    comp[4]++;
    comp[6]++;
  }
  else{
    tayf = 1.0;
    comp[5]++;
    comp[6]++;
```

```
  }
  return tayf;
}

void NormalizeQ(quat qtonorm){
  double mag = 0;
  for( int i = 0; i < 4; i++){
    mag += qtonorm[i]*qtonorm[i];
  }
  mag = sqrt(mag);
  for( int i = 0; i < 4; i++){
    qtonorm[i] /= mag;
  }
}
```

Appendix D

Code to nucleate a microstructure

```
/*
Input files
  micro.input ! input microstructure
  texin1      ! texture of deformed micro
  texin2      ! texture to be assigned to the nuclei
  quat.symm.cubic
  quat.symm.ort

Output files
  micro.nuc

The algorithm in brief
1. read the data microstructure, probability matrix
2. Build a list of sites on g. boundary
3. pick a site from this list
4. if recrystallized remove from list and go to 3
5. if site has 2 or more unrex neighbors proceed else go to 3
6. read the texture of this site
7. pick a nuclei texture (identical to picking a q value)
8. check with prob. matrix of putting a
nucleus at particular site
9. if succesful delete site from list go to 3 else go to 3
10. repeat above till required nuclei generated
```

```
component # def/rex comp
0 cube
1 brass
2 copper
3 S
4 rest

 */

#include <iostream>
#include <fstream>
#include <string>
#include <math.h>
#include <stdio.h>
#include <stdlib.h>
#include <algorithm>
#include <iomanip.h>
#include <vector.h>

using namespace std;

typedef double quat[4];
typedef double vect[3];
//typedef int * site;
typedef struct{
  int coord[3];
} site;


void VectToQ(vect v, quat q);
void QuatToV(quat q, vect v);
void Rotate(quat, quat, quat);
void NormalizeQ( quat);
int *** readData(int ***m, int &, int &, int &);
void writeData(int ***m, int, int, int, fstream &);
void getBoundary(int ***, int, int , int, vector<site> &);
void neighs(int , int , int , int , int [], int[]);
```

```
void readCSymm(quat []);
void readSSymm(quat []);
void readTex(quat []);
void readProb(int [5][5], long int &);
int closeTo(quat q1, quat sop[], quat sap[], float);

int main(){
  int ***micro;
  //float **tex;
  quat csymm[24];
  quat ssymm[4];
  int xdim, ydim, zdim;
  char buf[300];
  int temp, dim[3];
  vector<site> boun;
  site cursite;
  float nuc_frac = 0.06;
  long int target_frac;
  int q2 = 817;
  int q = 1634;
  quat tex[3501];
  int Pmatrix[5][5];

  micro = readData(micro, xdim, ydim, zdim);

  ifstream infD("micro100", ios::in);
  fstream outD("micro.nuc", ios::out);

  infD>>xdim>>ydim>>zdim;
  outD<<" "<<xdim<<" "<<ydim<<" "<<zdim<<" "<<endl;
  infD.getline(buf,300);
  infD.getline(buf,300);
  outD<<buf<<endl;
  infD.getline(buf,300);
  outD<<buf<<endl<<" ";
  target_frac = (long int)( (xdim*ydim*zdim) * nuc_frac);
  infD.close();
  //  outD.close();
```

```
  cout<<xdim<<" "<<ydim<<" "<<zdim<<" "<<endl;
  cerr<<"Read the data from micro.input"<<endl;

  readCSymm(csymm);
  readSSymm(ssymm);
  cout<<target_frac<<endl;
  readTex(tex);
  cout<<target_frac<<endl;
  readProb(Pmatrix, target_frac);

  for( int i = 0; i < 5; i++){
    for(int j = 0; j < 5; j++){
      cout<<Pmatrix[i][j]<<" ";
    }
    cout<<endl;
  }

  dim[0] = xdim;
  dim[1] = ydim;
  dim[2] = zdim;

//   int initial[xdim][ydim][zdim];
//   for(int i = 0; i < xdim; i++){
//     for(int j = 0; j < ydim; j++){
//       for(int k = 0; k < zdim; k++){
//  initial[i][j][k] = micro[i][j][k];
//       }
//     }
//   }

  getBoundary(micro, xdim, ydim, zdim, boun);
  //pickSite(micro);
  cout<<boun.size()<<"  "<<target_frac<<endl;

  int frac = 0;
  int fpflag = 0;
  while(target_frac > frac){
    int nuc_site = rand()%boun.size();
```

```
//trial site to insert a nuclei

    int loc[3]; // x, y and z coordinates of the trial site
    //x, y and z coordinates of the nearest neighbor
    int nnbr[3];
    int rex_nbrs = 0;
    int newspin = 0;
    int oldspin = 0;
    int nsite = 0;
    int rexcomp = 10;
    int defcomp = 10;

    if(frac % 1000 == 0 && fpflag != 1){
      cout<<frac<<endl;
      fpflag = 1;
    }
    loc[0] = boun[nuc_site].coord[0];
    loc[1] = boun[nuc_site].coord[1];
    loc[2] = boun[nuc_site].coord[2];

    //if the site already rex then delete from the list
    if( (micro[loc[0]] [loc[1]] [loc[2]]) > q2){
      boun.erase(boun.begin() + nuc_site);
    }
    else{
      for( int nbr = 0; nbr < 27; nbr++){
neighs(loc[0], loc[1], loc[2], nbr, nnbr, dim);

//check nbrs rex
if((micro[nnbr[0]] [nnbr[1]] [nnbr[2]] <= q2)){
  rex_nbrs++;
}
      }
      if(rex_nbrs >= 3){
oldspin = micro[loc[0]][loc[1]][loc[2]];
newspin = q2 + rand()%(q2 - 1) + 1;
rexcomp = closeTo(tex[newspin], csymm, ssymm, 15.0);
defcomp = closeTo(tex[oldspin], csymm, ssymm, 15.0);
```

```
if(rexcomp <= 3){
  rexcomp = 0;
}
else{
  rexcomp -= 3;
}
if(defcomp <= 3){
  defcomp = 0;
}
else{
  defcomp -= 3;
}

if(Pmatrix[rexcomp][defcomp] > 0 ){
  Pmatrix[rexcomp][defcomp] -= 3;
  (micro[loc[0]][loc[1]][loc[2]]) = newspin;
  boun.erase(boun.begin() + nuc_site);
  for( int nbr = 0; nbr < 27; nbr++){
    neighs(loc[0], loc[1], loc[2], nbr, nnbr, dim);
    if((micro[nnbr[0]] [nnbr[1]] [nnbr[2]] <= q2)
       && (nsite < 2) ){ //check nbrs rex
      micro[nnbr[0]] [nnbr[1]] [nnbr[2]] = newspin;
      nsite++;
    }
  }
  nsite = 0;
  frac += 3;
  fpflag = 0;
  //cerr<<"rexcomp "<<rexcomp<<" defcomp "<<defcomp<<endl;
}

      }
    }
  }
    cout<<boun.size()<<endl;

    writeData(micro, xdim, ydim, zdim, outD);
```

```
  for( int i = 0; i < 5; i++){
    for(int j = 0; j < 5; j++){
      cout<<Pmatrix[i][j]<<" ";
    }
    cout<<endl;
  }

    outD.close();
  return 0;
}
//-------------------------------------
//function declerations

int *** readData(int ***m, int &xdim, int &ydim, int &zdim){

  char buf[300];
  int temp;

  ifstream infD("micro100", ios::in);
  infD>>xdim>>ydim>>zdim;
  cout<<xdim<<" "<<ydim<<" "<<zdim<<" "<<endl;
  infD.getline(buf,300);
  infD.getline(buf,300);
  infD.getline(buf,300);

  m = (int***)calloc(xdim, sizeof(int**));
  for(int i = 0; i < xdim; i++){
    m[i] = (int**)calloc(ydim, sizeof(int*));
    for(int j = 0; j < ydim; j++){
      m[i][j] = (int*)calloc(zdim, sizeof(int));
    }
  }
  for(int k = 0; k < zdim; k++){
    for(int j = 0; j < ydim; j++){
      for(int i = 0; i < xdim; i++){
infD>>temp;
m[i][j][k] = temp;
      }
```

```
    }
  }

  infD.close();
  return m;
}

//-----------------------------
void writeData(int ***m, int xdim, int ydim,
       int zdim, fstream & outD){

  cout<<xdim<<" "<<ydim<<" "<<zdim<<" "<<endl;

  for(int k = 0; k < zdim; k++){
    for(int j = 0; j < ydim; j++){
      for(int i = 0; i < xdim; i++){
outD<<setw(5)<<m[i][j][k]<<" ";
if( (i + 1) == xdim && (j + 1) == ydim && (k + 1) == zdim )
{
  outD<<endl;
}
else if(((i+1)%20) == 0){
  outD<<endl<<" ";
}

//cout<<temp<<endl;
      }
    }
  }
  //  outD.close();
}

//---------

void readCSymm( quat symm[24]){
  ifstream infC("quat.symm.cubic", ios::in);
  if(!infC){
    cerr<<"could not open file "<<infC<<endl;
```

```
    exit(1);
  }
  char buf[300];
  int i = 0;

  infC.getline(buf,300);

  while(infC>>symm[i][0]>>symm[i][1]>>symm[i][2]>>symm[i][3]){
    i++;
  }
  assert(i == 24);
}

//--------

void readSSymm( quat symm[4]){
  ifstream infS("quat.symm.ort", ios::in);
  if(!infS){
    cerr<<"could not open file "<<infS<<endl;
    exit(1);
  }
  char buf[300];
  int i = 0;

  infS.getline(buf,300);

  while(infS>>symm[i][0]>>symm[i][1]>>symm[i][2]>>symm[i][3]){
    i++;
  }
  assert(i == 4);
}

//--------

void readTex(quat A[]){

  char buf[200];
  float dum1, dum2;
```

```
float phi1, Phi, phi2;
int countorts = 0;
vect v;
ifstream inT1("texin1", ios::in);
assert(inT1);
ifstream inT2("texin2", ios::in);
assert(inT2);

inT1.getline(buf,200);
inT1.getline(buf,200);
inT1.getline(buf,200);
inT1.getline(buf,200);
cout<<__FILE__<<"  "<<__LINE__<<endl;
while(inT1>>phi1>>Phi>>phi2>>dum1>>dum2){
  v[0] = phi1;
  v[1] = Phi;
  v[2] = phi2;
  VectToQ(v,A[countorts]);
  countorts++;
}
  cout<<countorts<<endl;

inT2.getline(buf,200);
inT2.getline(buf,200);
inT2.getline(buf,200);
inT2.getline(buf,200);

while(inT2>>phi1>>Phi>>phi2>>dum1>>dum2){
  v[0] = phi1;
  v[1] = Phi;
  v[2] = phi2;
  VectToQ(v,A[countorts]);
  countorts++;
}
cout<<__FILE__<<"  "<<__LINE__<<endl;
cout<<countorts<<endl;
assert(countorts == 3501);
```

```
  inT1.close();
  inT2.close();
}

//--------

void readProb( int A[5][5], long int & tot){

  int i = 0;
  int sites = 0;
  float B[5][5];
  ifstream inP("texTable.txt", ios::in);
  assert(inP);
  while(inP>>B[i][0]>>B[i][1]>>B[i][2]>>B[i][3]>>B[i][4]){
    for(int j = 0; j < 5; j++){
      A[i][j] = (int) (tot*B[i][j]);
      sites += A[i][j];
    }
    i++;
  }
  tot = sites;
  assert(i == 5);
  inP.close();
}

//--------

void neighs(int isite, int jsite, int ksite,
    int n, int nn[3], int dim[3]){

  int xdim = dim[0];
  int ydim = dim[1];
  int zdim = dim[2];


  nn[2] = (dim[2] + ksite + n%3 - 1)%dim[2];
  if( n < 3){
    nn[1] = (dim[1] + jsite - 1)%dim[1];
```

```
  }
  else{
    nn[1] = (dim[1] + jsite + (n/3)%3 - 1)%dim[1];
  }
  if( n < 9){
    nn[0] = (dim[0] + isite - 1)%dim[0];
  }
  else{
    nn[0] = (dim[0] + isite + (n/9)%3 - 1)%dim[0];
  }

}

//-------

void getBoundary(int ***m, int xdim, int ydim,
 int zdim, vector<site> &V)
{

  site cursite;
  int likes = 0;
  int nn[3], dim[3];
  int nspin, spin;

  dim[0] = xdim;
  dim[1] = ydim;
  dim[2] = zdim;

  for(int k = 0; k < zdim; k++){
    for(int j = 0; j < ydim; j++){
      for(int i = 0; i < xdim; i++){
likes = 0;
    for( int n = 0; n < 27; n++){
  if(n != 13){
    neighs(i, j, k, n, nn, dim);
    nspin = m[nn[0]][nn[1]][nn[2]];
    spin = m[i][j][k];
    if(nspin == spin){
```

```
      likes++;
    }
  }
}
if(likes < 17){
  cursite.coord[0] = i;
  cursite.coord[1] = j;
  cursite.coord[2] = k;
  V.push_back(cursite);
}
      }
    }
  }
}

void VectToQ(vect v, quat q){
  double pi = 4*atan(1);
  for( int i = 0; i < 3; i++){
    v[i] *=(pi/180);
    v[i] = fmod(v[i] + 2*pi, 2*pi);
  }
  q[0] = sin(v[1]/2)*cos((v[0] - v[2])/2);
  q[1] = sin(v[1]/2)*sin((v[0] - v[2])/2);
  q[2] = cos(v[1]/2)*sin((v[0] + v[2])/2);
  q[3] = cos(v[1]/2)*cos((v[0] + v[2])/2);
  NormalizeQ(q);
}

void QuatToV(quat q, vect v){

  double sum;
  double diff;
  double tmp = sqrt(q[2]*q[2] + q[3]*q[3]);
  if(tmp > 1){cerr<<"tmp > 1 "<<tmp<<endl;}
  v[1] = 2*acos(tmp);
  if(q[3] != 0){sum = atan2(q[2],q[3]);}
  else{ sum = 2*atan(1);}
  if(q[0] != 0){diff = atan2(q[1],q[0]);}
```

```
  else{ diff = 2*atan(1);}

  v[0] = sum + diff;
  v[2] = sum - diff;
}

void Rotate( quat qrot, quat qin, quat qout){

  NormalizeQ(qin);
  NormalizeQ(qrot);
  qout[0] = (qrot[0]*qin[3] + qrot[3]*qin[0] -
qrot[1]*qin[2] + qrot[2]*qin[1]);
  qout[1] = (qrot[1]*qin[3] + qrot[3]*qin[1] -
qrot[2]*qin[0] + qrot[0]*qin[2]);
  qout[2] = (qrot[2]*qin[3] + qrot[3]*qin[2] -
qrot[0]*qin[1] + qrot[1]*qin[0]);
  qout[3] = (qrot[3]*qin[3] - qrot[0]*qin[0] -
qrot[1]*qin[1] - qrot[2]*qin[2]);

  NormalizeQ(qout);

}


void invQuat(double a[], double ainv[]){
  for(int i = 0; i < 3; i++){
    ainv[i] = a[i];
  }
  ainv[3] = (-1)*a[3];
}

void pickAxisAngle(double a[], double b[]){
  sort(a, a + 4);
  double temp1 = a[3];
  double temp2 = (a[2] + a[3])/sqrt(2.0);
  double temp3 = (a[0] + a[1] + a[2] + a[3])/2;
  if( temp1 >= temp2 && temp1 >= temp3){
    for( int i = 0; i < 4; i++){
```

```
      b[i] = a[i];
    }
  }
  else if(temp2 > temp3){
    b[0] = (a[0] - a[1])/sqrt(2.0);
    b[1] = (a[0] + a[1])/sqrt(2.0);
    b[2] = (a[2] - a[3])/sqrt(2.0);
    b[3] = (a[2] + a[3])/sqrt(2.0);
  }
  else{
    b[0] = (a[0] -a[1] + a[2] -a[3])/2;
    b[1] = (a[0] + a[1] -a[2] -a[3])/2;
    b[2] = (-a[0] + a[1] + a[2] -a[3])/2;
    b[3] = (a[0] +a[1] + a[2] + a[3])/2;
  }
}

 void combineQuat(double a[], double b[], double c[]){
   c[0] = (a[0]*b[3] + a[3]*b[0] - a[1]*b[2] + a[2]*b[1]);
   c[1] = (a[1]*b[3] + a[3]*b[1] - a[2]*b[0] + a[0]*b[2]);
   c[2] = (a[2]*b[3] + a[3]*b[2] - a[0]*b[1] + a[1]*b[0]);
   c[3] = (a[3]*b[3] - a[0]*b[0] - a[1]*b[1] - a[2]*b[2]);
 }

void deltaQ( double q1[], double q2[], double dq[]){

  NormalizeQ(q1);
  NormalizeQ(q2);

  double q2inv[4];
  double tempq[4];

  invQuat( q2 , q2inv);
  combineQuat( q1, q2inv, tempq);
  for( int i = 0; i < 4; i++){
    tempq[i] = fabs(tempq[i]);
  }
  pickAxisAngle(tempq, dq);
```

```
}


int closeTo(quat q1, quat sop[], quat sap[], float angle){

  double pi = 4*atan(1);
  quat tsquat, mquat;
  float temp = 360;
  int rvalue = 15;
  float disort = 360;
  quat qr1;
  int compno = 8;
  vect vcomp[compno];
  quat qcomp[compno];


  //<components>
  //cube
  vcomp[0][0] = 0;
  vcomp[0][1] = 0;
  vcomp[0][2] = 0;

  //RDcube10
  vcomp[1][0] = 0;
  vcomp[1][1] = 10;
  vcomp[1][2] = 0;

  //RDcube20
  vcomp[2][0] = 0;
  vcomp[2][1] = 20;
  vcomp[2][2] = 0;

  //RDcube30
  vcomp[3][0] = 0;
  vcomp[3][1] = 30;
  vcomp[3][2] = 0;

  //copper
```

```
  vcomp[4][0] = 40;
  vcomp[4][1] = 65;
  vcomp[4][2] = 26;

  //brass
  vcomp[5][0] = 35;
  vcomp[5][1] = 45;
  vcomp[5][2] = 0;

  //S
  vcomp[6][0] = 64.9339981;
  vcomp[6][1] = 74.4990005;
  vcomp[6][2] = 33.6899986;

  for( int i = 0; i < compno; i++){
    VectToQ(vcomp[i], qcomp[i]);
  }

  //</components>

  //<new>

  for( int i = 0; i < 4; i++){
    Rotate(q1, sap[i], tsquat);
    for(int j = 0; j < 24; j++){
      Rotate( sop[j], tsquat, qr1);
    for( int k = 0; k < compno; k++){
  deltaQ(qr1, qcomp[k], mquat);
disort = acos(fabs(mquat[3]))*360/pi;
if(disort < temp){
  temp = disort;
  rvalue = k;
}
      }
    }
  }
  if(temp > angle){
    rvalue  = 7;
```

```
  }

  //</new>

  return rvalue;
}

void NormalizeQ(quat qtonorm){
  double mag = 0;
  for( int i = 0; i < 4; i++){
    mag += qtonorm[i]*qtonorm[i];
  }
  mag = sqrt(mag);
  for( int i = 0; i < 4; i++){
    qtonorm[i] /= mag;
  }
}


//--------------
```